

Phase-field modeling of unidirectionally solidified microstructures under diffusive-convective regime

Zur Erlangung des akademischen Grades eines
Doktors der Ingenieurwissenschaften
(Dr.-Ing.)

von der KIT-Fakultät für Maschinenbau
des Karlsruher Instituts für Technologie (KIT)

genehmigte
Dissertation

von

M. Sc, Pavan Laxmipathy Veluvali

Tag der mündlichen Prüfung: 8th April 2021

Hauptreferent: Prof. Dr. rer. nat. Britta Nestler

Korreferent: Prof. Dr. Hans Jürgen Seifert



This work is licensed under the Creative Commons Attribution-ShareAlike 4.0 International License (CC BY-SA 4.0). To view a copy of this license, visit <http://creativecommons.org/licenses/by-sa/4.0/> .

Abstract

Modern materials are often characterized by a wide spectrum of tailored mechanical, magnetic, electronic, or thermophysical properties. Connected to their underlying microstructure, the behavior of most engineered materials can be predicted via accurately modeling the novel characteristics with tailor-made morphologies. In general, the formation of solidification microstructures is governed by the interplay of thermal and solutal fields with capillarity. Often neglected due to its complexity, the presence of melt convection plays a significant role in the final structural properties of cast alloys. Since microstructure control is essential for any processing activity, in this dissertation, a phase-field model with liquid phase convection is employed, wherein the interaction of diffusive-convective fields and their effect on microstructure evolution is studied.

From grain boundaries to columnar dendrites, the numerical results under diffusive-convective regime are discussed in the following part. To begin with, a phase-field model is employed to study the phenomenon of grain boundary grooving under equilibrium conditions. The model is validated via comparing the groove kinetics with the volume diffusion governed grooving theory. In the form of melt convection, the role of an additional convective transport mechanism on grain boundary grooves is extensively investigated for the first time. The simulated grooves depict an excellent agreement with previous experimental as well as with the sharp interface theory. Besides, the migration of the solid-solid grain boundary is also captured, where the emergence of asymmetric ridges promote the lateral drift of the groove root along the downstream direction.

Moreover, the initiation of microstructural patterns for energetically isotropic interfaces is presented, where the prediction of tip splitting position is discussed through an analytical criterion. As a result of curvature driven fluxes, the fundamental and repeating unit of tip splitting microstructures is analyzed through a direct comparison between the phase-field and the sharp interface tip splitting position. As opposed to the existing studies, the proposed criterion successfully predicts the branching position in a solidifying interface. Subsequently, the influence of other parameters such as interfacial anisotropy, melt convection and surface energies on the structural transition of tip splitting microstructures is established. While a tip splitting morphology is observed for an isotropic crystal growth, the emergence of directionally dependent columnar dendrites is demonstrated for anisotropic interfaces.

Afterwards, the prediction of inter-dendritic arm spacing in the presence of melt convection is examined. In tune with earlier experimental studies, it is shown that the selection mechanism of primary arms by dendrite submergence in the diffusive regime translates into the overgrowth of tertiary arms in the diffusive-convective regime. Furthermore, it is revealed that the prediction of primary dendrite arm spacing is modified due to the presence of convective transport in the inter-dendritic region. Thereafter, phase-field simulations are performed to predict the growth competition of columnar dendrites converging at the grain boundary. Commonly studied during the production of single crystal turbine blades, the overgrowth behaviors of misoriented dendrites at the grain boundary are captured and analyzed. For the first time, it is shown that the presence of an additional mass transport in the bulk liquid phase advects the solute dendritic tips, which in turn modifies the overgrowth mechanism at the grain boundary. Through microstructural selection maps, it is also concluded that parameters such as misorientation angle and interfacial anisotropy largely control the overgrowth dynamics at the grain boundary.

Kurzfassung

Moderne Werkstoffe zeichnen sich oft durch ein breites Spektrum an maßgeschneiderten mechanischen, magnetischen, elektronischen oder thermophysikalischen Eigenschaften aus. In Verbindung mit der ihnen zugrundeliegenden Mikrostruktur kann das Verhalten der meisten technischen Werkstoffe durch genaue Modellierung der neuartigen Eigenschaften mit maßgeschneiderten Morphologien vorhergesagt werden. Im Allgemeinen wird die Bildung von Erstarrungsmikrostrukturen durch das Wechselspiel zwischen Kapillarität und Diffusion bestimmt. Das Vorhandensein von Schmelzekonvektion spielt eine bedeutende Rolle für die endgültigen Gefügeeigenschaften von Gusslegierungen und wird aufgrund seiner Komplexität oft vernachlässigt. Da die Kontrolle der Mikrostruktur für jede Verarbeitungsaktivität von wesentlicher Bedeutung ist, wird in dieser Dissertation ein Phasenfeldmodell mit Flüssigphasenkonvektion verwendet, in dem die Wechselwirkung von diffusiv-konvektiven Feldern und deren Auswirkung auf die Gefügeentwicklung untersucht wird.

Im folgenden Teil werden die numerischen Ergebnisse unter einem diffusionskonvektiven Regime von den Korngrenzen bis zu den Säulendendriten diskutiert. Zunächst wird ein Phasenfeldmodell verwendet, um das Phänomen des Korngrenzenrillens unter Gleichgewichtsbedingungen zu untersuchen. Das Modell wird validiert, indem die Rillenkinetik mit der volumendiffusionsgesteuerten Rillentheorie verglichen wird. In Form der Schmelzkonvektion wird erstmals die Rolle eines zusätzlichen konvektiven Transportmechanismus auf Korngrenzenrillen eingehend untersucht. Die simulierten Rillen zeigen eine hervorragende Übereinstimmung mit früheren experimentellen Theorien sowie mit der Theorie der scharfen Grenzflächen. Daneben wird auch die Wanderung der Fest-Fest-Korngrenze erfasst, wobei das Auftreten asymmetrischer Grate die seitliche Drift der Rillenwurzel entlang der stromabwärtigen Richtung fördert.

Darüber hinaus wird die Initiierung von Mikrostrukturmustern für energetisch isotrope Grenzflächen vorgestellt, wobei die Vorhersage der Spitzenaufteilungsposition anhand eines analytischen Kriteriums diskutiert wird. Infolge von krümmungsgetriebenen Flüssen wird die fundamentale und sich wiederholende Einheit von Mikrostrukturen mit Spitzenspaltung durch einen direkten Vergleich zwischen dem Phasenfeld und der Position der scharfen Grenzflächenspitze analysiert. Im Gegensatz zu den vorhandenen Studien sagt das vorgeschlagene Kriterium die Verzweigungsposition in einem erstarrenden Muster

erfolgreich voraus. Anschließend wird der Einfluss anderer Parameter wie der Grenzflächenanisotropie, der Schmelzkonvektion und der Oberflächenenergien auf den strukturellen Übergang von Mikrostrukturen mit Spitzenspaltung ermittelt. Während für ein isotropes Kristallwachstum eine Morphologie der Spitzenaufspaltung beobachtet wird, wird für anisotrope Grenzflächen das Auftreten von richtungsabhängigen säulenförmigen Dendriten demonstriert.

Anschließend wird die Vorhersage des interdendritischen Armabstands bei vorhandener Schmelzkonvektion untersucht. In Übereinstimmung mit früheren experimentellen Studien wird gezeigt, dass der Selektionsmechanismus von Primärarmen durch das Eintauchen von Dendriten in das Diffusionsregime zum Überwachsen von Tertiärarmen im Diffusionskonvektionsregime führt. Darüber hinaus zeigt sich, dass die Vorhersage des primären Dendritenarmabstands aufgrund des Vorhandenseins eines konvektiven Transports im interdendritischen Bereich modifiziert ist. Danach werden Phasenfeldsimulationen durchgeführt, um die Wachstumskonkurrenz von Säulendendriten vorherzusagen, die an der Korngrenze konvergieren. Während der Herstellung von Einkristall-Turbinenschaufeln häufig untersucht, wird das Überwuchsverhalten von falsch ausgerichteten Dendriten an der Korngrenze erfasst und analysiert. Zum ersten Mal wird gezeigt, dass das Vorhandensein eines zusätzlichen Massentransports in der flüssigen Massenphase die gelösten dendritischen Spitzen fördert, was wiederum den Überwuchsmechanismus an der Korngrenze modifiziert. Durch mikrostrukturelle Auswahlkarten wird auch gezeigt, dass Parameter wie der Fehlorientierungswinkel und die Grenzflächenanisotropie die Überwuchsdynamik an der Korngrenze weitgehend steuern.

Acknowledgements

Why do we fall Master Wayne? So we can learn to pick ourselves up - this quote by Alfred Pennyworth from The Dark Knight trilogy sums up my doctoral journey as I look back while writing this section.

Foremost, I would like to express my sincere gratitude to my advisor, Prof. Dr. rer. nat. Britta Nestler for accepting me as a doctoral candidate under her supervision at the Institute of Applied Materials - Computational Materials Science (IAM-CMS), Karlsruhe Institute of Technology. Thank you, Britta, for your immense support, encouragement and invaluable suggestions that allowed my doctoral studies to go the extra mile. Your insightful feedback pushed me to sharpen my thinking and brought my work to a higher level. Further, I would also like to thank and acknowledge the rest of my thesis committee members, namely, my second referee, Prof. Dr. Hans Jürgen Seifert, and my committee chair, Prof. Dr. -Ing. Wolfgang Seemann for discussing the doctoral examination procedure in detail.

I would also like to extend my gratitude to Prof. Kumar Ankit and Dr. Michael Selzer for helping me get started in the group. Thank you for your constructive comments, and warm encouragements that steered me through this research. Insightful discussions with my colleagues at IAM-CMS, Dr. Fei Wang, Dr. Amol Subhedar, Dr. E.S. Nani, and Dr. Arnab Mukherjee were vital in inspiring me to think outside the box, from multiple perspectives to form a comprehensive and objective critique. I am particularly grateful to Dr. Anastasia August for assisting and coordinating the Promotionskolleg program. I would also like to acknowledge Leon Geisen for his editorial support, and for translating the abstract into German. Heartfelt thanks to my colleagues at Raum 110.1, namely, Andres, Willi, Patrick, Farshid, Halil. To start the day with analyzing and discussing football games made my week eventful. Cheers to all our Go-karting, bowling and other activities in the pre-covid days.

I would also like to acknowledge and thank the cooperative ‘Gefügestructuranalyse und Prozessbewertung’ by the Ministry of Wissenschaft, Forschung und Kunst (MWK) of the state of Baden-Württemberg, Germany for funding my doctoral project.

My deepest gratitude belongs to my family members, especially my parents who have been supportive throughout my life. You are always there for me, and for which my mere

expression of thanks likewise does not suffice. Special thanks to my closest friend, Sriram, for keeping me sane with late night sessions on music, films, and thus providing happy distractions outside of my research. Lastly, although this feels like an end of a journey, it is, perhaps, the end of a beginning. Onwards and upwards to future endeavors in life.

Karlsruhe, April 2021.

Pavan Laxmipathy Veluvali

Contents

List of Figures	xi
List of Tables	xxiii
Introduction and Literature review	2
1 Introduction: Motivation and Outline	3
1.1 Motivation	3
1.2 Outline	4
2 Unidirectional solidification of microstructures	7
2.1 Interfacial instabilities in single crystals	8
2.2 Interfacial instabilities in polycrystals	9
2.3 Constitutional supercooling	12
2.4 Linear morphological stability	15
2.4.1 Microstructural patterns	16
2.5 Dendritic microstructures	17
2.5.1 Unidirectional growth of columnar dendrites	20
2.5.2 Dendritic growth competition	23
2.6 Diffusive-convective regime	24
Methods	27
3 Phase-field modeling	29
3.1 Phase-field variable and free energy functional	30
3.2 Dynamics of conserved and non-conserved order parameter	31

3.3	Interface structure and energy	33
3.4	Phase-field models for solidification	35
4	Grand potential based multi-phase field model	41
4.1	Grand chemical potential modeling approach	41
4.1.1	Anti-trapping current	45
4.1.2	Thermal fluctuations	46
4.2	Relation to sharp-interface limit	46
4.3	Incorporation of melt convection	47
4.3.1	Dimensionless parameter h	49
4.4	Thermodynamic bulk free energies	50
	Results and Discussion	53
5	Liquid grooving at grain boundaries	55
5.1	Grain boundary grooving: Revisiting Mullins's seminal theory	55
5.1.1	Grain boundary grooving by volume diffusion	57
5.1.2	Determination of slope m at groove root	62
5.1.3	Effect of surface energy	63
5.2	Grain boundary grooving under diffusive-convective regime	66
5.2.1	Comparison between sharp interface theory and phase-field simulation	69
5.2.2	Variation of groove depth in diffusive-convective regime	72
5.2.3	Grain boundary migration	73
5.2.4	Effect of surface energy	74
5.2.5	Polycrystalline thin films	76
5.3	Summary	78
6	Unidirectional solidification of tip splitting microstructures	81
6.1	Role of grain boundaries	81
6.2	Tip splitting microstructures under diffusive regime	83
6.3	Deterministic behavior of tip splitting microstructures	86
6.3.1	Analytical criterion for tip splitting position	86

6.3.2	Comparison between sharp interface criterion and phase-field simulation	88
6.3.3	Effect of lattice anisotropy	91
6.3.4	Effect of numerical noise	93
6.4	Structural transition of tip splitting microstructures under diffusive-convective regime	94
6.4.1	Morphological features	98
6.4.2	Effect of surface energy	99
6.4.3	Determination of local tilt angles	100
6.4.4	Effect of interfacial anisotropy	102
6.5	Summary	103
7	Prediction of inter-dendritic spacing	105
7.1	Initial and boundary conditions	105
7.2	Primary dendrite arm spacing under diffusive regime	106
7.2.1	Selection mechanism of primary dendritic spacing	107
7.2.2	Effect of computational domain size	112
7.2.3	Secondary dendrite arm spacing	113
7.3	Primary dendrite arm spacing under diffusive-convective regime	115
7.3.1	Selection mechanism	115
7.3.2	Morphology of secondary dendrites	120
7.4	Summary	121
8	Prediction of inter-dendritic growth competition	123
8.1	Dendritic overgrowth theory	123
8.2	Oriented dendritic array	124
8.2.1	Role of tip undercooling	124
8.2.2	Role of inter-dendritic spacing	125
8.3	Growth competition in converging dendrites	126
8.3.1	Initial and boundary conditions	126
8.3.2	Inter-dendritic growth competition under diffusive regime	127
8.4	Growth competition under diffusive-convective regime	129

8.4.1	Drift velocity	133
8.4.2	Effect of misorientation angle of UO dendrites	133
8.5	Unusual overgrowth mechanism	135
8.6	Effect of interfacial anisotropy	138
8.7	Summary	141
Conclusions and Outlook		143
9	Conclusions and Outlook	145
9.1	Summary	145
9.2	Future directions	147
Appendices		149
A	Effect of numerical parameters on grain boundary grooving	151
A1	Effect of temporal and spatial discretization	151
A2	Effect of third order parameter	153
A3	Determination of equilibrium angle	154
A4	Parameters	155
B	Effect of grid discretization and lattice anisotropy on tip splitting phenomenon	157
B1	Effect of interface width and spatial discretization	157
B2	Effect of lattice anisotropy	158
C	Influence of interfacial curvature on tip splitting phenomenon	161
Bibliography		163

List of Figures

2.1	(a) Morphological development of perturbations generate an array of interfacial structures along a planar interface in single crystals. (b) The solidifying interface returns to planarity via remelting the perturbed front. Reprinted from Kurz et al. [1] with permission.	8
2.2	(a)-(f) Morphological evolution of interfacial instabilities in a bicrystal SCN sample. Initial perturbations amplify at the grain boundary to generate symmetric ridges. With crystal growth, the instabilities amplify laterally to produce a periodic array of hillocks across the solid-liquid interface. Reprinted from Xing et al. [23] with permission.	9
2.3	Stability of an advancing solid-melt interface in a polycrystalline sample. After the formation of tri-junctions, three pre-dendritic disks appear along with a pair of ridges at the grain boundary grooves. As crystal growth continues, the hillocks spread across the grain boundary to produce a periodic array of hills. Reprinted from Glicksman et al. [17] with permission. . . .	10
2.4	(a)-(f) For anisotropic interfaces, the interfacial instabilities develop into dendritic structures near the grain boundary. Oriented dendrites compete with each other to produce a single crystal cast alloy. Reprinted from Xing et al. [23] with permission.	11
2.5	Schematic illustration of constitutional supercooling ahead of a planar solidification interface.(a) Composition profile ahead of the solid-liquid interface during steady-state solidification.(b) The temperature of the liquid phase ahead of the solidification front T_l , whereas the equilibrium liquidus temperature for the liquid adjacent to the interface varies as T_e . Constitutional supercooling arises when T_l lies under the critical gradient. . . .	14
2.6	(a)-(b) Schematic illustration of the Mullins-Sekerka instability	16

2.7	As calculated by Ref. [36], a schematic morphology diagram illustrating the structural transition, wherein a compact (CS) and fractal (FS) seaweed structure (CS) translates to fractal (FD) and compact dendrite (CD). The dynamic competition between the interfacial anisotropy and diffusional fields in the liquid phase regulates the microstructural transition.	18
2.8	Left: Experimental micrograph of an equiaxed dendritic crystal in a super-cooled melt of pure, transparent, SCN. Right: Advanced stage dendritic SCN crystal with the development of nearly periodic side arms along the downward-pointing primary stem. Reprinted from Glicksman et al. [17] with permission.	19
2.9	(a)-(f) Evolution of an unidirectionally solidified solid-liquid interface for various growth rates. Initial perturbations amplify with time to form a periodic array of columnar dendrites. Imposed solidification velocity and temperature gradient control the morphology as well as the inter-dendritic spacing of primary arms. Reprinted from Somboonsuck and Trivedi [47] with permission.	21
3.1	(a)-(b) Schematic representation of a sharp interface and a diffuse interface profile. While the white color with $\phi = 1$ depicts a solid phase, $\phi = 0$ represents the liquid phase with black color.	30
3.2	Realistic needle-like dendritic morphology simulated via phase-field method. Reprinted from Kobayashi et al. [91] with permission.	36
4.1	Schematic description of the velocity profiles for the Poiseuille flow with a sharp interface U_{sharp} and a diffuse interface $U_{diffuse}$. Here, $y = 0$ represents the solid-liquid interface $\phi = 0.5$. The walls at $y = L$ and $y = 0$ are considered stationary.	49
5.1	(a)-(c) Experimental micrographs of liquid grooving at the solid-solid grain boundary under equilibrium conditions. Reprinted from Xing et al. [23] with permission.	56
5.2	A diagrammatic illustration of the equilibrium angle Φ at the trijunction, where γ_{gb} , γ_{sl} represent the grain boundary and the solid-liquid interfacial energies, respectively.	58
5.3	Grain boundary grooving under the influence of volume diffusion in a semi-infinite bicrystal grain	59

5.4	Illustration of the groove root deepening via the $\phi = 0.5$ isolines, where the formation of symmetric groove profiles and ridges is evident. In complete agreement with the Mullins's seminal theory, the grain boundary grooving phenomenon is reproduced by phase-field simulations. Herein, the groove pit deepens with time as given by Eq. (5.2).	60
5.5	Variation of interfacial curvatures and chemical potentials across the grain boundary groove. The presence of unequal chemical potentials drive the material transport from the groove root towards the flat surfaces. The color bar illustrates the local interfacial curvatures and chemical potential fields according to the legend embedded below the snapshots.	60
5.6	Calculated groove depth d_g from the initially flat interface as a function of time. A non-linear analytical fit $d_g \propto t^n$ provides us with $n = 0.3330$. An excellent agreement with the Mullins's theory is observed.	61
5.7	Calculated groove depth $d_g + d_h$, from the maxima of the profile d_h as a function of time. A non-linear analytical fit $(d_g + d_h) \propto t^n$ provides us with $n = 0.3332$. An excellent agreement with the Mullins's prediction for volume diffusion governed kinetics is observed.	61
5.8	Determination of slope m at the groove root from phase-field simulations.	63
5.9	Effect of surface energies on the grain boundary groove profiles. As the ratio R_0 increases, the groove pit morphology is significantly modified. . .	64
5.10	Groove root slope m as a function of the ratio R_0 between the solid-solid grain boundary energy γ_{gb} to solid-liquid surface energy γ_{sl}	65
5.11	Simulation screenshots depicting the effect of surface energies on the grain boundary grooving in finite grains	65
5.12	Grain boundary grooving under diffusive-convective regime. A cooperative effect of liquid phase convection and volume diffusion in the liquid phase modifies the grooving mechanism at the grain boundary.	66
5.13	Temporal evolution of the groove profiles at an imposed convection velocity $U_x = 1.2$. With time, the groove root deepens and the asymmetry of the grain boundary ridges increases.	67
5.14	A direct comparison of the groove profiles under pure diffusive and diffusive-convective regime.	68
5.15	Ratio H_0 between the left and the right ridge heights as a function of time for various convection velocities. An increase in the convection velocity proportionately decreases the ratio H_0	69

5.16	Under pure diffusive conditions, a direct comparison between phase-field simulations and sharp-interface groove theory. For the limiting case $\xi \rightarrow 0$, the well known Mullins's symmetric groove profile by volume diffusion is reproduced.	70
5.17	Comparison between phase-field simulations and numerically calculated groove profile for different convection velocities U_x . A near agreement is observed between the $\phi = 0.5$ isolines and the sharp interface groove profile.	71
5.18	Calculated groove depth d_g as a function of time for various convection velocities. The temporal exponent increases with the increase in the velocity and significantly varies when compared with Mullins's prediction.	73
5.19	Isolines illustrate that the rate of grain boundary migration increases with an increase in the convection velocity.	74
5.20	Under diffusive-convective regime, the calculated groove depth as a function of time for various $R_0 = \gamma_{gb}/\gamma_{sl}$, where the temporal evolution of the groove depth decreases with the decrease in the ratio $R_0 = \gamma_{gb}/\gamma_{sl}$	75
5.21	For an imposed convection velocity $U_x = 2.4$, the influence of surface energy on the grain boundary grooving phenomenon.	76
5.22	Three-dimensional simulation of crystal growth in a polycrystalline thin film. As a result of grain boundary area minimization, the larger grains evolve at the expense of smaller grains.	77
5.23	Growth morphology of a three-dimensional polycrystalline thin film under the influence of lateral convection.	78
5.24	Temporal volume fractions of red colored solid grain under different convection velocities. Grain elimination increases with the increase in the convection velocity.	78
6.1	Temporal evolution of grain boundary ridges near the groove pit in an supersaturated melt of composition $\Delta = 0.5$. Throughout this chapter, the colors blue and red refer to the two distinct solid grains and green color represents the liquid phase.	82
6.2	1D concentration profiles at two different positions. Presence of steeper solutal gradients enhance the formation of ridges at the grain boundary.	83
6.3	Temporal evolution of interfacial instabilities along a bicrystal sample. In a supersaturated melt of composition $\Delta = 0.5$, the primary ridges developed at the grain boundary amplify into split structures along with the propagation of hillocks across the two solid grains.	84

6.4	(a)-(d) In a supersaturated melt, the formation of a tip splitting microstructure along a solidifying solid-liquid planar interface. Initial perturbations evolve with time to undergo successive branching at the tip position. Isolines with various colors represent different simulation time. .	85
6.5	Determination of tip splitting position for an initial parabolic profile with $\alpha_0 = 0.02$. For convenience, we take $h = 500$ and $p = 250$	87
6.6	Calculated analytical criterion for $\alpha_0 = 0.02$, as a function of the dimensionless position. The positive and negative regions indicate the crest and the trough positions during the tip splitting process. The forked region lies between the $\nabla_s^2 \kappa < 0$ region, whereas the two tips start to evolve at the $\nabla_s^2 \kappa > 0$ positions.	88
6.7	Temporal evolution of crests and trough region exhibits the tip splitting phenomenon in a two-dimensional phase-field simulation. A direct comparison with the sharp-interface prediction reveals that the tips are generated in the positive regions only, whereas the split region is determined by the negative sharp-interface region of the interface.	89
6.8	In accordance with the analytical criterion for a sphere, the absence of tip instability is also observed in our simulations. The color bar illustrates the phase-field according to the legend embedded near the simulation snapshots.	89
6.9	For an energetically isotropic interface $\delta_{\alpha\beta}$, the simulation of a spherical seed with radius $R_{00} = 45$ depicts a complete agreement with the sharp-interface theory. The obtained effective anisotropy $\delta_{\alpha\beta}^e = 0.0001$ shows minimal effect from the underlying lattice on our numerical results.	92
6.10	For a weak anisotropic solid-liquid interface $\delta_{\alpha\beta} = 0.005$ and radius $R_{00} = 45$, a direct comparison with the sharp-interface equilibrium shape shows an excellent agreement. Here, the obtained effective anisotropy $\delta_{\alpha\beta}^e = 0.0045$ has very minute variation when compared with the imposed value.	92
6.11	Comparison between the phase-field simulations performed with and without numerical noise. Both the interface isolines display the same splitting position, while simulations with noise (black dotted line) depict the boosted growth of the tip. Additionally, few perturbations also start to augment away from the tip which proceeds as branches.	93
6.12	Schematic illustration of the simulation setup to study the structural transition of tip splitting microstructures in the diffusive-convective regime. .	94
6.13	Structural transition of tip splitting microstructures under diffusive-convection regime. The degenerate seaweeds at low convection velocities gradually transform into strongly tilted seaweeds with an increase in the melt velocity.	95

6.14	Temporal volume fractions of solid grains at $U_x = 1.0 \times 10^{-2}$	97
6.15	Temporal volume fractions of solid grains at $U_x = 4.0 \times 10^{-1}$	97
6.16	A comparative study between the morphological evolution of two solid grains is depicted for different convection velocities.	98
6.17	Distinct morphological features illustrated schematically via the interface isolines. The degenerate seaweed structures with an alternating tip splitting event amplify along the growth direction, whereas, in the case of a strongly tilted seaweed, the branches are always oriented towards the inflow direction.	99
6.18	The influence of R_θ on the initiation of morphological instabilities along a bicrystal is illustrated in the diffusive-convective regime.	100
6.19	A quantitative image analysis is performed with an open source ImageJ software plug-in, OrientationJ. The local orientation properties of the solid phases show the distinctive features observed in degenerate and strongly tilted seaweed structures.	101
6.20	Microstructural map illustrating the effect of anisotropic strength and convection velocity. Based on the dynamic competition between $\delta_{\alpha\beta}$ and U_x , three different morphologies are discerned, namely, degenerate seaweed, strongly tilted seaweed and columnar dendrite.	103
7.1	Schematic setup with initial and boundary conditions to study the selection mechanism of primary dendrites	106
7.2	Selection mechanism of primary dendrite arm spacing under diffusive regime. Initial perturbations develop into an array of primary dendrites with time. Local growth competition enhances the adjustment of primary arm spacing, where the lagging dendrites are eliminated, a process widely known as dendritic submergence.	108
7.3	Columnar dendrites in a two-dimensional simulation domain, where the primary arms adjust themselves to produce a stable array spacing. Here, λ_{\min} and λ_{\max} represent the minimum and maximum array stability limits.	109
7.4	Concentration fields depicting the one-dimensional solutal profiles at two different positions during the selection of primary dendrite arm spacing.	110
7.5	Changes in the number of primary arms in the simulation domain. The total number of primary arms along a solidification front attain a steady state spacing with solidification time.	111

7.6	Primary dendrite arm spacing as a function of melt supersaturation. Inter-dendritic spacing decreases with an increase in the melt supersaturation. The best fit follows a non-linear analytical fit of the form $\lambda_{PDAS} \propto \Delta^{k_1}$. Error bars indicate the maximum and minimum array stability limits. . .	111
7.7	Primary dendrite morphology under various growth conditions. The inter-dendritic spacing decreases with an increase in the imposed melt supersaturation. Amplified secondary arms diminish as the primary arm spacing decreases.	112
7.8	Effect of domain size on the spacing selection of primary dendrites. . . .	112
7.9	Measured secondary dendrite arm spacings as a function of solidification time. The non-linear analytical fit provides us with the relationship $\lambda_{SDAS} \propto t^{0.32}$	114
7.10	Formation of symmetric secondary dendrites under diffusive regime. . . .	115
7.11	Secondary dendrite arm spacing as a function of melt supersaturation. Inter-dendritic spacing decreases with an increase in the melt supersaturation. The best fit follows a non-linear analytical fit of the form $\lambda_{SDAS} \propto \Delta^{k_3}$	115
7.12	Prediction of primary dendrite arm spacing, where the presence of strong convective forces enhance splitting of dendritic tips, which in turn modify the selection mechanism of a dendritic array.	116
7.13	Concentration and velocity fields near a dendritic array under diffusive-convective conditions. Strong convective transport near the dendritic tip stimulates the tip splitting instability to modify the selection mechanism of primary dendrite arm spacing.	117
7.14	Comparison between solutal profiles near the foremost dendritic tip under diffusive and diffusive-convective regime. The presence of strong concentration gradients assist tip-splitting driven selection mechanism of primary arms.	117
7.15	Primary dendrite arm spacing as a function of melt supersaturation under diffusive-convective regime. Inter-dendritic spacing decreases in the presence of lateral melt convection. The best fit follows a non-linear analytical fit of the form $\lambda_{PDAS} \propto \Delta^{k_2}$. When compared with diffusive regime, the exponent decreases $k_2 < k_1$	119
7.16	Primary dendrite arm spacing as a function of solidification velocity under diffusive-convective regime. Inter-dendritic spacing decreases in the presence of lateral melt convection. The best fit follows a non-linear analytical fit of the form $\lambda_{PDAS} \propto R^{a_2}$. When compared with diffusive regime, the exponent decreases $a_2 < a_1$	120

7.17	Comparison of secondary dendrite morphology under diffusive and diffusive-convective regimes. Symmetric side branches transforms into an asymmetric morphology as a result of convective transport in-between the interdendritic spaces. Convection induced tip splitting generate new primary arms.	120
8.1	(a)-(b) A schematic illustration of converging and diverging dendritic growth competition at the grain boundary. In accordance with the Walton and Chalmers theory [229], a conventional overgrowth phenomenon is showcased where the favorably oriented (FO) dendrites overgrow the unfavorably oriented (UO) dendrites at the grain boundary.	124
8.2	Dendritic morphologies with various misorientation angles (a) $\theta = 0^\circ$, (b) $\theta = 15^\circ$, (c) $\theta = 30^\circ$	125
8.3	Variation of tip concentration with inter-dendritic spacing for different misorientation angles.	126
8.4	Schematic illustration of the simulation setup along with the imposed initial simulation and boundary conditions. Ten equidistant spherical seeds are initialized in a supersaturated melt of composition Δ . Here, the blue seeds are oriented favorably along the growth direction at $\theta_{FO} = 0^\circ$, whereas, the unfavorably oriented seeds green in color are misoriented at $\theta_{UO} = 15^\circ$ in the anticlockwise direction.	126
8.5	Under pure diffusive regime, simulation screenshots demonstrate the growth competition of columnar dendrites converging at the grain boundary. (b)-(e) The temporal evolution of converging dendritic morphologies in a supersaturated melt, where the FO1 dendrite impinges and subsequently blocks the primary arm of the UO1 dendrite. Highlighted in Fig. 8.5(a), the dendrites that overgrow and dictate the growth process at the grain boundary are named as ‘GB dendrite’.	128
8.6	(a)-(e) Competitive growth of columnar dendrites under diffusive-convective regime converging at the grain boundary. The conventional overgrowth behavior transforms into an unusual overgrowth behavior as the melt velocity gradually increases.	130

- 8.7 (a)-(b) Temporal volume fractions of favorably and unfavorably oriented grains at the grain boundary. (a) The diverging point for each case indicates the most preferred and dominant grain during the dendritic growth competition. FO dendrites dominate growth competition in a conventional overgrowth behavior, while the unfavorably oriented dendrites protrude consistently to outgrow the FO dendrites during an unusual overgrowth phenomenon at the grain boundary. 132
- 8.8 Calculated average drift velocity of UO dendrite arm as a function of flow Peclet number. As the flow Peclet number increases, a strong convective regime displaces the UO1 dendrite arm towards the solid-solid grain boundary. A linear fit follows the relation $V_d^{avg} = n_1 * Pe_f + n_2$, where n_1 and n_2 are proportionality constants. 134
- 8.9 A microstructural selection map for various misorientation angles θ_{UO} and flow Peclet numbers Pe_f . The unusual overgrowth mechanism is limited within a narrow range only, and for $\theta_{UO} > 15^\circ$, the conventional overgrowth behavior dominates at the grain boundary. 134
- 8.10 Concentration and velocity fields during a conventional overgrowth event at the grain boundary. The FO1 dendrite impinges and eliminates the UO1 dendrite and undergoes the conventional overgrowth mechanism at the grain boundary. 135
- 8.11 Concentration and velocity fields during an unusual overgrowth event at $U_x = 2.5 \times 10^{-1}$. Here, the UO1 dendrite shifts towards the GB and subsequently eliminates the FO1 dendrite. Since the imposed melt velocity and the amount of advected solute near the tip is high, the UO1 dendrite outgrows its counterpart at the grain boundary. 136
- 8.12 Lateral solutal profiles near the FO1 and UO1 dendrites at two different convection velocities. Contrasting nature of the solutal field modifies the overgrowth mechanism for converging dendrites at the grain boundary. The fluctuations indicate the imposed noise in the supersaturated melt. 137
- 8.13 Growth competition of directionally solidified columnar dendrites at various anisotropic strengths $\delta_{\alpha\beta}$ under diffusive-convective regime. The unusual overgrowth phenomenon observed for $\delta_{\alpha\beta} \leq 0.04$ translates into a conventional overgrowth behavior at the grain boundary as the anisotropic strength gradually increases. A degenerate and a branched UO1 dendrite is generated for weaker anisotropic strengths. 138

8.14	At an imposed convection velocity $U_x = 2.5 \times 10^{-1}$, the grain boundary orientation θ_{GB} at various anisotropic strengths. The by-product of a positive GB orientation is the elimination of a FO dendrite, whereas, a negative GB orientation indicates the overgrowth of FO dendrites. A linear fit provides us with a scaling law $\theta_{GB} \propto \delta_{\alpha\beta}$. The blue colored line indicates the transition region between the two overgrowth behaviors.	139
8.15	A microstructural selection map for inter-dendritic growth competition at various combinations of $(\delta_{\alpha\beta}, P_{ef})$. While the unusual overgrowth phenomenon dominates at higher melt velocities, an increase in the anisotropic strength produces the widely known conventional overgrowth behavior at the solid-solid grain boundary. The schematic transition zone is represented by the solid line.	140
9.1	Graphical representation of the topics addressed in this dissertation.	146
A1	Effect of temporal discretization Δt on the grain boundary groove profile. The complete overlap of the isolines illustrate that the chosen numerical parameters have no influence on the groove geometry.	152
A2	For finite bicrystal grain, steady state groove root position d_g^{ss} as a function of the ratio $\frac{\Delta x}{\epsilon}$. For all two-dimensional simulation in Chapter 6, $\frac{\Delta x}{\epsilon} = 0.25$ is chosen, and thereby the grid discretization has no influence on our numerical results.	152
A3	Effect of spatial discretization Δx on the grain boundary grooving. The convergence of groove root velocities indicate that the spatial discretizations does not play any role in the present work.	153
A4	Effect of third-order term on the groove profiles. A pinning effect is observed for $\gamma_{\alpha\beta\delta} = 10.0$, where the grain boundary groove profile is significantly altered under steady state conditions.	154
A5	Effect of additional third-order term on the groove root position. For $\gamma_{\alpha\beta\delta} = 10.0$ the groove root position is affected under steady state conditions where a pinning effect at the trijunction is observed.	155
A6	Determination of the equilibrium groove angle from the phase-field simulations. A fourth-order polynomial is fitted to the extracted $\phi = 0.5$ isolines. Subsequently, the equilibrium angle made by the tangent to the polynomial at the point of intersection is calculated. The equilibrium angle is schematically represented at the trijunction.	156

- B1 Convergence at various interface widths confirms that the numerical result is not influenced by the finite width of the diffuse interface. 158
- B2 Tip velocity as a function of the ratio $\frac{\Delta x}{\epsilon}$. For all two-dimensional simulation in Chapter 6, $\frac{\Delta x}{\epsilon} = 0.25$ is chosen, and thereby the grid discretization has no influence on our numerical results. 158
- B3 (a)-(b) For an equilibrium shape with radius $R_{00} = 15$, the effect of lattice anisotropy at two different anisotropic strengths. A direct comparison shows an excellent agreement with the sharp interface theory for both cases. Here, the obtained effective anisotropies are $\delta_{\alpha\beta}^e = 0.0096$ for $\delta_{\alpha\beta} = 0.01$, and $\delta_{\alpha\beta}^e = 0.028$ for $\delta_{\alpha\beta} = 0.03$ respectively. 159
- B4 Effect of lattice anisotropy on an equilibrium crystal seed with radius $R_{00} = 15$, where an excellent agreement with the sharp interface theory is observed, and the obtained effective anisotropy $\delta_{\alpha\beta}^e = 0.0005$ 159
- B5 Effect of lattice anisotropy on an equilibrium crystal seed with radius $R_{00} = 30$, where an excellent agreement with the sharp interface theory is observed, and the obtained effective anisotropy $\delta_{\alpha\beta}^e = 0.0002$ 160
- B6 Effect of lattice anisotropy on an equilibrium crystal seed with radius $R_{00} = 60$, where an excellent agreement with the sharp interface theory is observed, and the obtained effective anisotropy $\delta_{\alpha\beta}^e = 0.00009$ 160
- C1 The influence of non-uniform curvature during the morphological evolution of tip splitting microstructure. Pronounced tips observed for large $\nabla_s \kappa$ diminish as $\nabla_s \kappa$ decreases. Finally, as predicted by the theory, the absence of splitting and perturbances for $\nabla_s \kappa = 0$ is observed. Here, α_0 is the dimensionless shape factor in $f(x) = -\alpha_0(x - h)^2 + p$ 162

List of Tables

5.1	Material and numerical parameters to simulate the phenomenon of liquid grooving at the grain boundaries.	58
6.1	Simulation parameters for tip splitting microstructures.	82
7.1	Simulation parameters to predict inter-dendritic spacing.	106
8.1	Parameters to simulate inter-dendritic growth competition under diffusive-convective regime.	127
A.1	Typical order of magnitudes for key phase-field parameters.	155

Part I

Introduction and Literature review

Chapter 1

Introduction: Motivation and Outline

1.1 Motivation

The art of solidification is one of the oldest in history, and microstructures are extremely interesting for scientific, technological as well as for aesthetic reasons. Driven by diffusive and convective contributions, the transport of solutal fields determines the morphology, the grain size, and the growth direction of self-organizing patterns [1]. Understanding solidification processes has always been an important step in predicting microstructure development, and though we have amassed a great deal of knowledge on various aspects of material synthesis, the role of convective transport has been elusive. Over the last few decades, a direct comparison between microstructures developed under terrestrial and microgravity conditions has demonstrated that the presence of convective regime adds new length and time scales to the selection of solidifying patterns, and eventually results in morphologies with redistributed solute. Besides, since melt convection is a key transport mechanism which controls important growth features, let us briefly discuss the impact of diffusive-convective regime on microstructures through the following examples.

For instance, a metallic plate in contact with a saturated liquid melt may bring on a phenomenon which is sometimes desirable, but often harmful. Since every real material has at least one exterior interface in contact with environment, the chemical and mechanical stabilities of polycrystalline thin films are important for controlling hot dip galvanization, welding, soldering and other materials processes [2, 3]. In the form of liquid metal corrosion, the grain boundary grooves in contact with a liquid melt often leads to intergranular penetration. In critical applications, such as the cooling circuits in nuclear reactors, corrosion induced solid-liquid interactions promote rapid degradation of the grain boundaries in solid metals. This persistent behavior limits the ductility, and hence the performance and reliability of high-strength alloys.

Similarly, investment casting is a key process to manufacture turbine blades for aircraft engines, where the ever increasing need to produce efficient turbine blades has encouraged the use of temperature and stress resistant materials. Freckles, hot cracking, low angle grain boundaries, and other solidification defects are generally found in directionally solidified single crystal superalloy castings [4]. Owing to high performance applications, the selection of process parameters with improved mechanical properties has enhanced the intricacies in advanced engineering materials. Under non-equilibrium conditions, the formation of freckles and cast imperfections is driven by the presence of convective flow in the mushy zone with large inter-dendritic spacing [4]. As these microscopic defects are highly undesirable due to their deleterious effect on mechanical and economical performance, the knowledge to control the convective regime at the inter-dendritic spaces via solidification parameters becomes an integral part of failure analysis.

From the aforementioned examples, the challenge for contemporary techniques is the necessity to avoid, at acceptable cost, the undesirable effects of melt flow. As the resulting structure controls the mechanical and structural properties of metal castings, it is important to quantitatively characterize the microstructure formation. Moreover, due to the lack of in-situ findings at each stage of pattern formation, a universal study that carefully considers the effect of convective transport at the grain boundary as well as at the inter-dendritic region is needed. Since the 1990s, the computational modeling of solidification processes has been an attractive discipline for investigating microstructure evolution, whereby an accurate description of the underlying physics at the solidifying interface is provided. By employing the well known phase-field approach, this dissertation addresses one of the pre-existing issues in this area, and examines the unidirectional solidification of microstructures under the cooperative influence of diffusion and convection for a representative binary alloy model system. An overview of the topics covered in this dissertation is presented in the following section.

1.2 Outline

Following the motivation for the present study, a comprehensive literature review on directional solidification is delineated in Chapter 2. Here, the influence of grain boundaries along with the evolution of morphological instabilities on a planar interface is discussed through the theory of constitutional supercooling. Later, the linear stability analysis for a perturbed interface is presented, where the solidifying interface evolves into various microstructural patterns depending upon the imposed conditions. Accordingly, the dendritic morphologies that are widely observed in directional solidification studies are elucidated. Beginning with the fundamental concepts of the phase-field approach in part II, the chronological development of phase-field models in dendritic solidification is elucidated in Chapter 3. Later, the multi phase-field model [5] that addresses the unidi-

rectional solidification of microstructures under diffusive-convective regime is introduced in Chapter 4. Part III of the thesis deals with the results and discussion section, and an extended abstract is presented in the following paragraphs.

In Chapter 5, the phase-field model is employed to address the grain boundary grooving phenomenon under the cooperative effect of convection and volume diffusion in the liquid phase. To begin with, the phase-field model is benchmarked and validated under pure diffusive conditions, wherein the formation of symmetric groove profiles across the grain boundary is compared with the Mullins's groove [6]. Next, the theory of liquid grooving at the grain boundaries is extended, thereby an additional convective transport mechanism in the liquid phase is incorporated [7]. Particularly, it is identified that the groove kinetics as well as the grain boundary grooving mechanism is significantly modified under diffusive-convective conditions. This chapter, while providing considerable insights into the mechanism of grain boundary grooving, also closes the gap with the experimental and sharp-interface theories. Moreover, the simulated grain boundary features in this chapter are of practical significance for understanding and controlling the nanocrystalline thin film experiments.

Subsequently in Chapter 6, the morphological evolution of interfacial instabilities in a constitutionally supercooled melt is simulated. Although the morphologies attain a random configuration, the deterministic behavior of tip splitting microstructures is demonstrated. Based on capillary fluxes, the tip splitting mechanism is described via an analytical criterion, such that the sign of the sharp-interface theory [8] predicts the tip splitting position. Following these numerical results, the study is extended to qualitatively investigate the role of melt convection on tip splitting microstructures [9]. Later, it is shown that the ramified tip splitting microstructures transform into columnar dendrites with the increase in the anisotropic strength. These hallmarks thereupon become the basis for studying microstructure formation in the following chapters.

An issue important from both a fundamental and industrial standpoint, the columnar dendrites simulated in the previous chapter is further analyzed in Chapter 7, where the prediction of inter-dendritic arm spacing is examined. The selection mechanism as well as the primary dendrite arm spacing is studied with and without convection. While the primary arm selection mechanism is determined in the diffusive regime, the growth of tertiary branches modifies the spacing selection of columnar dendrites in the presence of convective regime. Given that the misoriented dendrites are prevalent in cast microstructures, the prediction of inter-dendritic growth competition is investigated in Chapter 8, where the microstructural evolution of unidirectionally solidified dendrites with different crystal orientations is addressed. From a direct comparison between simulations with and without convection, it is shown that the conventional overgrowth mechanism transforms into an unusual overgrowth mechanism as the melt velocity gradually increases [10]. By investigating the mechanisms of dendritic overgrowth and the role of misoriented den-

ditions, it is noted that there exists a critical convection velocity to determine the growth competition at the grain boundary. In addition, the role of interfacial anisotropy is analyzed in detail, where it is discerned that the conventional overgrowth behavior is always dominant at large anisotropic strengths. Finally, the dissertation concludes in Chapter 9, wherein the numerical results are summarized along with the open topics for future work.

Chapter 2

Unidirectional solidification of microstructures

The domain of solidification has considerably advanced through the pioneering studies on segregation, morphological stability and microstructure selection. The rapid development of experimental and computational tools have yielded a wealth of new information and quantitative insights into the unidirectional solidification of microstructures in a variety of alloys [11]. Likewise, the knowledge to control microstructural transition is an essential requirement for ensuring the quality of finished products, hence the perpetual and intensive research interest in materials science [12]. Microstructure formation in non equilibrium systems typically occurs when two phases are driven out of coexistence so that one of the phases grows at the expense of the other phase. Replete with morphological instabilities, the solid-liquid interface is responsible for triggering mushy zones in cast products, wherein the solidifying phase forms a porous medium of growing dendrites.

Dendritic microstructures found in single and polycrystal castings are produced by many industrial metal molding methods, such as, shape casting [13, 14], directional casting [15] and die casting processes [16]. Their morphology is generally determined by the competition of cooperative diffusive and capillary effects at the solid-liquid interface. On one hand, the diffusion of solutal fields minimizes the scale of the morphology, and on the other hand, the role capillarity effects maximizes the scale [17]. In addition, the form of a microstructure depends not only upon the cooling conditions, but also upon the alloy composition of the material. Affecting the mechanical and structural properties of cast products, the microstructures originate during the crystallization of a solid-liquid interface, whereby a planar interface transforms into hills and valleys, and finally the solid-liquid interface develops into a complex microstructural network.

From a statistical point of view, the magnitude of dendritic microstructures can be dramatized by the fact that approximately 10^{10} metallic dendrites are produced per second in the world [12]. Similarly, along with the large number of snowflakes and frost

patterns [18], dendritic trees in neural networks [19] are some classic examples of ramified structures found in nature. In engineered materials, dendritic crystalline forms appear in melt-grown and electro-deposited metallic crystals. In such a way, the minute tree-like branched morphology is the most important structural component grouping our world [12]. In this regard, an understanding of dendritic structures is crucial for developing next-generation light weight alloys used in automotive and aerospace applications [20]. In what follows, a comprehensive literature review on the experimental and theoretical background for pattern formation in directional solidification is discussed in detail. Besides, in this chapter, an overview on the effect of convective transport on dendritic microstructures is also presented.

2.1 Interfacial instabilities in single crystals

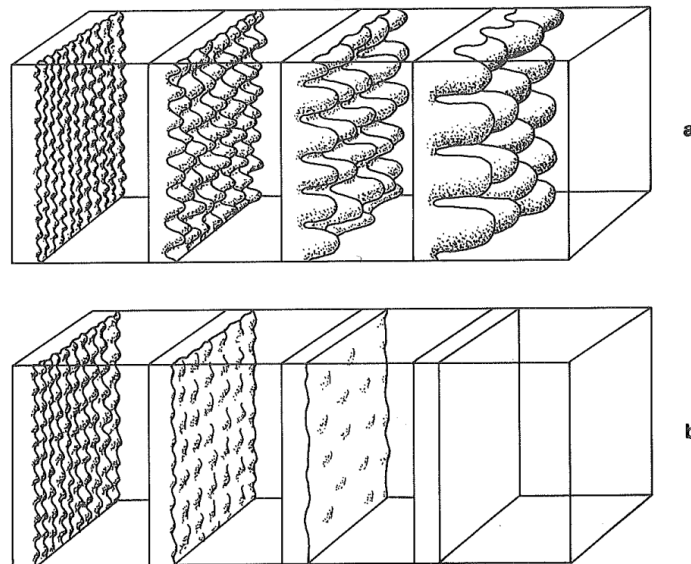


Figure 2.1: (a) Morphological development of perturbations generate an array of interfacial structures along a planar interface in single crystals. (b) The solidifying interface returns to planarity via remelting the perturbed front. Reprinted from Kurz et al. [1] with permission.

The pioneering experiments on single crystals were first performed by Chalmers et al. [21], where the distinct controlling parameters for a solidifying interface were appropriately classified. It was concluded that if a solidifying front had too high a concentration of solute, or impurities, or if the rate of solidification was too fast relative to the magnitude of the applied thermal gradient, then the single crystal alloy melt interface shall not remain planar. Chalmers et al. [21] also reported that throughout the course of solidification unstable growth conditions promote the development of distinctive interfacial microstructures along the solid-liquid interface. As shown in Fig. 2.1 and depending upon the growth conditions, the interfacial instabilities on a decanted alloy crystal amplify into

an array of microstructural patterns. In single crystals, these interfacial patterns were later described as periodic, square, or hexagonal arrays of pits, sequential parallel rows of or cells [21]. Likewise, the small-scale structures developed were categorized as complex tree-like patterns, namely *dendrites*. These amplified structures profoundly influenced the performance of solidified materials, and their morphological appearance strongly influenced the homogeneous single crystals in doped semiconductors [17]. However, in reality, a solidification front is replete with insoluble particles, infinitesimal thermal fluctuations and most importantly the grain boundaries (GBs). Consequently, they were considered as a major source for the initiation of instabilities due to the redistribution of the solutal field near the solid-liquid interface [22].

2.2 Interfacial instabilities in polycrystals

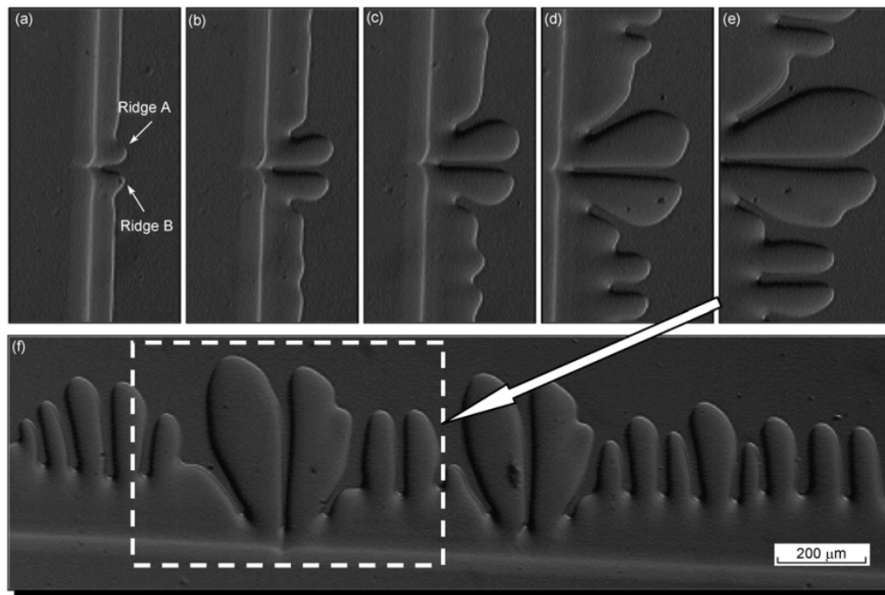


Figure 2.2: (a)-(f) Morphological evolution of interfacial instabilities in a bicrystal SCN sample. Initial perturbations amplify at the grain boundary to generate symmetric ridges. With crystal growth, the instabilities amplify laterally to produce a periodic array of hillocks across the solid-liquid interface. Reprinted from Xing et al. [23] with permission.

During directional solidification experiments, the solid-liquid interface generally consists of *imperfections* in the form of grain boundaries, impurities and persistent distortions which act as preferred locations for the initiation of interfacial instabilities. Most importantly, when interfacial instabilities are triggered by thermal or constitutional undercooling, they rapidly modify the dimensionality of the solutal fields [17]. In contrast to single crystals, it is worth mentioning that the solid-liquid interfaces in polycrystalline materials become unstable by passing through a different, slightly more complicated, sequence of morphological changes [17]. Schaefer and Glicksman [22] performed seminal experiments

to record the temporal development of morphological instabilities in a polycrystalline sample. For their study, a transparent body-centered cubic (BCC) compound, succinonitrile (SCN) was considered as the test sample, and solidification was initiated with a featureless and an initially stationary polycrystalline interface. At first, a few isolated pit-like depressions appeared at the triple-junction, which was formed by the intersection of the grain boundaries. As the interface advanced, it sequentially grew near the grooves, and generated pairs of ridges, running parallel to each other on either side of the grain boundary grooves, see Fig. 2.2. Concurrently, a shallow valley was formed adjacent to the grain boundary ridges, followed by a second pair of parallel ridges. Especially at the trijunctions, three distinct *pre-dendritic* disks were established at the termination of each ridge. As shown in Fig. 2.3, with progressive solidification, these disks extended the disturbance from the triple junction along the three intersecting ridge lines, thereby producing a distinctive periodic chain of hillocks. During the final stages of polycrystalline interfacial instability, it was reported that these protuberances extended farther out into the melt to sprout periodic bulges in the form of side arms, and branches. Although observed at low energy boundaries, the dendritic patterns were highly reproducible via the advancement of annular ridges and an irregular array of hills.

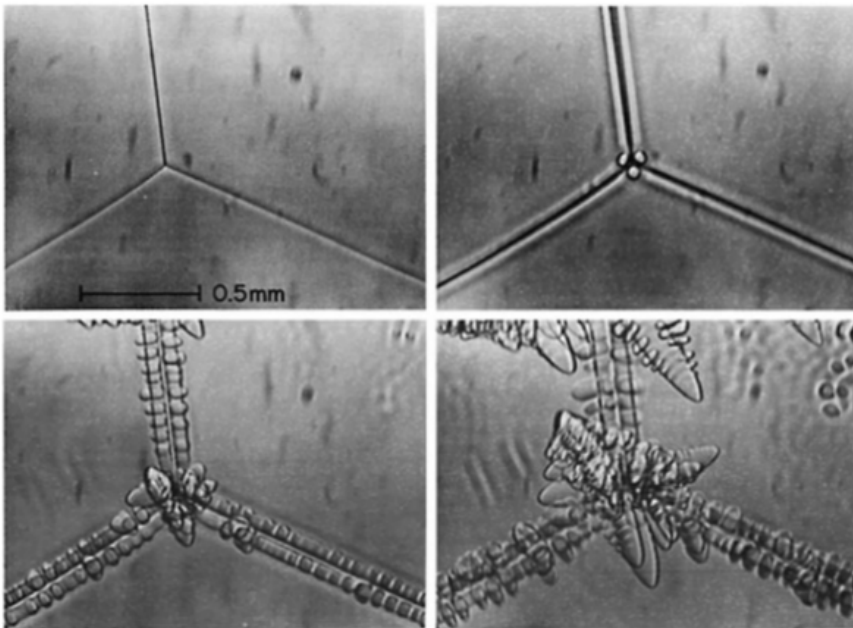


Figure 2.3: Stability of an advancing solid-melt interface in a polycrystalline sample. After the formation of tri-junctions, three pre-dendritic disks appear along with a pair of ridges at the grain boundary grooves. As crystal growth continues, the hillocks spread across the grain boundary to produce a periodic array of hills. Reprinted from Glicksman et al. [17] with permission.

In order to further study the lateral spreading of the perturbations along the grain boundaries, several experimental investigations [22–28] have been performed on SCN based alloys. Noel et al. [24] performed in-situ experiments to study the emergence of

non-planar patterns, and analyzed the cellular interfaces in a transparent binary alloy. It was confirmed that the initiation and the formation of a grain boundary groove lead to the propagation of ridges and depressions along a planar front. Similarly, for a directionally solidified organic alloy, Xing et al. [23] demonstrated the importance of a grain boundary during the birth of instabilities, where the dendritic growth direction was examined to be largely dependent on the crystalline orientation of the bi-crystal grains. As the solidification velocity was increased beyond the critical velocity, the initial instability occurred at the two slightly convex ridges. With time, these two cells-ridges coarsened and dominated the growth competition of cellular microstructures via suppressing the growth of neighboring cells. The importance of these tree-like reticulated structures in the microstructural characterization of cast and welded products is discussed in the upcoming sections.

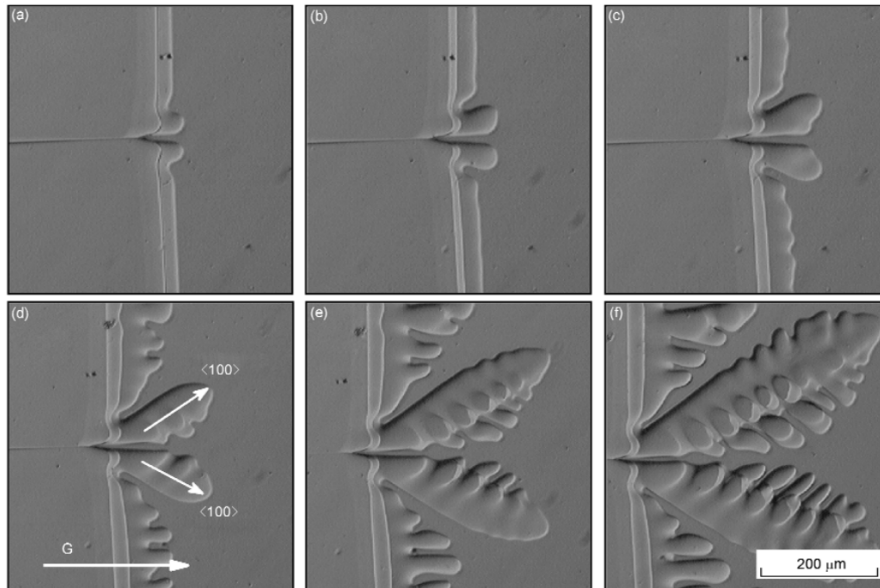


Figure 2.4: (a)-(f) For anisotropic interfaces, the interfacial instabilities develop into dendritic structures near the grain boundary. Oriented dendrites compete with each other to produce a single crystal cast alloy. Reprinted from Xing et al. [23] with permission.

For anisotropic interfaces, the transition from cellular to dendritic interface was evident in Fig. 2.4. Herein, the growth directions of the dendrites rotated from the imposed thermal gradient direction to their own preferred crystalline orientation. Subsequently, the cell to dendrite transition followed a tilted direction so that the morphological pattern represented a dendritic bicrystal. This competition between crystals with different orientation and bicrystal formation was systematically investigated by Borisov et al. [29], where it was concluded that the direction of the bicrystal solid grains at the grain boundary can be characterized by the orientation of the grain boundary.

2.3 Constitutional supercooling

The criterion for interfacial instability in alloys is complicated due to the variation of the local equilibrium melting point along the solid-liquid interface. During alloy solidification, and in the absence of stirring in the liquid phase, the pile up of solute is observed ahead of the interface as a result of the smaller solubility of the solid when the distribution coefficient is less than unity. Consequently, the excess solute rejected from the solid accumulates as an enriched boundary layer ahead of the interface. The steady state diffusion equation describing the system in the laboratory frame is given by

$$\left(\frac{\partial^2 C}{\partial x^2} + \frac{\partial^2 C}{\partial z^2} \right) + \frac{V}{D} \frac{\partial C}{\partial z} = 0, \quad (2.1)$$

where, C_0 is the original composition of the solid, V is the interface velocity, D is the solute diffusivity in the bulk liquid phase, and z is the solidification direction. With k as the equilibrium partition coefficient of the alloy, and applying the boundary conditions $z = 0, C = C_0/k$ and $z = \infty, C = C_0$ to the above equation gives us the concentration field which exponentially decreases from the maximum composition C_0/k at the interface to the original composition C_0 far from the interface as

$$C(z) = R_1 + R_2 \exp\left(-\frac{Vz}{D}\right). \quad (2.2)$$

After applying the far field condition, i.e, far from the interface, the concentration must be equal to the original composition, C_0 . Letting $C = C_0$ when $z \rightarrow \infty$ we get $R_1 = C_0$.

$$C(z) = C_0 + R_2 \exp\left(-\frac{Vz}{D}\right). \quad (2.3)$$

Now, let us apply the boundary condition at the solid-liquid interface, where the rate of solute rejection must be equal to the diffusional flux in the liquid at the interface

$$C(1 - k)V = -D \frac{dC}{dz} \quad (2.4)$$

Thus, when $z = 0$,

$$C = C_0 + R_2 \quad (2.5)$$

and

$$\frac{dC}{dz} = -\frac{VR_2}{D} \quad (2.6)$$

Substituting the expressions in the above equation gives us

$$R_2 = C_0 \frac{1-k}{k} = \Delta C_0 \quad (2.7)$$

Therefore, the complete solution for the solute distribution ahead of the planar interface under steady-state conditions can be written as

$$C(z) = C_0 + \Delta C_0 \exp\left(-\frac{Vz}{D}\right). \quad (2.8)$$

Now, from the above equation, the equivalent boundary layer δ_c can be derived as

$$\delta_c = \frac{2D}{V}. \quad (2.9)$$

This length is generally equal to the base-length of a right-angled triangle having a height which is equal to the excess solute concentration at the interface, and an area which is the same as that under the exponential curve, see Fig. 2.5(a). Moreover, according to above equations, the rate of rejection of solute at the interface is inversely proportional to the growth rate. For this reason, the accumulated solute must be carried away by diffusion down the interfacial concentration gradient, and as shown in Fig. 2.5(a), the boundary layer becomes steeper with increasing growth rate. From the above relationships, it is clear that during alloy solidification, the concentration substantially modifies ahead of the solid-liquid interface. However, the prediction of interfacial instabilities along a planar interface is difficult due to the presence of temperature gradients in the liquid.

Let us now consider a steady-state solidification at a planar interface as shown in Fig. 2.5. As a result of the varying solute concentration ahead of the solidification front there is a corresponding variation of the equilibrium solidification temperature, i.e. the liquidus temperature, as given by the line T_e in Fig. 2.5. Apart from the temperature of the interface, which is fixed by local equilibrium requirements, the actual temperature of the liquid melt can follow any line, for example T_l . If the imposed temperature gradient G is less than the critical value shown in Fig. 2.5(b), the liquid in front of the solidification front exists below its equilibrium freezing temperature, i.e. it is supercooled. Since the supercooling arises from compositional, or constitutional effects it is known as *constitutional supercooling*.

To sum up, a necessary condition required for the existence of a constitutionally supercooled zone is that the temperature gradient at the interface in the liquid should be lower than the gradient of liquidus temperature change in the melt. When the temperature gradient is greater than the liquidus temperature gradient at the solid/liquid interface $\frac{dT_l}{dx} > G_C$, the latter is stable, i.e., no perturbations. In contrast, an interfacial instability shall be observed whenever the slope of the local melting point curve (liquidus temperature) at the interface is greater than the slope of the actual temperature distribution

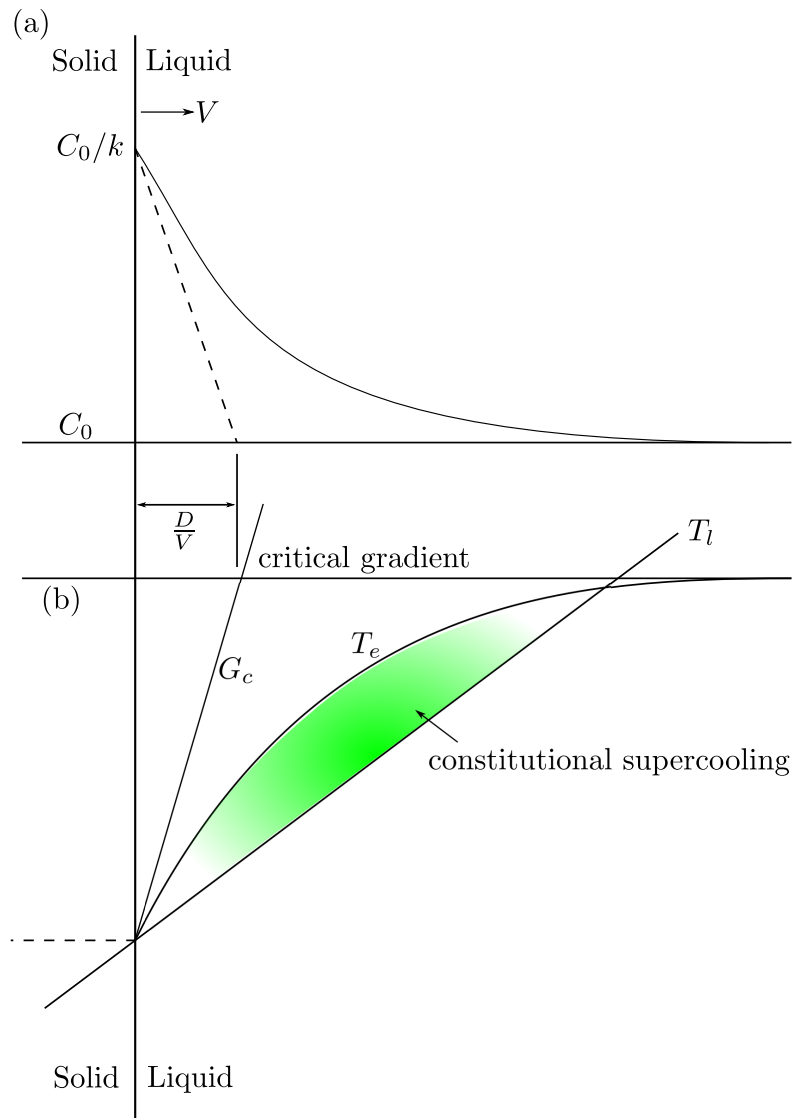


Figure 2.5: Schematic illustration of constitutional supercooling ahead of a planar solidification interface. (a) Composition profile ahead of the solid-liquid interface during steady-state solidification. (b) The temperature of the liquid phase ahead of the solidification front T_l , whereas the equilibrium liquidus temperature for the liquid adjacent to the interface varies as T_e . Constitutional supercooling arises when T_l lies under the critical gradient.

$\frac{dT_l}{dx} < G_c$. If the imposed temperature gradient ahead of an planar interface is gradually reduced below the critical value then the first stage of breakdown is the formation of interfacial instabilities as shown in Figs. 2.1 to 2.4. Hereafter, with the development of a constitutionally undercooled melt, there exists a driving force for the amplification and evolution of minute perturbations along a solid-liquid interface during alloy solidification. In conclusion, the theory of constitutional supercooling generally estimates the processing conditions that are useful to predict the growth of planar crystals in alloy solidification [17].

2.4 Linear morphological stability

Previous section focused on the criteria of stability, or instability, of an initially planar interface due to the development of constitutional supercooling ahead of the solid-liquid interface. In short, the stability of an interface depends if the liquidus temperature ahead of the moving interface is below or above the actual temperature in the melt. However, the theory of constitutional supercooling lacks significant effects that are to be introduced through the capillary phenomena of curved crystal-melt interfaces. Especially, the theory remains incapable of describing the full range of interfacial dynamics, nor does it include important material parameters that bear upon the general question of interfacial stability. In order to investigate such a possibility, and to examine the morphological changes occurring near to the limit of stability, it is necessary to assume that the interface has already been slightly disturbed under the constraints of diffusion and capillarity.

The theory of linear morphological stability of a planar interface was first examined by Mullins and Sekerka [30] through the introduction of a sinusoidal ripple in steady state conditions. Depending upon the wavelength, the classical dispersion relation predicted whether the perturbation decayed or advanced with time. Mullins and Sekerka provided the stability of a steady state perturbation by calculating the time dependence of the amplitude for different wavelengths, via performing a linear-stability analysis. To begin with, let us assume a small perturbation: $\zeta(x, t) = \zeta_k \exp(ik_w x + \omega t)$ introduced into a steady-state planar interface. Here, k_w is the wave number, ω is the amplitude of the perturbed interface and ζ_k is the disturbance in the linear order. In the frame of reference moving in the z -direction, the governing equation in the present case is a steady-state diffusion equation in two dimensions, given as,

$$\left(\frac{\partial^2 C}{\partial x^2} + \frac{\partial^2 C}{\partial z^2} \right) + \frac{V}{D} \frac{\partial C}{\partial z} = 0. \quad (2.10)$$

For zero diffusivity in the solid and for a phase diagram with parallel solidus and liquidus lines, the diffusion equation with appropriate boundary conditions provides us with a dispersion relation between the amplification rate and the wave number [31], expressed as

$$\omega = k_w V \left[1 - (1 + \beta_d) d_0 \frac{V}{D} k_w^2 \right]. \quad (2.11)$$

The above equation represents the phenomenological Mullins-Sekerka dispersion relation [30], where the amplification rate ω discloses whether the perturbed interface would grow or decay at different wave numbers k_w . In essence, this formula describes the fundamental mechanism of diffusion controlled pattern formation in crystals. The above equation consists of two parts, a positive, destabilizing term that is proportional to the velocity, and a negative capillary term that contributes to the interface stability, especially at large wavenumbers or small length scales of the perturbation. For large k_w , the perturbation decays with time and thereby the interface always gets back to a planar

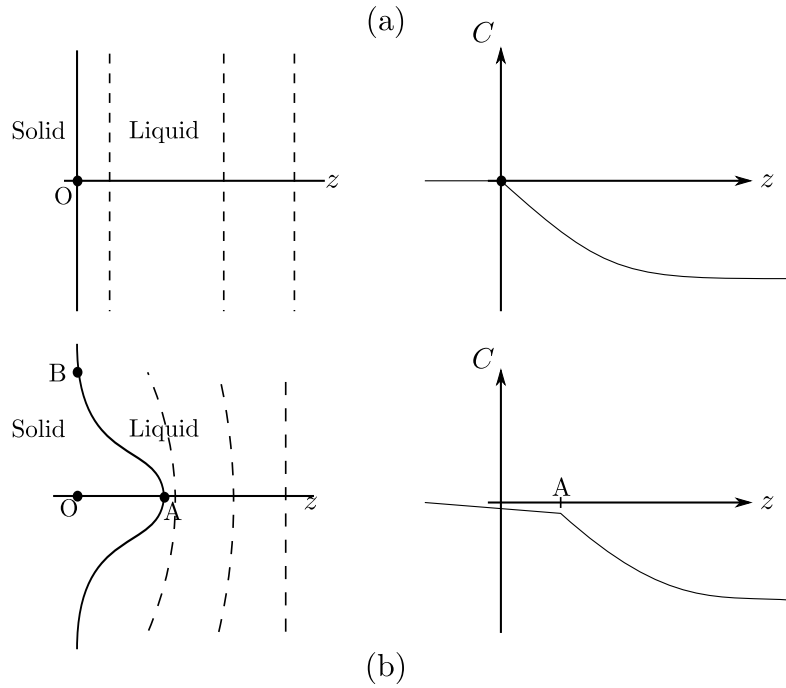


Figure 2.6: (a)-(b) Schematic illustration of the Mullins-Sekerka instability

surface. Whereas for small k_w , the perturbation grows with time and the interface is always unstable. The schematic depiction of the Mullins-Sekerka instability is shown in Fig. 2.6, where the solutal fields for planar as well as a perturbed interface are illustrated. Firstly, the steady-state function given in Eq. (2.10) is depicted in the right-hand side of part (a). In the absence of capillarity, a forward bulge at the interface A in Fig. 2.6(b) steepens the concentration fields in the melt, such that the solute is distributed rapidly away from the surface. In the same manner, a depression in position B melts back. However, with finite surface tension, the curvatures induces the concentration profiles at the two positions in order to restore the flatness of the interface. Therefore, the competition between these two effects determines the sign of ω in Eq. (2.11), and thus the overall stability of the interface. In summary, an interface subject to such a disturbance shall evolve into more complex structures over time if the stability criterion is attained. Using Eq. (2.11), the wavenumber at which ω vanishes, is known as the neutral stability point, given by $\lambda_s = 2\pi\alpha_f\sqrt{ld_0}$, where $l = \frac{V}{D}$ and $\alpha_f = [(1 + \beta_d)]^{1/2}$. Moreover, the perturbation which grows rapidly occurs at the wavenumber $k_w/\sqrt{3}$. Nonetheless, the microstructural patterns or perturbations that evolve from an instability along a planar interface shall have a characteristic size of the order λ_s .

2.4.1 Microstructural patterns

Obtaining quantitative measurements from an unstable planar interface is challenging. Generally, the experimental problems are associated with the strong interfacial distur-

bances caused by the grain boundary grooves, the contact menisci, and the dislocations [17]. Nonetheless, several investigators [32–34] have found quantitative agreement with the linear morphological instability theory. For example, the critical wavenumber was verified by de Cheveigné et al. [32] and later an agreement with the linear instability theory was shown. More recently, Losert et al. [33] performed careful experiments and concluded that the obtained wavenumber was in good agreement with the non-linear version of stability theory by Warren and Langer [34, 35]. Similar to previous experiments, Losert et al. [33] utilized SCN as a test alloy and reported a series of observations on directionally solidified microstructural patterns under steady-state conditions. At low solidification velocities, the solid-liquid front remains planar and evolves under steady-state conditions without any instability. However, as the growth rate is increased, a progressive development of the low-amplitude ripples is observed along the solidifying interface. These ripples subsequently amplify into deep finger-like cells. Nonetheless, at the highest growth velocity, the interface is fully evolved into an array of aligned dendrites. This transition from a cell microstructure to a dendritic array is of considerable interest in interpreting the cast microstructures in binary alloys. A morphological diagram is showcased in Fig. 2.7, wherein the patterns are categorized based on several growth parameters [36, 37]. The morphology diagram uses undercooling vs anisotropy as the principal axes and distinguishes seaweed and dendritic structures as the basic patterns. A second possible classification deals with the random looking structures, namely, fractal as opposed to compact patterns, which is distinguished with a self-similar internal structure [37]. In other cases, at velocities just above the planar-cellular instability, the growth orientation is more sensitive to the strength of the thermal gradient [20]. In the dendritic region, lower temperature gradients favour growth along the direction of the main crystalline axes, whereas higher thermal gradient strengths favour a tip splitting microstructure where the dendritic tip continuously splits and changes its orientation.

2.5 Dendritic microstructures

In the preceding section, it is illustrated that the onset of linear morphological instability initiates the exponential growth of local perturbations along a solidified front. The linear stability analysis disclosed that there exists a particular wavenumber for which an amplified interfacial instability is induced along a perturbed solid-liquid interface. The most fundamental repeating unit in a microstructure is dendritic in nature. The name *dendrite* derives from a Greek word *dendron* (a tree) which characteristically exhibits morphological features that display crystallographic directionality, in the form of straight primary stems, secondary side arms, and tertiary branches. These branches bear special angular relations between each other via displaying symmetries and reflecting the underlying crystal structure of the material [17]. Predominantly, the formation of dendritic

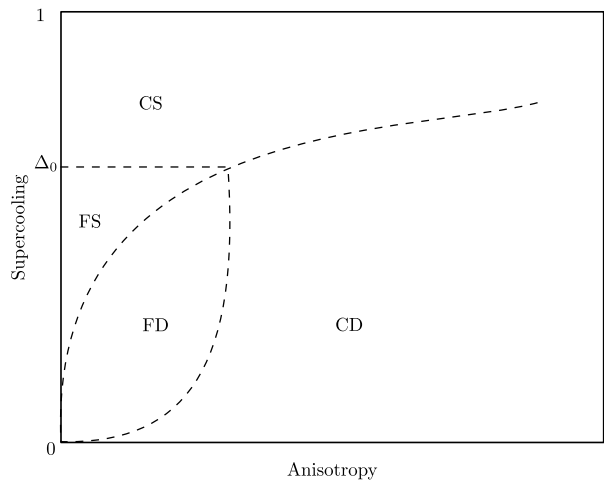


Figure 2.7: As calculated by Ref. [36], a schematic morphology diagram illustrating the structural transition, wherein a compact (CS) and fractal (FS) seaweed structure (CS) translates to fractal (FD) and compact dendrite (CD). The dynamic competition between the interfacial anisotropy and diffusional fields in the liquid phase regulates the microstructural transition.

microstructures leave a mark on the distribution of secondary phases, which are formed in the interdendritic spaces of supersaturated liquid as a result of solute rejection [20].

From a morphological point of view, there are two types of dendritic microstructures, namely, *equiaxed* and *columnar*. An equiaxed dendrite generally consists of primary arms of equal length as measured from the nucleation centre, see Fig. 2.8. In general, metallic dendrites are capable of growing rapidly under weak thermal gradients in highly supercooled melts [17]. Over the past five decades, the understanding of dendritic growth has advanced the engineering applications of cast alloys. The stability of undercooled melts has also allowed the initiation of dendritic growth by spontaneous nucleation at some favorable site within the melt or through controlled triggering events induced by contacting the melt with a seed crystal. Fig. 2.8 shows a classic example of a random nucleation event occurring within the transparent undercooled melt, where the early stage of an equiaxed, dendritic, cubic SCN crystal is initiated. With time, well developed side arms grow outward in orthogonal branching sheets, which are fin-like extensions of the $\langle 100 \rangle$ planes of this cubic crystal. In general, an equiaxed dendrite consists of three regions of different phases and compositions. The inner solid core, the mixture of solid and liquid of the dendritic branched structure (mush), and the surrounding liquid with the far field solutal field.

Based on fundamental observations, Ivanstsov deduced a three-dimensional thermal diffusion field of an isothermal steady-state needle crystal in the form of a paraboloid [38]. Phenomenologically, it was found that the dimensionless undercooling Δ_{IV} equals a function of the Peclet number Pe

$$\Delta_{IV} = Pe \exp(Pe) E_1(Pe), \quad (2.12)$$

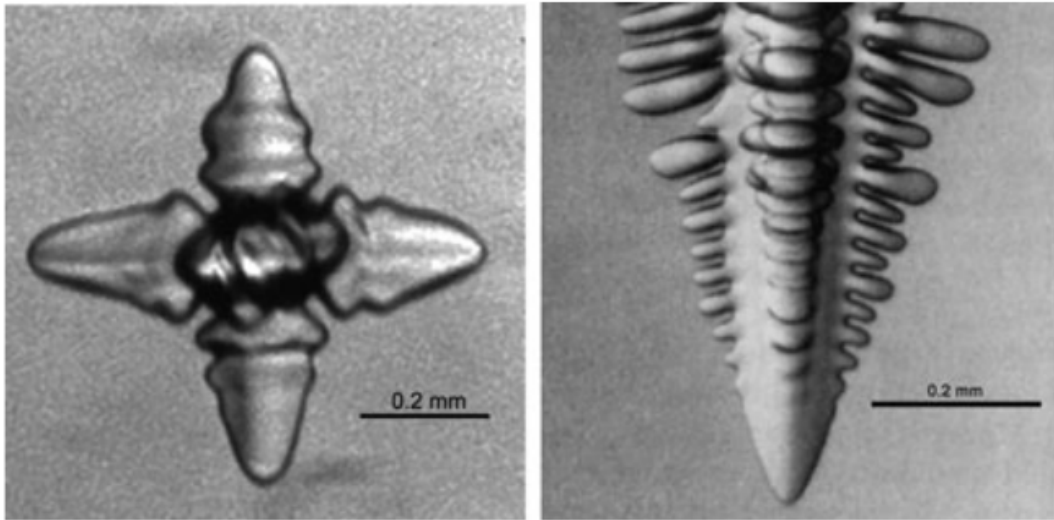


Figure 2.8: Left: Experimental micrograph of an equiaxed dendritic crystal in a supercooled melt of pure, transparent, SCN. Right: Advanced stage dendritic SCN crystal with the development of nearly periodic side arms along the downward-pointing primary stem. Reprinted from Glicksman et al. [17] with permission.

where $Pe = RV/2a$, is the ratio of the tip radius of the paraboloid R , to the thermal diffusion length $2a/V$, a is the heat diffusivity, V the tip velocity, and E_1 the exponential integral function. The right-hand side of the aforementioned equation is now referred to as Ivantsov function $Iv(Pe)$, which is a shape-preserving solution of a parabolic dendrite with an isothermal interface. For the next three decades, several improvements were proposed which subsequently constituted the basis for various theories on the growth of solid-liquid transformations. Temkin et al. [39] improved Ivantsov's model for an isothermal dendrite by including capillarity and interface kinetics. The dendritic shape was assumed to be paraboloidal and a solution was obtained for small undercooling or small Peclet numbers. Later, a non-isothermal dendrite model was developed by Bolling and Tiller [40, 41], where it was reported that the form of the dendrite tip would differ from that of a paraboloid due to the effects of curvature and attachment kinetics. Subsequently, Trivedi et al. [42, 42] considered the role of secondary arm branching on the dendritic shape. The study pointed out that although the inclusion of capillarity will open up the parabolic shape, the solutal field from the secondary branches shall tend to close the shape so that the tip region should be close to a parabola.

In the ensuing years, a significant contribution was made in the field of dendritic theories, where the marginal stability hypothesis of Langer and Müller-Krumbhaar [43] posited that the dendritic tip operates within the margin of stability, whereas the remainder of the dendritic interface grows in an unstable, time-dependent manner, producing quasi-periodic waves that amplify into side arms, or branches. Langer and Müller-Krumbhaar qualitatively suggested that the tip of a dendrite at the margin of stability implied that

the dendrite tip becomes as large as possible, but avoids becoming large enough to go unstable, and split. According to them, the tip radius R of the marginal stability criterion corresponds to the minimum wavelength for planar instabilities λ_s . This breakthrough led to several numerical studies, for example, Rappaz and Thevoz [44, 45] developed a deterministic equiaxed growth model that coupled heat and solute balance equations of the regions, and in this way an equiaxed dendritic growth was simulated. Later, an extension of the model to multicomponent alloys was developed, where Spittle and Brown [46] reported a two-dimensional microstructure using the Monte-Carlo technique, and included the phenomenon of nucleation, growth, remelting and solute redistribution.

However, in reality, the dendritic structures are rarely equiaxed (a filling with a sphere), but rather grains with the three cubic axes of similar length. If one of the axes becomes larger than the others they are widely called as a *columnar dendrite*. During the early stages of solidification, many grains tend to nucleate on or close to the cold wall of the mould with random orientations, and are of equiaxed form. A columnar structure (texture) is posteriorly developed by grain elimination through a phenomenon commonly known as equiaxed to columnar transition (ECT).

2.5.1 Unidirectional growth of columnar dendrites

Unlike the four-fold equiaxed dendrite in an undercooled melt, it is the positive temperature gradient in constraint directional growth which strongly influences the interface dynamics at the dendritic tip. This particular type of growth creates an array of dendrites with a characteristic range of primary trunk spacings, see Fig 2.9. One of the major aspects of columnar dendrites is the determination of the microstructural properties, the distribution of secondary phases, and the morphology of dendritic branches. The latter redistributes solute via microsegregation, and henceforth, the control of primary and secondary arm spacings is desirable. In the last few decades several experimental and theoretical studies have been devoted to this topic.

The primary dendrite arm spacing is defined as the mean distance between the dendrite trunks during columnar growth, and the secondary spacing is defined as the distance between the sidearms that form initially close to the dendrite tip and coarsen in the mushy zone during the course of solidification. Early measurements which related the inter-dendritic spacing to the solidification conditions dates back to 1960s. While Bell and Winegard were the first to examine the Sn-Pb system via directional solidification experiments [48], Somboonsuck and Trivedi [49] investigated the dynamics associated with the establishment of a steady-state arm spacing during the directional solidification of a succinonitrile-acetone alloy. It was found that the solidification velocity rapidly fixed the steady-state tip morphology but established the primary spacing slowly. In the early 1980s, the mechanisms of mean spacing near the tip region of a directionally solidified

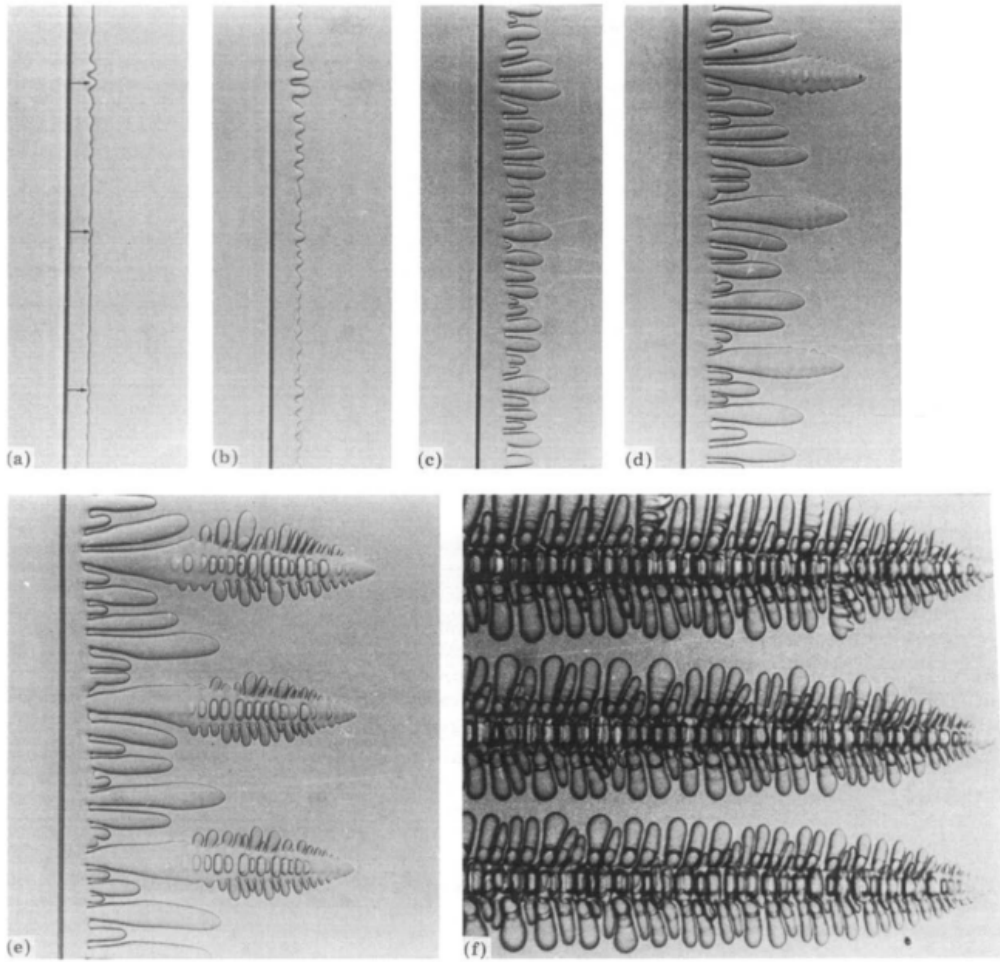


Figure 2.9: (a)-(f) Evolution of an unidirectionally solidified solid-liquid interface for various growth rates. Initial perturbations amplify with time to form a periodic array of columnar dendrites. Imposed solidification velocity and temperature gradient control the morphology as well as the inter-dendritic spacing of primary arms. Reprinted from Somboonsuck and Trivedi [47] with permission.

succinonitrile-acetone alloy were examined. Divergent grain boundaries were used in the experimental setup, where the inter-dendritic spacing between the trunks continuously increased. It was clearly shown that the competition between secondary and tertiary branches from neighbouring dendrites was responsible for the establishment of a stable primary arm spacing.

On the theoretical side, Hunt presented the first deterministic model to predict the primary spacing under constrained conditions [50, 51]. The model was based upon the mass balance equation which was matched to a spherical tip growing at the extremum. The predicted spacing for constrained primary dendrites was derived as,

$$\lambda_1 = B_K \Delta T_0^{0.25} G^{-0.5} V^{-0.25} \quad (2.13)$$

where ΔT_0 is the equilibrium melting temperature of the alloy, G is the imposed temperature gradient across the sample, B_K is the proportionality constant and V is the

solidification velocity. Later, Trivedi et al. [52] developed a model which was based upon mass balance and marginal stability theory, showing that for a constant G , the relationship $\lambda_1 - V$ goes through a maximum. Within the cellular regime, and at lower growth rates, the spacing increased with V , while, in the dendritic regime at higher rates, the spacing decreased. Han and Trivedi [53] further simplified the model and compared it with experiments on succinonitrile-acetone system. A new mechanism of spacing evolution was observed through the lateral motion of cells and dendrites. For a dendritic regime under constrained solidification conditions, all three models, by Hunt, Kurz and Fisher and by Trivedi [52, 54, 55] resulted in the above equation but with different proportionality constants.

Warren and Langer [34] performed a linear stability analysis on the primary dendritic array and concluded that under constant growth conditions, there exists a wide range of stable dendritic spacings rather than a unique value. Eventually, they also analysed non-steady-state diffusion effects during the evolution of primary arm spacings [35]. Similarly, Losert et al. [56] measured the stability of a dendritic array in an organic alloy under thermal perturbation, and found that the observations in the linear regime were qualitatively consistent with the Warren and Langer theory [34].

Hunt and Lu [50, 57, 58], using numerical simulations found a lower limit to the primary spacing of columnar dendrites. It was argued that the upper limit to the spacing regime is twice that of the lower stable regime. Likewise, Han and Trivedi [53], Huang et al. [59] and Pan et al. [60] also studied the dynamics and the spread of primary spacings along a planar solidification front. The lower limit found in these studies was consistent with the theoretical predictions of Warren and Langer [34], and of Lu and Hunt [58]. According to Han and Trivedi [53], the selection mechanism of a stable primary arm spacing can be described through the following steps

- Tip-elimination
- Tip-splitting
- Tertiary arm development
- Lateral migration and defect interaction with growth front

One intriguing feature of the microstructure, the influence of off-axis heat flow on the inter-dendritic spacing was experimentally studied by Grugel and Zhou [61], Akamatsu and Ihle [62] and Gandin et al. [63] in succinonitrile alloys. In contrast with the aforementioned selection mechanisms, it was concluded that the dynamic competition of secondary and tertiary branches was the main mechanism to generate new dendritic trunks at divergent grain boundaries.

2.5.2 Dendritic growth competition

Under realistic situations, the formation of axisymmetric dendrites is difficult as minute crystals often initiate at the inner surface of a chill or mould plate with several equiaxed grains from which columnar dendrites develop. The columnar dendrites compete with each other over a certain distance, and finally generate a texture with required microstructural properties. In such a scenario, the dendritic tip temperature varies with the misorientation angle between the grain and the growth direction. As a result, in a single crystal cast product, all but one grain with with cubic crystal structure $\langle 001 \rangle$ orientation is eliminated [64, 65]. Wagner et al. [64] performed experiments and found that the suppression of secondary arms by the diffusion field of neighbouring dendrites stops dendrite overgrowth and stabilises an unfavourably oriented grain. However, a few investigations [64, 66–69] have proposed other possible overgrowth mechanisms for competitive dendrites. Zhou et al. [66] performed bicrystal experiments on Ni-based superalloys and concluded that the growth behavior of converging dendrites is anomalous. It was reported that the solute interaction at the grain boundary has a significant impact on the overgrowth mechanism, where the unfavorably oriented dendrites overgrow at the expense of favorably oriented dendrites. This phenomenon referred to as *unusual overgrowth phenomenon* eliminates a favorably oriented dendrite by physically blocking and protruding over the primary arms. Furthermore, other experimental studies [64, 67, 69] have also endorsed the overgrowth of misoriented dendrites at the grain boundary.

Besides the in-situ experiments, several computational studies [70–73] have successfully examined and depicted the dendritic growth competition in cast alloys. For example, Tourret et al. [70] argued that the growth competition in columnar dendrites was dependent on the imposed temperature gradient, and the rate of suppression of unfavorably oriented dendrites was non-monotonic. The influence of the imposed temperature gradient G and the orientation of neighbouring grains on the primary spacing and on the orientation of grain boundaries were shown. Again, it was found that the overgrowth of misoriented grains was not related to the tip temperature difference and that under certain circumstances unfavorably oriented grains could persist. In addition, for diverging dendrites, it was suggested that the formation of secondary and tertiary arms was always accountable for the overgrowth of favorably oriented dendrites, thereby reiterating the importance of microscopic thermal fluctuations at the interface.

Although two-dimensional simulations effectively capture the physics of inter-dendritic growth competition, a three-dimensional dendritic network provides realistic solutal behavior near the dendritic tips. In an another study, Tourret et al. [74] studied with a phase-field model the competition between columnar grains in two and three dimensions for small sample thicknesses with an dendritic array. The grain orientation was varied around the growth axis and its effect on the grain competition was studied. Similarly, Guo et al. [75] presented a three-dimensional phase-field study of columnar grain compe-

tition due to secondary and tertiary branching behaviour in diverging grain boundaries with various crystallographic orientations. However, the rotation of secondary branches was not considered in this study. Especially for a converging dendritic network, Li et al. [71] performed phase-field simulations in two dimensions and examined the unusual overgrowth behavior at the grain boundary. In corroboration with the aforementioned experimental observations, it was concluded that the solute interaction at low pulling velocities was responsible for the overgrowth of an unfavorably oriented dendrite. These observations were further acknowledged by Takaki et al. [76], where the unusual overgrowth phenomenon was observed as a result of asymmetric diffusion layers at the grain boundary.

2.6 Diffusive-convective regime

Convective transport of solute near the solid-liquid interface is omnipresent in practical solidification processes, and therefore most dendritic theories tend to slightly differ from experimental results. It is well known that the cooperative effect of diffusive-convective regime adds new length and time scales to the selection of solidifying patterns, and eventually results in morphologies that are potentially much different from those generated by purely diffusive transport. Nonetheless, not only does convection influence the solidification pattern, but the evolving microstructure can also trigger unexpected and complicated flow phenomena. Convective transport near the solidification front is normally driven either by volume differences between the phases, or by density gradients temperature gradients in the alloy melt, or by surface tension gradient (Marangoni effect) or by an external melt flow effect such as pouring, electromagnetic stirring, etc [12].

Owing to the intricacies in a microstructure, the topic of dendritic growth in the presence of melt flow was treated extensively by Glicksman et al. [77], and Ananth and Gill et al. [78], where two different types of convective transport was considered. Firstly, natural flow, which arises from the gravitational effect on the motion of fluid due to density differences, and secondly, forced convective melt flow, which is induced by some external transport of diffusional fields. Glicksman and Gill performed systematic experiments and investigated the melt flow effects on dendritic growth for parabolic crystals in a thermal flow [78], and found a very good agreement between theory and experimental results.

A brief perusal on studies related to dendritic growth in the presence of fluid flow provides us enough evidence that melt convection has a large effect for enhancing morphological changes during microstructural evolution. For example, for the interfacial instabilities developed along a polycrystalline sample, Noel et al. [25] interestingly studied and reported the influence of melt convection during the unidirectional solidification of SCN alloys. It was reported that the liquid phase convection completely swept the solute layer near the growth front, and thereby delayed the emergence of hillocks in the

downstream solid ridges. In agreement with other studies [26, 27], Jamgotchian et al. [79] also exhibited the localization of microstructures in the presence of fluid flow. Focus and outward hexagonal flow type were the two localized patterns observed in agreement with the theoretical predictions of Davis et al. [80].

Despite these experimental studies, there have been limited numerical models to study the influence of flow on microstructural formation. Nevertheless, computational studies [81–83] have made quantitative predictions on the free evolution of a dendrite in both, two and three dimensions. Beckermann et al. [82] performed phase-field simulations with convection in the liquid phase, where the emphasis on the dendrite tip dynamics revealed that the tip velocities in upstream direction had a rapid growth rate than the tips along downstream direction. Similarly, other studies [81, 83] described the shape as well as the side branching dynamics due to the convective transport via two- and three-dimensional studies. Recently, Chen et al. [84] revealed the fundamental differences in flow patterns around a four fold dendrite in two and three dimensions, where the thermal fields along upstream and downstream directions were reported to be significantly different, in turn changing the appearance of secondary and tertiary branches. In addition, using an experimental setup, Shevchenko et al. [85] exhibited the effects of natural and forced convection on directionally solidified Indium dendrites. It was reported that the morphology as well as the growth direction of columnar dendrites was modified in the convective regime. In light of above and the literature available, there is however not enough studies devoted to investigate the influence of melt convection on an unconstrained microstructure, such as columnar or polycrystalline networks. In this regard, the present work intends to fill the gap in our understanding. As discussed above, the incorporation of convection in the melt could lead to the formation of distinct morphologies when compared with the diffusive regime. Moreover, the onset of convective and morphological instabilities during the unidirectional solidification of a binary alloy has been unexplored, and thereupon a precise understanding of the aforementioned problems need to be addressed. Henceforth, from grain boundaries to columnar dendrites, the present dissertation builds upon the experimental and theoretical studies in literature under diffusive regime, and extends it to address the influence of convective transport on microstructural patterns via phase-field modeling.

Part II
Methods

Chapter 3

Phase-field modeling

Formation of complex microstructures in alloy solidification has fascinated researchers in materials science and related areas for many years. However, the principal obstacle in predicting pattern formation is the accuracy in calculating the diffusive-convective transport near the solid-liquid interface [86]. Owing to the increase in computing power, much progress has been made in simulating solidification problems on the scale of microstructures [87]. Traditional simulation methods for treating the free-boundary problems were first based on the front-tracking of sharp-interface. Nonetheless, quantitative results were difficult to obtain as a result of the problems involved in tracking a sharp boundary in a complex morphology. Over past few years, the phase-field approach has become ubiquitous as of late and is gaining popularity as a method of choice to model complex microstructures in solidification, precipitation and strain induced transformations [88].

The principal idea of any phase-field model is to characterize the phases using a non-conserved order parameter that varies smoothly across the diffuse interface. In general, the governing equation ensures that the interface profile evolves in order to minimize the free energy of the system with time, and which is coupled to the diffusion field near the solid-liquid interface. Since it represents the sharp interface formulation of the problem in an accurate and a computationally efficient way, these models are found to be increasingly useful for the materials community because of its fundamental origins [89]. Using simple finite-difference algorithms, a dendritic pattern was the first and the most easiest simulated microstructure at high supercoolings (supersaturations) [90, 91]. The phase-field method has proved to be extremely powerful in the development of dendritic microstructures without the necessity to explicitly track the evolving interface. In addition, this method provides a visual impression of the microstructures which often matches the experimental observations. The primary objective of this chapter is to introduce the fundamental concepts of the phase-field approach, and to briefly summarize the historical developments in literature.

3.1 Phase-field variable and free energy functional

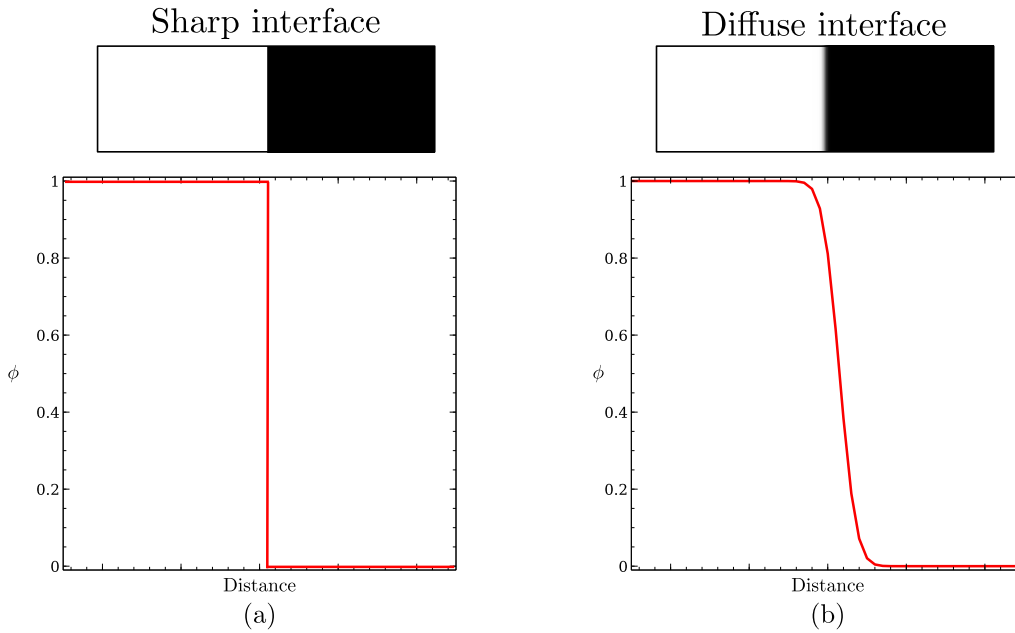


Figure 3.1: (a)-(b) Schematic representation of a sharp interface and a diffuse interface profile. While the white color with $\phi = 1$ depicts a solid phase, $\phi = 0$ represents the liquid phase with black color.

In order to describe the state of a system during phase transformation, traditional thermodynamics utilize variables such as pressure, volume etc. However, it is known that the condensed phases often display changes in positional and or rotational order during a phase transition. Ordered phases are often distinguished from disordered phases by a decreased number of geometric symmetries, and they may be scalars, vectors, or tensors [92]. For example, in ferromagnets, the magnetization is zero above the Curie temperature, but finite below. The popularity of the phase-field approach is due to the elegance with which it treats moving boundary problems in the regime of sharp interface methods. Here, the phase-field variable ϕ is defined as a scalar field that specifies the local state of matter (solid or liquid). In this thesis, it will be interpreted rather as being related to the local volume fraction of the solid phase, that is, the phase field ϕ is 0 in the liquid and 1 in the solid. Between these two values in the bulk phases, the phase-field varies smoothly across a region called the *diffuse interface*, as schematically depicted in Fig. 3.1(b). Subsequently, the phase-field variable is also used to interpolate the thermodynamic and kinetic properties across the interface. The spatial dependence of the phase-field variable presents the unique feature of the phase-field method, wherein the diffuse interface region is introduced by replacing the sharp one. Furthermore, if a single phase-field variable represents the phase transformation from a liquid to a solid phase, then multiple scalar phase-field variables can be used to treat situations where more than two solid phases appear, for example, eutectic and peritectic solidification

[93].

Investigating systems during phase transition involves the construction of a Landau-Ginzburg free-energy functional [94], which unlike the classical model, treats the system as a whole. Therefore, as discussed above, a phase-field ϕ variable is postulated which characterizes the phase of the system at each point in space and time. Under non-equilibrium conditions, the Ginzburg-Landau functional that governs the evolution of the phase-field variable can be expressed as

$$F(T, \phi, \nabla\phi) = \int_V \left[f_{\text{bulk}}(T, \dots) + \frac{K}{2}(\nabla\phi)^2 + f_{\text{dw}}(\phi) \right] dV. \quad (3.1)$$

In general, the bulk free energy term $f_{\text{bulk}}(T, \dots)$ as a function of temperature or concentration is a complex function, and it is typically approximated by a polynomial series that is interpreted as a Taylor series expansion. This formalism often allows for a mesoscopic description of that accounts for bulk thermodynamics and interfaces. On the right-hand side, further terms include the double-well potential energy $f_{\text{dw}}(\phi)$ and the gradient energy $\frac{K}{2}(\nabla^2\phi)$ terms. The bulk free energy term acts as the driving force which governs the phase transformation in a system. Therefore, in the above equation, in addition to the double-well and the gradient energy term a function, $f_{\text{bulk}}(\dots)$, is included. For example, the simplest form of the temperature dependent free energy functional may be approximated for a pure substance as $F = \int_V [f_{\text{int}}(\phi, \nabla\phi) + g(\phi)f_s(T) + (1-g(\phi))f_l(T)]$. Here, f_{int} represents the contribution of the interface which is equal to zero outside of the diffuse interface region. The terms $f_s(T)$ and $f_l(T)$ are the free energy densities of solid and liquid, respectively, and $g(\phi)$ is an higher order interpolation function that satisfies $g(0) = 0$, $g(1) = 1$, and $g'(0) = g'(1) = 0$. While more complex descriptions of the functional F are possible, for the present section, it is assumed that the only contribution to the energy functional from local gradients is that of the phase-field. A more general model might also include contributions due to the gradients of other variables, such as temperature and composition.

3.2 Dynamics of conserved and non-conserved order parameter

The nature of the order parameter, conserved or non-conserved, plays a significant role under non-equilibrium conditions, where, in addition to the spatial dependency, the scalar field also exhibits temporal dependency. The kinetic equations for the scalar fields are called *conserved* if they take on the form of a flux-conserving equation. Similarly, the temporal evolution of the scalar field whose global average need not be conserved is typically governed by a *non-conserved* equation [92]. At first, the dynamics of an order

parameter that represents a conserved quantity is elucidated, where a simple binary alloy is chosen. A disordered phase with average concentration $\phi = \phi_0$ shall undergo phase separation as the temperature decreases below the critical temperature. In an isothermal system, the dynamics of this process is fundamentally driven by the gradients in the chemical potentials μ . As ϕ represents the local concentration differences, the mass conservation equation is given by

$$\frac{\partial \phi}{\partial t} = -\nabla \cdot \mathbf{J} \quad (3.2)$$

where the mass flux is governed by $\mathbf{J} = -M\nabla \cdot \mu$, and M is the mobility. Substituting the flux in the above equation provides us with the following equation of motion for the order parameter of a phase separating alloy mixture

$$\frac{\partial \phi}{\partial t} = \nabla \cdot \left(M \nabla \frac{\delta F}{\delta \phi} \right). \quad (3.3)$$

Here, the chemical potential is derived from the Ginzburg-Landau free energy as a functional of the concentration, and represents a variational derivative rather than a partial derivative. The above equation is widely celebrated as the Cahn-Hilliard equation [95], or Model B as called in the condensed matter physics literature by Hohenberg and Halperin [96], where various order parameter models were classified to describe the associated physical phenomenon.

Next, some phase transformations involve order parameters that do not follow the conservation law. For example, magnetic domain growth, order-disordered transitions, or isothermal solidification of a pure material in the absence of a density jump are some well known physical processes. This is in complete contrast to the phenomenon of phase separation in an alloy mixture, where the the system evolves towards the equilibrium under the condition that total solute in the system be conserved. Therefore, the order parameters that evolve without global conservation are called non-conserved order parameters. In this scenario, the rate of change of a non-conserved order parameter is defined as $\delta F/\delta \phi$, as the global conservation of the variable ϕ is not required, the simplest evolution for a non-conserved order parameter is given by

$$\frac{\partial \phi}{\partial t} = -M \frac{\delta F}{\delta \phi} \quad (3.4)$$

The above equation is referred to as model A by Hohenberg and Halperin's classification of phase-field models [96], a paradigm used to describe the evolution of an order parameter without the requirement of global mass conservation law. In other words, a non-conserved order parameter evolves according to the steepest functional gradient of the free energy, which systematically pushes the order parameter to minimum of the free energy landscape. A classic example that is governed by the above equation is dynamics of a system of Ising spins in the absence of external field.

The evolution equations for both conserved and non-conserved order parameter underline the basic physics of many phase-field models, and have the following generic features

- an order parameter is appropriately chosen to address the physical phenomenon
- a Ginzburg-Landau type free energy density is constructed to include the bulk phases and the interfacial energy of the system
- evolution equations for the order parameter are constructed on the principle of free energy minimization and, if required, conservation laws.

In addition, due to the presence of thermal fluctuation at the microscopic range, and under equilibrium conditions, all quantities of a system continuously fluctuate in space and in time. Therefore, in order to accurately model thermal fluctuations at the solid-liquid interface, stochastic noise sources are also commonly included in the evolution equations.

3.3 Interface structure and energy

The existence of solid-liquid interfaces is inherent in solidification microstructures. Under equilibrium conditions, the bulk driving force is zero, and only the interface contribution remains in the free energy functional. Therefore, from Eq. (3.1), the general form of the interface free energy density F_{int} as suggested by Ginzburg-Landau theory [94] with a gradient and potential term reads

$$F_{\text{int}} = \frac{K}{2}(\nabla\phi)^2 + Hf_{\text{dw}}(\phi). \quad (3.5)$$

Here, $f_{\text{dw}}(\phi)$ is a function of the order parameter ϕ which has two minima $f_{\text{dw}}(\phi) = 0$ for $\phi = 0$ and $\phi = 1$, with a maximum in between these two values to form a double-well potential, and K and H are constants. To analyze further, the free energy density and H have energy/volume as its dimension, and $F_{\text{dw}}(\phi)$ is a dimensionless function, whereas K has dimension of energy/length. Let us now define

$$\epsilon = \sqrt{\frac{K}{H}} \quad (3.6)$$

such that the term ϵ has the dimension of length and represents the finite width of the diffuse interface. Also, \sqrt{KH} has the dimension of surface tension. Henceforth, the two coefficients determine the width and the excess free energy of the interface. At melting temperature, the planar interface at rest at the melting temperature is an equilibrium

state and must therefore satisfy $\frac{\partial \phi}{\partial x} = 0$. Now, calculating the variational derivative of a free energy functional at equilibrium

$$\frac{\delta F}{\delta \phi} = \frac{\partial F_{\text{int}}}{\partial \phi} - \nabla \frac{\partial F_{\text{int}}}{\partial \nabla \phi} = 0 \quad (3.7)$$

For a one-dimensional transition zone between liquid $\phi = 0$ and solid $\phi = 1$ where ϕ varies in the x direction normal to the interface, and considering a simplified form of the double-well function $F_{\text{dw}}(\phi) = \phi^2(1 - \phi)^2$, Eq. (3.5) yields

$$K \left(\frac{\partial \phi(x)}{\partial x} \right)^2 - H \phi^2(1 - \phi)^2 = 0. \quad (3.8)$$

From the above equation, the exact solution of the interface showing the smooth variation in-between the bulk phases is given as

$$\phi(x) = \frac{1}{2} \left[1 + \tanh \left(\frac{x}{2\epsilon} \right) \right] \quad (3.9)$$

where, $\epsilon = \sqrt{K/H}$. This value of the interface thickness is a balance between two opposing effects. Firstly, the interface tends to be sharp in order to minimize the volume of material. Secondly, the interface tends to be diffuse to reduce the energy associated with the gradient of ϕ [90]. In addition, it is important to note that the profile of the interface depends on the choice of the double-well potential f_{dw} and the spatial scale of the profile is set with the constant ϵ . Furthermore, the excess free energy associated with the compositional and/or structural inhomogeneities occurring at interfaces is the interfacial energy. Therefore, the interfacial energy γ is defined as the integral of the interface excess of the free energy

$$\gamma = \int_{-\infty}^{\infty} F_{\text{int}} dx \quad (3.10)$$

$$= \int_{-\infty}^{\infty} \left[\frac{K}{2} (\nabla \phi)^2 + H f_{\text{dw}}(\phi) \right] dx \quad (3.11)$$

$$= H \int_{-\infty}^{\infty} \left[\frac{1}{2} \epsilon^2 (\nabla \phi)^2 + f_{\text{dw}}(\phi) \right] dx \quad (3.12)$$

Now, in the above equation, the variable x is non-dimensionalized after substituting $\tilde{x} = x/\epsilon$, and rewritten as

$$\gamma = \sqrt{KH} \int_{-\infty}^{\infty} \left[\frac{1}{2} \frac{\partial^2 \phi(\tilde{x})}{\partial \tilde{x}^2} + f_{\text{dw}}(\phi) \right] d\tilde{x}. \quad (3.13)$$

Therefore last equation is dimensionless, and for the sake of convenience shall be called I . As a result, the interfacial energy γ is given by

$$\gamma = I \sqrt{KH} \quad (3.14)$$

and utilizing Eq. (3.6), one can obtain

$$\gamma = I\epsilon H. \quad (3.15)$$

From the above expression, we incur that the constant H is the amplitude of the double-well potential, and it determines the height of the energy barrier between the two equilibrium phases. The product of this barrier height H and the thickness of the interface ϵ thus phenomenologically relates the total interface excess energy γ . In general, interfacial energies are anisotropic due to the crystalline nature of solids. The degree of interfacial energy anisotropy can have a significant effect on the growth morphology and equilibrium shape of particles. A number of approaches have been proposed to introduce interfacial energy anisotropy in phase-field models [88]. In conclusion, the above discussed equilibrium solutions are a strict requirement for any phase-field model.

In the late twentieth century, the basic principles of the phase field theory have been extended to develop multi-phase or multi-order parameter phase-field models in an attempt to study numerous polycrystal, multi-phase or multi-component phenomena in phase transformations [92]. In particular, Steinbach et al. [97] developed a phase-field model of a multiphase system in which the phase-field variable was associated with each phase in the system. In this work, an underlying free-energy functional was chosen that involved the pairwise interactions between all the different phases. Analogous with the generic single phase-field models, multi-order and multi-phase-field models were typically constructed so as to respect the thermodynamic symmetries of bulk phases and to consistently reproduce the correct sharp interface kinetics in the limit when phase field interfaces become mathematically sharp. This method begins through defining N variables ϕ_i , and each of which is unity in the corresponding i th single phase region of the sample such that the constraint $\sum_{i=1}^N \phi_i = 1$ is followed [92]. The resulting governing equations are used to conduct numerical simulations in a variety of situations, and the feasibility of this methodology is demonstrated in peritectic and eutectic systems [98, 99]. In the following section, a brief history and the early development of phase-field methods in solidification are discussed in detail.

3.4 Phase-field models for solidification

In the last few decades, an important step in modeling solidification microstructures was initiated by J. S. Langer at the Department of Mathematical Sciences of Carnegie Mellon University (CMU), Pittsburgh [12, 100]. The developed model was based upon the Cahn and Hilliard's [95] approach who derived a formulation that accounted the gradients in thermodynamic properties in heterogeneous systems with diffuse interfaces. The principal idea for the phase-field model was constructed such that a non-conserved order parameter varied smoothly across the diffuse interface and thereafter evolved according

to a governing equation. This generic concept was given a more quantitative outlook by Caginalp et al. [101–103] and Langer [100] who showed that the phase-field model converged to the free-boundary problem in the limit of vanishing interface width.

Based on the seminal phase-field theory, Ryo Kobayashi was the first to simulate a dendritic microstructure [91, 104], where the scheme to solve the Stefan’s problem during the solidification of a pure substance in an undercooled melt was developed by replacing the sharp interface problem by a diffuse interface. Interfacial anisotropy was incorporated in the model which consequently produced realistic needle-like dendritic microstructures for the first time, see Fig. 3.2. While McFadden et al. [105] introduced a two-fold anisotropy, Grossmann et al. [106] applied the method to directional solidification. In subsequent years, the pioneering work of Kobayashi had a strong influence on the development of the phase-field models for simulating dendritic morphologies, wherein several assumptions and restrictions of the phase-field method were addressed in detail.



Figure 3.2: Realistic needle-like dendritic morphology simulated via phase-field method. Reprinted from Kobayashi et al. [91] with permission.

Following the preliminary investigations on pure materials, the next step towards the application of the phase-field theory in materials science was the development of a binary alloy model by Wheeler, Boettinger and McFadden [90, 107, 108]. Widely known as the WBM model, their fundamental approach was to construct a generalized free energy functional that was dependent on both concentration and phase by superposition of two single-phase free energies, and weighting them by the alloy concentration. Eventually, the governing equations were derived for the temporal and spatial variation of the phase-field, which identified the local state or phase, and composition.

The aforementioned phase-field models were initially applicable to large supersaturations only, where the diffusion boundary layer in the liquid ahead of the advancing solid-liquid interface was small. Another restriction was that the numerical parameters were largely dependent on the finite interface thickness. Moreover, the asymptotic analysis of the sharp-interface limit of the phase-field models was not applicable for quantitative computations. Since it was necessary to employ nanometer scale interface widths that

are generally much smaller than the microstructure scale, it became computationally expensive to perform large scale simulations through these models.

Limitations and disadvantages of the phase-field methodology were circumvented when Karma and Rappel [88, 109, 110] pioneered the criteria to choose the simulation parameters for an upscaled diffuse interface width. The thin-interface limit analysis was introduced so as to quantitatively model the physically relevant limit of local thermodynamic equilibrium at the solid-liquid interface (vanishing interface kinetic undercooling). A computationally tractable interface thickness was employed that was just an order of magnitude smaller than the dendrite tip radius, and thus much larger than the real nanometer scale interface width. This methodology permitted them to perform quantitative calculations at reasonably small undercoolings, and also in three dimensions. Subsequently, Murray et al. [111] compared the phase-field results with the dendritic growth experiments on pure undercooled SCN via considering a four-fold interfacial anisotropy. The obtained results were qualitatively in tune with the experimental observations of tip-splitting microstructures. In due course, the computational efficiency was strongly improved by Dantzig et al. [112] and Provatas et al. [113], who developed an adaptive method which refined the mesh in the vicinity of the interface but is left coarse away from the interface. In this manner, the size of the two-dimensional lattice was substantially increased and they found a good agreement with the solvability theory at high undercoolings.

Notwithstanding, for alloy solidification, a quantitative comparison between the interfacial phenomena at the atomistic scale and the simulated microstructure scale is considerably more difficult. A major restriction is that the solute diffusivity in the solid phase is generally much slower when compared in the bulk liquid melt. In these circumstances, the mesoscopic interface width ϵ artificially magnifies several non-equilibrium effects that are generally absent for two-sided diffusion. Almgren [114] was first to characterize these non-equilibrium artifacts via a thin interface analysis of a phase-field model with asymmetric diffusivities. The well known non-equilibrium effects included the diffusion of solutal atoms along the arc length of the interface, namely *surface diffusion*, an *interface stretching* term that modified the mass conservation associated with the local increase of arclength of a moving curved interface, and a discontinuous jump of the chemical potential across the solid-liquid interface, known as *solute trapping*. The magnitude of all these spurious artifacts scaled with the interface thickness. Since the phase-field simulations are performed at orders of magnitude larger than in reality, it is important to ensure that the results are unaffected by numerical artifacts. The advancement with respect to previous phase-field models was achieved by the addition of a phenomenological *anti-trapping solute current* in the mass conservation relation by Karma [89]. This term counterbalanced the physical, albeit the artificially large solute trapping effect generated when a mesoscopic interface thickness is imposed to simulate the interface evolution on

experimental length and time scales. Furthermore, it provided an additional freedom to suppress other spurious effects that scaled with the interface thickness when the diffusivity was unequal in solid and liquid phases [114]. This methodology also paved way for quantitative comparisons between experiments and simulations both in two and three dimensions, with the possibility of testing the theories and concepts used to interpret microstructural pattern formation [115].

Whenever the free energies are interpolated similar to the WBM models [90, 107, 108], there exists an additional length-scale arising from the variation of the grand potential excess across the interface. Especially for systems where the term becomes largely dominant, the surface energy and the interface thickness lose their independence. Consequently, this restricts advantage to simulate physical features, because the growth conditions that can be simulated with such an approach gets restricted. Additionally, one must pre-calculate the contribution of the chemical free energy excess to the surface energy, in order to choose the right simulation parameters. This introduces a non-physical interaction between the free energy bulk phases with the interface and imposes a constraint on the finite interface width.

As mentioned before, early phase-field models of alloy solidification were plagued by a dependence of the surface tension on the interface thickness that arose from the coupling between the phase-field and concentration equations. This problem was solved later through the introduction of *coarse-graining* approach, which generalized the pure substance model by introducing a concentration field in addition to the temperature field and by writing down a free energy functional that depends on the phase field, the temperature, and the concentration [107, 116]. In contrast, a second approach was developed by Kim, Kim and Suzuki [117], where different concentration fields were used for the respective phases, the concentration at a given point is written as an interpolation of the individual phase concentrations, and the equation is closed with the condition of equilibrium chemical potential among the phases, or alternatively a known partition relation among the phase concentrations which enables the determination of the phase concentrations. The common basis for both methodologies however, is that the driving force for phase transformation is the difference of the grand potentials of the phases, at the same chemical potential. Through this construction, it was evident that at equilibrium, there exists no terms arising from the chemical system, which contributed to the solution of the equilibrium phase-field profile. Implying that the equilibrium properties such as the interfacial energies can be fixed independently of the free energy of the respective phases. In this regard, Plapp [118] proposed a methodology where it was shown that the coarse-graining approach could be easily extended to more complex alloy systems if a grand-potential functional was used. Similarly, the limitations of a multi-phase-field model [119] was addressed in detail, and a new model was developed by Choudhury and Nestler [5], where a modified grand potential functional was considered rather than

the free energy functional with the thermodynamic variable as the chemical potential instead of the concentration field. Thereafter it was shown that the excess contribution to the interface was negated, and the length scale related to the interface thickness is independent of the chemical system. Moreover, the developed model was then applicable to simulate complex microstructures for various alloy systems [120–122].

Chapter 4

Grand potential based multi-phase field model

Phase-field models to simulate complex microstructures have been used for more than two decades. Having fairly understood the principal concepts, the governing equations describing alloy solidification are similar to the ones corresponding to pure material [31]. In this regard, the phase-field model for a pure material was extended straightforwardly to an alloy phase-field model, by matching the variables in the pure material problem to the alloy problem. Apart from the shortcomings mentioned in the earlier chapter, previous models [88, 90, 107, 108] were based on two unrealistic assumption. Firstly, the liquidus and solidus lines in the phase diagram were assumed to be parallel, and secondly, the solute diffusivity was constant throughout the system. In realistic systems, the slopes of liquidus and solidus lines are significantly different from each other in a phase diagram, and the solute diffusivity in the solid phases is much smaller than that in the liquid phase. Consequently, a modification of the multi phase-field model [119] was developed, where for a range of applications, the choice of the interface thickness limited the size of the simulation domain and, hence, the large scale microstructure evolution could not be observed. These restrictions were elegantly addressed by Choudhury and Nestler [5], and in this chapter, the modifications as well as the governing equations are described briefly, followed by the inclusion of liquid phase convection. Furthermore, since the solidification morphologies reported in this work are simulated under isothermal conditions, the temperature dependence of the thermodynamic parameters is ignored.

4.1 Grand chemical potential modeling approach

In general, the driving force for phase transformation in alloys in the sharp-interface limit is the difference of the grand potentials of the two bulk phases, and thereafter the evolution equations drive the system in a direction to reduce the difference of grand

potentials between the bulk phases. In this model, the phase evolution is determined by the minimization of the functional $d\Omega/dt \leq 0$, which is formulated as

$$\Omega(T, \boldsymbol{\mu}, \boldsymbol{\phi}) = \int_{\Omega} \left[\Psi(T, \boldsymbol{\mu}, \boldsymbol{\phi}) + \left(\epsilon a(\boldsymbol{\phi}, \nabla \boldsymbol{\phi}) + \frac{1}{\epsilon} w(\boldsymbol{\phi}) \right) \right] d\Omega. \quad (4.1)$$

Here, $\boldsymbol{\mu}$ represents the chemical potentials of the system at a given temperature and $\boldsymbol{\phi} = (\phi_{\alpha}, \dots, \phi_N)$ describes the phase vector with ϕ_{α} being the local volume fraction of the phase α . ϵ is a length scale related to the width of the diffuse interface. In this model, T is the temperature and N is the total number of phases in the system. $\epsilon a(\boldsymbol{\phi}, \nabla \boldsymbol{\phi})$ and $\frac{1}{\epsilon} w(\boldsymbol{\phi})$ are the gradient and obstacle potential type energy densities [123]. The bulk phase grand potential contribution $\Psi(T, \boldsymbol{\mu}, \boldsymbol{\phi})$ is expressed as the interpolation of individual contributions

$$\Psi(T, \boldsymbol{\mu}, \boldsymbol{\phi}) = \sum_{\alpha=1}^N \Psi_{\alpha}(T, \boldsymbol{\mu}) h(\phi_{\alpha}). \quad (4.2)$$

Here, $h(\phi_{\alpha})$ is the interpolation function, and to employ the chemical potential as the fundamental field which replaces the concentration, the thermodynamic function defining the functional needs to be reformulated. Generally, the free energy functional is based on the free energy density $f^{\alpha}(c^{\alpha})$, and the phase-dependent concentration variable in the function $f^{\alpha}(c^{\alpha})$ can be replaced by the intensive variable by considering the Legendre transform of the free energy which yields the expression for individual grand potentials Ψ_{α}

$$\Psi_{\alpha}(T, \boldsymbol{\mu}) = f_{\alpha}(c^{\alpha}(\boldsymbol{\mu}, T), T) - \sum_{\alpha=1}^N \mu c^{\alpha}(\boldsymbol{\mu}, T), \quad (4.3)$$

For a multiphase-field representation, the interpolation function $h(\phi_{\alpha})$ can be chosen of the form

$$h(\phi_{\alpha}) = \frac{\tilde{h}(\phi_{\alpha})}{\sum_{\beta} \tilde{h}(\phi_{\beta})}, \quad (4.4)$$

ensuring that the condition $\sum_{\beta} h(\phi_{\beta}) = 1$ is always fulfilled [124]. $\tilde{h}(\phi_{\alpha})$ is expressed as a third order polynomial

$$\tilde{h}(\phi_{\alpha}) = \phi_{\alpha}^2(3 - 2\phi_{\alpha}). \quad (4.5)$$

As given in Ref. [5], the phase concentrations is expressed by the following constraint

$$c = \sum_{\alpha=1}^N c^{\alpha}(\boldsymbol{\mu}, T) h(\phi_{\alpha}). \quad (4.6)$$

The evolution equation for N phase-field variables used to calculate the temporal change of the phases in each computational cell can be written as

$$\tau \epsilon \frac{\partial \phi_\alpha}{\partial t} = \epsilon \left(\nabla \cdot \frac{\partial a(\phi, \nabla \phi)}{\partial \nabla \phi_\alpha} - \frac{\partial a(\phi, \nabla \phi)}{\partial \phi_\alpha} \right) - \frac{1}{\epsilon} \frac{\partial w(\phi)}{\partial \phi_\alpha} - \frac{\partial \Psi(T, \boldsymbol{\mu}, \phi)}{\partial \phi_\alpha} - \Lambda, \quad (4.7)$$

where Λ is a Lagrange multiplier so that the local constraint $\sum_{\alpha=1}^N \phi_\alpha = 1$ is fulfilled. The relaxation constant τ is chosen according to the expression [5], such that the attachment kinetics at the interface vanishes.

Furthermore, the gradient energy in Eq. (4.1) is expressed as

$$a(\phi, \nabla \phi) = \sum_{\alpha, \beta=1}^{N, N} \gamma_{\alpha\beta} [a_c(\mathbf{q}_{\alpha\beta})^2] |\mathbf{q}_{\alpha\beta}|^2, \quad (4.8)$$

where $\gamma_{\alpha\beta}$ is the interfacial free energy per unit area of the α/β phase boundary. The generalized antisymmetric gradient vector $\mathbf{q}_{\alpha\beta}$ reads $\mathbf{q}_{\alpha\beta} = \phi_\alpha \nabla \phi_\beta - \phi_\beta \nabla \phi_\alpha$. The formulation for the generalized gradient vector $\mathbf{q}_{\alpha\beta}$ allows to distinguish the physics of each phase (or grain) boundary by providing degrees of freedom. The anisotropy of the surface entropy density is modeled by the factor $a_c(\mathbf{q}_{\alpha\beta})^2$ depending on the orientation of the interface. In this model, the phase boundaries with isotropic energies are realized by $a_c(\mathbf{q}_{\alpha\beta}) = 1$, and the anisotropic crystals with an underlying four-fold cubic symmetry is modeled by the expression

$$a_c(\mathbf{q}_{\alpha\beta}) = 1 - \delta_{\alpha\beta} \left(3 \mp 4 \frac{|\mathbf{q}_{\alpha\beta}|_4^4}{|\mathbf{q}_{\alpha\beta}|^4} \right), \quad (4.9)$$

where $|\mathbf{q}_{\alpha\beta}|_4^4 = \sum_{i=1}^d (q_i^4)$ and $|\mathbf{q}_{\alpha\beta}|^4 = [\sum_{i=1}^d (q_i^2)]^2$. The strength of the anisotropy of the $\alpha - \beta$ phase or grain boundary is given by the parameter $\delta_{\alpha\beta}$.

The multiobstacle type potential which is previously described [119] can be written as

$$w(\phi) = \frac{16}{\pi^2} \sum_{\alpha < \beta} \gamma_{\alpha\beta} \phi_\alpha \phi_\beta + \sum_{\alpha < \beta < \delta} \gamma_{\alpha\beta\delta} \phi_\alpha \phi_\beta \phi_\delta. \quad (4.10)$$

Presence of spurious and artificial phases increases the potential in the two-phase region, and in order to avoid third-phase contributions in a two-phase interface, additional third order terms $\sim \phi_\alpha \phi_\beta \phi_\delta$ are added to the multiobstacle potential $w(\phi)$. Although the analytics and numerical handling of this term are discussed in detail by Hoetzer et al. [125], the effect of the third order term on numerical results is discussed in Appendix A.

Starting from the mass diffusion equation, the evolution equation for the concentration fields can be written as

$$\frac{\partial c}{\partial t} + \nabla \cdot (\mathbf{U}c) = \nabla \cdot \left(M(\phi) \nabla \mu - \mathbf{J}_{at} - \mathbf{q}_n \right). \quad (4.11)$$

In the above mass conservation equation, the right hand side has contributions from diffusion as a result of gradients in the chemical potential, and the mobility $M(\phi)$ is defined as

$$M(\phi) = \sum_{\alpha=1}^N M^\alpha g(\phi_\alpha), \quad (4.12)$$

where the individual phase mobilities M^α is written as

$$M^\alpha = \sum_{i=1}^N D_i^\alpha \frac{\partial c^\alpha(\boldsymbol{\mu}, T)}{\partial \mu}. \quad (4.13)$$

Here, D_i^α accounts for the transport of solutal fields inside the respective phase volumes, and $g(\phi_\alpha)$ is an interpolation function of the form similar to $h(\phi_\alpha)$ in Eq. (4.5). However, strictly speaking, the functions to interpolate mobilities and the grand potentials need not be the same. In general, the order of magnitude of solute diffusivity in the solid phases is much lower $D_i^\alpha \lll D_i^\beta$ when compared within the bulk liquid phases. Henceforth, in the present thesis, as a good approximation for alloy solidification, the diffusion of solutal species in the solid phases is considered negligible (zero diffusivity in the solid phase). In addition, the term \mathbf{U} represents the liquid velocity vector. All the remaining terms in the above equation are discussed in the detail in the upcoming sections. Now, from Eq. (4.6), rewriting the time derivative of the concentration fields gives us

$$\frac{\partial c}{\partial t} = \sum_{\alpha=1}^N \frac{\partial c^\alpha(\boldsymbol{\mu}, T)}{\partial \mu} \frac{\partial \mu}{\partial t} h(\phi_\alpha) + \sum_{\alpha=1}^N \frac{\partial c^\alpha(\boldsymbol{\mu}, T)}{\partial T} \frac{\partial T}{\partial t} h(\phi_\alpha) + \sum_{\alpha=1}^N c^\alpha(\boldsymbol{\mu}, T) \frac{\partial h(\phi_\alpha)}{\partial \phi} \frac{\partial \phi}{\partial t}. \quad (4.14)$$

In the present thesis, the unidirectional solidification of microstructures under diffusive-convective regime is performed under isothermal conditions only. In this regard, the variation of temperature fields across diffuse interface is constant $\frac{\partial T}{\partial t} = 0$, and the second term on the left hand side of the above equation is neglected. Therefore, the evolution equation for the chemical potentials can be obtained by substituting the above equation in Eq. (4.11)

$$\sum_{\alpha=1}^N \frac{\partial c^\alpha(\boldsymbol{\mu})}{\partial \mu} \frac{\partial \mu}{\partial t} h(\phi_\alpha) + \sum_{\alpha=1}^N c^\alpha(\boldsymbol{\mu}) \frac{\partial h(\phi_\alpha)}{\partial \phi} \frac{\partial \phi}{\partial t} = \nabla \cdot \left(M(\phi) \nabla \mu - (\mathbf{U}c) - \mathbf{J}_{at} - \mathbf{q}_n \right). \quad (4.15)$$

Rearranging the terms we get

$$\frac{\partial \mu}{\partial t} = \left[\sum_{\alpha=1}^N h(\phi_\alpha) \frac{\partial c^\alpha(\boldsymbol{\mu})}{\partial \mu} \right]^{-1} \times \left\{ \nabla \cdot \left(M(\phi) \nabla \mu - \mathbf{U}c - \mathbf{J}_{at} - \mathbf{q}_n \right) - \sum_{\alpha=1}^N c^\alpha(\boldsymbol{\mu}) \frac{\partial h(\phi_\alpha)}{\partial \phi} \frac{\partial \phi}{\partial t} \right\}. \quad (4.16)$$

The evolution equations are discretized using finite differences in space, and the time derivative follows an explicit scheme. The phase-fields variables are computed in the center of the cells, whereas the chemical potentials and the velocity components are solved in the center for the faces in three-dimensions. The numerical algorithm is parallelized via message passing interface and a detailed description of the implementation is given in Ref. [126].

4.1.1 Anti-trapping current

It is well known that the phase-field simulations are generally performed at a mesoscopic thickness, and the presence of non-equilibrium artifacts influences the large-scale pattern evolution via competing with, or even superseding, the capillary effects [114]. These artifacts are observed especially in alloy solidification, since the solute diffusivity varies asymmetrically through the solid-liquid diffuse interface, from zero in the solid (for a one-sided model) to a constant value D_i^β in the liquid phase. The best known effect is *solute trapping*, which is associated with the chemical potential jump at the interface. As the magnitude of these non-equilibrium artifacts scales with the thickness of the interface, its magnitude is greatly exaggerated as the simulations are upscaled. As a result, the solute trapping artifact will appear for solidification velocities that are much smaller than those observed in experiments. Therefore, in order to perform accurate phase-field simulations, it has to be eliminated from the phase-field model. For isothermal and directional solidification [89, 115], an additional contribution, namely *anti-trapping current* \mathbf{J}_{at} in the flux was proposed to counteract the solute trapping effect. In this regard, a supplementary term is introduced in the mass conservation equation Eq. (4.16), where the corrective anti-trapping term produces a mass flux along the normal direction, and thereby counterbalances the trapping current due to the presence of non-equilibrium artifacts, expressed as

$$\mathbf{J}_{at} = -\frac{\pi\epsilon}{4} \frac{g(\phi_\alpha)[1-h(\phi_\alpha)]}{\sqrt{\phi_\alpha(1-\phi_\alpha)}} \times [c^\beta(\boldsymbol{\mu}, T) - c^\alpha(\boldsymbol{\mu}, T)] \frac{\partial\phi_\alpha}{\partial t} \frac{\nabla\phi_\alpha}{|\nabla\phi_\alpha|}. \quad (4.17)$$

A complete description of the above anti-trapping term is discussed in detail by Choudhury and Nestler[5], where the anti-trapping term \mathbf{J}_{at} is proportional to the interface thickness and to the growth velocity, and directed from the solid to the liquid in order to assist the solute transport from solid to liquid phase along the unit normal vector. Furthermore, as said above, the inclusion of the above term also provides additional freedom in the model to suppress other spurious effects that scale with the interface thickness for studies with unequal diffusivities in the solid and liquid phases.

4.1.2 Thermal fluctuations

Imperfections along a solidifying planar interface are prevalent in directional solidification experiments [127]. In the form of thermal fluctuations at the solid-liquid interface, these random fluctuations assist the initiation of initial perturbations across the solidification front. For dendrites, further developments [128–131] reported a physical picture, where small noisy perturbations amplified to a macroscale along the sides of a steady-state crystal, in qualitative agreement with some experiments [131]. Henceforth, the numerical noise term \mathbf{q}_n in Eq. (4.16) is included to accurately capture the presence of thermal fluctuations at the solid-liquid interface. Especially, for typical growth conditions in binary alloys where the attachment kinetics is negligible, the conserved noise in the mass flux is the most appropriate manner to account the role of thermal fluctuations. Through the fluctuation-dissipation theorem [132, 133], the term \mathbf{q}_n follows a Gaussian distribution with a variance

$$\langle \mathbf{q}_m(\mathbf{x}, t) \mathbf{q}_n(\mathbf{x}', t) \rangle = 2D_i^\beta F_u \delta_{mn} \delta(\mathbf{x} - \mathbf{x}') \delta(t - t') \quad (4.18)$$

Here, δ is the Dirac function, δ_{mn} is the Kronecker delta, \mathbf{q}_n , is the random variable along the normal direction, while \mathbf{q}_m , with $m = x, y, z$, are the generated random variables in space and time, respectively, through the conventional Polar Marsaglia method [134]. The magnitude of the numerical noise $F_u = 0.06$ is calculated according to Karma and Rappel [133].

4.2 Relation to sharp-interface limit

In order to make the phase-field model a numerical tool for simulating free-boundary problems, the equivalence between the phase-field model and the free-boundary problem needs to be established. Therefore, it remains to be demonstrated that the phase-field model generates the correct boundary conditions at the interfaces, and to relate the parameters of the phase-field model to those of the free-boundary problem. In this regard, a comprehensive asymptotic analysis is generally performed of the phase-field model for a two phase binary alloy solidification problem with the assumption of one-sided diffusion in the liquid phase. The general idea is as follows, two different coordinate systems are defined by the technique of matched asymptotic expansions, often also called boundary-layer calculations. The first one corresponds to the sharp-interface problem, *outer scale*, and the second one is attached with the interface, *inner scale*, scaled by the interface thickness. Next, these fields are expanded as a power series in the parameter ϵ , which gives an outer expansion and an inner expansion. Then, the equations of the phase-field model are solved perturbatively order by order in ϵ in each region are solved, using the relevant coordinate system. Lastly, the two expansions are matched order by

order using the condition that the limit of the inner expansion far from the interface must coincide with the limit of the outer expansion when the interface is approached. The result of this procedure are the boundary conditions for the relevant fields on the outer scale, which are determined by the equations on the inner scale. The asymptotic analysis accompanying the early phase-field models were confined to the sharp interface limit wherein the model was analysed for the condition that the interface width tends to zero $\epsilon \rightarrow 0$ [113]. This analysis unravels the compliance of the phase-field approach to the physical laws, particularly the Gibbs-Thomson relation, in addition to other sharp interface solutions. The analysis was subsequently extended to included finite interface limit [88], and the expressions for the kinetic coefficient in the thin-interface limit were performed via an asymptotic analysis, and the matched asymptotics is presented in detail by Choudhury and Nestler [5]. In the upcoming chapters, the simulation conditions are imposed such that the attachment kinetics is negligible. The interface relaxation coefficient τ is calculated through a thin-interface analysis [5, 88] as

$$\tau = \epsilon \frac{[c_{\text{eq}}^{\beta} - c_{\text{eq}}^{\alpha}](M + F)}{D_i^{\beta} \frac{\partial c^{\beta}}{\partial \mu}} \quad (4.19)$$

For the third order interpolation function $h(\phi_{\alpha})$ in Eq. (4.5), when used in combination with the obstacle potential, the values of F and M are 0.063828 and 0.158741 respectively [5].

4.3 Incorporation of melt convection

The presence of melt flow in the liquid phase strongly influences the microstructural evolution in solidification patterns, where its dominant effect is to speed up the transport of solute near the solid-liquid interface. Fundamental equations of fluid dynamics are called Navier-Stokes equations, wherein the case of an isothermal flow, they represent two physical conservation laws, namely, the conservation of fluid momentum and the conservation of mass, given as

$$\rho \left(\frac{\partial}{\partial t} (\mathbf{U}) + \mathbf{U} \cdot \nabla \mathbf{U} \right) = -\nabla p + \nabla \cdot [\eta (\nabla \mathbf{U} + \nabla \mathbf{U}^T)] \quad (4.20)$$

and

$$\nabla \cdot (\mathbf{U}) = 0. \quad (4.21)$$

Here, \mathbf{U} , ρ , p , η denote the liquid velocity, density, pressure and the dynamic viscosity of the liquid melt respectively. Apart from the imposed convection velocity, the flow parameters $\rho = 1.0$ and $\eta = 1.0$ are considered constant throughout the dissertation. Furthermore, in this work, an incompressible melt flow is considered such that the density change of the alloy melt is negligible, and no additional body forces are present in the

system. Over the last few years, different methodologies to incorporate convective transport into phase-field models have been developed. One is to treat the solid as a highly viscous liquid, where the viscosity depend on the phase field in the standard Navier-Stokes equations. Another method is to use the the diffuse interface region as a rigid porous medium, where the porosity is identified with the phase-field variable. Widely known as the Beckermann approach [82], in this method, the usual no-slip condition at a sharp solid-liquid interface is enforced through a varying interfacial force term in the diffuse interface region. Using a thin-interface approach, this method has shown that the interface thickness only needs to be small compared to the mesoscale of the flow field. The above equations are coupled with the phase-field vector ϕ , where the velocity vector is expressed as

$$\mathbf{U} = \phi_\alpha \mathbf{U}_\alpha + \phi_\beta \mathbf{U}_\beta, \quad (4.22)$$

where a non-conserved quantity ϕ_β for the liquid phase and ϕ_α for solid, $\phi_\alpha = 1 - \phi_\beta$ is introduced, on the basis of the local constraint $\sum_{\alpha=1}^N \phi_\alpha = 1$. In this thesis, the solid phase is considered stationary and rigid, such that the velocity of the solid phases are considered negligible $\phi_\alpha \mathbf{U}_\alpha = 0$. Henceforth, the convection velocity vector is expressed as

$$\mathbf{U} = \phi_\beta \mathbf{U}_\beta \quad (4.23)$$

Therefore, the fluid momentum and mass balance equations are reformulated as

$$\rho \left(\frac{\partial}{\partial t} (\phi_\beta \mathbf{U}_\beta) + \phi_\beta \mathbf{U}_\beta \cdot \nabla \mathbf{U}_\beta \right) = -\phi_\beta \nabla p + \nabla \cdot [\eta (\nabla \phi_\beta \mathbf{U}_\beta + \nabla \phi_\beta \mathbf{U}_\beta^T)] - \mathbf{M}_I^d, \quad (4.24)$$

and

$$\nabla \cdot (\phi_\beta \mathbf{U}_\beta) = 0. \quad (4.25)$$

Again, similar to Beckermann et al. [82], the last term \mathbf{M}_I^d explains the dissipative viscous stress, expressed as

$$\mathbf{M}_I^d = \eta h \phi_\beta \frac{\mathbf{U}}{\epsilon} |\nabla \phi_\beta|, \quad (4.26)$$

Here, h is the dimensionless parameter. This particular term provides a distributed momentum sink in the diffuse interface region, thus forcing the liquid velocity to zero as $\phi \rightarrow 1$, such that while approaching towards the liquid side of the diffuse interface, the convection velocity becomes linear. The dimensionless parameter h is generally evaluated via performing an asymptotic analysis [135] and in the present model, h has the value 7.989 for the obstacle type potential Eq. (4.10).

4.3.1 Dimensionless parameter h

The dimensionless parameter h in the dissipative stress term \mathbf{M}_l^d in Eq. (4.26), and the discontinuity of the velocity profile is treated via performing an asymptotic analysis, i.e., matching the inner solution of the diffuse interface with the outer velocity profile corresponding to the sharp interface. In general, the term h plays a vital role in determining the accuracy of the velocity profiles at the solid-liquid interface. To begin with, let us consider a Poiseuille flow in-between the two plates at $y = 0$ and $y = L$ oriented parallel to the x -axis, see Fig. 4.1. Here, the no-slip condition is applied at the solid-liquid interface $\phi = 0.5$, and the solid-liquid interface $\phi = 0.5$ is expected to be at $z = 0$. Now, using $\phi_\beta \mathbf{U}_\beta = u_l$, the steady state momentum equation for a sharp interface reads

$$\eta \frac{d^2 u_l}{dy^2} = \frac{dp}{dx}. \quad (4.27)$$

After applying the no-slip boundary conditions at the two stationary walls, the analytical

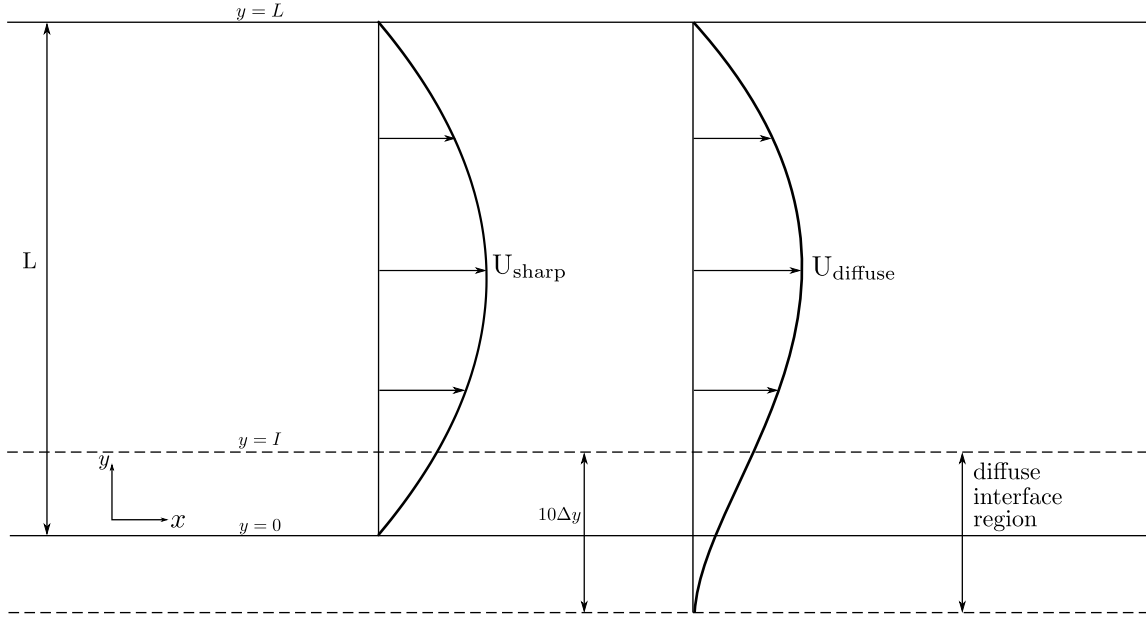


Figure 4.1: Schematic description of the velocity profiles for the Poiseuille flow with a sharp interface U_{sharp} and a diffuse interface U_{diffuse} . Here, $y = 0$ represents the solid-liquid interface $\phi = 0.5$. The walls at $y = L$ and $y = 0$ are considered stationary.

solution to the above equation is given as

$$u_l(y) = -\frac{L^2}{2\eta} \frac{dp}{dx} \left[1 - \left(\frac{y}{L} \right)^2 \right]. \quad (4.28)$$

Similarly, the momentum equation for a diffuse interface approach is expressed as

$$\eta \frac{d^2 u_l}{dy^2} - \frac{4}{\pi \epsilon^2} h \eta \frac{(1-\phi)}{\phi} \sqrt{\phi(1-\phi)} u_l = \phi \frac{dp}{dx}. \quad (4.29)$$

Here, the second term represents the dissipative stress term \mathbf{M}_l^d , rewritten for the multi-obstacle potential in Eq. (4.13). Nevertheless, the term \mathbf{M}_l^d acts such that if $h = 0$, we get back to the sharp interface description in Eq. (4.27). The above equation can now be rewritten after introducing a variable $y = Y\Delta y$ and substituting $\epsilon = 4\Delta y$ [5, 119]

$$\eta \frac{d^2 u_l}{dY^2} - \frac{h\eta(1-\phi)}{4\pi\phi} \sqrt{\phi(1-\phi)} u_l = \Delta y^2 \phi \frac{dp}{dx}. \quad (4.30)$$

Considering the limit when Δy is very small, the right hand side in the above equation can be neglected and expressed as

$$\eta \frac{d^2 u_l}{dY^2} - \frac{h\eta(1-\phi)}{4\pi\phi} \sqrt{\phi(1-\phi)} u_l = 0. \quad (4.31)$$

Similar to Beckermann [82], it is believed that the solution to the above momentum equation varies exponentially within the diffuse interface region, i.e., $u_l(Y) = \exp(\sqrt{h}Y)$. The value of h should be obtained such that at $y = I$, the velocity profiles of the sharp and the diffuse interface match. Thereby, the solution of the Eq. (4.30) within the diffuse interface is determined numerically with a 4th order Runge-Kutta solver and compared with the outer solution defined by Eq. (4.28). Henceforth, it is estimated that with a value of $h = 7.989$ the velocity profile of the diffuse interface matches closely with that of the sharp interface with minimum deviation. Lastly, as the obstacle potential is given by Eq. (4.10), the value of the dimensionless term h differs with Beckermann [82], further information on the dimensionless term h is discussed in detail by Selzer [135].

4.4 Thermodynamic bulk free energies

To mimic realistic microstructures, the thermodynamic properties of the material system under investigation is a prerequisite for alloy solidification. Therefore, attempts were made to thermodynamically describe the system based on the corresponding phase diagrams of the components involved. A key component in modeling real multi-component alloys is the utilization of thermodynamic information from the well-known collection of databases. Incorporating CALPHAD database, CALculation of PHase Diagrams [136, 137] in phase-field models acts as a source for these essential material properties, and has a significant influence on the course of the simulated phase transitions. Integrating phase-field models with thermodynamic databases has been described in detail by Moelans et al. [124] and others [138, 139]. The most essential methodologies are as follows, the first requires the direct computation of the thermodynamic driving force in the equations of motion of the interfaces, using the computation routines embedded in the optimization engines which are usually part of softwares developed to calculate phase diagrams, for example, PANDAT, THERMOCALC. However, the procedure to evaluate the driving forces from the respective databases at every time-iteration is computationally intensive and therefore rarely performed. Especially for phase-field models, since one

does not require the information of the free-energies in the whole range of concentrations. The second approach deals with the formulation of simplistic bulk free energies which incorporates the thermodynamic attributes in the locality of compositions around which the system is expected to exist during dynamic evolution.

In order to describe the thermodynamics of the respective bulk phases, the variation of the grand potentials with composition of the respective phases is approximated using a second degree polynomial in a method proposed by Choudhury et al. [140]. For the solid phase α , we define the bulk free energy of an isothermal binary alloy model system in the following polynomial form

$$f_{\alpha}(c_i, c_j) = A^{\alpha}c_i^2 + B^{\alpha}c_j^2 + D^{\alpha}c_i + E^{\alpha}c_j + F^{\alpha}. \quad (4.32)$$

Here, c_i and c_j are the mole concentrations of the components i and j , respectively. In addition, the coefficients $A^{\alpha}, B^{\alpha}, D^{\alpha}, E^{\alpha}, F^{\alpha}$ represent the fitted free-energy coefficients. Since we consider a two component binary alloy model, we follow the local constraint $c_i + c_j = 1$, and express the above equation in terms of c_i as

$$f_{\alpha}(c_i) = (A^{\alpha} + B^{\alpha})c_i^2 + (D^{\alpha} - E^{\alpha} - 2B^{\alpha})c_i + E^{\alpha} + F^{\alpha} + B^{\alpha}, \quad (4.33)$$

which is further reformulated as

$$f_{\alpha}(c_i) = A_{12}^{\alpha}c_i^2 + A_{13}^{\alpha}c_i + A_{14}^{\alpha}, \quad (4.34)$$

where $A_{12}^{\alpha} = A^{\alpha} + B^{\alpha}$, $A_{13}^{\alpha} = D^{\alpha} - E^{\alpha} - 2B^{\alpha}$ and $A_{14}^{\alpha} = E^{\alpha} + B^{\alpha} + F^{\alpha}$. Here, the coefficients A_{12}^{α} , A_{13}^{α} and A_{14}^{α} are determined using the free energy densities, chemical potential as well as the equilibrium mole fractions of a binary isothermal model alloy system. Now, the thermodynamic functions required for the grand potential model can be derived through the above expression. Hereafter, one can again calculate a function for the chemical potentials, which is expressed by the first derivative of the polynomial

$$\mu(c_i) = \frac{\partial f^{\alpha}}{\partial c_i} = 2A_{12}^{\alpha}c_i + A_{13}^{\alpha}. \quad (4.35)$$

Next, the phase concentrations can be derived as functions of the chemical potential by inverting the above expression,

$$c_i(\mu) = \frac{(\mu - A_{13}^{\alpha})}{2A_{12}^{\alpha}}, \quad (4.36)$$

and their derivatives with respect to μ is given as

$$\frac{\partial c_i}{\partial \mu} = \frac{1}{2A_{12}^{\alpha}}. \quad (4.37)$$

Finally, by substituting the expression for $c_i(\mu)$ in $f_{\alpha}(c_i) - \mu c_i$ we obtain the approximated grand potential densities

$$\Psi^{\alpha}(\mu) = A_{14}^{\alpha} - \frac{(\mu - A_{13}^{\alpha})^2}{2A_{12}^{\alpha}} \quad (4.38)$$

$$\Psi^\alpha(\mu) = -\frac{1}{4A_{12}^\alpha}\mu^2 + \frac{A_{13}^\alpha}{2A_{12}^\alpha}\mu + A_{14}^\alpha - \frac{A_{13}^\alpha}{4A_{12}^\alpha} \quad (4.39)$$

From the above, all the thermodynamic functions for the grand potential model in the case of a binary system are now obtained. As discussed before, the grand potential densities are given as quadratic polynomials depending on the chemical potentials. In the context of quantitative phase-field modelling, the approach of data fitting can be used to derive simplified thermodynamic functions from the CALPHAD database with an acceptably small error inside of the data range of interest [140]. In the present work, the least squares method is adapted to perform the fits, which is a commonly used tool for regression analysis. Hereby, the bulk free energy coefficients in Eq. (4.34) are calculated such that they represent the typical data from CALPHAD database for a binary alloy model system. In our present purpose, we choose the coefficients to be $A_{12}^\alpha = 1.00$, $A_{13}^\alpha = -0.40$, $A_{14}^\alpha = 0.04$ for the solid, and, $A_{12}^\beta = 2.00$, $A_{13}^\beta = -3.20$, $A_{14}^\beta = 1.28$ for the liquid phase respectively. Moreover, since we are simulating the generic features of solidification microstructures coupled with convection in the liquid alloy melt, the chosen methodology in the present work can be extended straightforwardly to other binary alloy systems [71, 72]. In the present work, the equilibrium mole fractions in the solid α and liquid β phases are set as $c_{\text{eq}}^\alpha = 0.2$ and $c_{\text{eq}}^\beta = 0.8$ respectively. Also, the dimensionless melt supersaturation Δ is given as

$$\Delta = \frac{c_{\text{eq}}^\beta - c^\beta}{c_{\text{eq}}^\beta - c_{\text{eq}}^\alpha}, \quad (4.40)$$

In an isothermal system the driving force for phase transformation is developed through the growth of a product phase into a supersaturated parent phase. In the scope of this thesis, the phase-field simulations for alloy solidification are carried out on the assumption of isothermal conditions, and therefore the numerical results presented in the upcoming chapters are performed for constant temperature.

Part III
Results and Discussion

Chapter 5

Liquid grooving at grain boundaries

Grain boundaries are of considerable scientific and technological interest due to their significant influence on structural and material properties. Initiation of transport pathways, formation of voids in the inter granular regions [141], secondary phase nucleation sites [142], sintering [143, 144], and formation of sinks during creep mechanism [145, 146] are some widely known examples of grain boundary (GB) induced phenomena. From a technological point of view, in nanocrystalline thin films, the deepening of grain boundary grooves at interface trijunctions was suggested as the primary mechanism for thin film breakup [147, 148]. This limited their applicability as surface protective coatings for tribological applications, diffusion barriers in microelectronics and hard wear resistant cutting tools [149, 150]. Understanding and predicting the grain boundary behavior in crystalline materials is therefore important. In this chapter the phenomenon of liquid grooving is reproduced, and the groove kinetics is compared with the classical Mullins's theory. Subsequently, the grain boundary grooving is extended, wherein the cooperative effect of volume diffusion and melt convection in the liquid phase is extensively investigated. *Parts of the results presented in this chapter has been published in Acta Materialia [7].*

5.1 Grain boundary grooving: Revisiting Mullins's seminal theory

Under isothermal conditions, a polycrystalline material in contact with a saturated liquid melt develops a groove at the interphase junctions. In order to minimize the excess interfacial free energy at the solid-solid grain boundary, the V-shaped groove deepens with time. In addition, the difference in the chemical potentials between the curved surface near the groove root and the relatively even surface further from the groove pit causes a drift of the material by various mechanisms, such as evaporation-condensation, volume

diffusion or surface diffusion. In a realistic scenario, all of these transport mechanisms operate concurrently at the solid-liquid interface [6, 151], but under some conditions one may dominate. In general, there are two types of grain boundary grooves, namely, thermal and liquid. When an interface separates a solid phase from vacuum or from saturated metal vapour, the grooves are referred to as *thermal grooves* (TGs). But, when it separates a liquid and a solid phase, the grooves are classified as *liquid grooves* (LGs). Experimental micrographs of grain boundary grooves under equilibrium conditions are presented in Fig. 5.1, where the two solid grains are separated by the solid-solid grain boundary. The seminal theory of grain boundary grooving was addressed by Mullins [6, 152], where the formation of a symmetric V-shaped groove in-between the two semi-infinite solid grains was investigated for the very first time. The classical theory of Mullins was based upon the following assumptions:

- The grain boundary is perpendicular to the surface of the bi-crystal sample.
- The grain boundary does not participate in the material transport, i.e., there is no grain boundary diffusion.
- The surface properties, especially the surface energies are independent of the crystallographic orientation.
- The transport mechanisms of solute atoms are independent from one another.
- The presence of lateral flow near the grain boundary is negligible.

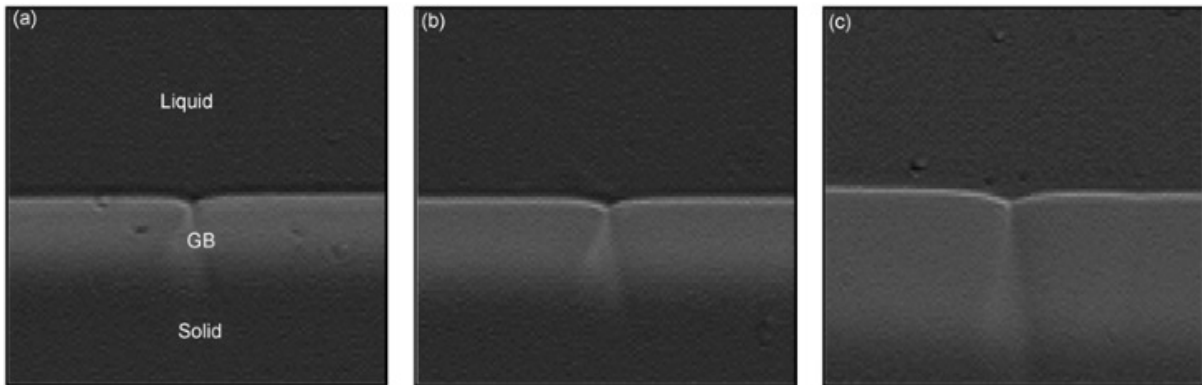


Figure 5.1: (a)-(c) Experimental micrographs of liquid grooving at the solid-solid grain boundary under equilibrium conditions. Reprinted from Xing et al. [23] with permission.

Based on the mechanism of material transport, it was proposed that the groove geometries increased with a temporal exponent of $1/3$, $1/4$ and $1/2$ for volume diffusion, surface diffusion and evaporation and condensation, respectively. In addition, it was reported that the groove profiles corresponding to these mechanisms were not identical. In the case of surface diffusion and volume diffusion, the groove root conserved mass

to generate symmetric ridges on either side of the grain boundary, whereas, in the case of condensation-evaporation, the formation of ridges was absent. Thereafter, Mullins's theory motivated others to identify the mechanism responsible for experimentally developed grooves through both kinetic and profile properties. In addition, the grooving mechanism was also predicted by the physical properties of the material and experimental environments.

Later, Mullins's theory was extended for an entire range of dihedral angles by Hardy [153], where the theoretical predictions were in close agreement with the volume diffusion dominated grooving experiments. For practical conditions, Mullins's theoretical analysis was further extended by considering polycrystalline samples and mobile grain boundaries [154]. GB grooving studies were subsequently employed to experimentally determine the diffusion coefficients in binary alloys [155, 156].

5.1.1 Grain boundary grooving by volume diffusion

In the present section, the volume diffusion induced grain boundary grooving phenomenon is simulated, and the groove kinetics is compared with the classical theory of Mullins [6]. It is well known that if the phase boundaries are isotropic and independent of the crystallographic orientation, the formation of an equilibrium dihedral angle Φ is attained by the force balance at the interfacial trijunction. A schematic representation of the local equilibrium angle at the trijunction is depicted in Fig. 5.2, where the equilibrium angle is given by Young's law

$$\Phi = 2 \cos^{-1} \frac{\gamma_{gb}}{2\gamma_{sl}}. \quad (5.1)$$

Here, γ_{gb} , is the surface energy of the grain boundary and γ_{sl} is the solid-liquid interfacial energy. The dihedral angle at the triple junction decreases as the grain boundary energy increases, and the dihedral angle ceases to exist as the grain boundary energy is greater than twice the solid-liquid interfacial energy.

At first, the simulation domain is initialized with two distinct semi-infinite solid grains, as shown in Fig. 5.3 in blue and red colors, respectively. Here, the periodic boundary condition is considered for the left and right, and the no-flux boundary condition is imposed on the top and the bottom sides of the simulation domain, respectively. The lateral domain boundaries are far away from the groove root and have no influence on the numerical results. For the present simulations, $\gamma_{gb}/\gamma_{sl} = 1.0$ is considered, where γ_{gb} , is the surface energy of the grain boundary and γ_{sl} is the solid-liquid interfacial energy. Lastly, in this thesis, the set of common parameters will be in dimensionless units, and for the sake of completeness, order of magnitudes for the parameters are listed in Appendix. A. The material and simulation parameters to model the phenomenon of grain boundary grooving are given in Table. 5.1.

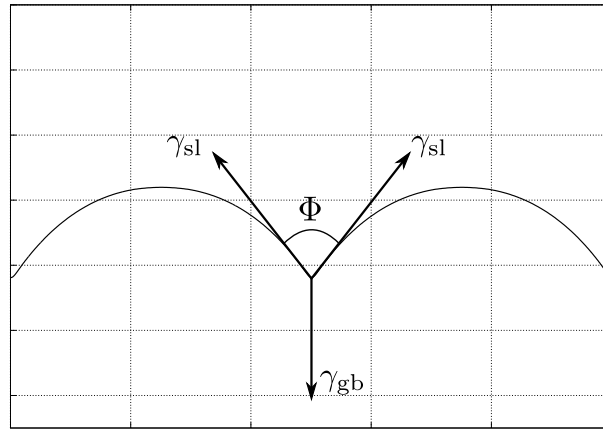


Figure 5.2: A diagrammatic illustration of the equilibrium angle Φ at the trijunction, where γ_{gb} , γ_{sl} represent the grain boundary and the solid-liquid interfacial energies, respectively.

Table 5.1: Material and numerical parameters to simulate the phenomenon of liquid grooving at the grain boundaries.

Description	Parameter	Value
Diffusivity	D_i^β	2.00
Partition coefficient	k	0.25
Interface width	ϵ	2.00
Third order term	$\delta_{\alpha\beta\gamma}$	2.0
Discretized grid space	$\Delta x = \Delta y$	0.5
Time step	Δt	0.03

In order to maintain the local equilibrium at the trijunction, the groove root deepens with time and a V-shaped symmetric groove is systematically established in-between the two adjacent semi-infinite grains under isothermal conditions. According to Mullins's theory [6, 152], the groove dimensions are proportional to the annealing time, and follows a kinetic law of the form

$$d_g(t) = Bt^n, \quad (5.2)$$

where, d_g represents the groove depth which is defined as the distance between the initial planar interface and the groove root, B is materials constant. Although, the temporal exponent n varies depending upon the mechanism of material transport, as per Mullins's solution for volume diffusion [6], $n = 1/3$ is expected for the present study.

Initialized with a dihedral angle $\Phi = 180^\circ$ at the interface junction, the system will form a groove, in order to minimize the interfacial free energy, as shown in Fig. 5.3(a)-(b). The temporal evolution of the bicrystal solid grains is depicted in Fig. 5.3(b), where the solute atoms tend to leave the curved surface and consequently force the groove to deepen with time. As the mass transport ahead of the solid-liquid interface is controlled by bulk diffusion in the liquid phase, the symmetric nature of the V-shaped groove profiles is evident through the $\phi = 0.5$ isolines in Fig. 5.4. The variation of interfacial curvature

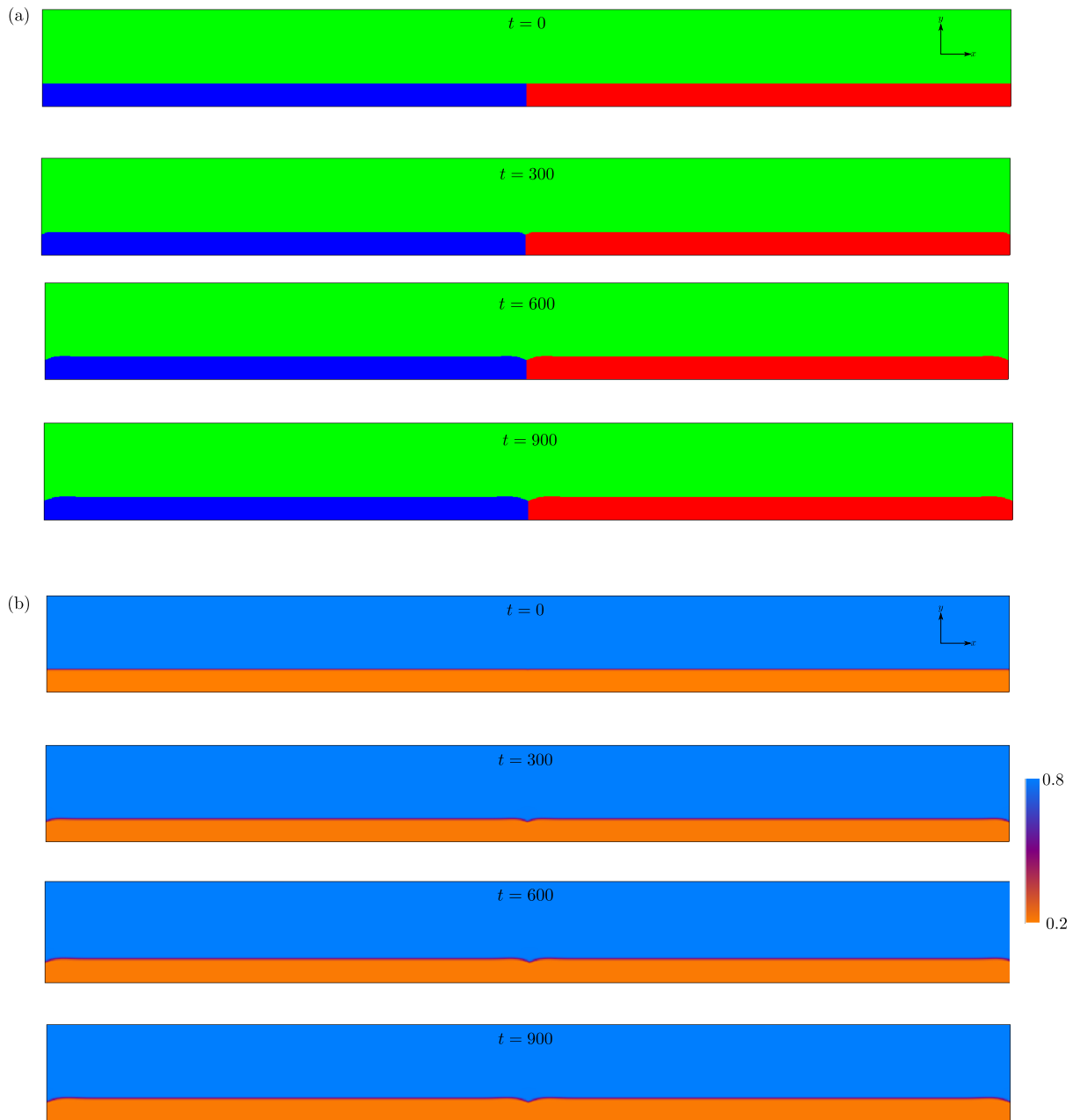


Figure 5.3: (a)-(b) Temporal evolution of phase and concentration fields for a semi-infinite bicrystal grain under the influence of volume diffusion. At $t = 0$, the initial simulation condition is depicted, where the grain boundary forms a T-shaped interface junction in-between the solid grains. In order to minimize the excess interfacial free energy at the grain boundary, the groove deepens with time. Here, the blue and red colors indicate the two solid grains, respectively. The color bar illustrates the concentration field according to the legend embedded near the snapshots.

and thereby the chemical potentials at the groove pit region is shown in Fig. 5.5, where the non-uniform curvature across the grain boundary drives the solute atoms away from the root position towards the grain centers. As time elapses, the bicrystal grain attains a time independent profile depending upon the imposed surface energies. This mechanism of liquid groove deepening in Fig. 5.3 is similar to the groove channels studied by Bokstein

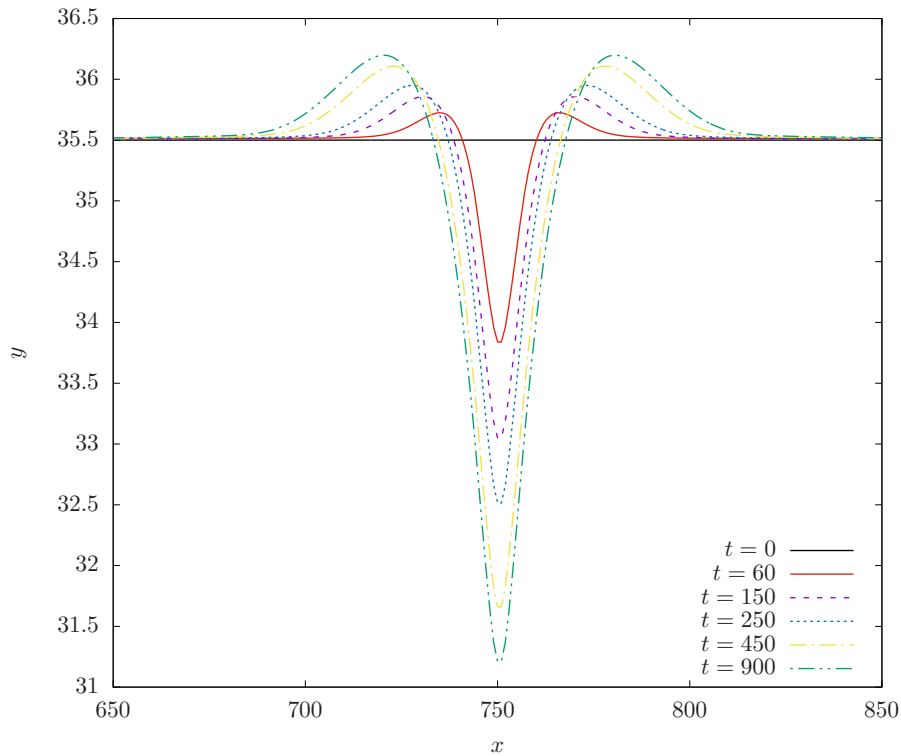


Figure 5.4: Illustration of the groove root deepening via the $\phi = 0.5$ isolines, where the formation of symmetric groove profiles and ridges is evident. In complete agreement with the Mullins's seminal theory, the grain boundary grooving phenomenon is reproduced by phase-field simulations. Herein, the groove pit deepens with time as given by Eq. (5.2).

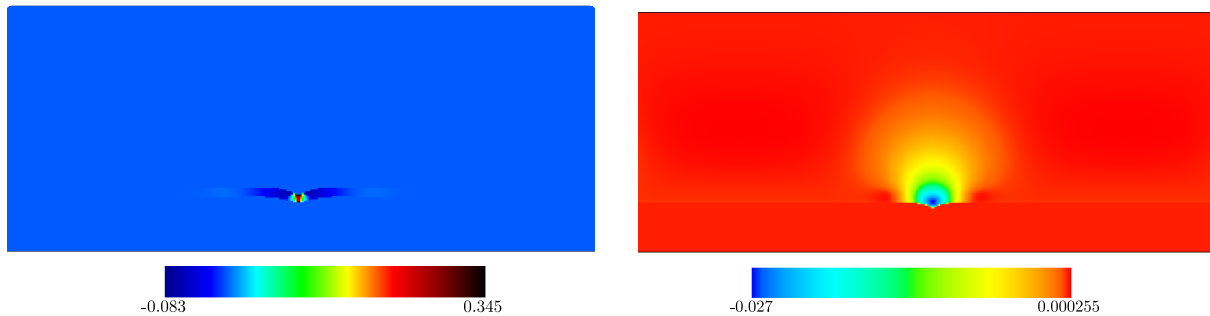


Figure 5.5: Variation of interfacial curvatures and chemical potentials across the grain boundary groove. The presence of unequal chemical potentials drive the material transport from the groove root towards the flat surfaces. The color bar illustrates the local interfacial curvatures and chemical potential fields according to the legend embedded below the snapshots.

et al. [157], where the rate-determining factor was diffusion in the liquid phase. Furthermore, sincerely reproduced by the phase-field model, the symmetric groove profiles at the grain boundaries in Fig. 5.4 are in complete agreement with the seminal theory of Mullins [6], where volume diffusion was the main transport mechanism near the grain boundary groove. In contrast with the grooves developed by surface diffusion [158], it is worth mentioning that the groove profiles in the present study exhibit only maxima at

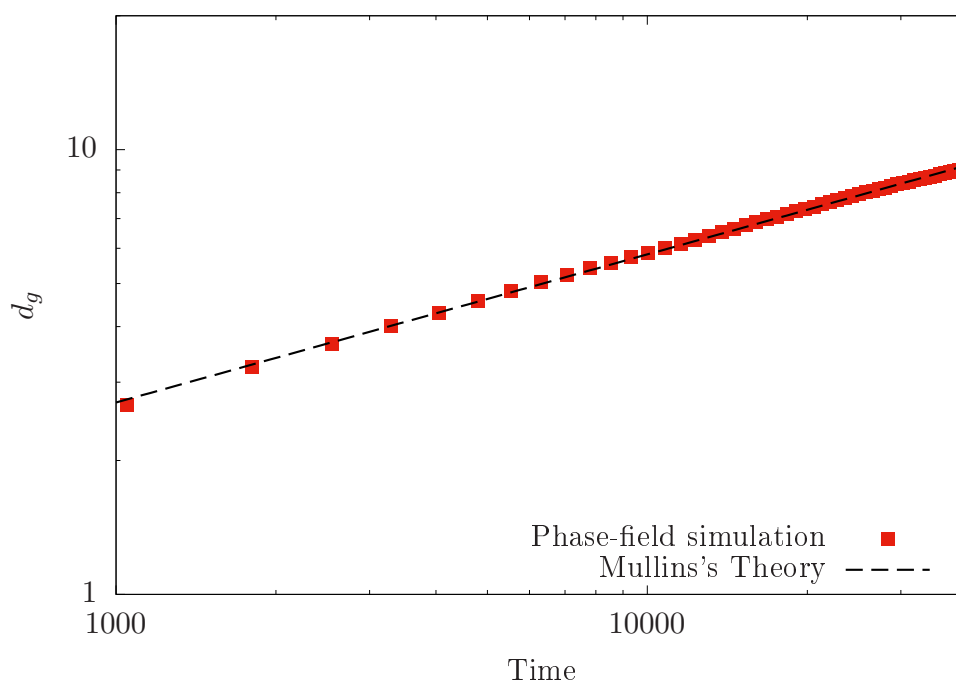


Figure 5.6: Calculated groove depth d_g from the initially flat interface as a function of time. A non-linear analytical fit $d_g \propto t^n$ provides us with $n = 0.3330$. An excellent agreement with the Mullins's theory is observed.

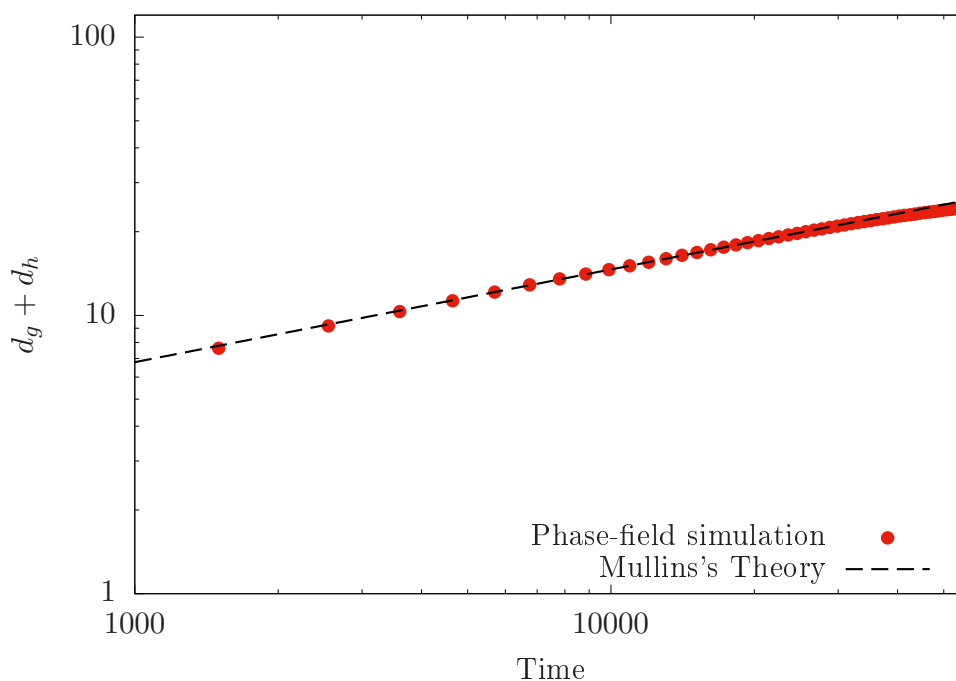


Figure 5.7: Calculated groove depth $d_g + d_h$, from the maxima of the profile d_h as a function of time. A non-linear analytical fit $(d_g + d_h) \propto t^n$ provides us with $n = 0.3332$. An excellent agreement with the Mullins's prediction for volume diffusion governed kinetics is observed.

the grain boundary ridges, see Fig. 5.4. Due to the presence of mass transport along the arc length, a characteristic dip below the flat surface following the maximum is observed for a surface diffusion governed groove profiles. However, in the present scenario, as the GB grooving is driven by volume diffusion only, the mass transport in the liquid phase does not produce such minima near the symmetric grain boundary ridges. Again, in agreement with Mullins's observation, the transport mechanisms during GB grooving are independent from one another and the groove profiles subsequently differ.

Next, Fig. 5.6 depicts the temporal evolution of the groove depth and an analytical fit provides us with a temporal exponent $n = 0.3330$. Furthermore, the groove depth from the maxima of the groove profiles is also calculated and shown in Fig. 5.7, where the non-linear fit gives us $n = 0.3332$. From the above two-dimensional simulations, both the groove geometries have shown an excellent agreement with the Mullins's predicted kinetics [6]. When compared, the proportionality constant corresponding to the groove pit is greater than for the root, which qualitatively complies with the previous study of Gladwell et al. [159]. Likewise, in accordance with previous studies [155, 160], the applicability of the grooving kinetics is successfully reproduced for the ratio $\gamma_{gb}/\gamma_{sl} = 1.0$. Lastly, the effect of spatial and temporal discretization on the grain boundary grooving phenomenon is investigated in detail in Appendix. A.

5.1.2 Determination of slope m at groove root

In the present section, the slope at the groove root obtained from the phase-field simulations is verified. Assuming that the phase boundaries are isotropic, the slope m of the grain boundary groove profile at the groove root with respect to the initially flat interface is given by $m = \cot\left(\frac{\phi}{2}\right)$. In the present study, the ratio $\frac{\gamma_{gb}}{\gamma_{sl}} = 1.0$ is considered, and henceforth, from the aforementioned equation and Eq. (5.1), the calculated slope m at the groove root is 0.577. Next, the slope m at the groove root is derived from the simulated two-dimensional grain boundary profile. Since the present methodology is a diffuse-interface approach, the intersection between the two polynomials is considered as the root position. In order to calculate the slope m at the groove root, the $\phi = 0.5$ iso-line is fitted on the either side of the grain boundary with a fourth order polynomial, as shown in Fig. 5.8 with a solid black line, and the point of intersection between these two polynomials is first determined. Next, the slope made by the tangent to the polynomial at this point of intersection is calculated analytically to be 0.566. A direct comparison of the theoretically obtained slope m , and the fourth order polynomial fit of the interface shapes shows an excellent agreement between the two methods.

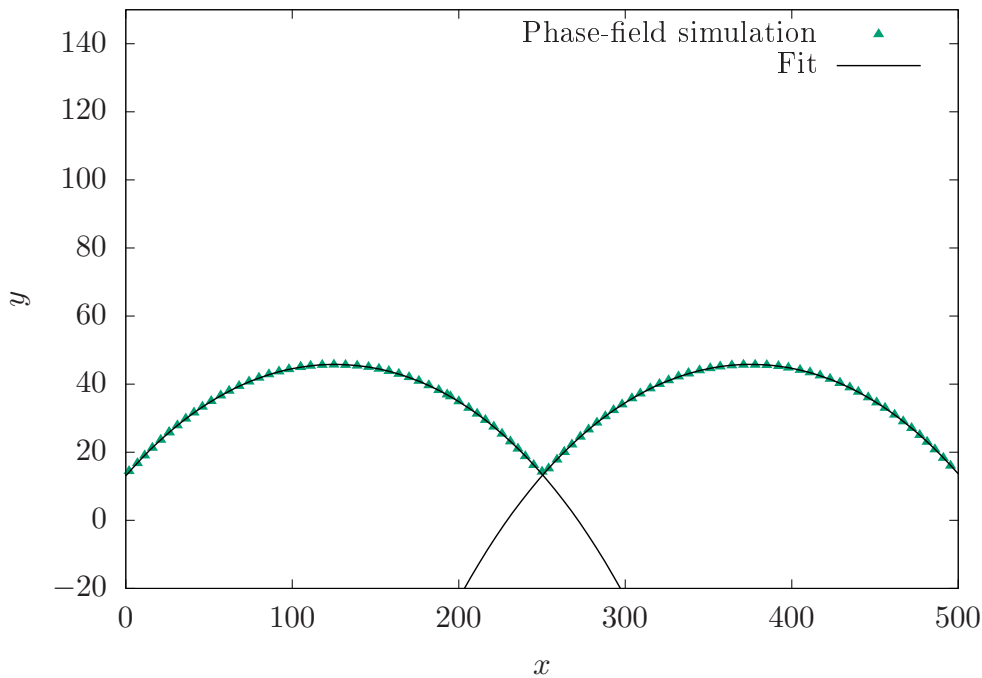


Figure 5.8: Determination of slope m at the groove root from phase-field simulations. A fourth-order polynomial is fitted to the extracted $\phi = 0.5$ isolines. Subsequently, the slope made by the tangent to the polynomial at the point of intersection is calculated.

5.1.3 Effect of surface energy

The dihedral angle at the interface trijunction is known to influence the morphology and break-up of solid grains in thin film polycrystals [161]. Since the relative surface energies play a pivotal role, the effect of the solid-solid grain boundary and solid-liquid interfacial energy on the grain boundary grooving phenomenon is examined for finite grains in the present section. It is well known that the direct measurement of the solid-liquid interfacial energies via experiments is rigorous, and therefore not straightforward. In general, most of the calculations are based on the indirect interpretation of nucleation experiments, or by theoretical approaches [162]. Utilizing the phase-field approach, the numerical parameters are modified such that the ratio R_0 decreases, where R_0 is the ratio between the grain boundary energy to the solid-liquid interfacial energy.

Fig. 5.9 showcases the grain boundary groove profiles for different ratios R_0 . As the equilibrium angle differs, it is observed that the morphology of the groove pit region is significantly modified. However, the profiles indicate that the groove width, as measured from the profile maximas is nearly independent of the imposed surface energies. Consequently, Fig. 5.9 depicts that the relative value of the groove height increases with an increase in the ratio R_0 . Thereafter, as the contribution from the grain boundary energy dominates, the profile becomes relatively steeper and bends sharply with pronounced grain boundary ridges.

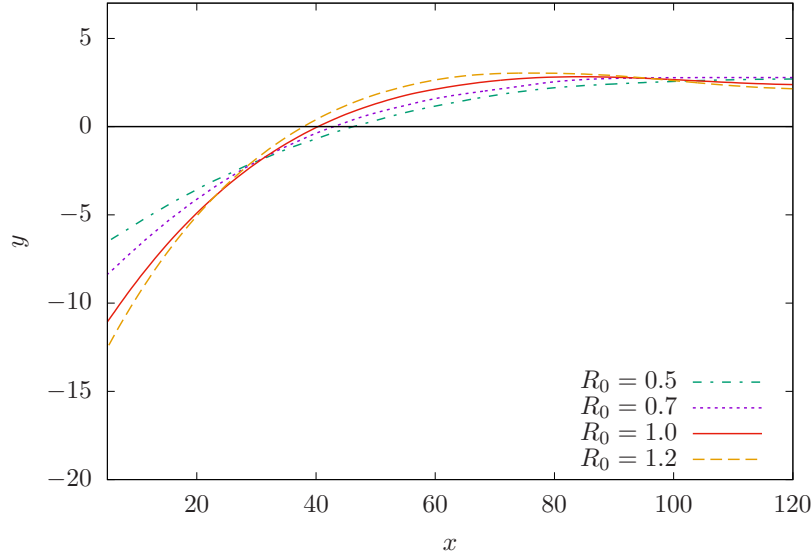


Figure 5.9: Effect of surface energies on the grain boundary groove profiles. As the ratio R_0 increases, the groove pit morphology is significantly modified.

Based on the groove profiles, it is important to understand as to what values of slope m are observed in actual experiments. From Eq. (5.1), for a solid-solid grain boundary which is normal to the free surface, the relation between the equilibrium angle Φ and the surface energies is given by $\frac{\gamma_{gb}}{\gamma_{sl}} = 2 \cos\left(\frac{\Phi}{2}\right)$. As discussed in the previous section, the slope m of the groove profile at the root position with respect of the initial flat interface is given as $m = \cot\left(\frac{\Phi}{2}\right)$. Combining the two yields a relation between m and R_0

$$m = \cot\left(\frac{\Phi}{2}\right) \quad (5.3)$$

$$m = \frac{\cos\left(\frac{\Phi}{2}\right)}{\sqrt{1 - \cos^2\left(\frac{\Phi}{2}\right)}} \quad (5.4)$$

Substituting $\cos\left(\frac{\Phi}{2}\right) = \frac{R_0}{2}$, where $R_0 = \frac{\gamma_{gb}}{\gamma_{sl}}$, we get

$$m = \frac{R_0}{\sqrt{4 - R_0^2}} \quad (5.5)$$

The above derived relation is depicted in Fig. 5.10, where an excellent agreement with the systematic two-dimensional simulations is observed. As the ratio $\frac{\gamma_{gb}}{\gamma_{sl}}$ varies from 0 to 2, the slope m varies from 0 to infinity, see Fig. 5.10. For the majority of the grain boundary grooves observed in bicrystal experiments [23, 157, 163], the slope m is less than unity. In this thesis, the calculated slope m is 0.5666, and correspondingly agrees well with the typical values observed in experimental studies [23, 157]. For the limiting case $R_0 \rightarrow 0$, the contribution from the grain boundary decreases and thereby the grain

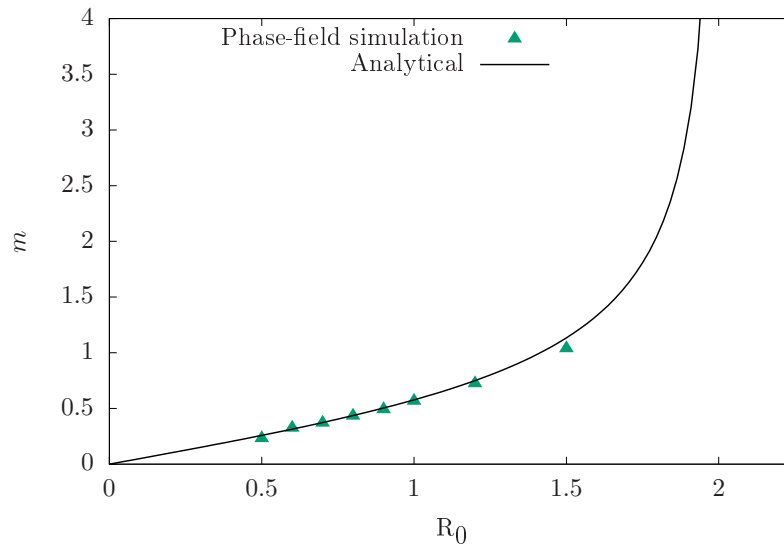


Figure 5.10: Groove root slope m as a function of the ratio R_0 between the solid-solid grain boundary energy γ_{gb} to solid-liquid surface energy γ_{sl} .

boundary vanishes to produce a single crystal. Furthermore, $R_0 = 2.0$ corresponds to the separation of the bicrystal grain into two separate crystals, as pictorially depicted for finite grains in Fig. 5.11. The bicrystal separation for $R_0 = 2.0$ is widely known as a common mode of failure in polycrystalline thin films, wherein the grain boundary groove penetrates through the film thickness and results in the breakup of thin films during annealing [164, 165].

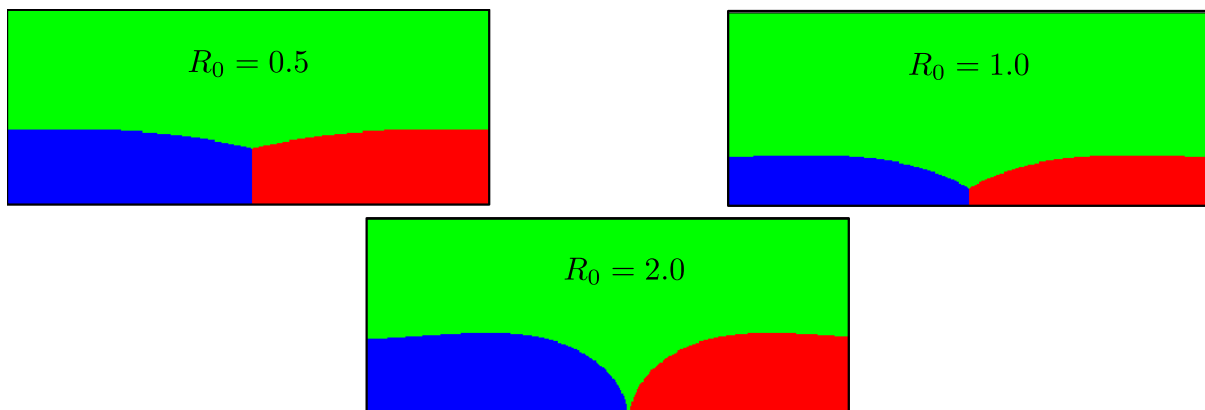


Figure 5.11: Grooving phenomenon at various R_0 in finite grains. As the contribution from the solid-liquid interfacial energy decreases, a separation of the bicrystal into two individual solid grains is observed. Here, the blue and red colors indicate the two solid grains, respectively

Based on the above analysis and profile shapes of the grain boundary groove, the phase-field model is successfully benchmarked and validated, and in the forthcoming sections we elucidate the role of an additional convective mass transport mechanism on the grooving phenomenon.

5.2 Grain boundary grooving under diffusive-convective regime

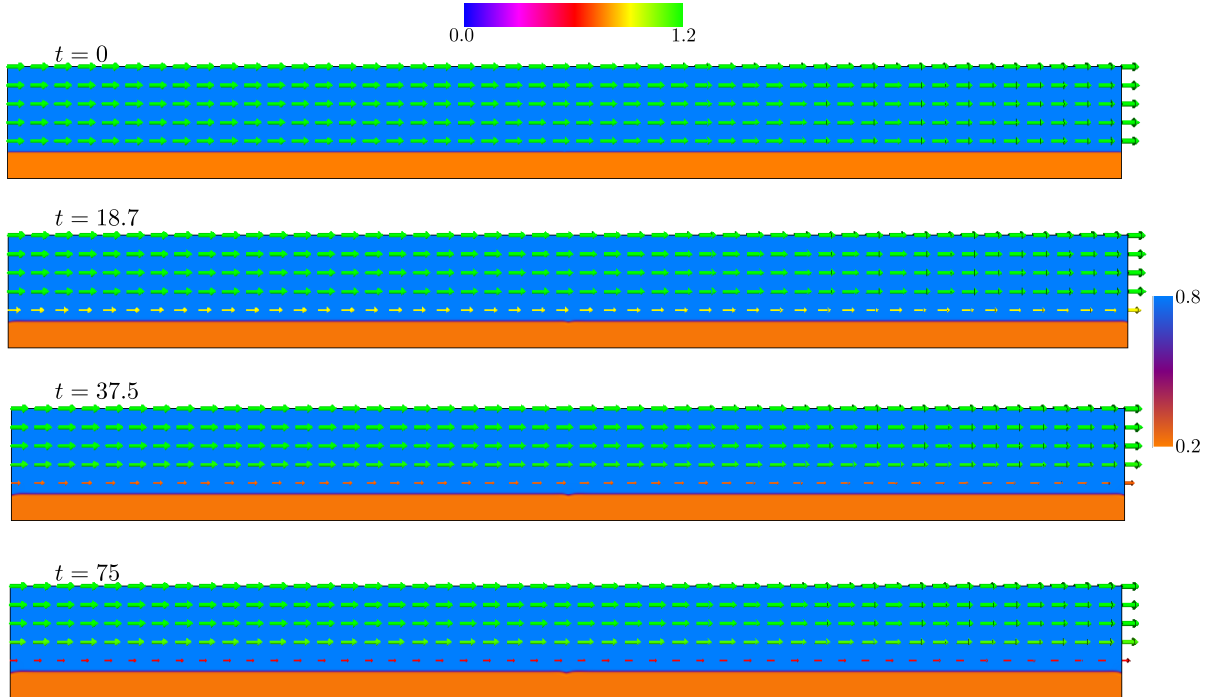


Figure 5.12: At an imposed convection velocity $U_x = 1.2$, where U_x is the magnitude of the convection velocity along the x -direction, the concentration and velocity fields illustrate the grain boundary grooving phenomenon in the presence of liquid phase convection. A cooperative effect of melt convection and volume diffusion in the liquid phase modifies the grooving mechanism at the grain boundary. The right and the top color bars represent the magnitude of the solutal and the velocity fields, respectively.

As discussed at the beginning of this chapter, Mullins's theory [6] on grain boundary groove kinetics was limited to pure diffusive regimes only, and the role of convective transport near the solid-liquid interface was considered negligible. In this regard, Mullins's theory is extended and the role of liquid phase convection on the mechanism of grain boundary grooving for finite grain sizes is explored in detail. Along with the initialization, all the simulation parameters are kept same so as to have a direct comparison with the groove kinetics under pure diffusive regime. In addition to the concentration and phase fields, the boundary conditions for the velocity fields are periodic in the left and right sides. Again, the lateral boundaries act as a far field conditions, and do not have any influence on the numerical results. The slip boundary condition is imposed on the top and bottom sides of the simulation domain, respectively. Finally, a no-slip boundary condition is also applied at the solid-liquid interface.

In Fig. 5.12, the evolution of the grain boundary groove is illustrated via the simulation screenshots in the presence of melt convection $U_x = 1.2$, where U_x is the magnitude

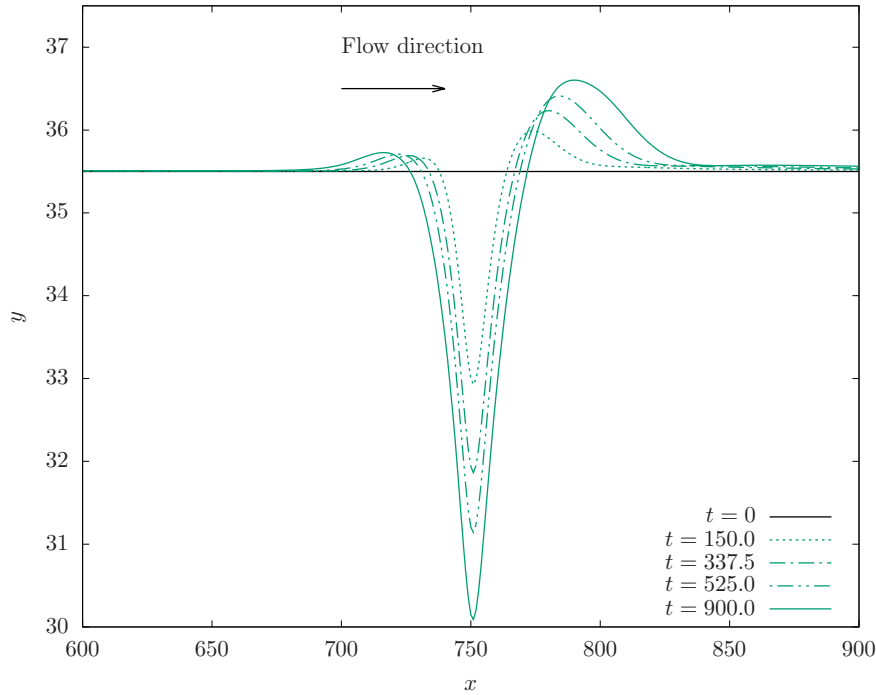


Figure 5.13: Temporal evolution of the groove profiles at an imposed convection velocity $U_x = 1.2$. With time, the groove root deepens and the asymmetry of the grain boundary ridges increases. The deposition of solute atoms at the right-sided ridge by convective transport generates wider and higher peaks. The direction of melt flow is schematically represented.

of the convection velocity along the x -direction. In the present section, the alloy melt flow direction is perpendicular to the solid-solid grain boundary. During the initial stages of grooving, it is observed that the grain boundary ridges on either side of the groove pit develop similar to the well known Mullins's profile [6]. However, as time elapses in Fig. 5.13, the migration of the solute atoms from the groove root intensifies towards the right-sided ridge, and therefore, the asymmetry of groove profile increases with time. In contrast with pure diffusive conditions, the variation of the local curvature produces an unequal solute deposition at the grain centers. Qualitatively, the groove profiles in Fig. 5.13 display similar characteristics when compared with previous bicrystal experiments with lateral convection in the liquid phase [163]. Using a Bridgman-process, it was successfully shown that the V-shaped groove profile developed asymmetrically for finite convection velocities in a binary alloy system. Lastly, it is interesting to note that the width of the groove pit increases with time and significantly differs with Mullins's solution, see Fig. 5.13.

In order to further understand the grooving phenomenon, the convection velocity along the x -direction is systematically increased and a direct comparison of the groove profiles with and without convection is shown in Fig. 5.14. In the case of volume diffusion governed grooving, it is discerned that the groove profile is always symmetrical to the

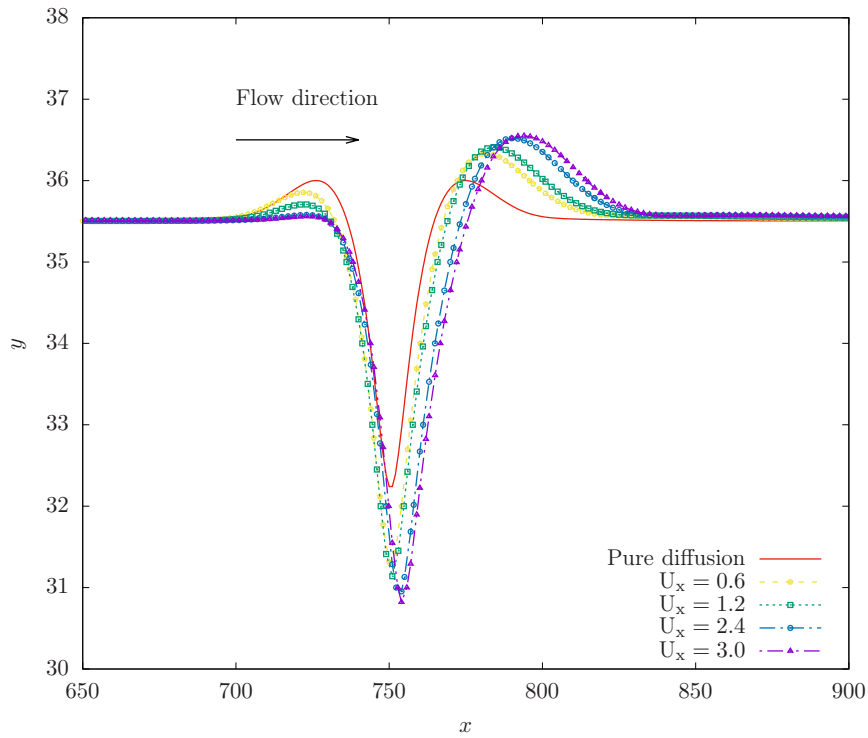


Figure 5.14: A direct comparison of the grain boundary groove profiles at various convection velocities. The groove morphology at the trijunction is always symmetric under pure diffusive conditions, whereas, with increasing lateral velocity, the groove profiles become asymmetric. The ridge on the left side is completely removed for $U_x = 3.0$.

grain boundary, see the solid red isoline in Fig. 5.14. However, as the rate of solute deposition differs, the asymmetry of the groove profiles increases with the increase in the melt velocity, see Fig. 5.14. Whenever the solute transport is driven by only one transport mechanism, the groove profile is defined by a fixed shape under steady-state conditions. On the other hand, a cooperative effect in the diffusive-convective regime no longer produces a symmetric groove profile, and the grain centers evolve with dissimilar interfacial curvatures. Since the imposed melt flow is perpendicular to the grain boundary, a lateral drift of the groove root towards the downstream direction is also noticed. As shown Fig. 5.14, it is noteworthy that the left-sided ridge height continuously diminishes as the convective transport dominates in the alloy melt. From the above set of results and comparisons, it is successfully demonstrated that the employed multiphase-field model accurately simulates the combined influence of liquid phase convection and volume diffusion on the grain boundary grooving phenomenon.

The ratio H_0 between the left and right-sided ridge heights that are established on either side of the grain boundary groove is now calculated for various convection velocities. As shown Fig. 5.15, while the ratio H_0 remains unity for pure diffusive conditions, it proportionately decreases with the increase in the convection velocity. Here, the right-sided grain boundary ridge evolves at a faster rate when compared with its counterpart during

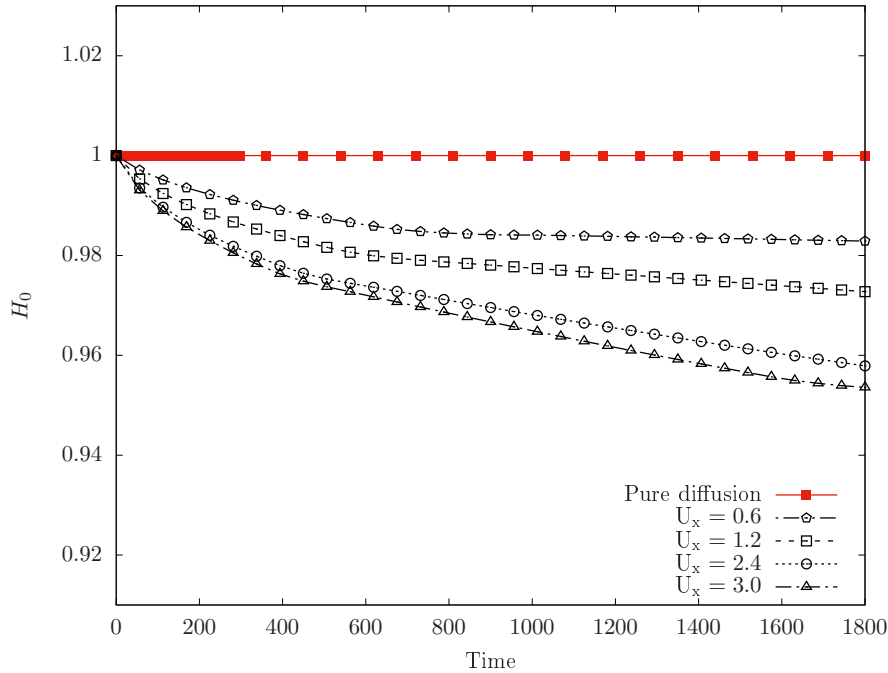


Figure 5.15: Ratio H_0 between the left and the right ridge heights as a function of time for various convection velocities. An increase in the convection velocity proportionately decreases the ratio H_0 .

the grain boundary grooving process. It is therefore also believed that the formation of anomalous peaks generate irregular and wider groove pits at the grain boundary. In particular, for polycrystalline thin films, such a groove behavior is known to alter the growth kinetics, such as the formation of pin holes [147, 148, 166].

5.2.1 Comparison between sharp interface theory and phase-field simulation

The grain boundary grooving phenomenon under the influence of melt convection is studied by extending the well known theory of Mullins [6]. In addition to diffusion in the liquid phase, the role of an additional convective transport mechanism was included [163], and the sharp interface groove profile W of the grain boundary groove was derived from the stationary transport equation

$$\frac{\partial C}{\partial x} = \frac{D_i^\beta}{U_x} \left(\frac{\partial^2 C}{\partial x^2} + \frac{\partial^2 C}{\partial y^2} \right) \quad (5.6)$$

with the boundary conditions

$$C(x, 0, t) = C_\infty + A_0 K(x, t) \quad (5.7)$$

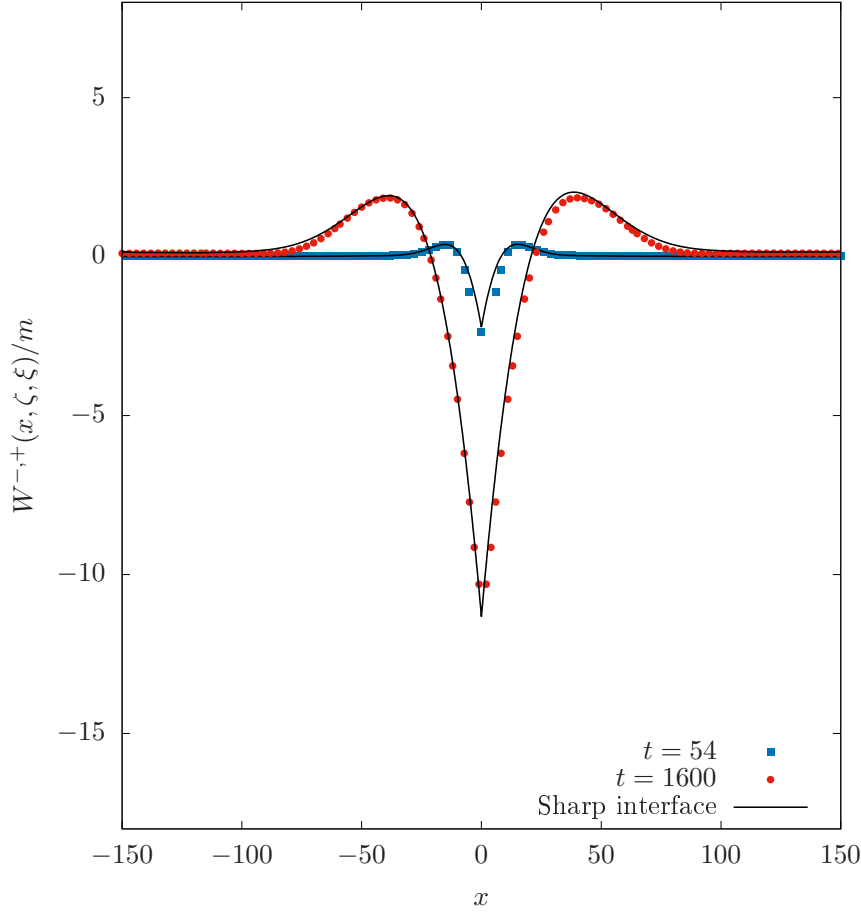


Figure 5.16: Under pure diffusive conditions, a direct comparison between phase-field simulations and numerically calculated sharp-interface groove profile from Eqs. (5.8) and (5.9). An excellent agreement with the sharp-interface groove profile is observed. For the limiting case $\xi \rightarrow 0$, the well known Mullins's symmetric groove profile by volume diffusion is reproduced. Here, the simulated groove profiles from the phase-field simulations are scaled such that the groove root is at $x = 0$.

where A_0 is the materials constant, C_∞ is the equilibrium concentration at the planar interface and $K(x, t)$ is the interfacial curvature across the groove. Applying the boundary conditions and for $y \rightarrow \infty$, the solution to the above differential equation is first obtained. After integrating the curvature with respect to x and using the small slope approximation (slope of the profile is small), the profile $W(x, \zeta, \xi)$ of the grain boundary groove is derived as

$$W^+(x, \zeta, \xi) = -\frac{2m}{\xi\pi} \exp(\xi x) \int_0^\infty \frac{G(\omega, \zeta_c)}{1 + \omega^2} \cos(2\zeta_c \omega \sqrt{1 + \omega^2} - 2 \tan^{-1}(\omega) + \xi x \omega) d\omega + 2mx \quad (5.8)$$

$$W^-(x, \zeta, \xi) = -\frac{2m}{\xi\pi} \exp(\xi x) \int_0^\infty \frac{G(\omega, \zeta_c)}{1 + \omega^2} \cos(2\zeta_c \omega \sqrt{1 + \omega^2} - 2 \tan^{-1}(\omega) + \xi x \omega) d\omega \quad (5.9)$$

Here, the superscripts $+$ and $-$ represent the positive and negative side of the groove root at $x = 0$, respectively. In addition, $\xi = \frac{U_x}{2D_i^\beta}$, $\zeta_c = \xi^3 \zeta$, $\zeta = B_0 t$, where B_0 is the

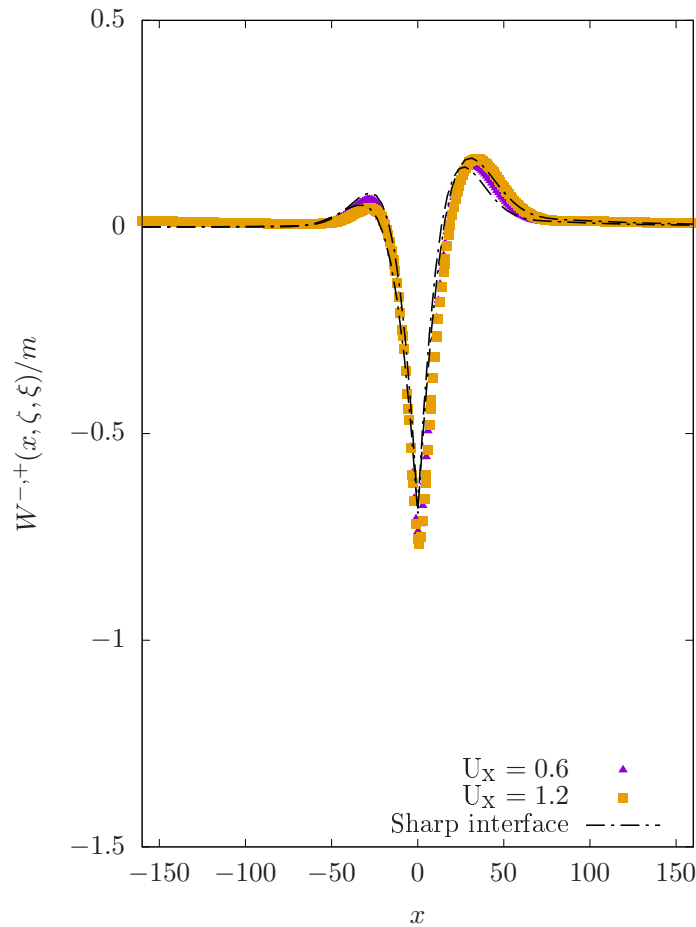


Figure 5.17: Comparison between phase-field simulations and numerically calculated sharp interface groove profile for different convection velocities U_x . A complete agreement is observed between the $\phi = 0.5$ isolines and the sharp interface groove profile. The asymmetry of the groove profile increases with an increase in the lateral melt velocity. Here, the simulated profiles from phase-field simulations are scaled such that the groove root is at $x = 0$.

materials constant, and $G(\omega, \zeta_c) = \exp[\zeta_c \sqrt{1 + \omega^2} (1 - \omega^2)]$. The derivation for the above groove profiles has been provided in detail by Ratke and Volgel [163]. The slope of the groove profile at the groove root with respect to the initially flat interface is calculated as $m = 0.566$.

At first, the phase-field groove shapes under pure diffusive conditions is compared with the sharp interface theory, and the groove profile in Eqs. (5.8) and (5.9) is calculated numerically for the limiting case $\xi \rightarrow 0$. In Fig. 5.16, a direct comparison of the groove profiles is shown, where it is observed that the phase-field results are in near agreement with the numerically calculated groove profile for different simulation timesteps. As illustrated in the previous section, the ridges evolve symmetrically across the solid-solid grain boundary for $\xi \rightarrow 0$, and the Mullins's groove [6] for volume diffusion is reproduced in Fig. 5.16. Next, under diffusive-convective regime, the simulated groove profile is systematically compared with Eqs. (5.8) and (5.9) in Fig. 5.17. For various convection

velocities, the phase-field model befittingly captures the asymmetric groove profile at the grain boundary, wherein the grain boundary ridges evolve asymmetrically and the depth of the groove root deepens when compared with the diffusive regime. Furthermore, the groove shapes observed in this work are very different from the classical Mullins groove, which suggests the presence of an additional convective transport that contribute to the total mass balance at the groove root. In the theoretical study [163], a laminar fluid with a constant velocity was considered perpendicular to the solid-solid grain boundary through the slip boundary condition at the solid-liquid interface. In contrast, following the assumptions of Beckermann model [82], a physically accurate no-slip boundary condition is applied such that the lateral melt velocity is zero at the solid-liquid interface. Additionally, the root position was fixed at $x = 0$ and the groove profile was theoretically derived [163]. However, as a result of lateral migration of the grain boundary, a slight drift of the groove root along the x -direction is captured in our simulations. Widely observed in previous theoretical and computational studies [158, 167–169], the lateral drift of the groove root along the downstream direction increases with the increase in the asymmetry of the groove profile. It is therefore believed that the aforementioned differences between the sharp-interface theory and our phase-field simulation account for the small deviation near the groove pit region in Fig. 5.17. Lastly, it is reiterated that the growth of the asymmetric hillocks near the groove is independent and they do not overlap with each other, and henceforth it is reiterated that the lateral boundary conditions do not play any role in the grooving phenomenon. Nevertheless, owing to computational and numerical challenges, the deviation at the grain boundary ridges is expected to diminish for phase-field simulations performed at higher resolution.

5.2.2 Variation of groove depth in diffusive-convective regime

In the present section, the grain boundary groove kinetics is estimated under the cooperative effect of volume diffusion and melt convection in the liquid phase. The groove depth as a function of time for various convection velocities is shown in Fig. 5.18, where it is observed that the groove deepens at a faster rate, and therefore significantly differs when compared with the classical theory of Mullins under pure diffusive regime. Under the influence of bulk diffusion as a transport mechanism only, the kinetic law by Mullins [6] provides us with the exponent $n = 1/3$. However, in the diffusive-convective regime, it is perceived that the temporal exponent n increases with the increase in the convection velocity. From a non-linear analytical fit in Fig. 5.18, it is found that the exponent n varies in-between 0.34 – 0.40 for the given set of initial flow conditions. The two-dimensional GB grooving simulations performed in the present chapter and the groove kinetics are in excellent agreement with the analytical and experimental study by Ratke and Vogel [163], where it was proposed that the introduction of liquid phase convection significantly modifies the Mullins’s kinetic law [6]. It was extensively reported that the grain boundary

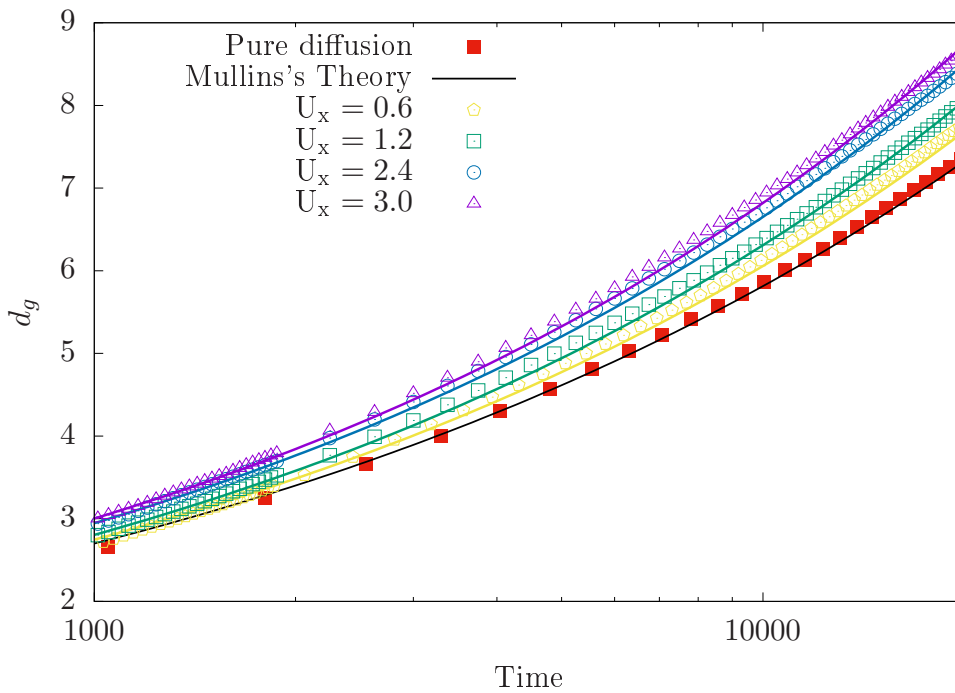


Figure 5.18: Calculated groove depth d_g as a function of time for various convection velocities from phase-field simulations. For all the various results, the non-linear analytical fit follows the kinetic law of the form $d_g \propto t^n$. The temporal exponent increases with the increase in the velocity and significantly varies when compared with Mullins's classical prediction. The solid lines represent the corresponding analytical fits to the numerical data.

groove geometry was asymmetric and the temporal exponent increased proportionately due to the introduction of liquid phase convection perpendicular to the solid-solid grain boundary. Although it has not captured in the present study, it is worth mentioning that for the limiting case $U_x \rightarrow \infty$, Ratke and Vogel [163] reported that the kinetic law as well as the grain boundary groove profile behaved similar to the condensation and evaporation of atoms along the grain boundary.

5.2.3 Grain boundary migration

Under elevated temperatures, the solid-solid grain boundary migration oversees the rate of grain growth during annealing, and is important for materials synthesis [148, 161]. Several studies [166, 170–172] on polycrystalline thin films have reported that the formation of grain boundary grooves can often traverse and consequently break up the entire thickness of the thin film within a reasonable amount of time. In this regard and in this section, the role of grain boundary grooving on the initiation of GB migration is addressed in detail. Generally, when a solid-solid grain boundary ends at a free surface, the formation of an isothermal liquid groove affects its lateral migration. At various melt velocities the semi-infinite bicrystal solid grain isolines are depicted in Fig. 5.19, where it is observed that

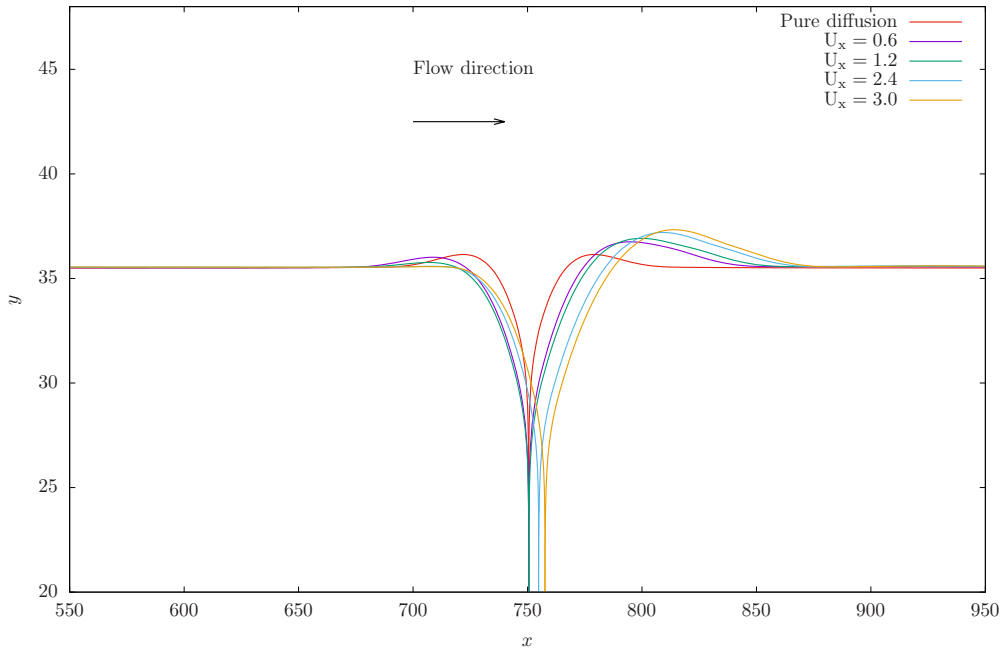


Figure 5.19: Phase isolines depicting the bicrystal grain morphology for different convection velocities. The lateral drift of the solid-solid grain boundary along the downstream direction (right side) is evident and the rate of grain boundary migration increases with an increase in the melt velocity.

the solid-solid grain boundary drifts laterally along the x -direction with an increase in the melt velocity. As the rate of solute advection is increased at the groove pit region, a lateral root drift is clearly noticed. Henceforth, a slight bending of the grain boundary drives the migration along the flow direction. Such an effect results in the solute accumulation along the right-sided ridge, which in turn produces an asymmetric groove profile.

The present observation agrees in spirits with a theoretical investigation [169], where the effect of grain boundary migration on the ridge position was extensively examined. It was reported that the solid-solid grain boundary motion results in the formation of an asymmetric groove profile, and the lateral motion of the solid-solid grain boundary increases with the increase in the groove profile asymmetry. In the present study, it is believed that while the solid-solid grain boundary and the groove pit remain mobile along the x -direction, a rapid grain boundary migration allows the groove root to deepen, and eventually affects the thermochemical and kinetic properties of polycrystalline thin films [161, 171, 172].

5.2.4 Effect of surface energy

Under the influence of volume diffusion alone, the role of surface energy was previously discussed, and thereby in the present section, an additional transport mechanism in the

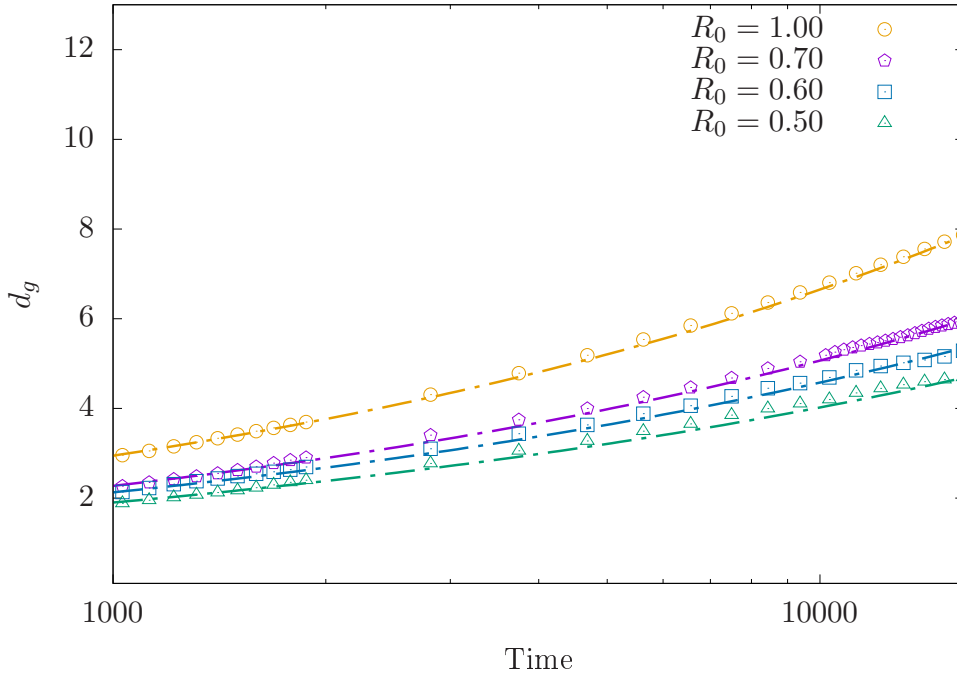


Figure 5.20: Calculated groove depth as a function of time for various $R_0 = \gamma_{gb}/\gamma_{sl}$. At an imposed convection velocity $U_x = 2.4$, the temporal evolution of the groove depth decreases with the decrease in the ratio $R_0 = \gamma_{gb}/\gamma_{sl}$. The solid lines represent the corresponding analytical fits to the numerical data.

form of lateral convection is investigated. In Fig. 5.20, at an imposed convection velocity $U_x = 2.4$, the calculated groove depth as a function of time is depicted for various R_0 , where the rate of groove deepening decreases with the decrease in the ratio R_0 . Here, the fitted numerical data follows the well known kinetic law of the form $d_g \propto t^n$, and the temporal exponent n varies with the decrease in the ratio R_0 . Moreover, with an increase in the contribution from the solid-liquid interfacial energy, the solutal transport towards the grain boundary ridges maintains the force balance at the groove cavity. Resultantly, the rate of groove pit deepening decreases with the decrease in the ratio R_0 . Nonetheless, for the limiting case $R_0 \rightarrow 0$, the contribution from the grain boundary energy is negligible, and the grooving phenomenon will be diminished at the interphase junctions.

From a qualitative point of view, Fig. 5.21 depicts the groove profiles for $R_0 = 0.7, 1.0$ at $U_x = 2.4$, where it is observed that the position of the groove pit rapidly decreases with the increase in the ratio R_0 . Along with the flattening of the grain boundary ridges, it is noticed that the width of the groove pit widens as the contribution from the solid-liquid interfacial energy increases. For $R_0 = 1.0$, the grain boundary rapidly migrates along the downstream direction, which in turn leads to greater advection of the solutal fields near the solid-liquid interface. Distinctly, the lateral migration of the solid-solid grain boundary is completely hindered when the groove angle increases for $R_0 = 0.7$.

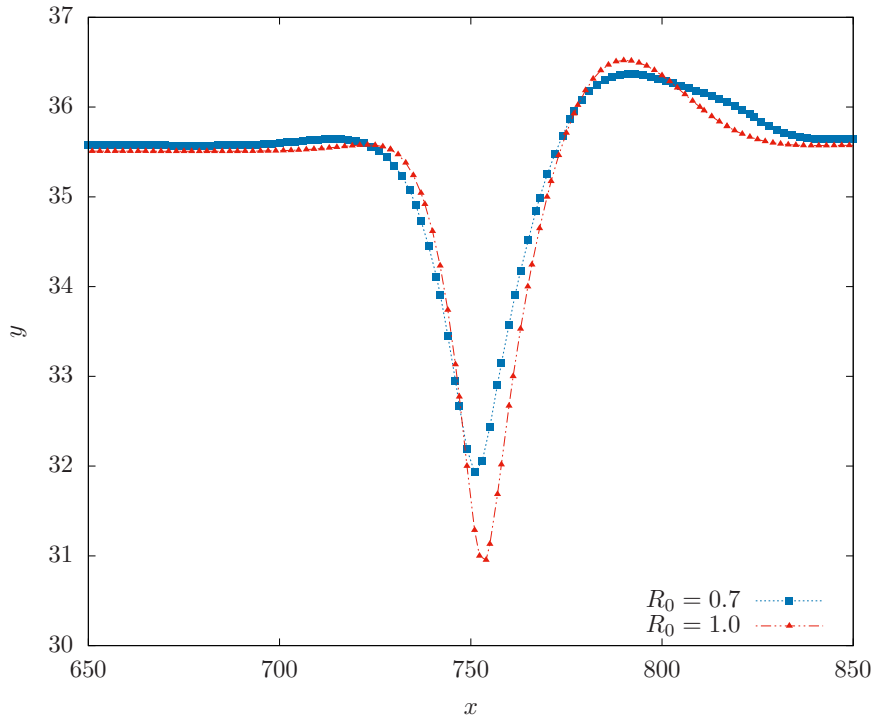


Figure 5.21: For an imposed convection velocity $U_x = 2.4$, the influence of surface energy on the grain boundary grooving phenomenon. With the increase in the ratio $R_0 = \gamma_{gb}/\gamma_{sl}$, the groove pit deepens. Additionally, as the dihedral angle increases, a significant difference between the ridge morphology is observed.

Although the groove profiles continue to evolve asymmetrically, a sharp root morphology transforms to a blunted form as the ratio R_0 decreases. Depending upon the groove angle and its subsequent kinetics, several intergranular defects such as void formation, solute segregation can be further studied in detail for thin film polycrystals [161, 172].

5.2.5 Polycrystalline thin films

Polycrystalline thin films are found in diverse applications ranging from dielectric layers to optical, magnetic, and tribological coatings, to diffusion and thermal barriers [161, 172, 173]. The presence of multiple grain boundaries also represent a key microstructural element of polycrystalline thin films, and in many cases they determine their physical, mechanical and functional properties [174]. As discussed earlier, the phenomenon of liquid groove deepening promotes surface roughness, and possibly break-up of thin films [161]. In this regard, it is important to have a concise overview of the microstructural evolution in polycrystalline thin films. Hitherto, the grain boundary grooving phenomenon is investigated for semi-infinite solid grains with the presence of an isolated grain boundary. However, in reality, since several solid are interconnected, the stability as well as the performance of polycrystalline thin films are strongly affected.

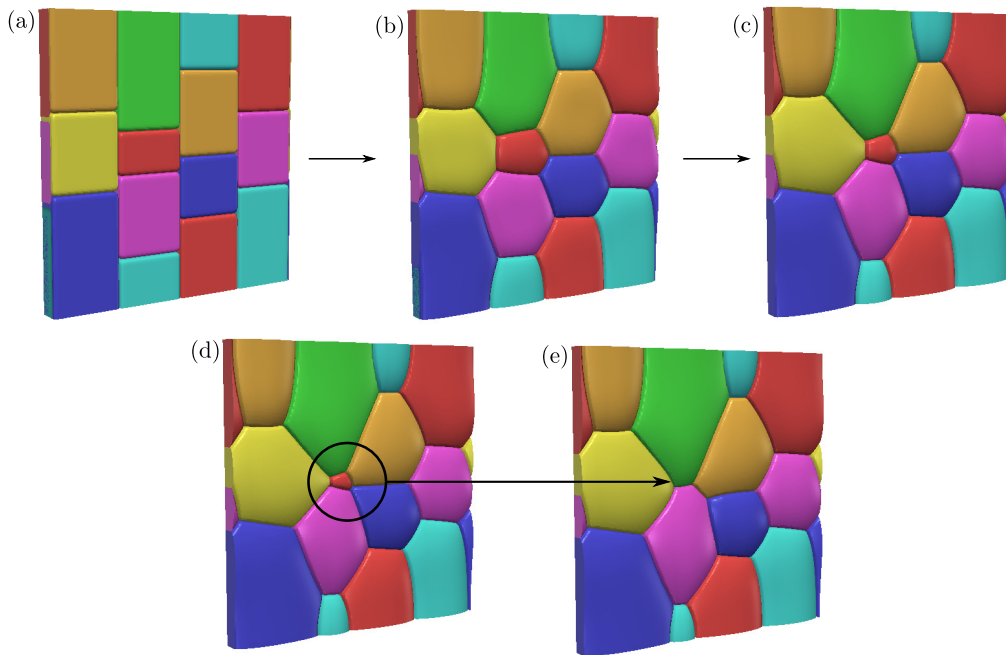


Figure 5.22: (a)-(e) Three-dimensional simulation of crystal growth in a polycrystalline thin film. As a result of grain boundary area minimization, the larger grains evolve at the expense of smaller grains. (d)-(e) Elimination of the red colored grain is highlighted schematically.

Therefore, in the present section, the growth behavior of a polycrystalline solid is briefly studied. In this section all the simulation parameters are kept the same and a three-dimensional simulation domain is considered with $200 \times 100 \times 200$ cells in each direction, and the growth behavior of liquid grooving in a multi-grain boundary system is simulated.

Fig. 5.22 demonstrates the morphological evolution of a polycrystalline film without lateral convection. Under pure diffusive conditions, the minimization of grain boundary area and the excess energy associated with the grain boundaries drive the growth behavior of isotropic grains. Widely known as the *normal grain growth* behavior, the larger grains continue to grow while impinging and inhibiting the growth of smaller grains. As illustrated in Fig. 5.22(a)-(e), the temporal evolution of the polycrystal grains lead to the shrinkage and the elimination of some grains, see the highlighted red colored grain in Fig. 5.22(d)-(e). Similarly, in the presence of lateral convection in Fig. 5.23(a)-(b), the solid grain evolve continuously and impinge the growth of smaller grains. As the convection velocity increases, the growth kinetics is slightly modified, where the rapid grain boundary migration for $U_x = 3.0$ eliminates the red colored grain at a faster rate when compared with its counterpart. As observed previously in the two-dimensional simulations, it is important to note that the lateral drift of the grain boundary plays an important role in controlling the kinetic behavior of polycrystalline solids. Fig. 5.24 quantitatively depicts the temporal evolution of the phase fractions of the grain 5 (red colored highlighted grain) for different conditions, where the rate of decrease in the volume fraction is inversely related to the convection velocity.

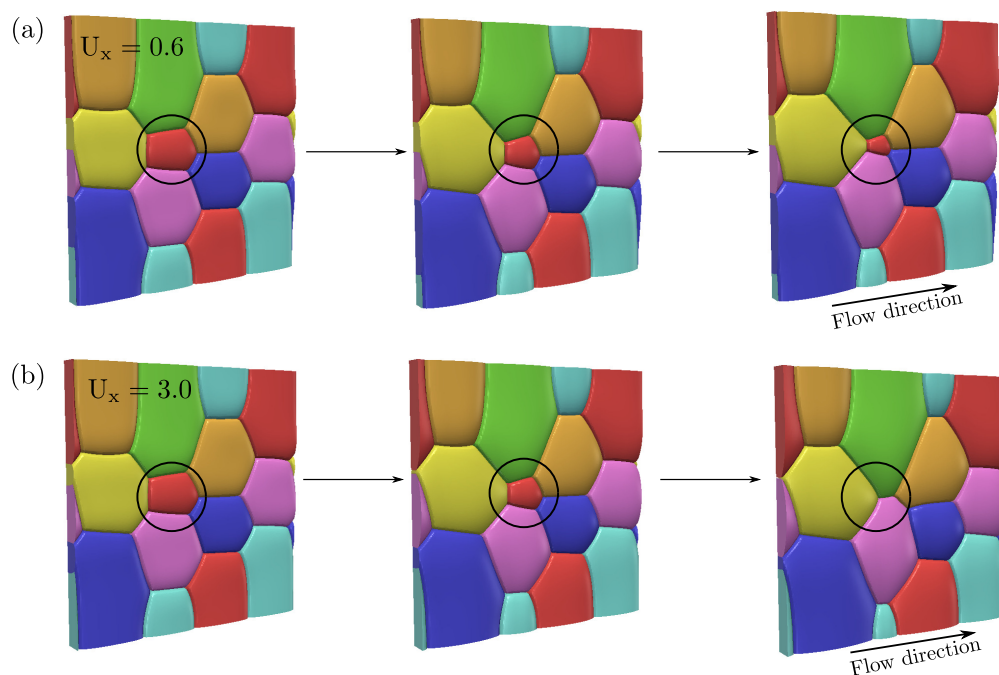


Figure 5.23: (a)-(b) Growth morphology of a three-dimensional polycrystal under the influence of lateral convection. As the magnitude of convection velocity increases, the rate of elimination of the red colored grain increases.

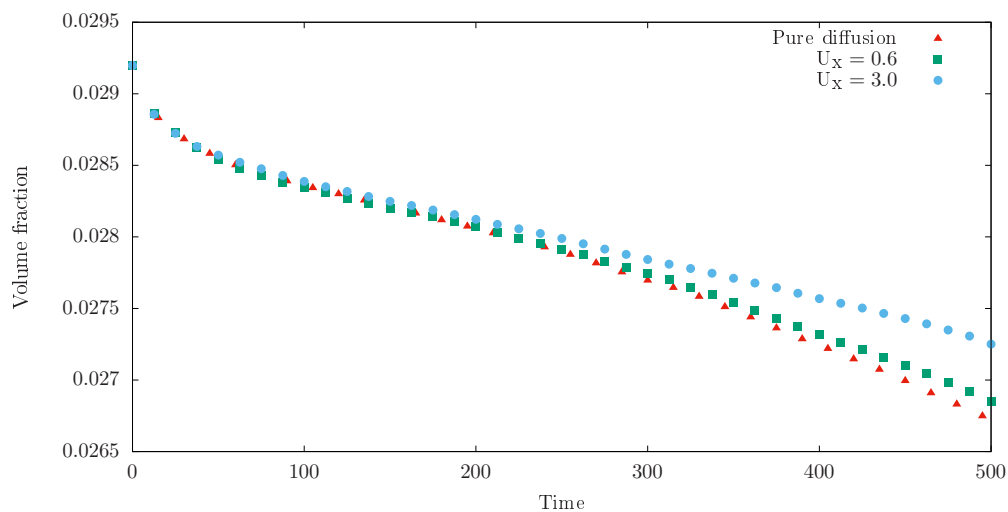


Figure 5.24: Temporal volume fractions of red colored solid grain under different convection velocities. Grain elimination increases with the increase in the convection velocity.

5.3 Summary

In this chapter, two-dimensional phase-field simulations have been performed to capture the grain boundary grooving phenomenon under diffusive-convective conditions. At first, the multiphase-field model is validated and benchmarked by simulating and comparing

the grooving process with Mullins's theory for volume diffusion. As time elapses, it is shown that the groove pit systematically deepens, and follows the well known kinetic law $d_g \propto t^{1/3}$. Thereupon, under pure diffusive conditions, it is shown that the groove profiles and kinetics are in excellent agreement with Mullins's seminal theory.

Next, the grain boundary grooving is extended and the synchronous effect of convection and volume diffusion is investigated for the first time via the phase-field approach. The groove morphology along with other groove properties are completely modified due to the presence of an additional convective mass transport in the liquid phase. Since the distribution of the solutal fields near the V-shaped groove is unequal, it is shown that the asymmetry of the groove profiles increases with the increase in the convection velocity. A direct comparison of the simulated groove profiles with the sharp interface theory is also shown. For simulations with and without convection, the groove profiles from our phase-field model have shown an excellent agreement with the theoretically derived sharp interface groove profile. Moreover, the groove depth at various convection velocities follows the classical law $d_g \propto t^n$, but the temporal exponent n is modified significantly when compared with the Mullins's seminal theory. In the diffusive-convective regime, the temporal exponent varies in-between 0.33 and 0.4, and the groove depth is always larger when compared with volume diffusion. Nonetheless, the qualitative and quantitative findings in the present study are in excellent agreement with previous analytical and experimental studies.

Afterwards, the lateral drift of the grain boundary along the flow direction is shown where the rate of GB migration increases with the increase in the convection velocity. Furthermore, since the relative surface energies primarily control the equilibrium groove angle, an increase in the ratio R_0 distinctly modifies the groove depth as well as the groove morphology at the grain boundary. For the limiting case $R_0 \rightarrow 0$, the solid-liquid interfacial energy dominates and the grooving phenomenon is diminished at the grain boundary. Lastly, the growth behavior of three-dimensional polycrystals is investigated, where the rate of elimination of solid grains increases with the increase in the convection velocity. It is henceforth concluded that the numerical results in this chapter provide new insights into the grain boundary grooving mechanism, and the cooperative effect of convective and diffusive forces in the liquid phase modifies the groove kinetics.

Liquid grooving at grain boundaries is limited to equilibrium conditions, where the solid-solid grain boundary is in contact with a saturated alloy melt. Whenever the interface velocity exceeds the critical velocity of a planar interface, it has been experimentally studied [22] that several interfacial instabilities typically grow at the grain boundaries. In the forthcoming chapter, the directional solidification of a bicrystal and the morphological evolution of a solid-liquid interface is presented in detail.

Chapter 6

Unidirectional solidification of tip splitting microstructures

The selection of solidification patterns has been a long-standing fundamental interest in scientific and engineering significance. The local competition between the diffusion fields and the interfacial dynamics (interfacial anisotropy) determines the shape of a solidifying microstructure [175]. During crystal growth, the onset of morphological instabilities along a planar interface has a tendency to influence the microstructural characteristics of a cast alloy. However, since the solidification front is replete with imperfections, i.e., grain boundaries and foreign particulate matter, the problem becomes more complex as the solute interacts with the groove pits at the triple junction. Henceforth, in this chapter, the role of grain boundaries in a constitutionally supercooled melt is focused, where the initiation and the mechanism of tip splitting microstructures along a solidifying interface is investigated in detail. Later, the structural transition of microstructural patterns in the presence of lateral convection is studied. *Results presented in the first half of this chapter are a part of a manuscript under submission, whereas results discussed in the second half of this chapter has been published in Computational Materials Science [9].*

6.1 Role of grain boundaries

In the present section, the role of grain boundary in a constitutionally supercooled melt is investigated, and the formation of a grain boundary ridge as an early onset instability is simulated. In Fig. 6.1, under pure diffusive regime, it is observed that in a supersaturated melt of composition $\Delta = 0.5$, the region adjacent to the grain boundary pit becomes unstable. When compared with the grain centers, the instabilities at the grain boundary amplify at a faster rate into primary ridges. It is noticed that the parts of the grain centers, not immediately adjacent to the grain boundary remain featureless and undistorted. Afterwards, while the shape of the perturbations depends on whether it decays or grows,

the initial perturbation from a liquid groove always coarsens [157]. These primary ridges evolve into a periodic array of hills and later transform into a ramified dendritic network depending upon the interfacial anisotropy. Nonetheless, the local growth competition of these primary ridges is always dependent on the initial orientation of the solid grain [23].

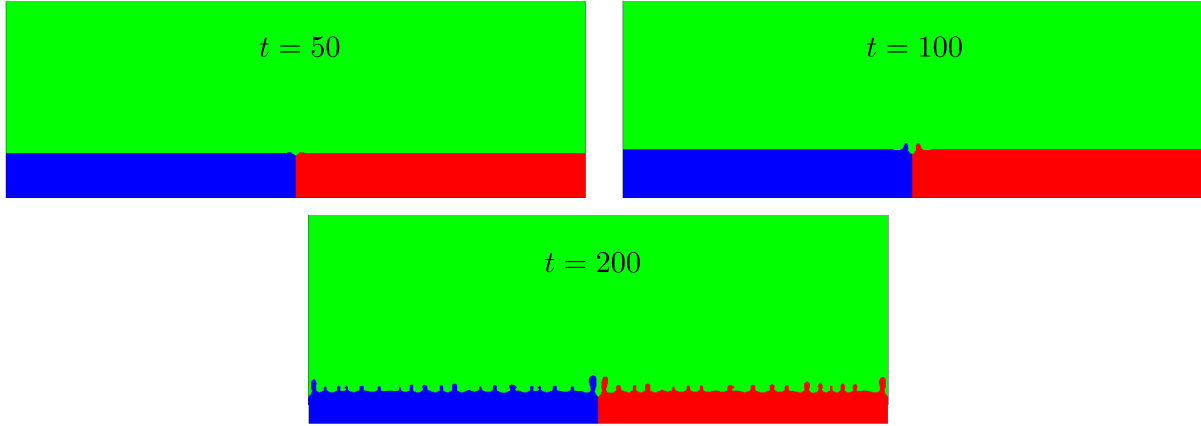


Figure 6.1: Temporal evolution of grain boundary ridges near the groove pit in an supersaturated melt of composition $\Delta = 0.5$. Throughout this chapter, the colors blue and red refer to the two distinct solid grains and green color represents the liquid phase.

Table 6.1: Simulation parameters for tip splitting microstructures.

Description	Parameter	Value
Diffusivity	D_i^β	1.00
Melt supersaturation	Δ	0.5
Anisotropic strength	$\delta_{\alpha\beta}$	0.0
Interface width	ϵ	4.00
Simulation Domain	$N_x \times N_y$	1000 \times 1000
Discretized grid space	$\Delta x = \Delta y$	1.0

From the above set of two-dimensional simulations, it is evident that the grain boundaries in a bicrystal specimen play an important role during the initiation of morphological instabilities as a result of solute redistribution near the groove pit. The 1D concentration profiles at two different positions are extracted and depicted in Fig. 6.2, where the solute diffuses across the grain boundary and reduces the solute segregation. This decrease in the solute concentration increases the interface height to form an amplified ridge at the grain boundary. In general, the groove acts as a solute pit which decreases the solute concentration near the trijunction, while the solute profiles away from the grain boundary are not much affected. In contrast with the perturbations developed along a planar interface, the ridges simulated in the present study have only been found to appear near the grain boundaries [22, 23, 79, 176].

As a ridge is developed near a grain boundary, the solute is laterally rejected outwards, leading to the formation of secondary depressions, which may, in turn, initiate secondary

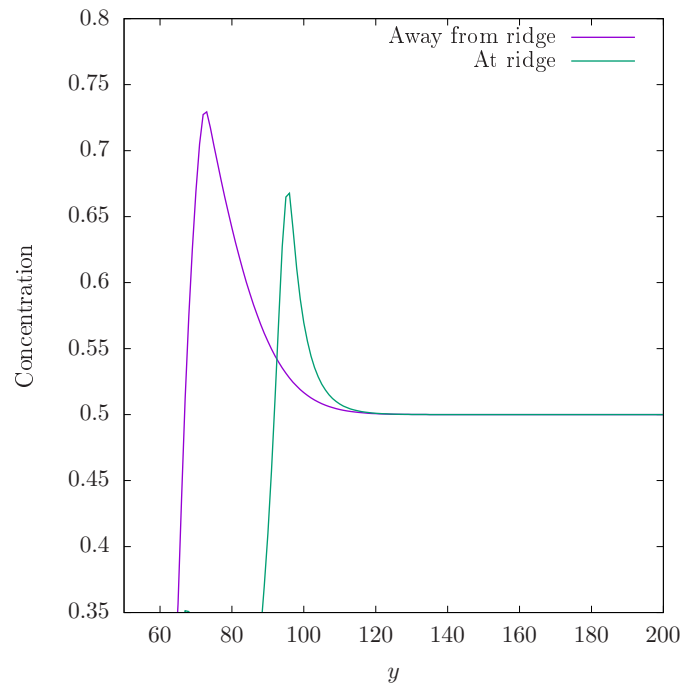


Figure 6.2: 1D concentration profiles at two different positions. Presence of steeper solutal gradients enhance the formation of ridges at the grain boundary.

ridges and rings. Therefore, the average interface height is greater at the grain boundary than the minute perturbation away from the pit. The effect of grain boundaries on pattern formation is highly reproducible, although the solute distribution depends on the equilibrium groove profile. In agreement with experimental [22, 176] and phase-field studies [177], it is believed that the formation of a grain boundary groove acts as a sink for the morphological evolution of a solid-liquid interface, which consequently results in the lateral development of instabilities in a polycrystal. Since the interfacial energy is considered isotropic, these amplified tips split in a fork like manner and develop into a non-planar pattern over a period of time. Nonetheless, in tune with Noel et al. [24] and others [23, 178], the grain boundary operates as a potential site for the initiation and generation of hill shaped perturbations at the center of the solid-liquid interface. Finally, it is also worth noting, that during the course of further solidification, these primary ridges and protuberances developed at the grain boundary influence the growth competition of columnar dendrites.

6.2 Tip splitting microstructures under diffusive regime

Initiated at the grain boundary, the temporal evolution of a solidifying pattern is depicted in Fig. 6.3, where the solid-liquid interface along with the grain boundary ridges solidify into a ramified tip splitting microstructure. Since the concentration decreases in front of the solid-liquid interface, the local thermodynamic equilibrium is maintained as a result

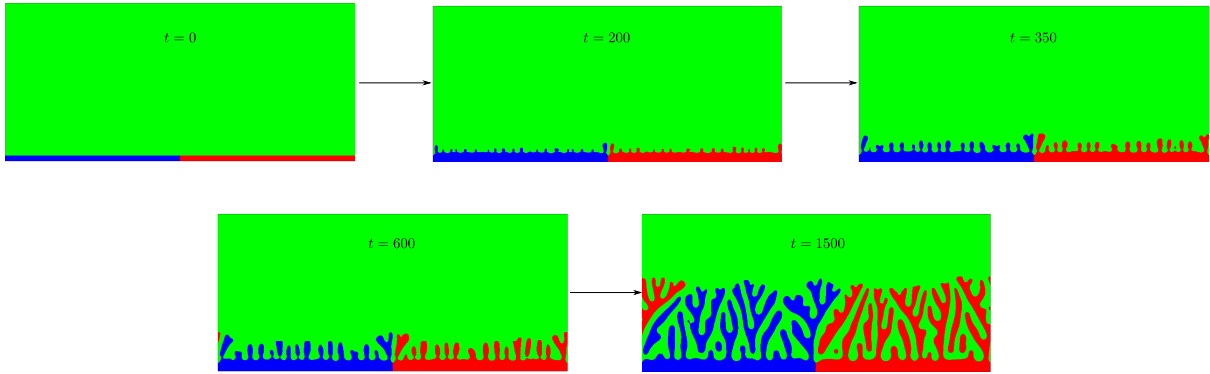


Figure 6.3: Temporal evolution of interfacial instabilities along a bicrystal sample. In a supersaturated melt of composition $\Delta = 0.5$, the primary ridges developed at the grain boundary amplify into split structures along with the propagation of hillocks across the two solid grains.

of unidirectional solidification. At the initial growth stage, the interface keeps planar and advances slowly towards the liquid region. With the accumulation of the solutal fields ahead of the solid-liquid interface, the planar interface loses its stability and undergoes the well known Mullins-Sekerka instability [30], which states that the stability of a solid-liquid interface is governed by the critical wavelength of the perturbation and the extent of constitutional supercooling. The dynamic evolution of the interface instability is simulated at $\delta_{\alpha\beta} = 0.0$, where random tip splitting structures are observed. The non-planar tip splitting microstructures are known as *seaweed structures*, originally observed in several experimental investigations [36, 179–182], a different growth morphology compared with the dendrites [36]. While the anisotropic dendrites are directionally dependent, the tip splitting microstructures in Fig. 6.3 are considered as patterns without orientational order.

The fundamental and repeating characteristic of a seaweed structure is the successive and continuous splitting of the tips, as shown in Fig. 6.4(a)-(d). Similar to the diffusion limited growth of isotropic crystals [180–182], the formation of seaweed patterns is inherently related to the low anisotropic property of the solid-liquid interface. As illustrated in Fig. 6.4(a)-(c), when growth conditions are imposed for which a planar interface just becomes unstable, a zone of supercooled liquid exists ahead of the planar interface which causes the interface to become unstable and to form a perturbed shape, see Fig. 6.4(a). The threshold value of the interface velocity is exceeded such that the lateral diffusion of solute reduces the solute concentration at the cell tip. Consequently, the tips along the planar interface travel ahead to become a branched morphology, see Fig. 6.4(d). Nevertheless, the absence of anisotropy promotes an uninhibited, omnidirectional growth via irregular branching and splittings of an evolving interface [183].

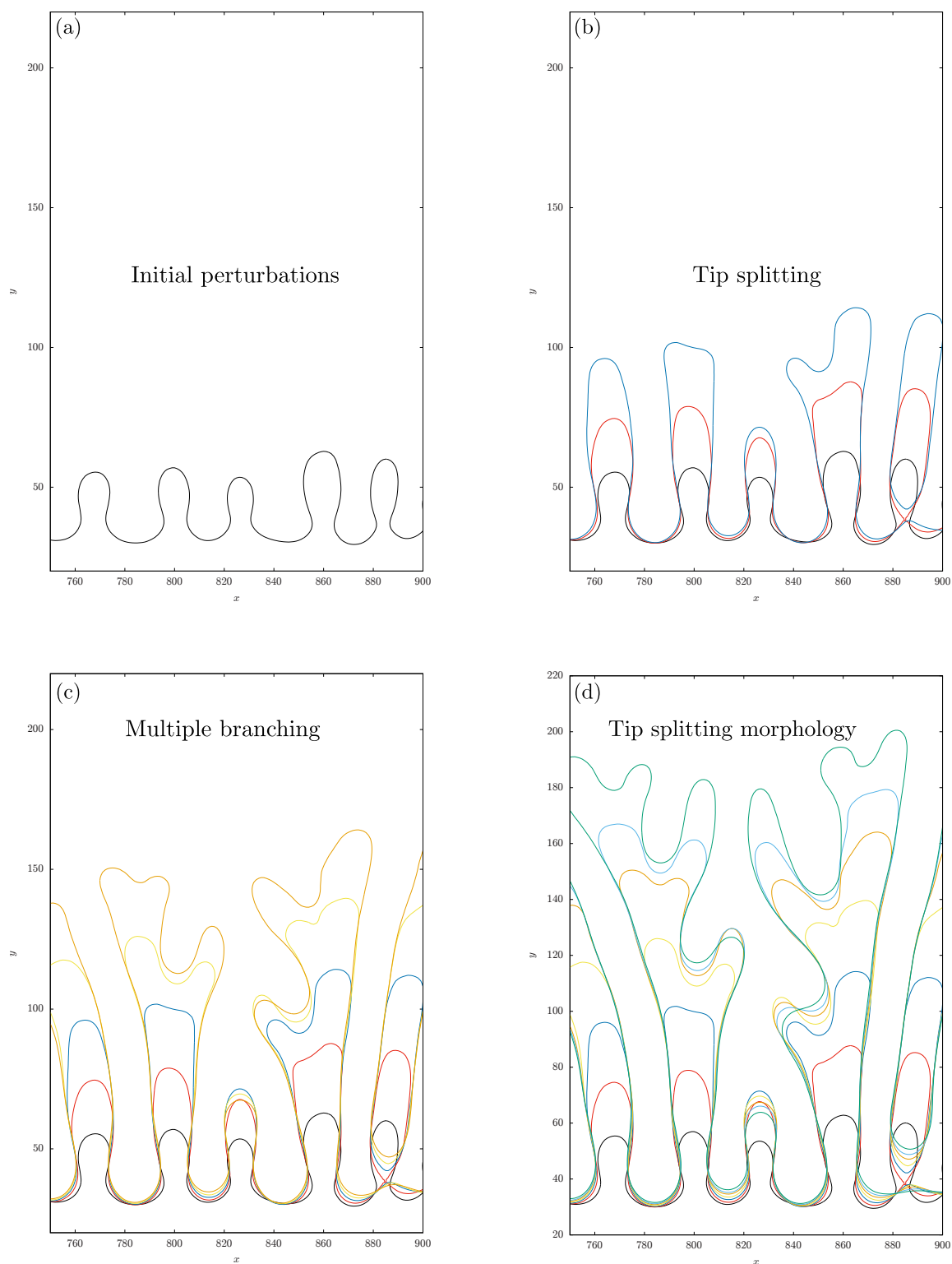


Figure 6.4: (a)-(d) In a supersaturated melt, the formation of a tip splitting microstructure along a solidifying solid-liquid planar interface. Initial perturbations evolve with time to undergo successive branching at the tip position. Isolines with various colors represent different simulation time.

6.3 Deterministic behavior of tip splitting microstructures

6.3.1 Analytical criterion for tip splitting position

The stability of tip splitting morphologies was first determined, and it was concluded that the solidification patterns evolve into doublon or seaweeds depending upon the imposed undercooling and interfacial anisotropy [184]. In addition, it was shown that the presence of numerical noise at the solid-liquid interface was another factor to enhance the formation of tip splitting microstructures. However, one of the major drawbacks of this argument is that such a study shows no clarity on the position of tip splitting. Recently, Glicksman [8] proposed an analytical criterion $v_b = B_g \nabla_s^2 \kappa$, where B_g is materials constant, for the branching mechanism through the Gibbs-Thomson temperature distribution as an active interfacial energy. According to this theory, the sign of the surface divergence of the interfacial curvature $\nabla_s^2 \kappa$, where κ is the interfacial curvature, determines whether the interface moves towards the melt or the crystal. It was reported that a positive $\nabla_s^2 \kappa$ represented the growth of the interface, whereas, a negative $\nabla_s^2 \kappa$ promoted a hindered growth of the interface [8]. Consequently, the rotation points developed a wrinkle, which later evolved into a sidebranch. The local analysis was proved to be successful in kinematically determining the rotation points for branching, wherein the crystal experienced an accelerated growth. The present section builds upon this mechanism and addresses the fundamental tip splitting behavior of seaweed structures. In the forthcoming segments, the expressions for capillary mediated analytical theory for a convex profile in two dimensions is derived, and subsequently compared with the two-dimensional phase-field simulations.

Since the main objective of the present section is to demonstrate the tip splitting instability, the initial condition is similar to the convex parabolic perturbations developed in Fig. 6.4(a). Here an axisymmetric parabolic interface is considered as a solid phase and the rest of the domain is bulk liquid phase to avoid any mathematical complexity. To begin with, the sharp-interface criterion for a two-dimensional surface is determined in the following manner. Let $f(x)$ be the equation of a parabola in a two-dimensional domain, given as

$$f(x) = -\alpha_0(x - h)^2 + p, \quad (6.1)$$

where, α_0, h, p are the scaled dimensionless parameters controlling the width and the position of the parabola. In the present study, α_0 is taken as 0.02 to study the influence of the dimensionless shape factor on the tip splitting position, see Fig. 6.5. Let us begin the calculation of the analytical criterion, starting with the expression of curvature $\kappa(x)$, for a two-dimensional convex interface,

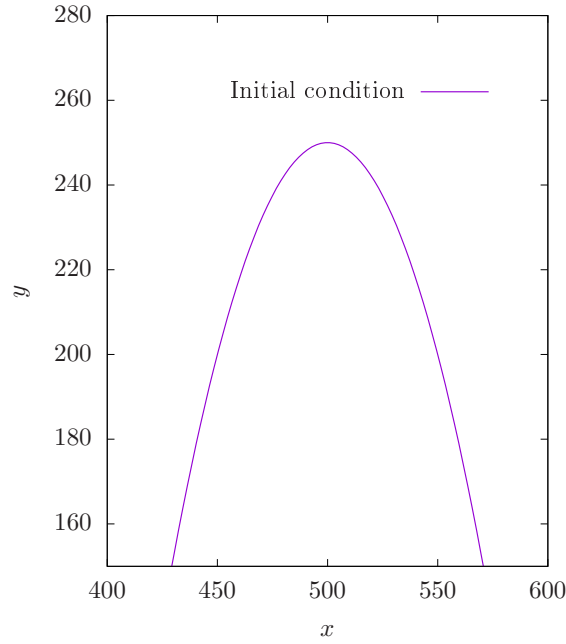


Figure 6.5: Determination of tip splitting position for an initial parabolic profile with $\alpha_0 = 0.02$. For convenience, we take $h = 500$ and $p = 250$.

$$\kappa(x) = \frac{f''(x)}{(1 + f'(x)^2)^{\frac{3}{2}}}. \quad (6.2)$$

Now, the gradient of the curvature along the arc length s can be written as

$$\frac{\partial \kappa}{\partial s} = \frac{\partial \kappa}{\partial x} \frac{\partial x}{\partial s}, \quad (6.3)$$

$$\frac{\partial \kappa}{\partial s} = \frac{1}{\sqrt{1 + \left(\frac{\partial y}{\partial x}\right)^2}} \frac{\partial \kappa}{\partial x}. \quad (6.4)$$

Let the above equation be termed as $g(x)$, thus

$$g(x) = \frac{1}{\sqrt{1 + \left(\frac{\partial y}{\partial x}\right)^2}} \frac{\partial \kappa}{\partial x}. \quad (6.5)$$

Finally, in order to calculate the surface Laplace, the surface divergence of the gradient along the arc length is taken. Using Eq. (6.5) we get

$$\nabla_s^2 \kappa = \frac{\partial g(x)}{\partial x} \frac{\partial x}{\partial s} = \frac{1}{\sqrt{1 + \left(\frac{\partial y}{\partial x}\right)^2}} \frac{\partial g(x)}{\partial x}. \quad (6.6)$$

The above derivation can be rewritten by substituting $f(x)$ from Eq. (6.1) into Eq. (6.2) as

$$\nabla_s^2 \kappa = \frac{\frac{576\alpha_0^5(x-h)^2}{(1+4\alpha_0^2(x-h)^2)^4} - \frac{24\alpha_0^3}{(1+4\alpha_0^2(x-h)^2)^3}}{\sqrt{1 + 4\alpha_0^2(x-h)^2}}. \quad (6.7)$$

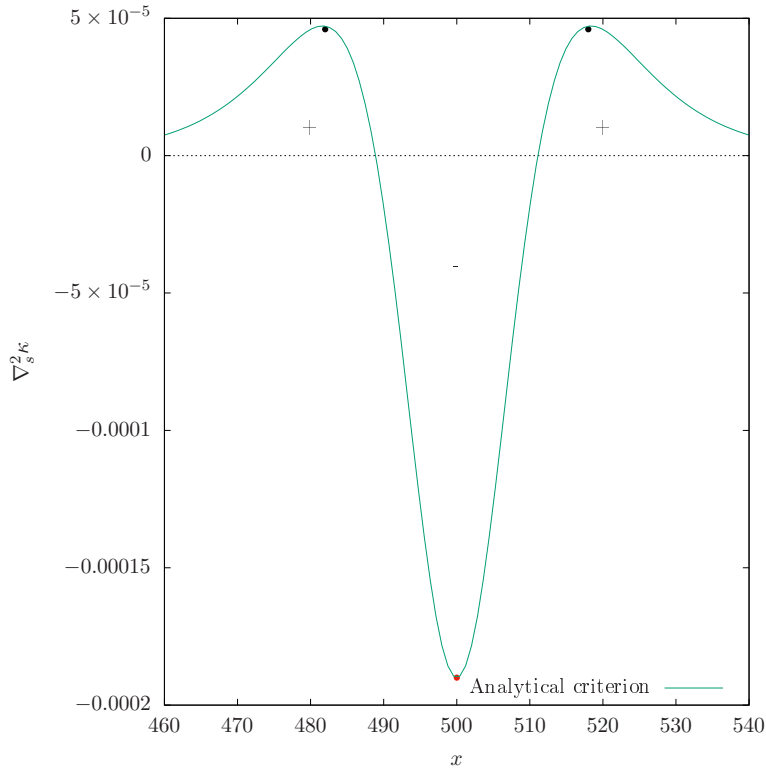


Figure 6.6: Calculated analytical criterion for $\alpha_0 = 0.02$, as a function of the dimensionless position. The positive and negative regions indicate the crest and the trough positions during the tip splitting process. The forked region lies between the $\nabla_s^2 \kappa < 0$ region, whereas the two tips start to evolve at the $\nabla_s^2 \kappa > 0$ positions.

Depicted in Fig. 6.6, Eq. (6.7) represents the analytically predicted position for a convex parabolic interface. It is observed that the analytical criterion $\nabla_s^2 \kappa$ for $\alpha_0 = 0.02$ has two positive regions at $x < 490$ and $x > 510$, whereas, the negative region lies in-between $490 < x < 510$. During crystal growth, the minimum at $\nabla_s^2 \kappa = -0.000191$ (red dot in Fig. 6.6) starts to evolve towards the solid in a retarded manner. The two maxima at $\nabla_s^2 \kappa = 4.6 \times 10^{-5}$ (black dots in Fig. 6.6) will accelerate towards the opposite direction in order to generate the foremost point during the freezing process. Therefore, the tip splitting region is predicted where the interface undergoes a hindered growth, and begins when the sharp-interface criterion passes through zero. The form of the plot in Fig. 6.6 is a direct comparison with the normal flux reported by Glicksman [8], where the solid-liquid interface evolved accordingly to undergo systematic branching.

6.3.2 Comparison between sharp interface criterion and phase-field simulation

In the present section, two-dimensional phase-field simulations are performed and compared with the analytically predicted sharp interface tip splitting position. To begin with,

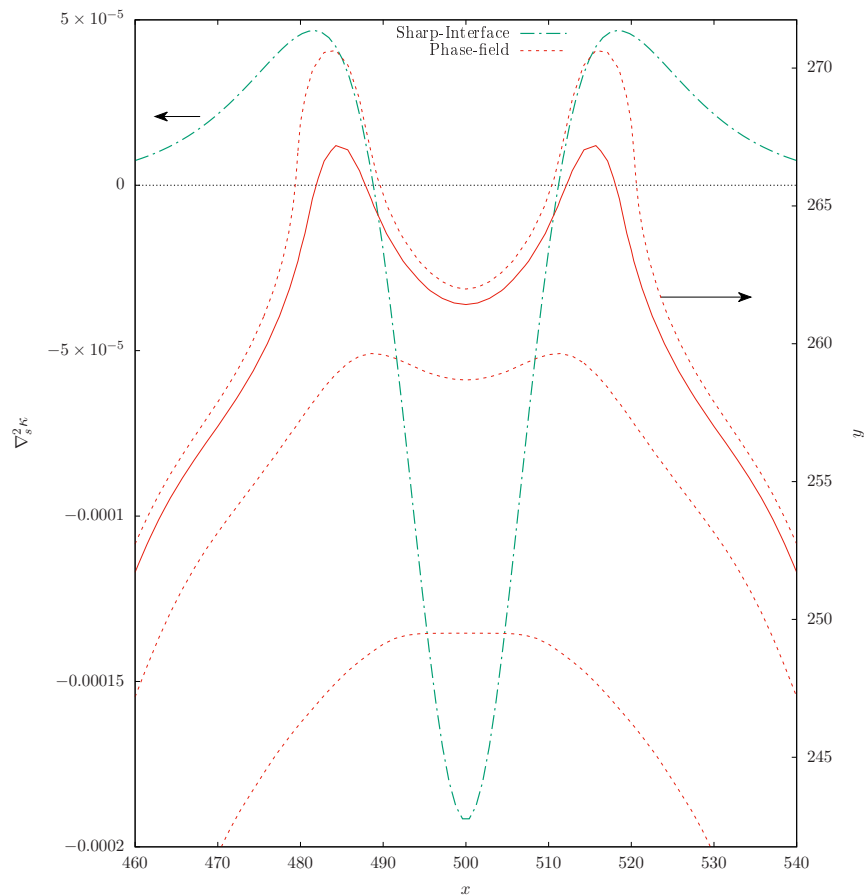


Figure 6.7: The temporal evolution of crests, at $x = 490$, $y = 510$, and the formation of a trough region at $490 < x < 510$ exhibits the tip splitting phenomenon in a two-dimensional phase-field simulation. A direct comparison with the sharp-interface prediction reveals that the tips are generated in the positive regions only, whereas the split region is determined by the negative sharp-interface criterion region of the interface. The left and right arrows indicate the $\nabla_s^2 \hat{\kappa}$ and the grid positions (y), respectively.

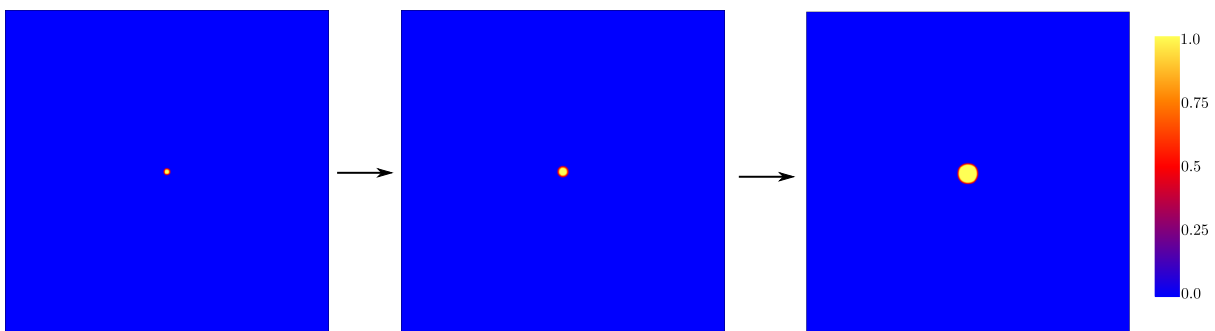


Figure 6.8: In accordance with the analytical criterion for a sphere, the absence of tip instability is also observed in our simulations. The color bar illustrates the phase-field according to the legend embedded near the simulation snapshots.

the initial seed condition is the same as the parabolic interface $\alpha_0 = 0.2$ in Fig. 6.5, and in order to conserve the shape of the parabola, a weak anisotropic strength is imposed. Here,

the simulation is performed in a domain of 1000×1000 numerical cells, in the absence of numerical noise, and an interface width $\epsilon = 4 \times \Delta x$ is considered, where $\Delta x = 1.0$. The temporal evolution of the solid-liquid interface via the dashed isolines is shown in Fig. 6.7. The red isoline in Fig. 6.7 depicts the formation of crest and trough positions, which in turn indicate that the evolving crystal has undergone tip splitting. The projection of Fig. 6.6 (dashed green line) in Fig. 6.7 (solid red line) illustrates that the interface evolves into a crest where the analytical criterion is positive, while the negative $\nabla_s^2 \hat{\kappa}$ corresponds to a hindered forked region. In Fig. 6.7, it can be seen that this segment now proceeds in the opposite direction, compared with the two hillocks developed on either side. The positions where $\nabla_s^2 \kappa$ passes through zero are known as Laplace or rotation points, i.e. the sign of the analytical criterion reverses [183]. These points determine the rotation of the crystal, where the hindered growth region transforms into an evolving region with solidification time. The present analysis agrees in spirits with Kessler and Koplik et al. [185, 186], where a geometrical approach proved that the curvature at the tip decreases with time and finally the tip splitting event is initiated once the tip curvature passes through zero. Additionally, an analytical criterion for sidebranching in anisotropic dendrites was reported with similar remarks [187], wherein the evolution of a perturbation was tracked, and the difference between the time-dependent curvature and the curvature of a steady-state crystal ($\Delta(\kappa, s) = \kappa(s, t) - \kappa^*(s)$) was plotted to present different scenarios for the generation of sidebranches. Moreover, since the tip splitting phenomenon is simulated via a diffuse-interface approach, the selection of a finite interface width is critical. Therefore, in order to investigate the role of diffuse interface width and discretization noise, a convergence study is performed in Appendix B.

Here, the gradients developed parallel to the interface, relatively close to the bulk, contribute towards the generation of an inflection point, especially at the tip region. However, as these fluxes are proportional to the interfacial curvature, they recede significantly away from the tip, where the bulk fluxes are dominant. The surface accelerates due to cooling and retards by virtue of heating. A combination of such effects sets in the development of an inhibited interface at the negative $\nabla_s^2 \kappa$ region, facilitating the forking process at the precise position. In other words, the initiation of the cusped region transpires when $\nabla_s^2 \kappa$ turns negative. The concave portion of the interface also indicates some sort of energy sink along the U-shaped interface. The present analysis agrees well with a recent study by Mullis et al. [188], where it was illustrated that the location of the tangential flux and the first perturbation are to be consistent at high undercoolings. Finally, the two tips that are triggered by means of positive tangential flux dominate the evolution process, and multiply into several tip splitting formations during the later stages of the simulation.

While the initiation and the mechanism of a tip splitting event is discussed, the absence of such instabilities is also observed when a sphere is considered as an initial

condition, see Fig. 6.8. For a sphere with an isotropic interfacial energy, in a noise less simulation environment, the curvature-dependent analytical criterion is defined by the absence of crest and trough regions. With such an initial condition, the sphere evolves consistently without forking in accordance with the sharp-interface analytical theory. Lastly, as the simulated results are in accordance with the analytical prediction for different shapes, it is now well established that the forking mechanism is not driven by a particular initial condition. Nonetheless, a detailed study to address the importance of a non-uniform curvature which varies non-linearly with its arc length is provided in Appendix C.

6.3.3 Effect of lattice anisotropy

In the present section, the effect of lattice anisotropy on our numerical results is investigated in detail. In order to accurately analyze the tip splitting phenomenon, and minimize the pinning effect of the lattice on the interface, the equilibrium shapes of a spherical crystal seed are systematically compared between the phase-field simulation and with its corresponding shape in the sharp-interface theory [189, 190], expressed in the Cartesian coordinates as

$$x = R_{00} \left[f(\theta, \varphi) \sin(\theta) \cos(\varphi) + \frac{\partial f(\theta, \varphi)}{\partial \theta} \cos(\theta) \cos(\varphi) - \frac{\partial f(\theta, \varphi)}{\partial \varphi} \sin(\varphi) / \sin(\theta) \right], \quad (6.8)$$

$$y = R_{00} \left[f(\theta, \varphi) \sin(\theta) \sin(\varphi) + \frac{\partial f(\theta, \varphi)}{\partial \theta} \cos(\theta) \sin(\varphi) + \frac{\partial f(\theta, \varphi)}{\partial \varphi} \cos(\varphi) / \sin(\theta) \right], \quad (6.9)$$

$$z = R_{00} \left[f(\theta, \varphi) \cos(\theta) - \frac{\partial f(\theta, \varphi)}{\partial \theta} \sin(\theta) \right], \quad (6.10)$$

and,

$$f(\theta, \varphi) = 1 + \frac{4\delta_{\alpha\beta}^e}{1 - 4\delta_{\alpha\beta}^e} \left[\cos^4(\theta) + \sin^4(\theta)(1 - 2\sin^2(\varphi)\cos^2(\varphi)) \right]. \quad (6.11)$$

Here, (θ, φ) are the spherical angles along the normal direction to the solid-liquid interface. Since the study is restricted to two-dimensional simulations, the comparison is performed for the equilibrium shapes of the sphere along the $x - y$ plane only. Additionally, in the above equation, $\delta_{\alpha\beta}^e$ represents the effective anisotropic strength of the solid-liquid interface, given as $\delta_{\alpha\beta}^e = \frac{R_{10}/R_{11}-1}{R_{10}/R_{11}+1}$, where R_{10} and R_{11} are the radial distances from the origin to the crystal-melt interface along the y axis, and along the $x = y$ line, respectively from the phase-field simulation.

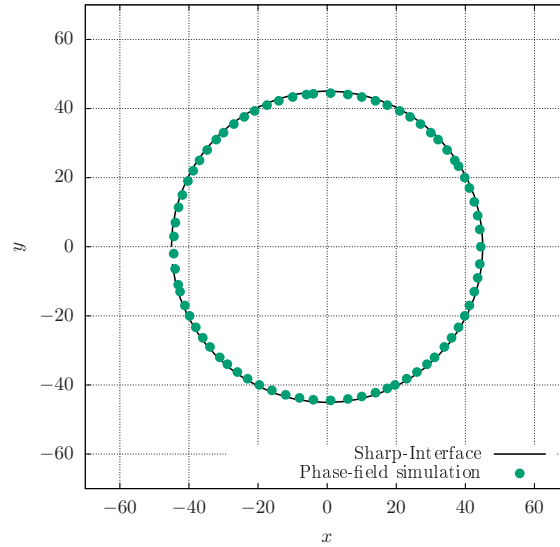


Figure 6.9: For an energetically isotropic interface $\delta_{\alpha\beta}$, the simulation of a spherical seed with radius $R_{00} = 45$ depicts a complete agreement with the sharp-interface theory. The obtained effective anisotropy $\delta_{\alpha\beta}^e = 0.0001$ shows minimal effect from the underlying lattice on our numerical results.

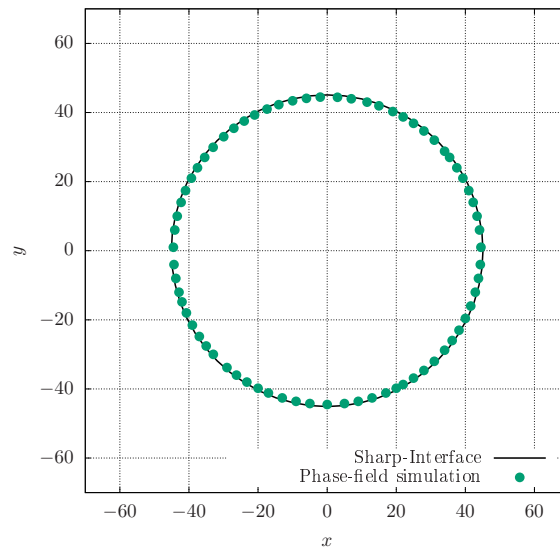


Figure 6.10: For a weak anisotropic solid-liquid interface $\delta_{\alpha\beta} = 0.005$ and radius $R_{00} = 45$, a direct comparison with the sharp-interface equilibrium shape shows an excellent agreement. Here, the obtained effective anisotropy $\delta_{\alpha\beta}^e = 0.0045$ has very minute variation when compared with the imposed value.

To begin with, the equilibrium shape obtained from the phase-field study is first initialized with a spherical solid seed of radius $R_{00} = 45$. Moreover, the melt supersaturation $\Delta = 0.8$ is selected such that the bulk phases are in equilibrium, and the spherical seed would neither shrink nor grow with time. As shown in the earlier section, the tip splitting

microstructures are widely observed for $\delta_{\alpha\beta} < 0.01$, and thereby, two different anisotropic strengths, $\delta_{\alpha\beta} = 0$ for the isotropic case, and $\delta_{\alpha\beta} = 0.005$ for weakly anisotropic interfaces is considered for the present section. Fig. 6.9 and Fig. 6.10 illustrates the equilibrium shapes from the phase-field simulations, and an excellent agreement with the obtained sharp-interface profiles for two different cases is observed. Henceforth, from the the above analysis, the grid or lattice anisotropy has minimal effect on the crystal-melt shapes, and therefore represents the accuracy of our phase-field results. Nonetheless, the direct comparisons for simulations with strong anisotropic strengths and different crystal radii have been discussed in detail in the Appendix B.

6.3.4 Effect of numerical noise

In the present section, Fig. 6.11 portrays a comparative study between the phase-field simulations conducted with and without numerical noise in the system. Here, the conven-

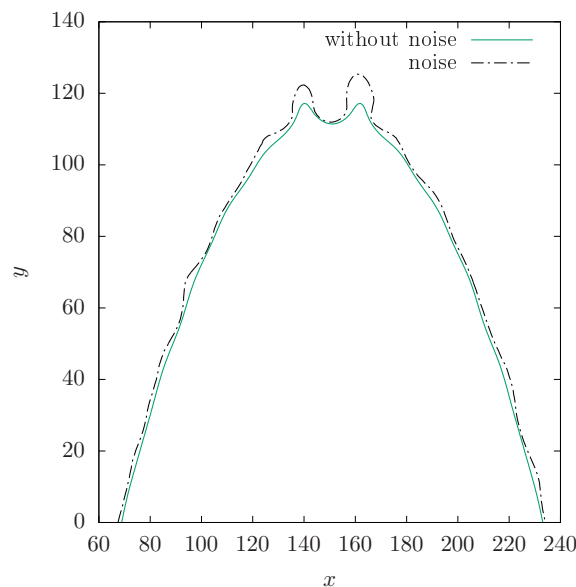


Figure 6.11: Comparison between the phase-field simulations performed with and without numerical noise. Both the interface isolines display the same splitting position, while simulations with noise (black dotted line) depict the boosted growth of the tip. Additionally, few perturbations also start to augment away from the tip which proceeds as branches.

tional Marsaglia polar method [134] is employed to generate a random pseudo-numerical noise that obeys a typical Gaussian distribution. The green solid color in Fig. 6.11 refers to an isoline for tip splitting in the absence of numerical noise, whereas the black dotted isoline illustrates the augmented tip as a consequence of the numerical noise in the system. When compared with Fig. 6.6, the trough position always lies within the negative $\nabla_s^2\kappa$ region, and the two tips emerge across $\nabla_s^2\kappa > 0$, which is in agreement with the present criterion. The amplified tips that astride the trough region is attributed to the noise

strength, whose growth seems to be inhibited in the case of simulations performed in the absence of noise. In addition, the imposition of numerical noise causes an asymmetrical growth of the tips, whereas the present criterion predicts a proportional growth of the two tips. Henceforth, the presence of numerical noise has very little influence, especially on the determination of the tip splitting position. A recent study by Glicksman [183] has also reported that the added noise in the system purely aids the profound growth of the tips or sidebranches during dendritic growth. Similarly, by performing rigorous three-dimensional simulations, a phase-field study [191] concluded that the branching mechanism was deterministic rather than a result of frivolous noise. As anticipated, the presence of numerical noise merely contributes to the amplified and asymmetric growth of the tip as well as to the appearance of small perturbations away from the tip region.

6.4 Structural transition of tip splitting microstructures under diffusive-convective regime

The formation of tip splitting patterns in the presence of melt convection is investigated in the present section. In Fig. 8.4, a simulation setup is considered with 1000×1000 numerical cells and the grains ' α_1 ' and ' α_2 ' represent the solid phase, and β denotes the liquid phase.

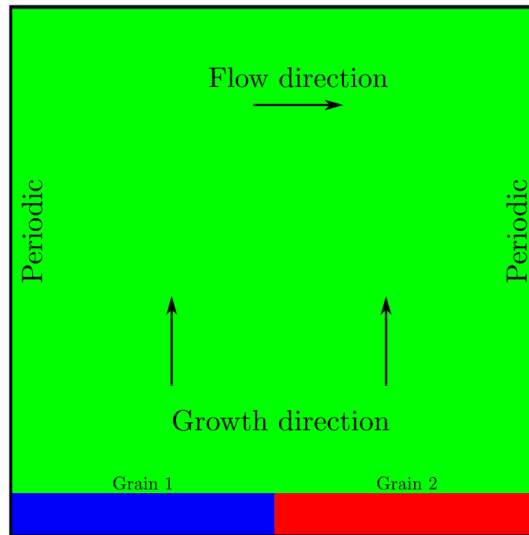


Figure 6.12: Schematic illustration of the simulation setup along with the imposed initial and boundary conditions. A two-dimensional simulation box captures 1000×1000 cells in the $x-y$ dimensions. The Neumann boundary condition is applied for the concentration fields at $y = 1000$, and the direction of melt flow is perpendicular to the growth direction.

As illustrated in Fig. 6.12, the periodic boundary conditions for the concentration fields in the x -direction assists the free growth of the two solid phases across the domain.

Structural transition in tip splitting microstructures

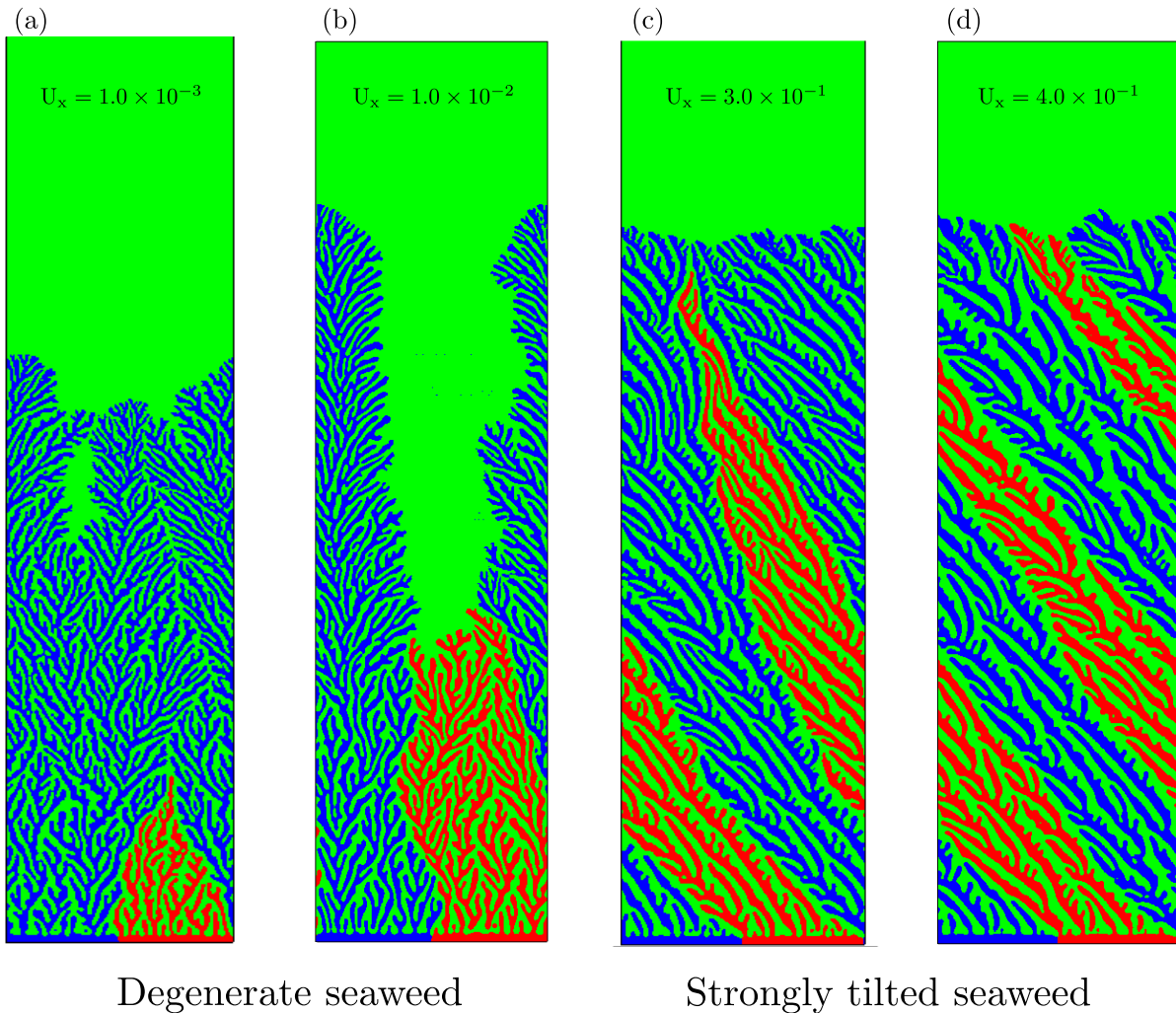


Figure 6.13: (a)-(d) Structural transition of tip splitting microstructures under diffusive-convection regime. Here, the colors blue and red refer to the two distinct grains of the solid phase, and green color represents the liquid phase. The degenerate seaweeds at low convection velocities gradually transform into strongly tilted seaweeds with an increase in the melt velocity.

At the top boundary, the Neumann boundary condition is applied for concentration and phase fields. Along with the periodic boundary conditions at $x = 0$ and $x = 1000$, the melt flow is introduced along the x -direction and perpendicular to the growth direction. Additionally, the slip boundary condition is applied for the velocity fields at $y = 1000$. A sliding window technique [192] at $y = 1000$ results in an infinite domain in the y -direction. In order to increase the computational efficiency, the sliding window algorithm allows us to simulate the region around the solid-liquid interface only. For the sake of convenience, in this chapter, two solid grains are employed to represent a binary polycrystalline alloy. Here, the solid-solid and solid-liquid surface energies for both grains are identical. With the current simulation setup and a supersaturated melt of composition $\Delta = 0.5$, the structural transition of tip splitting morphologies is shown in Fig. 6.13 as a result of

various convection velocities.

Among the different types of seaweed morphologies, the directionally solidified microstructures in Fig. 6.13(a)-(c) are known as degenerate seaweeds, due to the presence of small amount of degeneracy in their growth dynamics. The most striking feature for a degenerate seaweed is generally spotted in their tip splitting behavior. The foremost tip splits at alternate sides towards left and right, making them unique and distinct among all other complex patterns [181]. It is important to note that the degenerate structures are observed for the simulations performed at low convection velocities. With an increase in the imposed convection velocity, a strong orientation of the growth front towards the flow direction is noticed in Fig. 6.13(d)-(e). Such type of patterns as known as strongly tilted seaweeds [193], characterized by their tips evolving in an inclined manner. Furthermore, the large wavelengths λ , i.e., the mean spacing between the main branches are a distinct feature in tilted seaweeds, wherein, after a tip splitting event, the growth of a sidebranch is completely restricted. The stabilized growth of such tilted seaweeds is explained from the spatiotemporal diagrams of Akamatsu et al. [37], where the presence of wide liquid grooves assisted the tilted trajectory of the pattern.

Moreover, in the present scenario, a moderate growth competition between the two solid grains is also observed. For most of the simulations performed, it is noticed that the two grains compete and overgrow each other in a random manner, and this behavior tends to neutralize as the melt velocity gradually increases. Generally, the competition between isothermal microstructures happens in three different kinds of spacing adjustment mechanisms, namely, tip submergence, tip splitting and overgrowth of side branches. As these microstructures are observed for isotropic interfaces, tip splitting and tip submergence are the main factors that promote local growth competition of solid grains. This phenomenon is quantitatively depicted in Figs. 6.14 and 6.15, where the temporal volume fractions of the two solid phases at two different convection velocities are shown respectively. In Fig. 6.14, the red colored grain loses the growth competition at an early stage, however, as shown in Fig. 6.15, the inclined nature of the tip splitting structure dominates, the red colored grain parallelly to the blue grain. This behavior tends to increase with the increase in the convection velocity. However, due to a degree of influence from the numerical fluctuations, a prediction for such a behavior is still unclear.

Fig. 6.16 illustrates the early stages of the solidification process at two different convection velocities. From an initial configuration, the interface contours are compared for the instabilities developed at $U_x = 1.0 \times 10^{-2}$ and $U_x = 3.0 \times 10^{-1}$, respectively. In Fig. 6.16(a), it is observed that the perturbations emerge across the two solid grains with proportional amplification. Initialized across the grain boundary, these ridges spread laterally with time across the bicrystal solid grain. Due to the presence of weak and symmetric velocity fields across the planar interface, the morphological behavior in Fig. 6.16(a) is analogous. However, when compared with its counterpart, the influence of convection

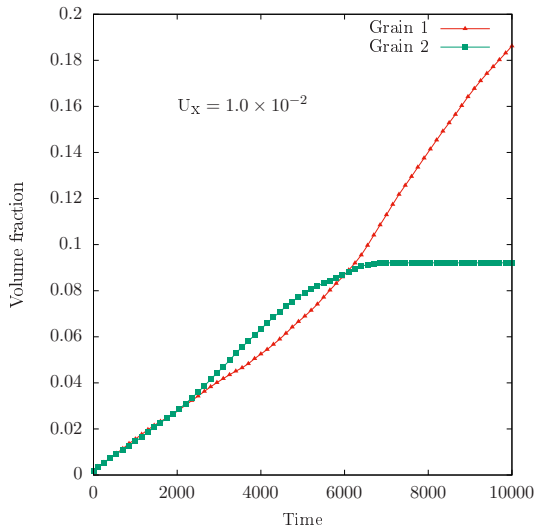


Figure 6.14: Temporal volume fractions of solid grains at $U_x = 1.0 \times 10^{-2}$.

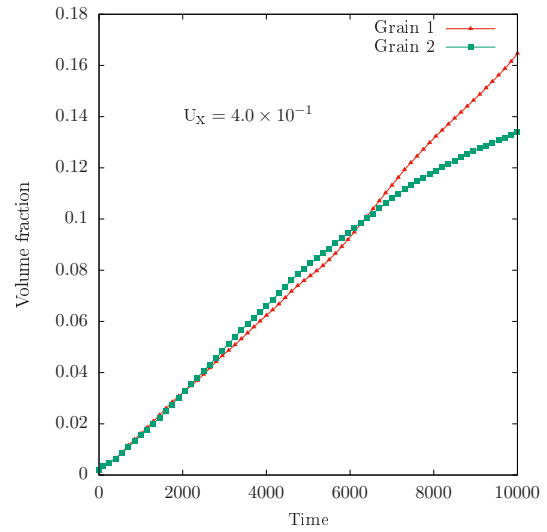


Figure 6.15: Temporal volume fractions of solid grains at $U_x = 4.0 \times 10^{-1}$.

is clearly visible at $U_x = 3.0 \times 10^{-1}$. Fig. 6.16(b) demonstrates that the tips at the grain boundary are oriented towards the upstream (left) direction. Furthermore, as opposed to Fig. 6.16(a), the symmetric and the augmented growth across the planar interface is completely absent. Herein, as a result of strong convection fields at $U_x = 3.0 \times 10^{-1}$, the solute is completely swept away and henceforth the ridges at the grain boundary amplify at a faster rate. Consequently, the advected solute ensures the development of asymmetric velocity fields and thereby the protuberances at the center of the grain are hindered in nature. The present findings are in qualitative agreement with an experimental work [25], where the effect of natural convection in a transparent organic alloy was examined in detail. In Fig. 6.16(b), the combined presence of convex ridges and convection fields at the grain boundary strikingly influences the propagation of the tip splitting instabilities across the planar interface. The ridges at the center of the grains proceed with time and generate an inclined seaweed structure. Another interesting feature of the solidification process is the growth direction of the perturbations. The tilting nature of the hills towards the inflow direction results in a grid like pattern. Shorter the distance from the grain boundary, the larger the tilt angle. This hallmark of the primary ridges results in the growth competition between the two solid grains throughout the solidification process. Therefore, through the above distinct attributes, it is now well established that convection in the liquid phase plays a vital role in the propagation and amplification of instabilities in a bicrystal sample. Although a critical value for the transition is not determined, the transition region is predicted to be around $1.0 \times 10^{-1} \leq U_x \leq 3.0 \times 10^{-1}$.

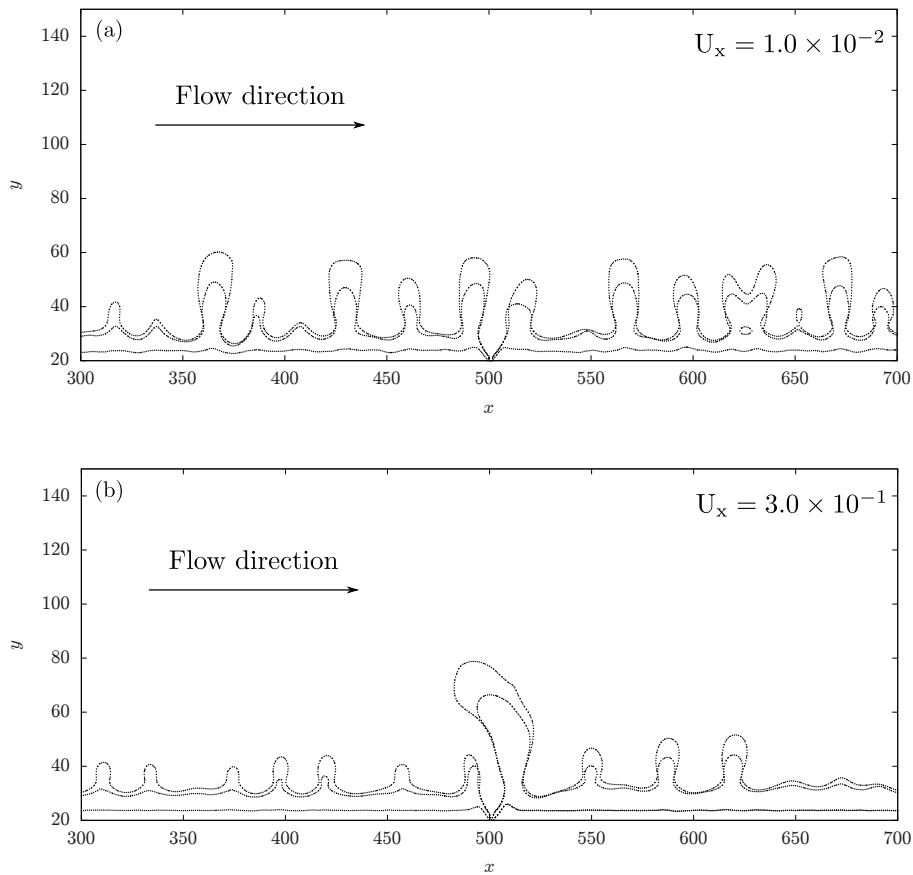


Figure 6.16: A comparative study between the morphological evolution of two solid grains is depicted for different convection velocities. (a) The perturbations are aligned in the initial growth direction across the domain. The lateral development of the hillocks at the center of the grain is significant and symmetric. (b) In contrast, in the presence of strong convection fields, the ridges are amplified and oriented at the grain boundaries only. The small humps at the center of the bicrystal grains evolve slowly.

6.4.1 Morphological features

Next, in order to explain the morphological differences and the tip splitting behavior in degenerate and strongly tilted seaweed structures, the interface isolines ($\phi = 0.5$) are depicted in Fig. 6.17. The two morphologies when compared with each other in Fig. 6.17 display remarkable differences in their patterns. An initial examination suggests that the tip splitting event occurs more frequently at low convection velocities while the same phenomenon occurs scarcely as the velocity gradually increases. Similar to an experimental study [181], in Fig. 6.17(a), during crystal growth the tip characteristically splits left and right sides. Whenever a tip undergoes forking, one of the two lobes survives, while the other is left behind. These leftover branches either evolve in the growth direction of the parent lobe or they are completely inhibited due to the presence of an adjacent tip.

However, for a strongly tilted seaweed, the post-splitting process is completely dif-

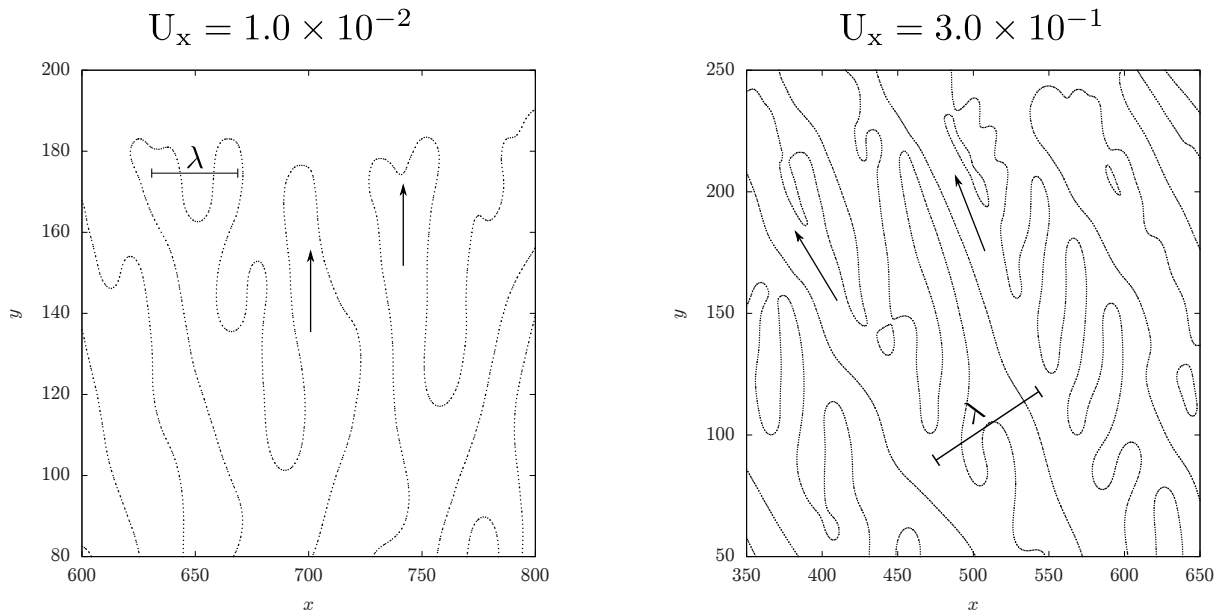


Figure 6.17: The distinct morphological features are schematically illustrated via the interface isolines $\phi = 0.5$. The degenerate seaweed structures with an alternating tip splitting event amplify along the growth direction. Since there is no preferred orientation, the tips proportionately incline from -70° to $+70^\circ$. However, in the case of a strongly tilted seaweed, the branches are always oriented at -35° to -75° along the x -direction. Here, x and z are the dimensionless grid points. The black arrows indicate the growth direction for both cases. The wavelength λ , is defined as the mean distance between the main branches of a structure. In general, large wavelengths are a characteristic feature for the patterns generated in regime II.

ferent. Owing to the influence of velocity and concentration gradients, the tips and the sidebranches incline in the opposite direction. In Fig. 6.17, the mean spacing λ is schematically shown and defined as the distance between the medial axis of the main branches. The leftover small branches are neglected due to the overgrowth of the nearby tips. Here, the width of an individual branch is generally of an order greater than the tip radius. In Fig. 6.17(b), the oriented nature of the individual branches is schematically illustrated via the black arrows, thereby representing the vast differences in the growth directions of the structures, respectively.

6.4.2 Effect of surface energy

As discussed in the previous chapter, depending upon the imposed surface energies, the initial shape of the grain boundary groove is modified, and subsequently the propagation of primary ridges is affected. Here, in a constitutionally undercooled melt, the lateral spread of the perturbations towards the center of the grain is elucidated for different scenarios. Fig. 6.18 depicts the influence of the grain boundary energy γ_{gb} and the solid-liquid interfacial energy γ_{sl} on the inception of a tip splitting microstructure. As the solidification of the interface commences from an initial configuration, for $R_0 = 2.0$ in

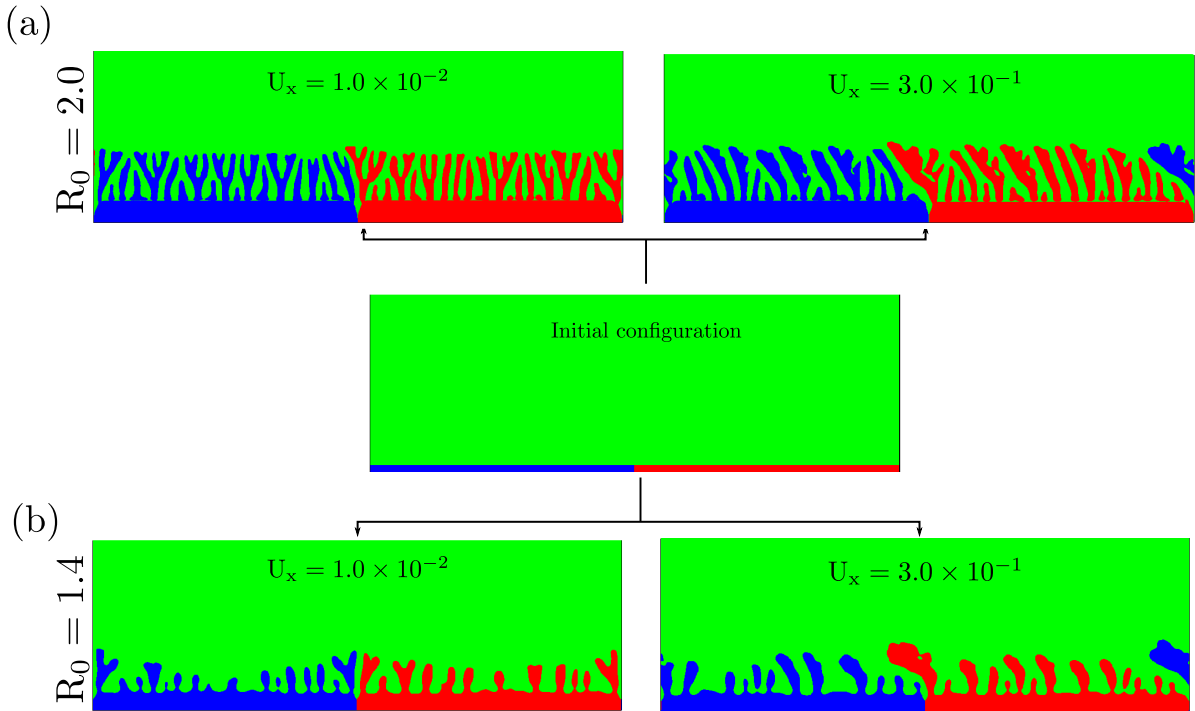


Figure 6.18: The influence of R_0 on the initiation of morphological instabilities along a bicrystal is illustrated for two different cases. (a) $R_0 = 2.0$ and (b) $R_0 = 2.0$. With the decrease in the ratio R_0 , the enhancement of protrusions along the bicrystal interface decreases.

Fig. 6.18(a), it is observed that in both regimes the perturbations amplify in a robust manner. The crests and troughs are uniformly generated with minimum spacing between the primary branches, especially at the core region of the solid grains. In contrast, when $R_0 = 1.4$, the sideward advancement is concentrated at selective positions, as the interfacial energy is decreased shown in Fig. 6.18(b). Although, the hillocks develop into seaweed structures, there exists sporadic colonies where neither depressions nor fluctuations are developed. This populous and limited growth of the tips along the solid-liquid interface are consistent with the previous experimental and phase-field studies [23, 25, 194], where the localized growth of the protuberances due to the grain partitions were reported for a binary polycrystallite. Here, the joint ridges that are involved during the birth of the instabilities are largely dependent on the driving force and the interfacial energy of the system. Although the melt supersaturation in the present case is considered to be constant, in general, these two aforementioned thermodynamic parameters can be further manipulated to generate tip splitting to cellular microstructures [195].

6.4.3 Determination of local tilt angles

Visual examination of the tip splitting patterns indicate a preferential orientation for the instabilities along the x -direction. Consequently, a quantitative image analysis is performed through an open source *ImageJ* software plug-in, *OrientationJ* [196]. Based

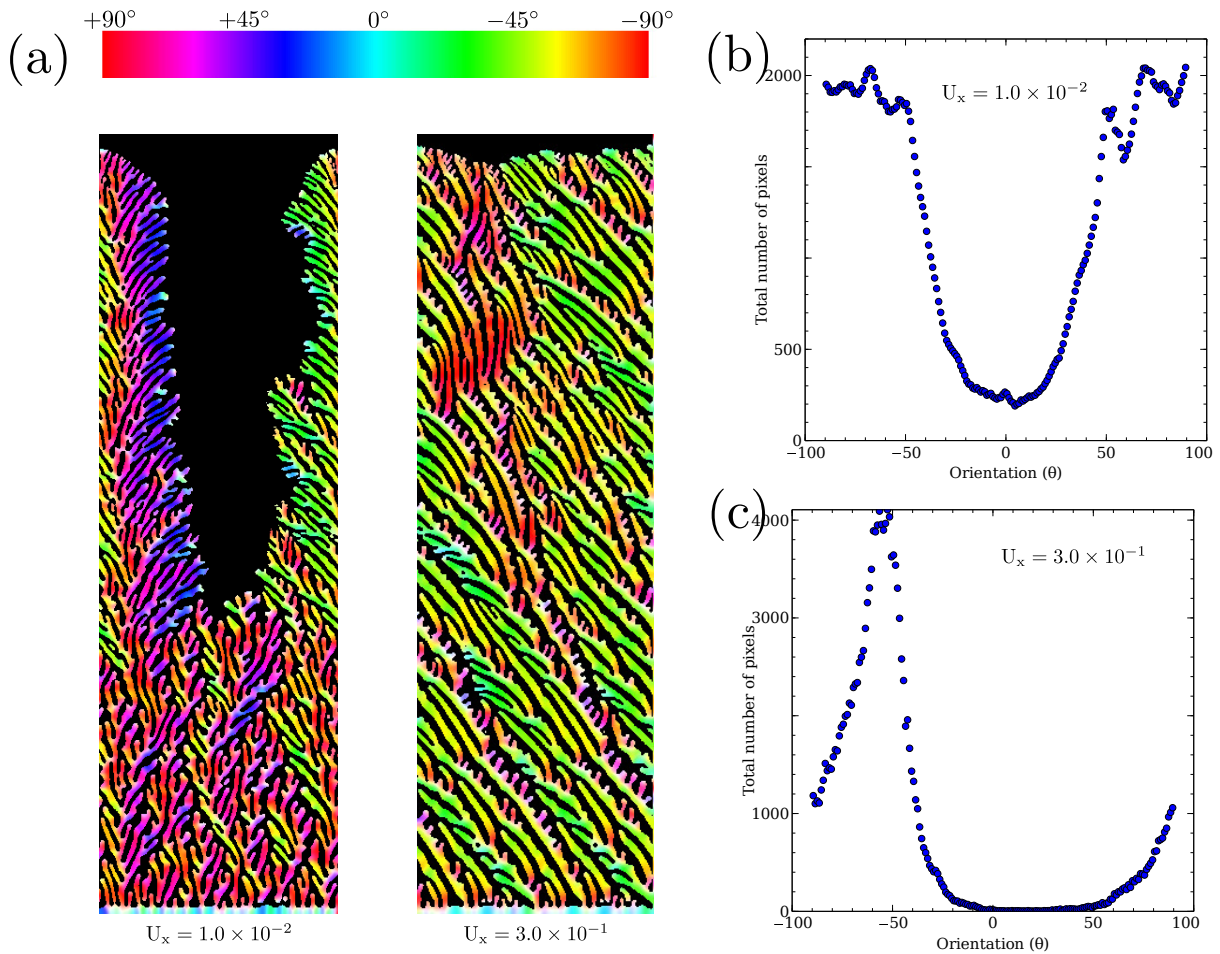


Figure 6.19: A quantitative image analysis is performed with an open source ImageJ software plug-in, OrientationJ [196], for the patterns generated at two different convection velocities. (a) The local orientation properties of the solid phases show the distinctive features observed in degenerate and strongly tilted seaweed structures. The color bar indicates the orientation of each pixel from -90° to $+90^\circ$, where θ is orientation of the y-axis. (b)-(c) The local angle distribution confirms the preferred direction, where the maximum number of pixels orient at $+70.5^\circ$, -67.5° and at -52.5° for $U_x = 1.0 \times 10^{-2}$ and $U_x = 3.0 \times 10^{-1}$, respectively.

on the structure tensors, i.e. the matrix representatives that are derived from the gradient of the image, the directional change in the image intensity. This method calculates the local orientation and the isotropic properties of every pixel in an image, commonly used in several pattern formation investigations [197, 198]. The local orientation θ [196] is calculated as

$$\theta = \frac{1}{2} \arctan \left(2 \frac{\langle f_x, f_y \rangle_w}{\langle f_y, f_y \rangle_w - \langle f_x, f_x \rangle_w} \right). \quad (6.12)$$

Here, f_x and f_y are the partial spatial derivatives of the image intensity function $f(x, y)$, along the principal directions x and y , respectively. The weighted inner product between the two arbitrary images g and h is defined as $\langle g, h \rangle_w = \int \int_{R^2} w(x, y) g(x, y) h(x, y) dz dx$, where $w(x, y)$ is the Gaussian weighting function that specifies the area of interest.

Fig. 6.19(a) describes the local tilt angles of the solid phases at two different melt velocities. The color bar indicates the orientation from -90° to $+90^\circ$, where 0° represents orientation along the y -axis. The random tip splitting pattern observed in Fig. 6.19(a) lays out a distinct characteristic when compared with the inclined framework. The alternative tip splitting event along with the presence of low melt velocities produces a wide range of local tilt angles, thereby indicating the disordered nature of the structure. In contrast, in the presence of strong velocity fields at the tip, a formidable inclination against the flow direction is observed universally among strongly tilted seaweeds.

The local angle distributions for both regimes provides a clear evidence in Fig. 6.19(b)-(c), where The y -axis in Fig. 6.19(b)-(c) represents the total number of pixels in each image with the same orientation. In Fig. 6.19(b), it is observed that the generated patterns have no favored orientation. Most of the tips in the microstructure tend to incline from $+70^\circ$ to -70° in the same proportion, with two peaks observed at $+70.5^\circ$ and -67.5° . However, as shown in Fig. 6.19(c), the inclined patterns evolve in such a manner that the local angles always vary in-between -35° to -75° . The generation of a single peak emphasizes that a large number of branches incline at -52.5° . The sidebranches in inclined microstructures tend to amplify in the opposite direction, i.e. with a local orientation of $+50^\circ$. Lastly, findings in Fig. 6.19 strongly testify that the tilting structure is mainly influenced by the presence of strong convection fields near the solid-liquid interface. For all the structures, the image analysis also confirms the symmetric and the skewed nature of the local orientation distribution for degenerate and strongly tilted seaweeds, respectively.

6.4.4 Effect of interfacial anisotropy

In this section, a novel microstructural selection map is depicted to investigate the effect of interfacial anisotropy on the structural transition of tip splitting patterns. Fig. 6.20 illustrates a morphological selection map, where the random tip splitting pattern are limited to weak anisotropic strengths and low convection velocities only. As the imposed velocity increases, a strongly tilted seaweed is observed upto $\delta_{\alpha\beta} = 0.02$. However, the presence of stronger anisotropic strengths produce columnar dendrites for various convection velocities. The microstructural selection map shows a direct resemblance with the selection map in Chapter 2, where the structural transition of microstructural patterns under various growth conditions was discussed. As the contribution from the surface energy dominates, the dendrite tip aligns along the heat flow direction, and the effect of liquid phase convection on the tip orientation diminishes. Henceforth, the critical velocity to predict the transition between tip splitting patterns is also dependent on the anisotropic strength of the solidifying interface. In addition, for anisotropic strengths $\delta_{\alpha\beta} \geq 0.02$, columnar dendrites are always generated irrespective of the strength of the

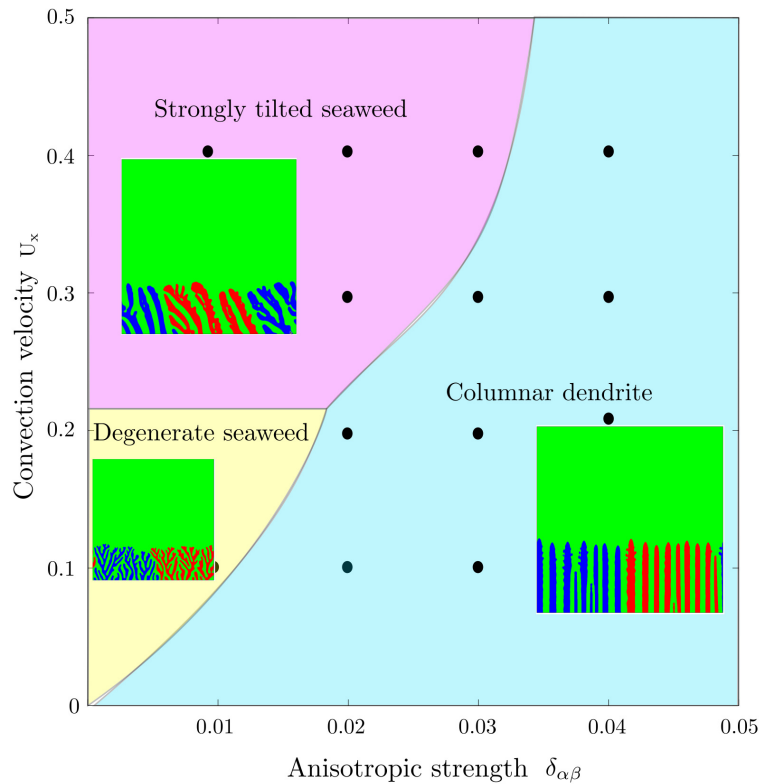


Figure 6.20: Microstructural map illustrating the effect of anisotropic strength and convection velocity. Based on the dynamic competition between $\delta_{\alpha\beta}$ and U_x , three different morphologies are discerned, namely, degenerate seaweed, strongly tilted seaweed and columnar dendrite.

convective forces in the liquid phase.

6.5 Summary

In the present chapter, the directional solidification of tip splitting microstructures is extensively discussed, wherein the formation and the temporal evolution of perturbations along a solidifying interface as a result of the constitutional supercooling near the solid-liquid interface is showcased. It is shown that the presence of grain boundaries in polycrystalline samples promote ridge shaped perturbations near the GB grooves. Furthermore, a methodology to predict the tip splitting positions in a solidifying pattern is investigated, where the calculated analytical criterion acts as the focal point to analyze the tip splitting position for a convex profile. The analytically obtained tip splitting position is dynamically compared and validated via performing phase-field simulations, and an excellent agreement with the sharp interface theory is observed. In this chapter, the discussed tip splitting behavior builds upon the previous experimental and theoretical studies, and successfully provides the regions for tip splitting for the first time. Besides, through the present analytical criterion, it is suggested that a tip splitting phenomenon is deterministic and predictable vis-à-vis the interfacial curvature of the crystal varies

non-linearly with its arc length.

In addition, the structural transition of tip splitting microstructural patterns in the presence of melt convection is studied for a binary polycrystalline alloy. In the absence of crystalline anisotropy, initiated at the grain boundaries, the protuberances generated along the bicrystal periodically split into random fork like structures, namely seaweeds. The traditional degenerate seaweeds observed at weak convection velocities transform into strongly tilted patterns. In particular, it is observed that the ridges and tips amplify uniformly at low convection velocities. It is interesting to note that the alternative tip splitting event in a degenerate type develops into an oriented splitting after the formation of strong velocity fields around an unstable tip. The role of surface energies at the triple junction is also demonstrated through the comparison of microstructures. The relative GB groove angle and with the decrease in the solid-solid grain boundary energy σ_{gb} , we observe that the localization of the tip splitting instabilities along the solid-liquid interface is limited.

The local orientation for different microstructures is classified via an open source plugin *OrientationJ*, where the local tilt angles are calculated through the structure tensors. Quantitatively, the symmetric feature of the distribution results in the generation of peaks at $+70.5^\circ$ and -67.5° . In contrast, the skewed distribution provides a clear evidence that the strongly tilted structures incline with a preferred local tilt angle at -52.5° .

A novel microstructural selection map is also showcased, wherein three different dendritic morphologies are illustrated. The present chapter also captures the important transition between seaweed and columnar dendritic morphologies and sheds light on the role of convective transport near a directionally solidified isotropic interface. As we have studied and simulated the structural transition of tip splitting microstructures into columnar dendrites, the prediction of primary dendrite arm spacing is investigated in the forthcoming chapter.

Chapter 7

Prediction of inter-dendritic spacing

From a practical viewpoint, an understanding of dendritic and cellular structures is critical since they commonly occur during the solidification of binary alloys in casting and welding processes. In earlier chapters, the role of grain boundaries and the mechanism by which an unstable planar interface re-stabilizes into a complex tip splitting or a dendritic pattern were investigated. However, the inter-dendritic spacing selection of unidirectionally solidified microstructure remained unanswered. The prediction as well as the understanding of primary dendrite arm spacing in the mushy zone is among the most important unsolved problems [35]. Nonetheless, owing to experimental conditions, previous studies [34, 54, 199, 200] were limited to the constrained growth of transparent organic alloys and cellular structures, and an investigation of an unconstrained columnar growth is missing. Therefore, in this chapter, the prediction of inter-dendritic primary and secondary arm spacing is explored under diffusive regime, and subsequently the role of convective transport in the bulk liquid phase is elucidated in detail, wherein a reasonable agreement with the experimental microstructures is also established.

7.1 Initial and boundary conditions

In the present chapter, the prediction of inter-dendritic arm spacing is simulated in two dimensions, and as shown in Fig. 7.1, a computational domain of $1500\Delta x \times 750\Delta y$ numerical cells is selected, where $\Delta x = \Delta y = 1.0$, see Table. 7.1. As an initial condition, the simulation starts with a single large solid crystal with no misorientation at the bottom of the domain. The solid-liquid interface is perturbed with numerical noise such that thermal fluctuations are realistically induced at the solidification front. Here, the blue and green colors in Fig. 7.1 represent the solid and the liquid phases respectively. The boundary conditions for the left and right side of the simulation domain is considered periodic for all the fields. In order to account for convection in the liquid phase, lateral melt flow is introduced from the left boundary wall and travels along the horizontal direction

perpendicular to the axisymmetric dendrite. In addition, on the top and bottom sides, the Neumann boundary condition is applied for the phase and solutal fields, whereas, a slip condition is applied for the velocity fields. Similar to previous chapters, a moving frame method [192] is applied when the total number of cells between the foremost solid-liquid interface and the top boundary is less than 450 numerical cells. Thereafter, for every time step, the bottom cells along the y -direction are shifted downwards and cutoff. This method generally saves time and computational effort, and also ensures that the concentration fields are unaffected by the boundary conditions.

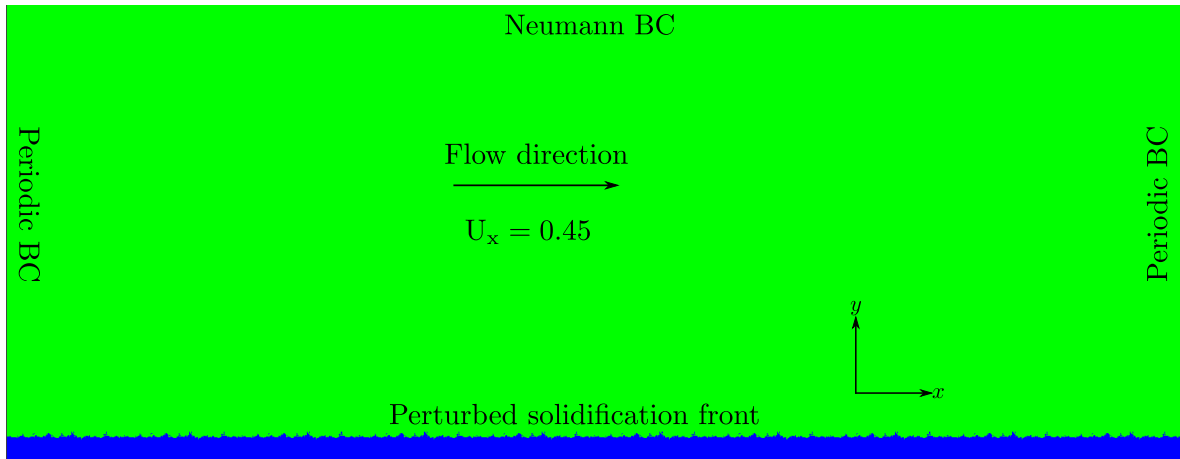


Figure 7.1: Schematic setup with initial and boundary conditions to predict the primary dendrite arm spacing under diffusive-convective regime.

Table 7.1: Simulation parameters to predict inter-dendritic spacing.

Description	Parameter	Value
Convection velocity	U_x	0.45
Anisotropic strength	$\delta_{\alpha\beta}$	0.04
Interface width	ϵ	4.00
Simulation Domain	$N_x \times N_y$	1500×750
Discretized grid space	$\Delta x = \Delta y$	1.0

7.2 Primary dendrite arm spacing under diffusive regime

It has been well known that the variation of solutal gradients between the advancing dendrite and the surrounding inter-dendritic region gives rise to microsegregation within the solidified crystal [201, 202]. Normal to the dendrite growth direction, this segregation is generally characterised by the primary dendrite arm spacing (PDAS). The inter-dendritic

arm spacing usually controls the maximum length scale for the microsegregation [203], the solutioning heat treatment times [204], and the mechanical properties of a directionally solidified cast alloy [205–207]. In addition, the PDAS directly influences the mushy zone convection, the formation of low melting point secondary phase eutectics, as well as the inception of incoherent precipitates and pores in the inter-dendritic region [208–210]. Therefore, the characteristics of a steady-state dendritic array morphology is important for investigating the selection mechanism of primary dendrites, and for scrutinizing the growth behavior of a cast alloy.

In the present section, the primary dendrite arm spacing is first simulated under pure diffusive regime, where the spatiotemporal evolution of a solidification front is illustrated in Fig. 7.2. At an imposed supersaturation $\Delta = 0.52$, Fig. 7.2(a)-(d) shows that the transient patterns exhibited by the interface reorganizes into a periodic array of columnar dendrites with time. This behavior is consistent with previous experimental and numerical studies [22, 24, 127, 176], where the initial perturbations at the solidification front developed into microstructural patterns. Moreover, the general evolution of the dendritic pattern in Fig. 7.2(a)-(d) is profoundly comparable to that described by Huang and Glicksman [127], where the columnar dendrites were grown from an undercooled transparent SCN alloy. As the velocity of the advancing interface becomes equal to the externally imposed velocity, a steady state growth of the advancing interface is noticed in Fig. 7.3. Likewise, Morris and Winegard [28] also observed that the initial break-up of a planar interface in a cubic crystal produced elongated cross sections if the growth direction was $\langle 110 \rangle$, and a regular hexagonal pattern was generated for crystals growing in the $\langle 100 \rangle$ direction.

7.2.1 Selection mechanism of primary dendritic spacing

The selection mechanism of primary dendrites transpires in the following manner

- Initial planar instability
- Adjustment of primary dendrites via systematic elimination
- Stable growth of primary arms

During the inaugural stages of solidification, the imposed supersaturation in the alloy melt decreases the solutal distribution ahead of the solid-liquid interface. Correspondingly, the solidification front travels forward in order to maintain the local thermodynamic equilibrium, and a boundary layer ahead of the planar interface is formed. Once the critical wavelength is reached, the solid-liquid interface undergoes the Mullins-Sekerka instability [30] and the interfacial instability amplifies as a random hill type perturbation across the planar interface. As the instability becomes visible, the forward pointing

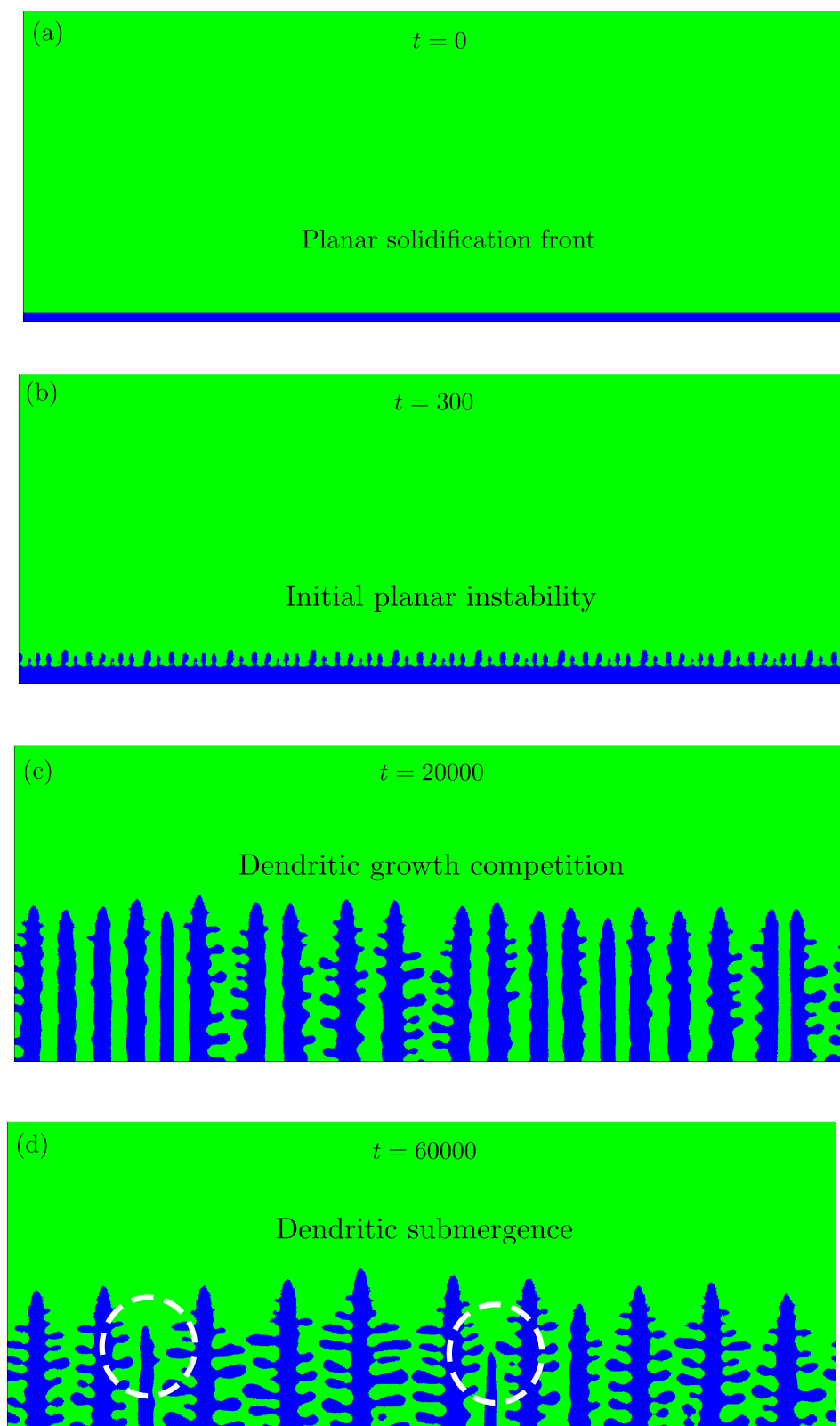


Figure 7.2: (a)-(d) Temporal development of a solid-liquid interface in a supersaturated melt $\Delta = 0.52$. Initial perturbations develop into an array of primary dendrites with time. Local growth competition enhances the adjustment of primary arm spacing, where the lagging dendrites are eliminated, a process widely known as dendritic submergence.

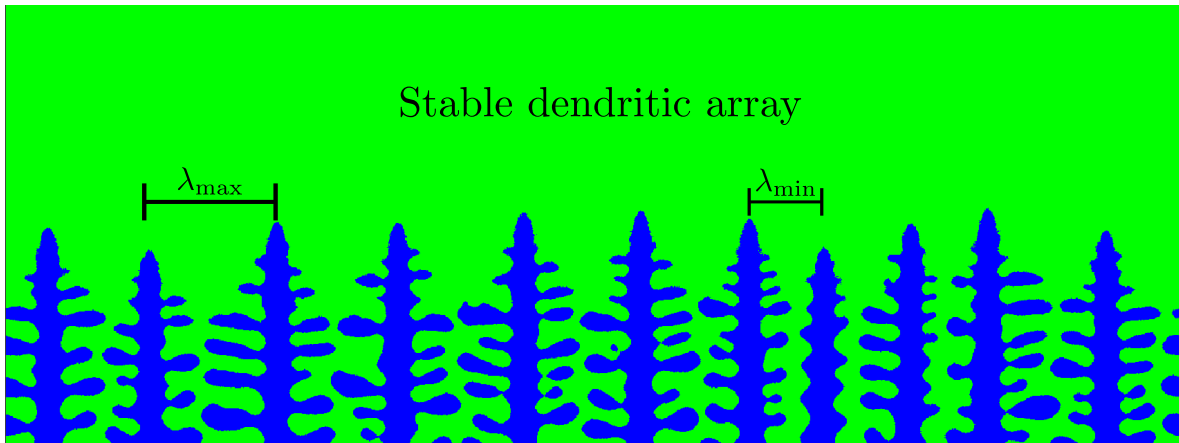


Figure 7.3: Columnar dendrites in a two-dimensional simulation domain, where the primary arms adjust themselves to produce a stable array spacing. Here, λ_{\min} and λ_{\max} represent the minimum and maximum array stability limits.

perturbations develop into an array of dendritic tips with secondary arms in a nonlinear regime, see Fig. 7.2(b)-(c).

After the initial amplification of the perturbations across the solidification front, a local growth competition along the planar front is discovered, where the primary dendrites tend to overgrow via competing with each other, see Fig. 7.2(c). As the solute redistribution near the lagging dendrites is insufficient due to the neighbouring interactions in an array growth, the lagging dendrite will be eliminated by its neighbours. Depicted in Fig. 7.2(d), this process is widely known as *dendritic submergence* [34, 50] in directional solidification. Here, the columnar dendrites locally compete with each other until the array stability limit is recovered, and the total number of primary arms is constant under a given set of growth conditions. Moreover, in order to depict the intensity of the solutal interaction in-between the primary arms, the concentration fields at two different positions is shown in Fig. 7.4. The distinct solutal fields in the inter-dendritic region promote the overgrowth of primary arms to attain a steady-state morphology. Furthermore, in the early stages, the repetitive submergence of primary arms also indicates that the corresponding primary arm spacing is much smaller than the lower array stability limit. Herein, the total number of primary arms decreases with time, and subsequently a constant number of primary arms is established in the simulation domain, see Fig. 7.5. The dendritic morphology in Fig. 7.2(d) shows the absence of tertiary arms, which reiterates that the submergence of columnar dendrites is the main selection mechanism under pure diffusive regime. Nonetheless, tip splitting, another possible mechanism for primary spacing adjustment is also not observed in Fig. 7.2(c), which is attributed to the imposed interfacial anisotropy of the solid-liquid interface. As reported in previous studies [34, 50] and discussed in the previous chapter, the selection mechanism via tip splitting usually occurs in seaweed or cellular growth [211].

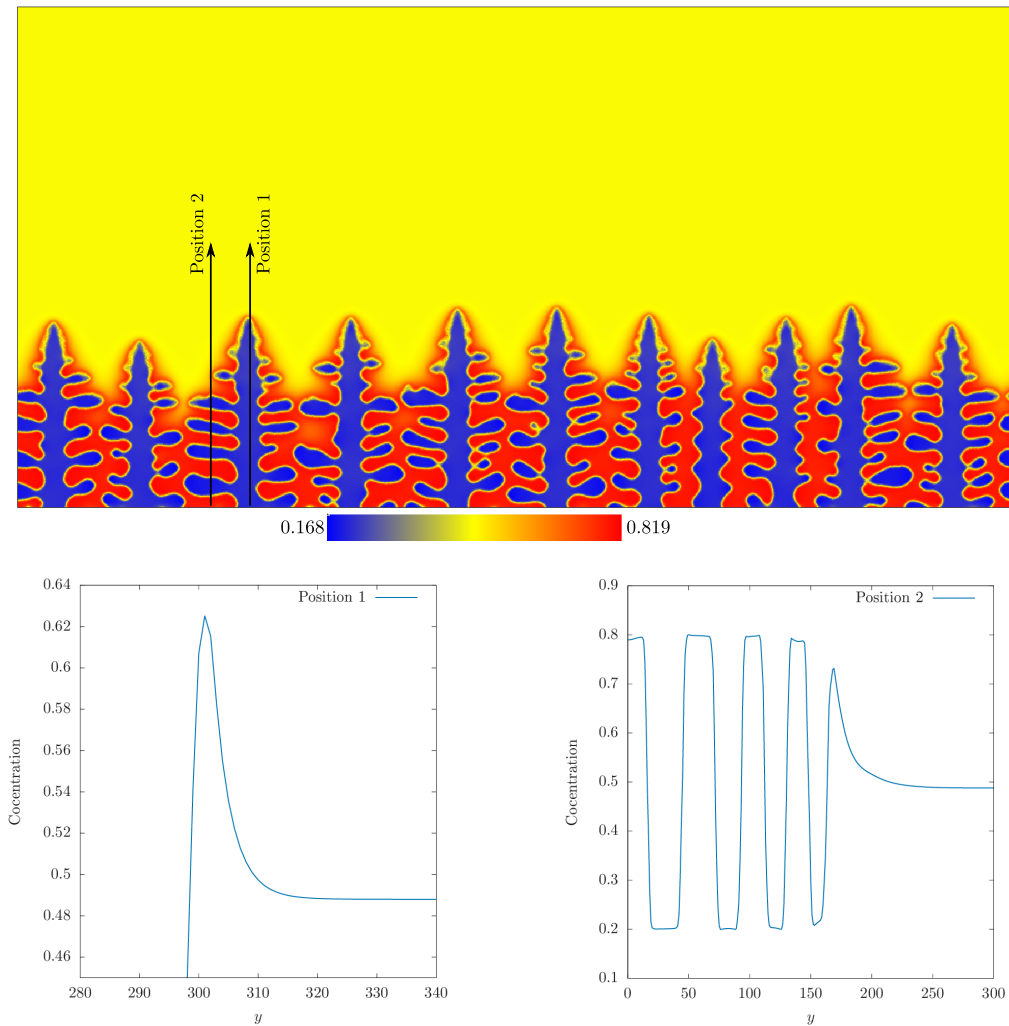


Figure 7.4: Concentration fields depicting the one-dimensional solutal profiles at two different positions during the selection of primary dendrite arm spacing.

Next, the two-dimensional simulations are repeated for various melt supersaturations, and a relation between the primary dendrite arm spacing λ_{PDAS} and the imposed melt supersaturation Δ is depicted in Fig. 7.6 and Fig. 7.7, wherein the primary dendrite arm spacing decreases with an increase in the imposed supersaturation in the alloy liquid melt. A non-linear best fit provides us with a relation of the form $\lambda_{\text{PDAS}} \propto \Delta^{k_1}$, with $k_1 = -8.5$. The distinct columnar dendrites under various growth conditions is shown in Fig. 7.7, where the inter-dendritic spacing decreases and a prominent morphology change is observed. The present numerical results are in tune with earlier experimental and theoretical studies [34, 54, 199], where Kurz and Fisher [199] predicted that the primary dendrite arm spacing decreases as the driving force at the solidification front increases. As the melt supersaturation and the solidification velocity increases, the diffusion length near the solid-liquid interface becomes small, and thereby the presence of strong solutal gradients decreases the primary dendrite arm spacing. Here, all the simulations are run long enough such that the total number of primary arms are constant for a long

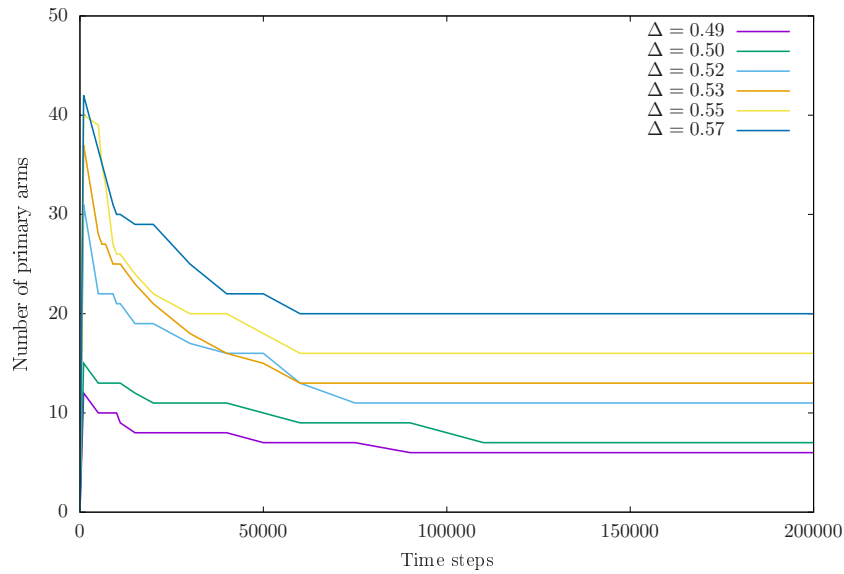


Figure 7.5: Changes in the number of primary arms in the simulation domain. The total number of primary arms along a solidification front attain a steady state spacing with solidification time.

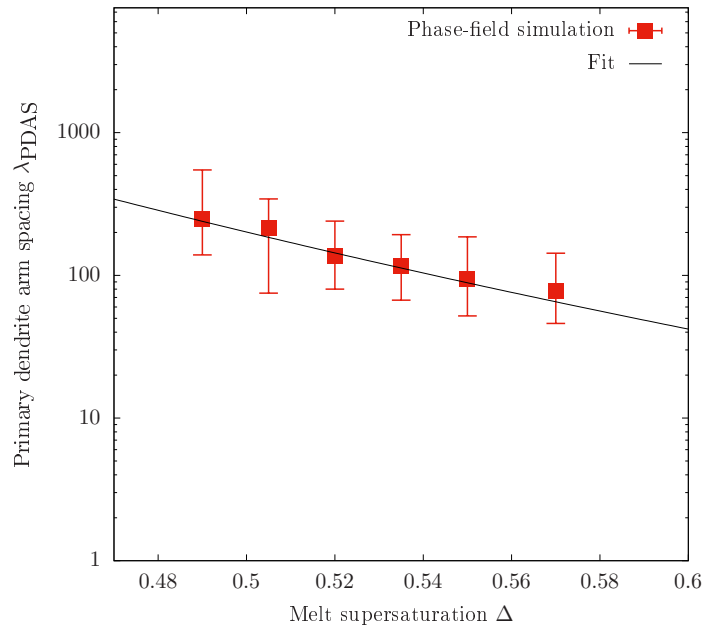


Figure 7.6: Primary dendrite arm spacing as a function of melt supersaturation. Inter-dendritic spacing decreases with an increase in the melt supersaturation. The best fit follows a non-linear analytical fit of the form $\lambda_{\text{PDAS}} \propto \Delta^{k_1}$. Error bars indicate the maximum and minimum array stability limits.

period of time, see Fig. 7.5. For the present study, the primary dendrite arm spacing λ_{PDAS} is calculated by averaging the number of primary arms across the computational domain under steady state conditions. The possible range with minimum and maximum limits of the primary arm spacing is also included in Fig. 7.6. If the spacing is too wide and greater than the maximum stability limit, a tertiary arm catches up the front and

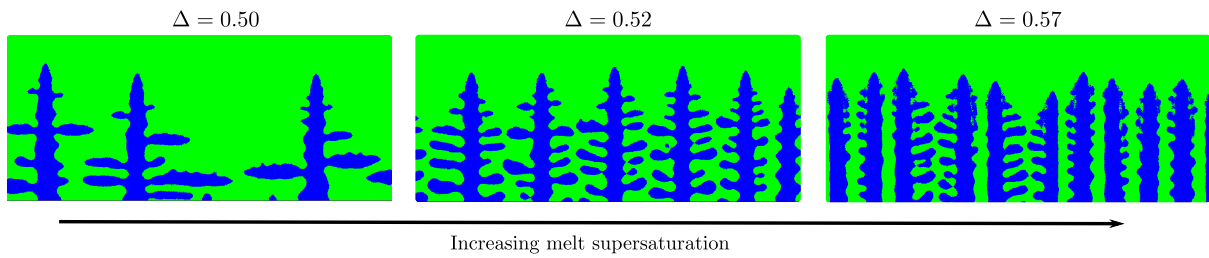


Figure 7.7: Primary dendrite morphology under various growth conditions. The inter-dendritic spacing decreases with an increase in the imposed melt supersaturation. Amplified secondary arms diminish as the primary arm spacing decreases.

becomes a new primary arm. Correspondingly, when the spacing is too narrow for cells and dendrites, a slightly smaller member of the array gets smaller and becomes overgrown by its neighbours. From the above discussion it is now clear that the lower and upper array stability limits depends on the inter-dendritic interactions, and the allowable range of spacing limits can be predicted by the inter-dendritic solutal distribution ahead of the foremost interface. This physical feature is in agreement with the primary dendrite arm spacing studies by Warren-Langer stability [35] and Hunt-Lu multi-dendrite model [50].

7.2.2 Effect of computational domain size

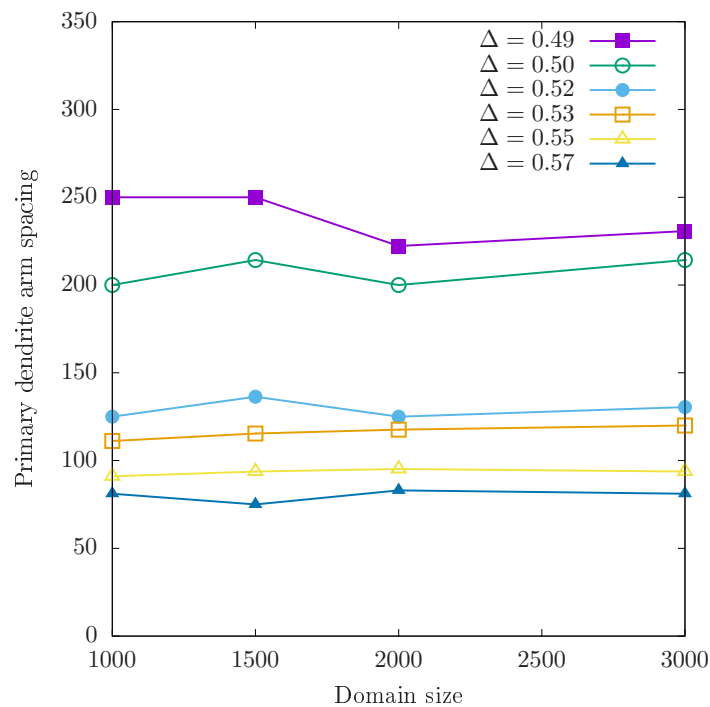


Figure 7.8: Effect of domain size on the spacing selection of primary dendrites.

Several numerical and experimental studies [35, 212–214] have reported that the ini-

tial spacing evolution determines the selection of the final primary arm spacing. Inherent to alloy melts, thermal fluctuations are generally weak to affect the dynamics of pattern formation. However, they do have an important role in situations where the perturbations become amplified to a macroscopic scale by intrinsic linear instabilities. It was also concluded that the primary arms observed in experiments must depend on the sample preparation, and thereby the dendritic spacing must be history dependent [212, 213]. Likewise, because of the lateral boundaries, the transient spacing adjustment process and the steady state selection in the present study are affected by the domain size. Henceforth, several simulations are performed with different domain sizes, and the variation of the primary dendrite arm spacing is determined, see Fig. 7.8, where it is observed that the PDAS is less sensitive to domain sizes as the melt supersaturation in the liquid phase increases. Even though big simulation domains promote large scale interfacial perturbations along the planar interface, the primary arms adjust themselves such that the final configuration is proportional to the imposed growth conditions. From these results, it is now clear that the prediction the primary dendrite spacing at a given melt supersaturation means that there exists a range of growth velocities over which a given primary dendrite arm spacing is stable.

7.2.3 Secondary dendrite arm spacing

The dominant morphological features of a dendritic network are the primary arm spacing, the secondary dendrite arm spacing SDAS, and the dendrite tip radius. In general, once the primary arm spacing is established in a system, it does not change during or after solidification. Nonetheless, during the course of solidification, the secondary arms undergo a ripening process [211], whereby, the secondary dendrite arm spacing determines the microsegregation pattern as well as the cooling rate of cast alloys. Several experimental studies on secondary dendrite spacing have been carried out, for example, Sharp and Hellawell [215] studied the secondary dendrite arm coarsening in the Al-Cu system. It was suggested that the initial secondary dendrite spacing may be of the order of twice the dendrite tip radius. For metallic systems, the ripening phenomenon in secondary arms was observed experimentally through examining the microstructure after a period of steady-state growth [216]. Thereafter, the rate of coarsening was limited by the rate of mass diffusion in alloys, and the SDAS was related to solidification time by a kinetic law of the form $\lambda_{\text{SDAS}}^3 = K_{\text{SD}}t$, where λ_{SDAS} is the average secondary dendrite arm spacing and K_{SD} is the materials constant [217]. Generally, the secondary dendrite arm spacing is manually measured on micrographs, which involves counting the number of secondary arms that intersect a straight line drawn along a primary dendrite arm [218]. In the present section, the secondary dendrite arm spacing (SDAS) is measured by the most common methodology, namely, the linear intercept method. As reported and suggested in an earlier study [218], the SDAS was measured using the following equation

$$\lambda_{\text{SDAS}} = \frac{L_{\text{PA}}}{N_{\text{SA}} - 1}. \quad (7.1)$$

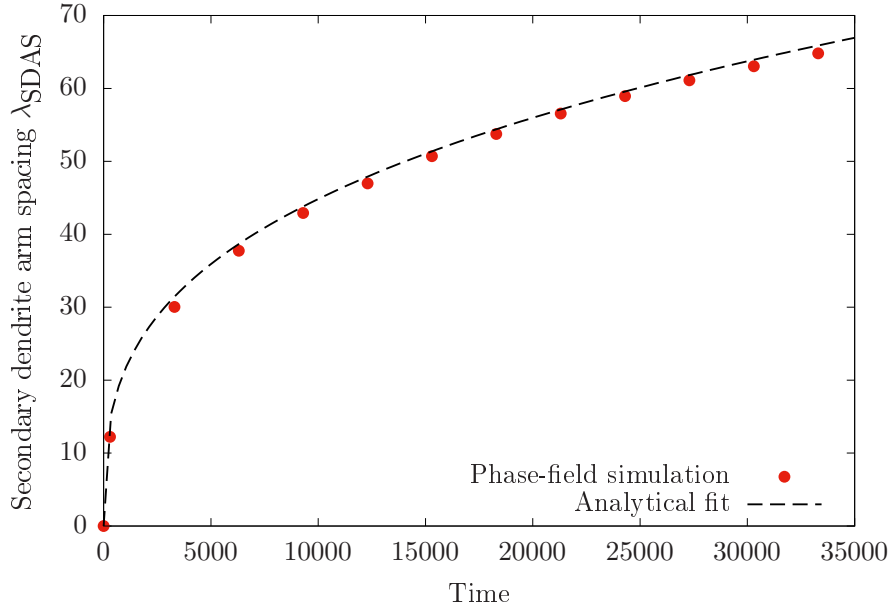


Figure 7.9: Measured secondary dendrite arm spacings as a function of solidification time. The non-linear analytical fit provides us with the relationship $\lambda_{\text{SDAS}} \propto t^{0.32}$.

Here, L_{PA} is the length of the primary arm dendrite and N_{SA} represents the total number of secondary dendrites along the primary arm. Fig. 7.9 illustrates the secondary arm spacing with time, where at short times there is a single relationship of the form $\lambda_{\text{SDAS}} \propto t^{0.32}$. Furthermore, from a morphological point of view, this process of back diffusion is further complicated by the coarsening of secondary and higher order arms as observed by Kattamis [219], whereby the smaller arms dissolve into the melt and solid is effectively transferred to the larger arms. The melting of small arms dilutes the composition of the liquid phase and thus contributes indirectly to homogenization [220]. Besides, in the absence of any convective transport, a symmetric nature of the secondary arms across the dendritic array is noticed in Fig. 7.10.

Next, the secondary arm spacing is calculated in a similar manner for different growth conditions, and a scaling law between λ_{SDAS} and Δ is established. As shown in Fig. 7.11, the SDAS decreases with the increase in the alloy melt supersaturation. This behavior is consistent with previous experimental and numerical studies [216, 221, 222], where the secondary arm spacing was reduced as a result of increasing driving force in the liquid. Nonetheless, while the secondary arms are always arranged linearly along the primary arm, the two-dimensional calculation in the present section gives us a good estimation for the arm spacing in three-dimensions.

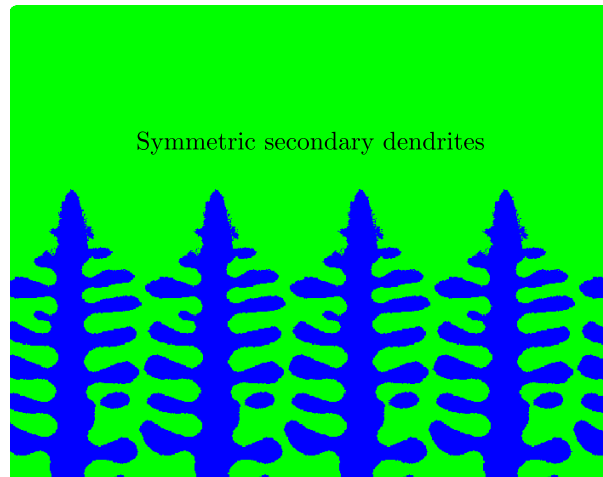


Figure 7.10: Formation of symmetric secondary dendrites under diffusive regime.

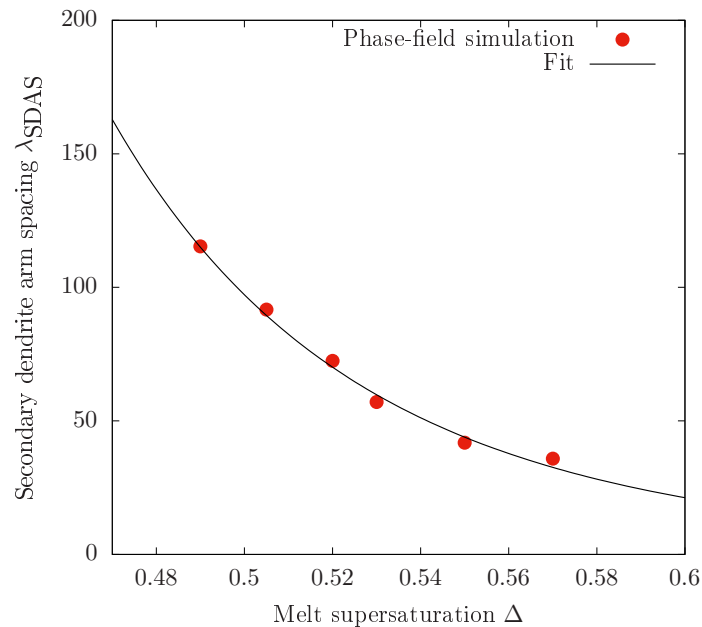


Figure 7.11: Secondary dendrite arm spacing as a function of melt supersaturation. Inter-dendritic spacing decreases with an increase in the melt supersaturation. The best fit follows a non-linear analytical fit of the form $\lambda_{SDAS} \propto \Delta^{k_3}$.

7.3 Primary dendrite arm spacing under diffusive-convective regime

7.3.1 Selection mechanism

In the present section, the prediction of inter-dendritic spacing under the influence of melt convection is studied, where the direction of melt flow is perpendicular to the axisymmetric dendritic growth direction. At an imposed convection velocity $U_x = 0.45$, the

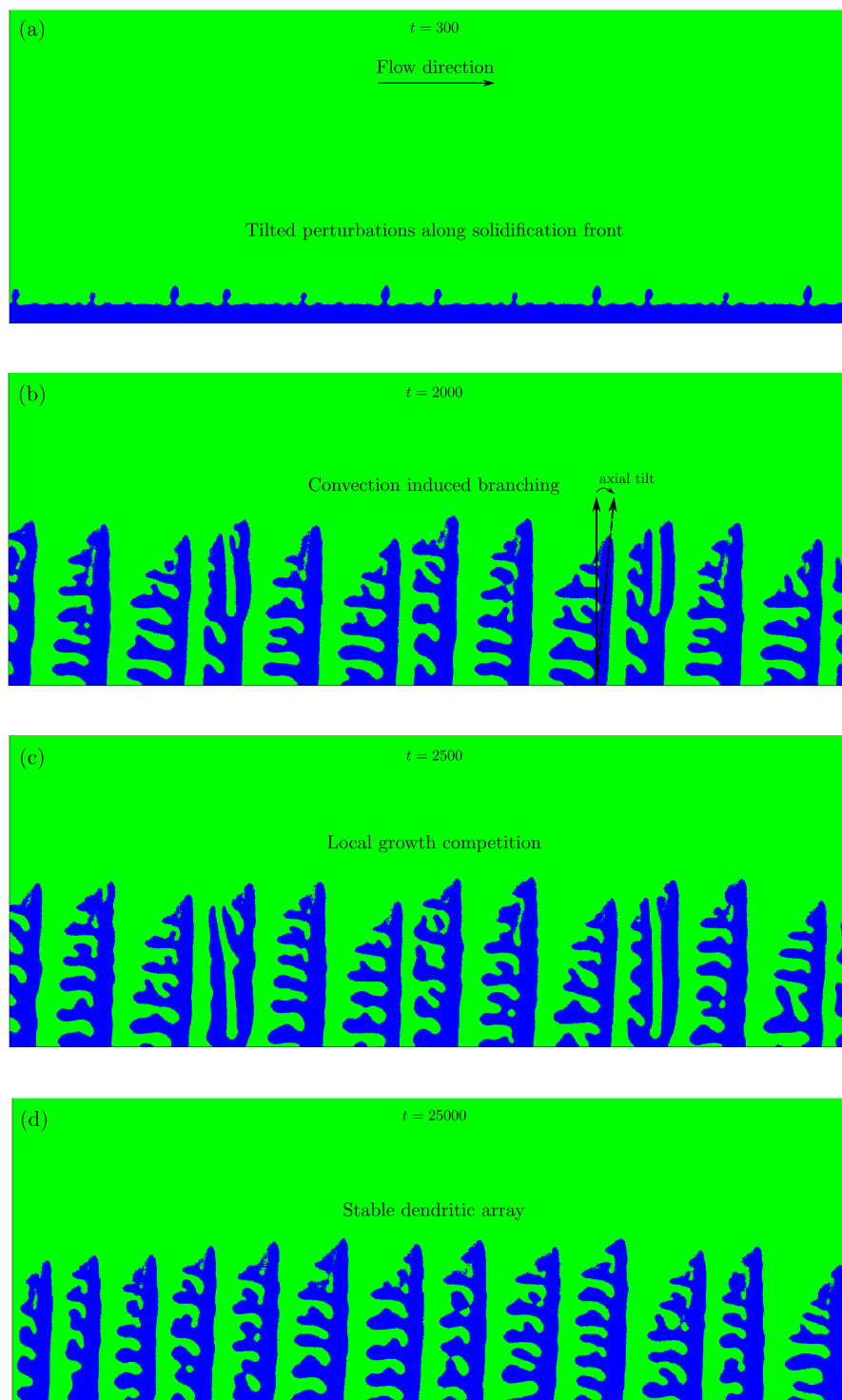


Figure 7.12: (a)-(d) Primary dendrite arm spacing with solidification time, where inclined perturbations develop along the solid-liquid interface as a result of lateral convection. Presence of strong convective transport mechanism enhances the splitting of dendritic tips, which in turn modify the selection mechanism of the primary dendrite array. Formation of a stable dendritic array under the influence of melt convection, where secondary branches are biased along the upstream (left) direction only as result of convection driven solute enrichment in the interdendritic spaces.

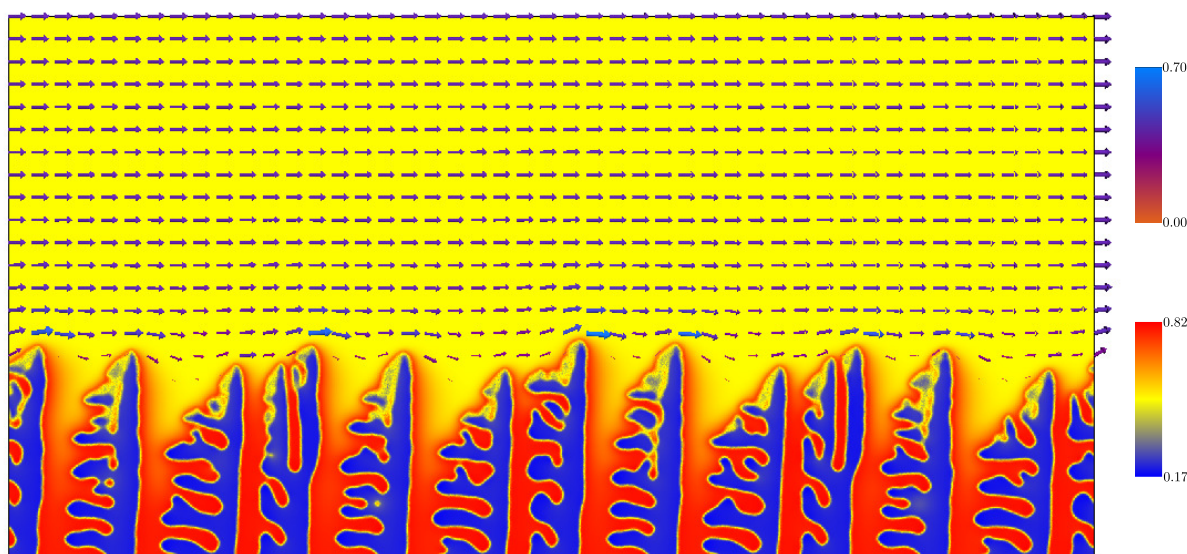


Figure 7.13: Concentration and velocity fields near a dendritic array under diffusive-convective conditions. Strong convective transport near the dendritic tip stimulates the tip splitting instability to modify the selection mechanism of primary dendrite arm spacing. The side branches also undergoes splitting to generate isotropic seaweed type branches.

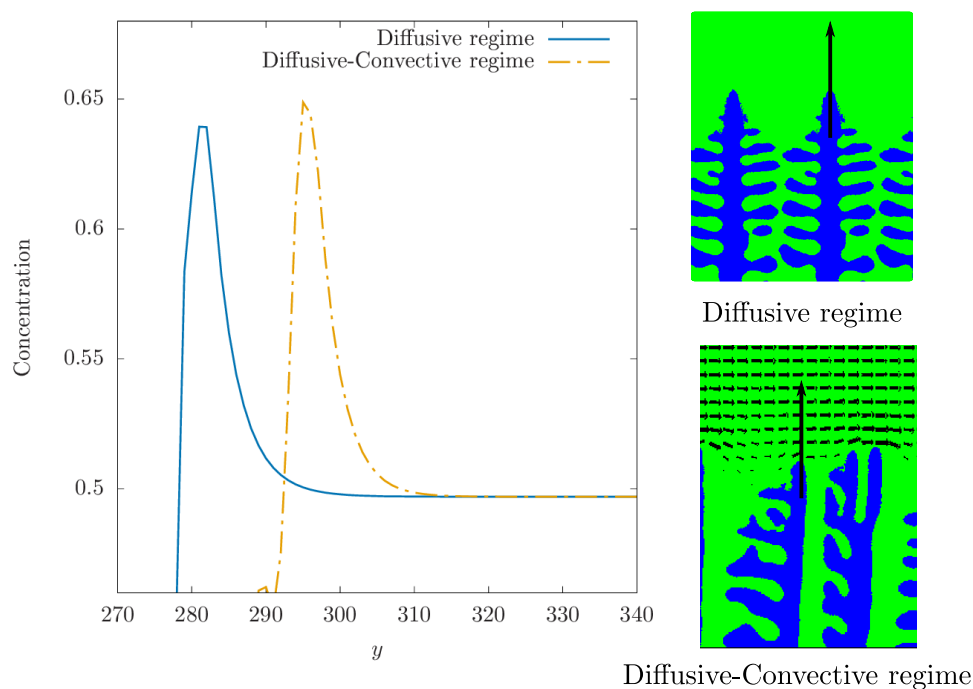


Figure 7.14: Comparison between solutal profiles near the foremost dendritic tip under diffusive and diffusive-convective regime. The presence of strong concentration gradients assist tip-splitting driven selection mechanism of primary arms.

spatiotemporal evolution of the dendritic array is depicted in Fig. 7.12(a)-(d), wherein the primary arms developed along a planar interface front transform into a steady state

dendritic array. As a result of an additional convective transport mechanism in the bulk liquid phase, it is discovered that the solutal fields near the dendritic tips as well as the inter-dendritic interaction are completely affected, see Fig. 7.13. Similar as in the earlier sections, the Mullins-Sekerka instability [30] initiates the amplification of random perturbations along the length of the planar interface. However, from the initial stages of solidification itself and as depicted in Fig. 7.12(a), the perturbations evolve towards the downstream direction (right boundary). Since the rejected solute at the boundary layer is swept away by the imposed convection velocity, an axial tilt of the primary arms is noticed throughout the later stages of directional solidification, see Fig. 7.13(b). This tilting behavior is consistent with previous numerical and experimental studies [85, 223], where the imposed lateral flow modified the axial orientation of the primary arms. As shown in Fig. 7.12(c), the presence of convective solute flow nearby the dendritic array enhances the solutal gradients, and encourages the secondary branches arms to grow into new primary dendrites. This behavior is captured through the comparison of one-dimensional solutal fields near the foremost dendritic tip. Depicted in Fig. 7.14, the steeper diffusion length near the primary arm tip promotes the dynamic branching of the tips, and consequently new dendritic arms are developed in order to maintain the stability limit of the primary arm spacing. Afterwards, due to flow-induced solutal gradients near the axisymmetric dendrites, the selection mechanism of the primary dendrites under diffusive-convective regime is modified by the successive branching of secondary arms developed along the upstream direction.

Similar as to pure diffusive conditions, the primary arm spacing is calculated at various melt supersaturations and the relation between PDAS and Δ in the presence of melt convection is shown in Fig. 7.16, and the best fit follows an analytical relationship $\lambda_{\text{PDAS}} \propto \Delta^{k_2}$, where the exponent $k_2 = -9.8$. When compared with the primary dendrite arm spacing under diffusive conditions, it is observed here that the PDAS decreases, and the magnitude of the exponent k_2 is also smaller than for diffusive regime. It is also important to note that the primary arm spacing under diffusive-convective regime is smaller than the minimum array stability limit for approximately all growth conditions. Thereby, although the primary arms attain a stable configuration, the generation as well as the amplification of secondary arms for large supersaturations are completely inhibited. Furthermore, the PDAS as a function of solidification velocity R is also depicted in Fig. 7.15, where the non-linear fit also follows the scaling law of the form $\lambda_{\text{PDAS}} \propto R^{a_2}$. As well as the proportionality constant, the exponent a_2 decreases when compared with the exponent a_1 under pure diffusive regime. When the solidification velocity is small, the interface movement is controlled by the presence of a large solutal diffusion boundary layer ahead the dendritic tip. Subsequently, with the increase of the interface velocity, the solutal boundary layer becomes thinner and thinner, which sequentially results in decrease in the arm spacing. From the simulations, it can be elucidated that the secondary branches grow opposite to the flow direction, and thereby establish a tertiary arm. As a consequence, a

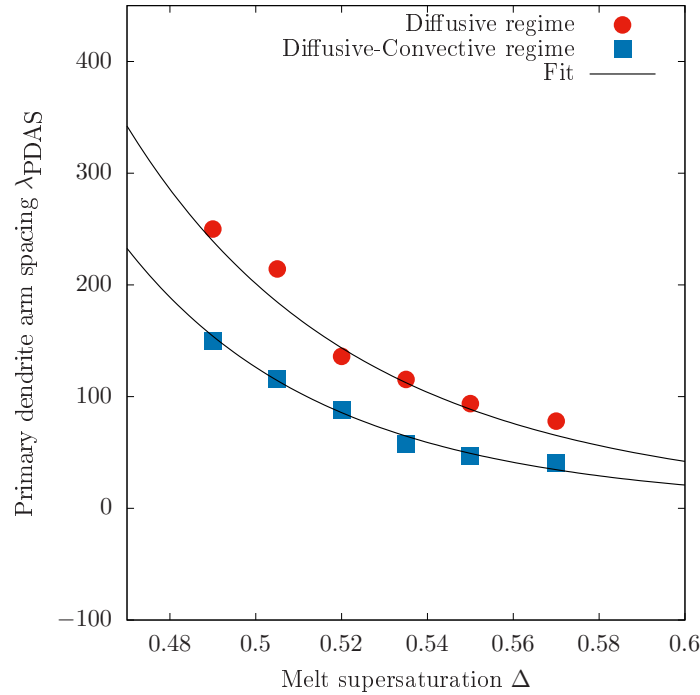


Figure 7.15: Primary dendrite arm spacing as a function of melt supersaturation under diffusive-convective regime. Inter-dendritic spacing decreases in the presence of lateral melt convection. The best fit follows a non-linear analytical fit of the form $\lambda_{PDAS} \propto \Delta^{k_2}$. When compared with diffusive regime, the exponent decreases $k_2 < k_1$.

new primary stem is generated to systematically reduce the primary dendrite arm spacing. Therefore, based on the series of two-dimensional simulations, it can thus be concluded that the introduction of lateral convection in the bulk alloy melt modifies the selection mechanism of a dendritic array, and the primary dendrite arm spacing decreases when compared with pure diffusive conditions.

The present observation is in complete agreement with an experimental study [224], where it was concluded that the magnetically driven melt created an inter-dendritic flow, which subsequently carried the enriched solutal liquid through the mushy zone. Later, the primary dendrite arm spacings were fitted with the Hunt and Lu [50] theory, and the best fit scaling law elucidated that the primary arm spacing systematically decreased as the solidification velocity was increased. Furthermore, simulations with $U_x < 0.45$ have also shown that due to the presence of weak convection velocities in the melt, the primary dendrite arms spacing is unaffected. Similarly, while Sharp and Hellawell [215] concluded that the alloy composition has little effect on the prediction of primary dendrite arm spacing, Spittle and Lloyd [225] found that for steady-state growth under low temperature gradients, the primary arm spacing decreased as the alloy concentration was increased in the liquid phase. It was also concluded that the experimental observations were independent of alloy composition for high temperature gradients. Nevertheless, in many cases it was assumed that the inter-dendritic spacing decreased as the alloy

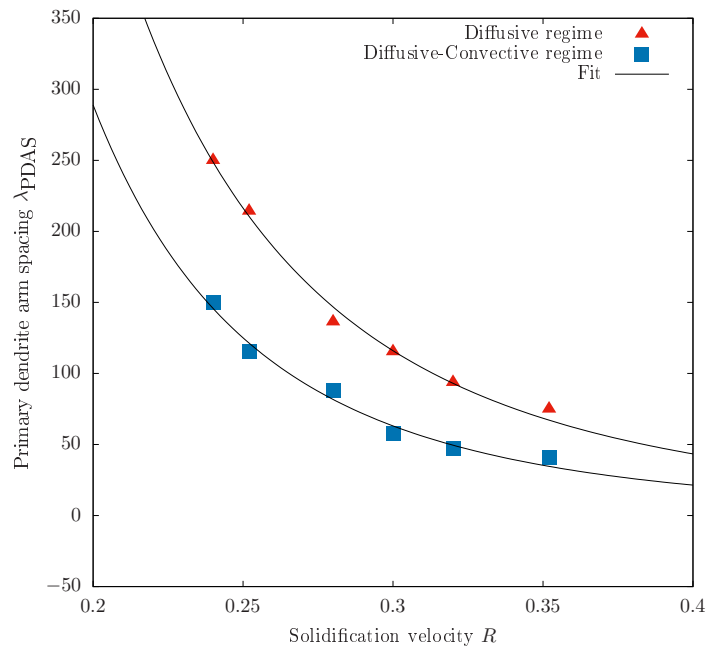


Figure 7.16: Primary dendrite arm spacing as a function of solidification velocity under diffusive-convective regime. Inter-dendritic spacing decreases in the presence of lateral melt convection. The best fit follows a non-linear analytical fit of the form $\lambda_{PDAS} \propto R^{a_2}$. When compared with diffusive regime, the exponent decreases $a_2 < a_1$.

concentration increased for any growth condition [61, 226].

7.3.2 Morphology of secondary dendrites

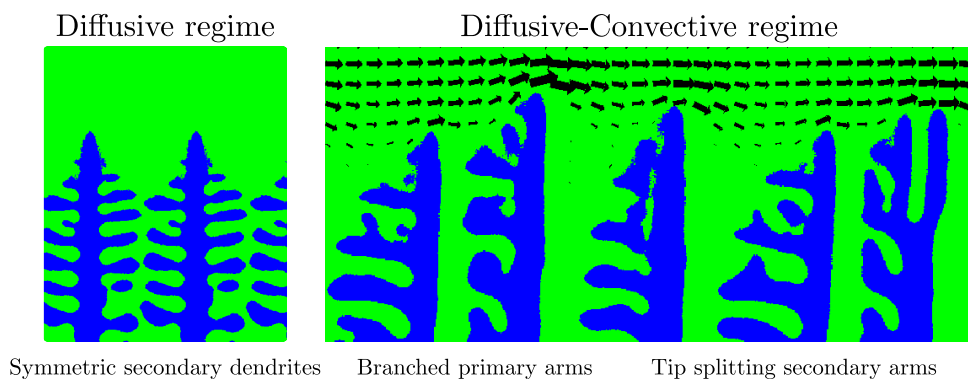


Figure 7.17: Comparison of secondary dendrite morphology under diffusive and diffusive-convective regimes. Symmetric side branches transform into an asymmetric morphology as a result of convective transport in-between the inter-dendritic spaces. Convection induced tip splitting generates new primary arms.

From the stable dendritic array, the most notable effect is observed through the development of asymmetric secondary arms along the primary trunks. As a result of non-uniform distribution of the solute concentration between the inter-dendritic spaces, the

secondary arms amplify along the upstream direction. Shown in Fig. 7.17, the high solute concentration at the downstream side of the dendrites inhibits the formation of secondary branches, thereby altering the microstructural characteristics of a cast alloy [224]. Fig. 7.17 also depicts the distinct characteristics of secondary branches when compared with the primary dendrite morphology under diffusive. In accordance with the present observation, the formation of asymmetric side branches was reported by Shevchenko et al. [85], wherein the solute accumulation was caused by the obstructed of solute drain off via forced flow. It was also concluded that the melt flow perpendicular to the growth direction provokes a preferential growth of the secondary arms at the upstream side. Moreover, it is also important to note that the morphology of the secondary arms also depends on the direction of melt flow.

In Chapter 6, the formation of tip splitting microstructures was attributed to systems with isotropic interfaces. The ramified pattern underwent tip splitting alternatively to generate a degenerate seaweed microstructure. In the present scenario, even for an anisotropic columnar dendrite there exists a possibility to observe the branching mechanism in the presence of convective transport near the dendrite tip. As shown in Fig. 7.17, the isotropic behavior of secondary arms is enhanced by the curl of the convective forces near the solid-liquid interface. From an imposed anisotropic strength $\delta_{\alpha\beta} = 0.03$, under the cooperative effect of diffusive and convective transport near the primary dendrite tip, the side branches transform into a frequent tip splitting structure along the inflow direction. After an initial branching event, the side branch now develops towards the direction of its steepest gradient, and thereafter transform into a tip-splitting branch with coarsening. Lastly, this phenomenon is noticed only in the upper range of the stability limit, where the inter-dendritic spacing is wide enough for the secondary arms to evolve perpendicular to the primary branch.

7.4 Summary

In this chapter, the prediction of primary dendrite arm spacing is investigated under the cooperative effect of diffusion and convection in the liquid phase. Firstly, under pure diffusive regime, it has been established that there exists a wide allowable range of primary dendrite spacing for a given set of growth conditions. The selection mechanism of primary stems is driven by the *dendritic submerging instability* limit at the minimum rather than the *branching instability*. Besides, the microstructural evolution from the onset of planar instability during directional solidification can be divided into three stages: an initial competition stage, a submerging stage and a lateral adjustment stage. It is shown that the primary dendrite arm spacing decreases with the increase in the melt supersaturation, and a scaling law of the form $\lambda_{PDAS} \propto \Delta^{k_1}$ is established. Next, the coarsening behavior of secondary arms is captured which follows the well known kinetic

law. In addition, the calculated secondary dendrite arm spacing also decreases with the increase in the alloy composition in the liquid phase.

The role of liquid phase convection is also studied, where it is observed that the inter-dendritic arm spacing decreases with an increase in the melt supersaturation. Similar to as pure diffusive conditions, a scaling law is established, where the exponent appreciably decreases $k_2 < k_1$ when compared with pure diffusive conditions. The submerging and the overgrowth mechanism of the dendritic arms are analyzed via the inter-dendritic solutal distribution. From the numerical results it is concluded that the presence of an additional mass transport in the bulk liquid phase advects the solute near the dendritic tips, which in turn modifies the selection mechanism of the primary dendrites. The present numerical results suggest that the convection-drive selection mechanism is a dominant regime at $U_x = 0.45$ and if is chosen larger, the selection mechanism of PDAS is dominated by branching instability along the upstream direction. Furthermore, the morphology of secondary dendrites is significantly different for simulations with and without convection. The symmetric amplification of the side arms translates into an asymmetric growth along the upstream direction in the presence of lateral convection. Moreover, due to the presence of convective rolls in the inter-dendritic spaces, a seaweed type behavior of the secondary arms is also captured.

In casting processes, randomly oriented seeds nucleate first on the chill casting surface, and later grow along their preferred crystalline orientations in the shape of columnar dendrites. Since the competitive growth of multiple grains with different orientations has a profound influence on the final microstructure as well as on the segregated pattern [72], the inter-dendritic growth competition is addressed in detail in the forthcoming chapter.

Chapter 8

Prediction of inter-dendritic growth competition

Over the last few decades the unidirectional solidification of metallic alloys has garnered interest in industrial as well as in scientific domains [227, 228]. Especially, in the form of single-crystals, high performance materials have been routinely produced through the directional solidification of Ni-based super alloys. Depending upon the interplay between heat and solute, a wide range of oriented dendritic grains are produced. In polycrystals, the misaligned dendrites typically interact and compete with each other to affect the microstructural and crystallographic hallmarks of a cast alloy, and thereby a competitive growth between various oriented grains is a key factor to obtain the desirable texture. In the presence of a grain boundary, the dendritic sidebranches may become new primary dendrites, making sidebranching the principal mechanism for the creation of new primary spacings, and hence for the selection of inner grain structure. Moreover, the dendritic growth competition determines which of the two grains will occupy the liquid space in between the two crystals, and thereby governs the shape of the resulting GB. In order to improve the applicability, and to understand the microstructural evolution, it is important to investigate the mechanism of grain selection in columnar dendrites. In this regard, the inter-dendritic growth competition at a converging grain boundary under the cooperative effect of diffusion and convection is investigated in this chapter. *The results described in this chapter have been published in Computational Materials Science [10].*

8.1 Dendritic overgrowth theory

The classical overgrowth model by Walton and Chalmers [229] addressed the inter dendritic growth competition in converging and diverging crystals. Whenever two grains converged at the solid-solid grain boundary (GB), the overgrowth model predicted that a favorably oriented (FO) dendrite shall overgrow an unfavorably oriented (UO) dendrite.

Predominantly, the dendrites that evolve along the direction of heat flow are called as *favorably oriented* (FO) dendrites, and the dendrites that grow with a finite inclination with respect to the growth direction are called as *unfavorably oriented* (UO) dendrites, as diagrammatically illustrated in Fig. 8.1. It was suggested by Walton and Chalmers that the UO dendrites typically require a larger undercooling to keep up with the position of a FO dendrite, and thus the persistent lag of a misoriented UO dendrite results in the overgrowth of a FO dendrite. This widely accepted *conventional overgrowth model* was later reported by Rappaz et al. [230, 231], where an UO dendrite was sequentially blocked by the primary arms of a favorably oriented dendrite. Additionally, for diverging grains, the development of secondary and tertiary branches along the arms of FO dendrites was regarded as the deterministic factor to eliminate an UO dendrite arm.

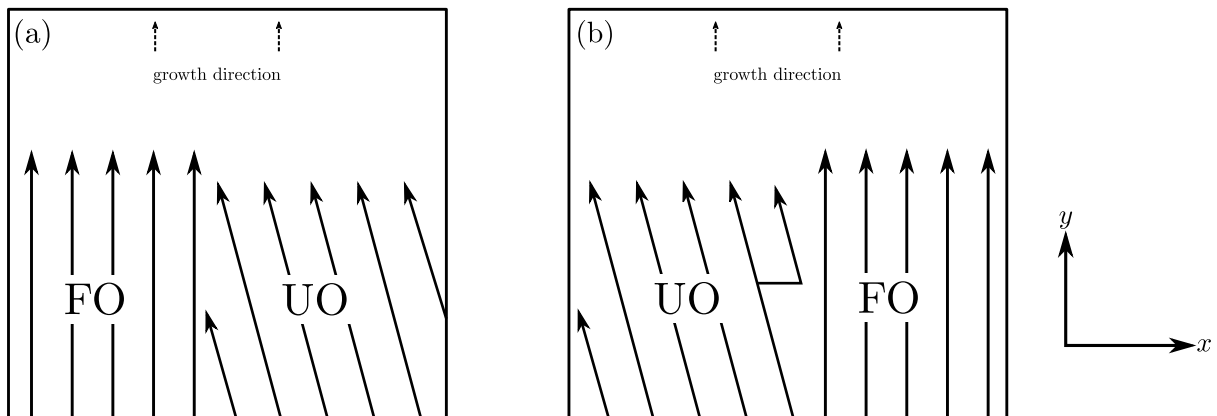


Figure 8.1: (a)-(b) A schematic illustration of converging and diverging dendritic growth competition at the grain boundary. In accordance with the Walton and Chalmers theory [229], a conventional overgrowth phenomenon is showcased where the favorably oriented (FO) dendrites overgrow the unfavorably oriented (UO) dendrites at the grain boundary.

8.2 Oriented dendritic array

Generally, the inter-dendritic growth competition is affected by several thermodynamic material parameters. Nonetheless, the main factors that affect the overgrowth behavior of columnar dendrites are briefly discussed. To begin with, the growth of a single dendritic array with different crystal orientations is studied, where the growth direction is misaligned when compared with the axial direction.

8.2.1 Role of tip undercooling

Since the leading dendritic tip with a small undercooling blocks the growth of an adjacent dendrite with a large tip undercooling, the variation of tip undercooling with crystal orientation angle is first investigated. In an supersaturated melt of composition $\Delta = 0.525$

and an anisotropic strength $\delta_{\alpha\beta} = 0.03$, the dendritic arrays with different misorientation angles are depicted in Fig. 8.2. As shown, the tip position of the dendritic array lowers as the misorientation angle of the dendritic array increases, and therefore, the undercooling at the tip position increases with the increase in the misorientation angle. Thereafter, in order to overgrow an aligned dendrite and dominate the inter-dendritic growth competition, the misoriented dendrites require a larger tip undercooling. However, the sole position of dendritic tips cannot explain the growth competition at the grain boundary.

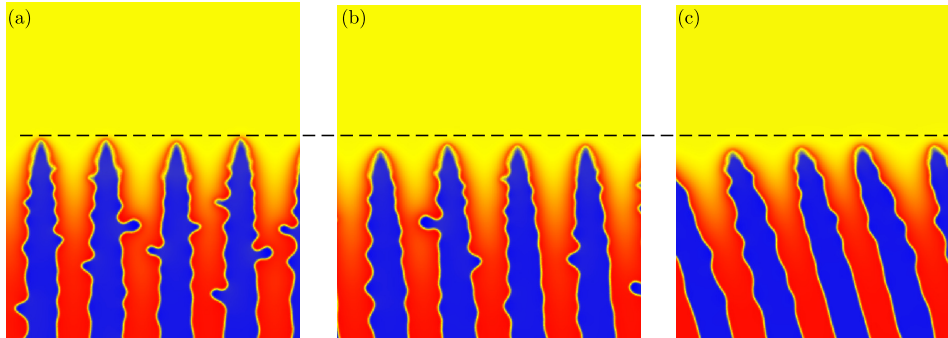


Figure 8.2: Dendritic morphologies with various misorientation angles (a) $\theta = 0^\circ$, (b) $\theta = 15^\circ$, (c) $\theta = 30^\circ$.

8.2.2 Role of inter-dendritic spacing

As discussed in the previous chapter, it is well known that the imposed melt supersaturation produces a wide range of inter-dendritic spacing along a solidifying interface. However, the study was limited to axis-symmetric primary dendrites only, and therefore in the present section, the variation of tip concentration for different inter-dendritic spacing and misorientations is shown in Fig. 8.3. In tune with an earlier experimental observation [232], our simulations have also indicated that the tip concentration decreases with large inter-dendritic spacing. It is important to note that for the tilted dendrites, the difference in the tip concentration is significant when compared with the aligned ones. Fig. 8.3 also indicates that when the spacing of the misaligned dendrite array is larger than that of the aligned one, its tip concentration can be smaller and its tip position can be higher. Nevertheless, it should be noted that these simulations are carried out for a single-oriented dendritic array, and therefore any conclusion remarking that the UO dendrite array with large spacing may be ahead of the FO dendrite that is obtained only by comparing the individual growth behavior of differently oriented dendrites is insufficient. A direct comparison with Fig. 8.1 also illustrates that the impingement of converging dendrites brings out new dynamics at the grain boundary. Henceforth, the prediction of the inter-dendritic overgrowth is incomplete by only analyzing the growth behavior of single grains, and hereafter systematic simulations of two converging dendritic arrays are needed to explore the manner of the overgrowth.

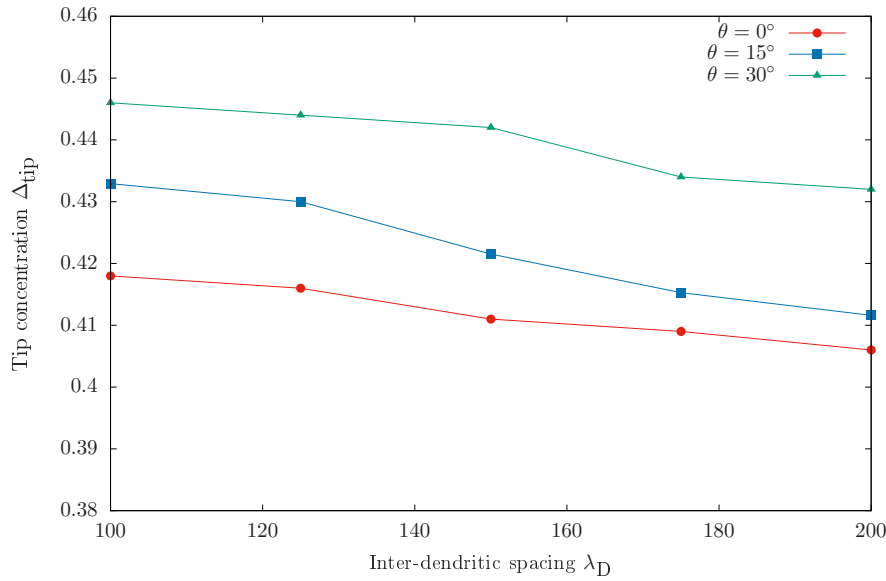


Figure 8.3: Variation of tip concentration with inter-dendritic spacing for different misorientation angles.

8.3 Growth competition in converging dendrites

The growth competition among converging dendritic grains is studied in this section, where the UO dendrite with a misorientation angle of $\theta_{UO} = 15^\circ$ is simulated. The competition of converging dendrites under different growth conditions is systematically analyzed so as to reveal the mechanism of grain selection in polycrystallites.

8.3.1 Initial and boundary conditions

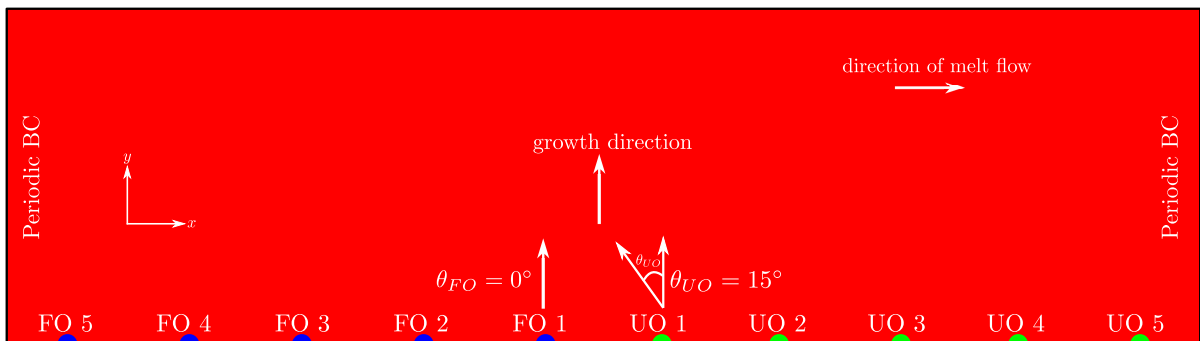


Figure 8.4: Schematic illustration of the simulation setup along with the imposed initial simulation and boundary conditions. Ten equidistant spherical seeds are initialized in a supersaturated melt of composition Δ . Here, the blue seeds are oriented favorably along the growth direction at $\theta_{FO} = 0^\circ$, whereas, the unfavorably oriented seeds green in color are misoriented at $\theta_{UO} = 15^\circ$ in the anticlockwise direction.

As shown in Fig. 8.4, a computational domain of $1000\Delta x \times 750\Delta y$ numerical cells is selected for the present chapter. As an initial condition and in a uniformly supersaturated melt of composition $\Delta = 0.525$, the phase-field simulation starts with 10 equidistant spherical seeds at the bottom of the computational domain with the simulation parameters shown in Table. 8.1. Depicted in blue and green colors in Fig. 8.4, the first five seeds are named as favorably oriented (FO) dendrites with $\theta_{FO} = 0^\circ$, whereas, the next five seeds are called unfavorably oriented (UO) dendrites, inclined at $\theta_{UO} = 15^\circ$ in the anticlockwise direction with respect to the growth direction. In this study, the crystal orientation along the y -direction is defined as $\theta_0 = 0^\circ$ and the anticlockwise direction is always taken as positive. Moreover, based on their orientation and position, all the spherical seeds have been numbered accordingly in Fig. 8.4. As the present chapter explores the role of liquid phase convection, the initial distance between the spherical seeds is kept constant for all the simulations. Similar to previous chapter, the boundary conditions for the left and right side of the simulation domain is considered periodic for all the fields. The lateral flow is introduced from the left boundary wall and travels along the horizontal direction of the domain. Likewise, on the top and bottom sides, the Neumann boundary condition is applied for the phase and solutal fields, whereas, a slip condition is applied for the velocity fields. Additionally, a moving frame method [192] is applied whenever the total number of cells between the foremost solid-liquid interface and the top boundary is less than 450 numerical cells. Thereafter, for every simulation time step, the bottom cells along the growth direction are shifted downwards and cutoff. This methodology typically saves computational time, and also ensures that the concentration fields at the dendritic tips are unaffected by the imposed boundary conditions.

Table 8.1: Parameters to simulate inter-dendritic growth competition under diffusive-convective regime.

Description	Parameter	Value
Melt supersaturation	Δ	0.525
Anisotropic strength	$\delta_{\alpha\beta}$	0.03
Interface width	ϵ	4.00
Simulation Domain	$N_x \times N_y$	1000×750
Misorientation	θ_{UO}	15°
Discretized grid space	$\Delta x = \Delta y$	1.0

8.3.2 Inter-dendritic growth competition under diffusive regime

At first, a two-dimensional competitive growth of converging dendrites is simulated in pure diffusive regime. During the progressive solidification of a dendritic network in Fig. 8.5(a), it is observed that the favorably oriented dendrites overgrow the unfavorably

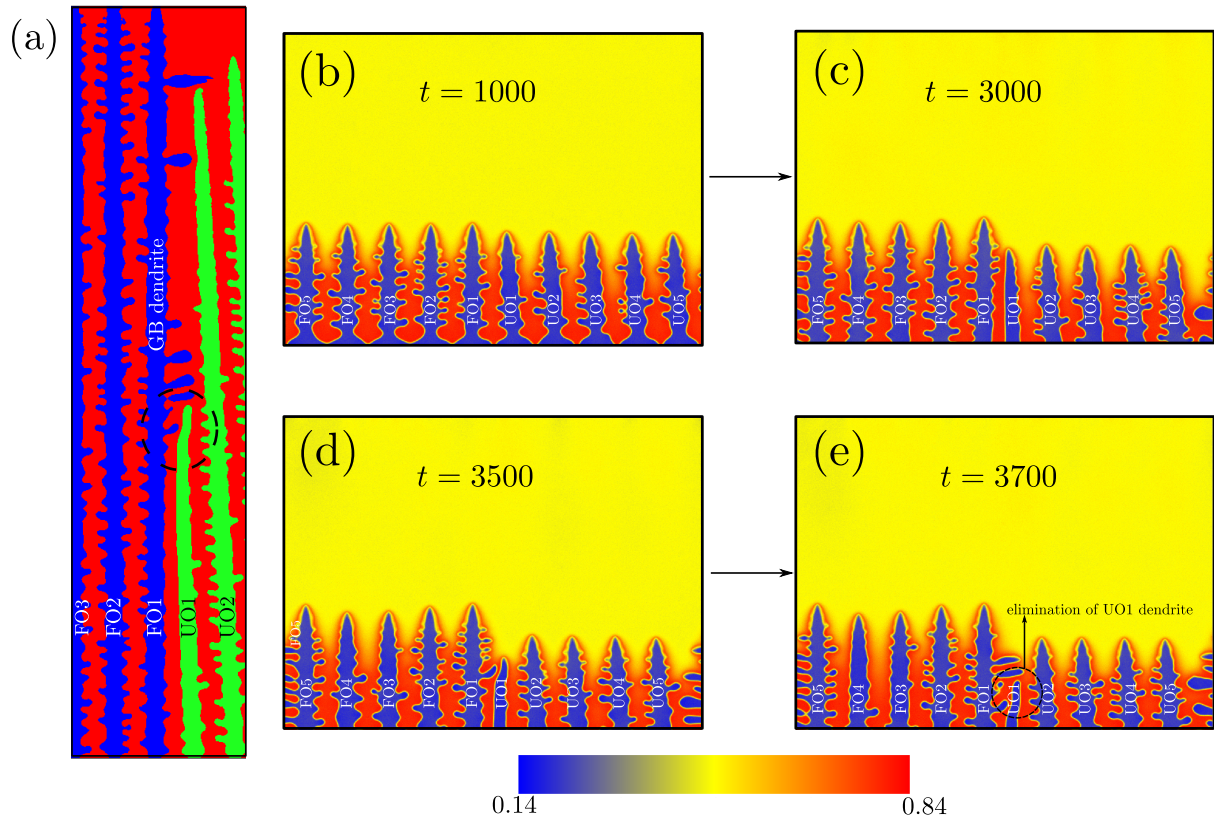


Figure 8.5: (a) Under pure diffusive regime, simulation screenshots demonstrate the growth competition of columnar dendrites converging at the grain boundary. The blue colored dendrites represent the favorably oriented dendrites, whereas, the green colored dendrites correspond to unfavorably oriented dendrite. (b)-(e) The temporal evolution of converging dendritic morphologies in a supersaturated melt, where the FO1 dendrite impinges and subsequently blocks the primary arm of the UO1 dendrite. This dendritic overgrowth at the grain boundary is commonly known as the conventional overgrowth phenomenon. Highlighted in Fig. 8.5(a), the dendrites that overgrow and dictate the growth process at the grain boundary are named as ‘GB dendrite’.

oriented dendrites over a period of time. The temporal evolution of the concentration fields in Fig. 8.5(b)-(e) depicts the overgrowth mechanism of columnar dendrites converging at the grain boundary. At $t = 1000$ in Fig. 8.5(b), it is found that the tip position of the dendrite UO1 is already behind the FO1 dendrite. As the solidifying front advances, the dendrite FO1 migrates towards the UO1 dendrite without producing amplified secondary arms, such that the GB orientation remains in parallel to the FO1 dendrite. Subsequently, the inter-dendritic spacing decreases and the position of the UO1 dendrite tip rapidly descends. After the elimination of an unfavorably oriented primary arm at $t = 3700$, the dendrite FO1 now becomes a GB dendrite, as schematically denoted in Fig. 8.5(a). Such an overgrowth phenomenon usually happens due to the overlap of the concentration fields at the solid-solid grain boundary and the difference in the tip undercooling between the FO1 and UO1 dendrites. Since the position of the tips differ and the lag of a misaligned dendrite is significant, the UO1 dendrite is always blocked by the primary arm of the FO1 dendrite. Besides, as reported recently by Takaki et al. [76], the rate of elimination of an UO dendrite also increases with an increase in the orientation angle of UO dendrites. From a morphological point of view, the simulated inter-dendritic structure at the grain boundary is completely in agreement with an experimental micrograph [68].

The present observation in Fig. 8.5, commonly known as the conventional overgrowth phenomenon is corroborated by the classical dendritic overgrowth theory of Walton and Chalmers [229], where the FO dendrites overgrew as a consequence of low undercooling at the tip position. Furthermore, as described by Li et al. [71], the conventional overgrowth phenomenon is also independent of the inter-dendritic seed spacing. Since the lateral migration of an UO dendrite is principally towards the FO dendrite, its spacing with an adjacent dendritic neighbour decreases, and thereafter the misoriented dendrite is invariably blocked at the grain boundary.

8.4 Growth competition under diffusive-convective regime

In the present section, the microstructural evolution of converging dendrites is systematically investigated under the cooperative effect of diffusion and convection in the liquid phase, where the direction of melt flow is perpendicular to the dendritic growth direction. The first two microstructures in Fig. 8.6 represent the competitive growth of converging columnar dendrites at low melt velocities, from $U_x = 1.5 \times 10^{-1}$ to $U_x = 1.5 \times 10^{-1}$, where U_x is the magnitude of convection velocity along the x -direction. Similar as in the previous section, from the outset, the FO1 dendrite primary arm blocks the UO1 dendrite, and appropriately dominates the inter-dendritic growth competition. This impingement

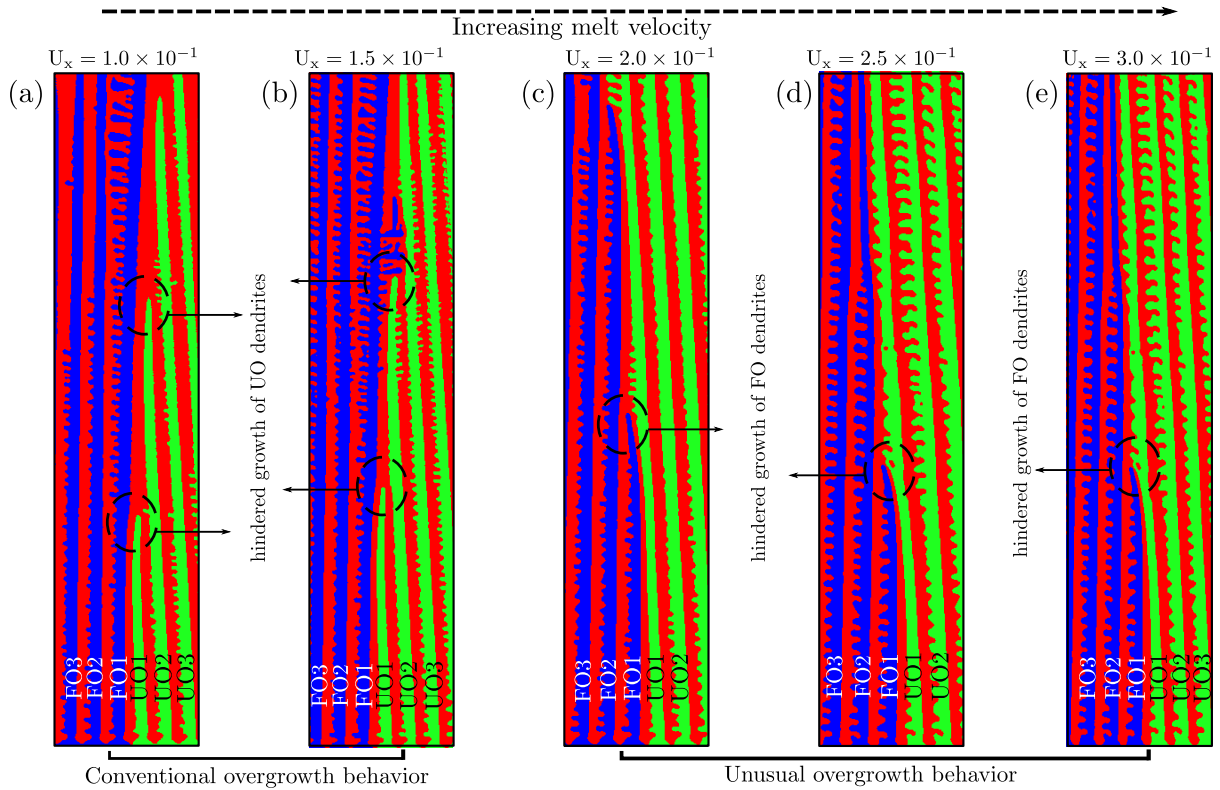


Figure 8.6: (a)-(e) Competitive growth of columnar dendrites under the influence of melt convection converging at the grain boundary. The conventional overgrowth behavior transforms into an unusual overgrowth behavior as the convection velocity gradually increases. (a)-(b) While the FO1 dendrite arm dominates the inter-dendritic growth competition upto $U_x = 1.5 \times 10^{-1}$, (c)-(e) the misoriented UO1 dendrite overgrows and sequentially eliminates the favorably oriented dendrites at high melt velocities. The lateral migration of the converging grain boundary towards the upstream direction (left direction) is observed for $U_x > 1.5 \times 10^{-1}$. The overgrowth events are highlighted schematically for each case.

of FO and UO dendrites at low melt velocities in Fig. 8.6(a)-(b) is associated with the conventional overgrowth phenomenon, and accordingly, the influence of velocity fields near the dendrite tips is marginally noticed, where the growth front deflects the primary trucks towards the downstream (right) direction, see Fig. 8.6(a)-(b). Since the evolution of the FO1 dendrite is controlled by the interfacial anisotropy under pure diffusive regime, the lateral tilt is completely absent. However, the presence of convective transport near the solidifying front tilts the FO1 dendrite arm along the flow direction. Corroborated by previous experimental and computational studies [85, 223], the solutal gradients are weakened as a result of an overgrowth event, and the solute distribution near the FO1 tip shifts entirely along the outflow (right) direction, thereby generating different tilting modes under diffusive-convective regime.

Next, as the convection velocity is increased, from $U_x = 1.5 \times 10^{-1}$ to 3.0×10^{-1} , the overgrowth behavior at the grain boundary is unconventional. As shown in Fig. 8.6(c)-(e), the unfavorably oriented dendrites with $\theta_{UO} = 15^\circ$ overgrow at the expense of FO dendrites. From Fig. 8.6(c)-(e), it is noticed that the primary arm of the UO1 dendrite converges at the GB and sequentially retards the growth of the FO1 dendrite. This anomalous behavior of dendrites in Fig. 8.6(c)-(e), namely, the *unusual overgrowth phenomenon* [66, 68], has been primarily observed in various experimental [64, 66, 68] and phase-field studies [71, 72, 76]. Recently, the in-situ findings of D'souza et al. [68] and Zhou et al. [66] concluded that a misoriented primary dendrite shall indeed overgrow at the expense of a well oriented columnar FO dendrite. The study argued and proposed that the solute interaction at the grain boundary plays a key role during the dendritic growth competition which was neglected in the earlier overgrowth models [229, 231, 233]. Based on the available literature, such an overgrowth transition in a bicrystal dendritic network in Fig. 8.6 has never been reported before, especially under the cooperative influence of diffusion and convection in the liquid phase.

The dendritic growth competition is further analyzed in Fig. 8.7, where the temporal volume fractions of favorably and unfavorably oriented grains are depicted. The dominance of favorably oriented dendrites in a conventional overgrowth phenomenon is depicted in Fig. 8.7(a), where the grain volume fraction diverges after the initial stages of columnar solidification. After the first overgrowth event at the grain boundary Fig. 8.7(a), the favorably oriented dendrites dominate the growth competition as a result of physically blocking the primary dendritic arms of UO dendrites. In contrast, due to successive unusual overgrowth events at the grain boundary, the volume fraction of an UO grain overtakes the FO dendritic grain in Fig. 8.7(b). Since the UO1 dendrite drifts towards the grain boundary to protrude a favorably oriented dendrite, the volume fraction of UO dendrite increases with time. Once the overgrowth mechanism is entrenched at the grain boundary, the GB dendrite dictates the growth competition. Furthermore, the lateral spacing between the UO1 and the FO1 dendrite tip position increases with the

misorientation angle such that the leading FO1 dendrite continuously blocks the lagging UO dendrites with time. As a result, the volume fractions of UO dendrites diverge immediately in a conventional overgrowth. Conversely, the solutal layer near the UO1 tip becomes thinner and the UO1 dendrite overcomes the leading FO1 dendrite in an unusual overgrowth model. In order to travel laterally towards the converging grain boundary and to overgrow a FO dendrite, the time taken by the UO1 dendrite increases, and therefore the temporal volume fractions diverge during the later stages of inter-dendritic growth competition. In both overgrowth behaviors, the diverging nature of volume fractions indicates the individual grain superiority during the inter-dendritic growth competition. Hereafter, for a polycrystalline solidification with several grains oriented with various misorientations, the dendritic growth competition can be predicted via analyzing the individual grain volume fractions at the grain boundary.

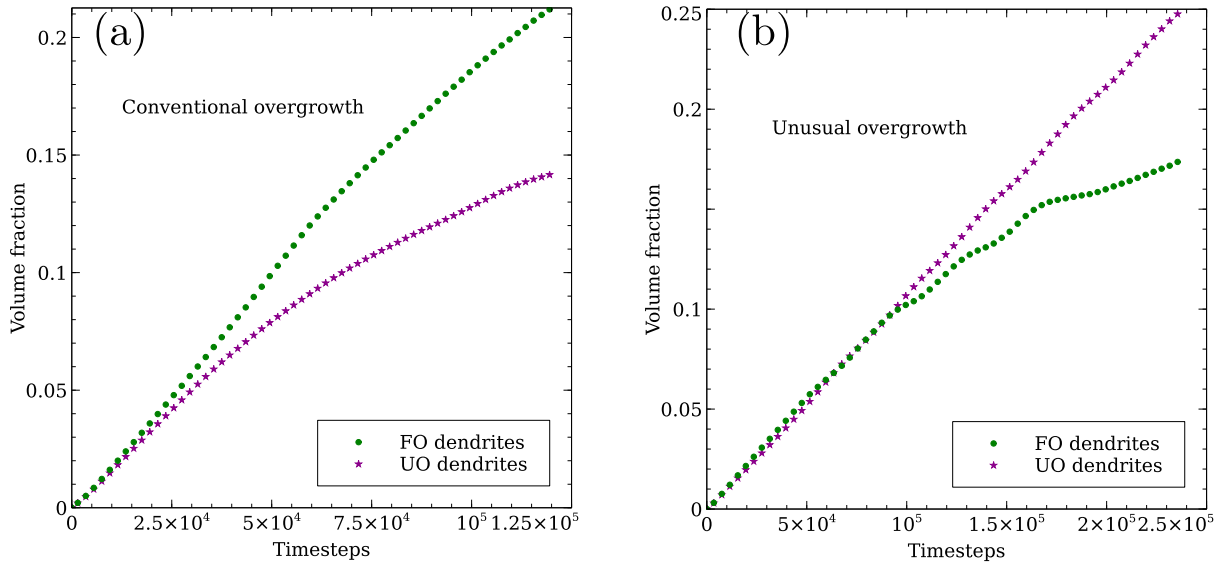


Figure 8.7: (a)-(b) Temporal volume fractions of favorably and unfavorably oriented grains at the grain boundary. (a) The diverging point for each case indicates the most preferred and dominant grain during the dendritic growth competition. FO dendrites dominate growth competition in a conventional overgrowth behavior, while the unfavorably oriented dendrites protrude consistently to outgrow the FO dendrites during an unusual overgrowth phenomenon at the grain boundary.

Likewise, from the present set of two-dimensional simulations, it is noteworthy that the minute secondary and tertiary branches play no major role in the overgrowth mechanism and thus far the imposed numerical noise has also no influence on the dendritic growth competition. Again, as mentioned in the previous section, the unusual growth phenomenon shown here does not depend on the inter-dendritic spacing and therefore a FO dendrite shall always be eliminated for conditions greater than the melt velocities $U_x > 1.5 \times 10^{-1}$.

8.4.1 Drift velocity

Whenever the misoriented UO1 dendrite travels laterally towards the grain boundary, the drift velocity of the primary arm is calculated as

$$V_d = \left| \frac{dx_t}{dt} \right| \quad (8.1)$$

where, x_t is the position of the UO1 arm along the x -axis, and t is the solidification time. As depicted in Fig. 8.8, an analytical fit provides us with a relationship $V_d^{\text{avg}} \propto \text{Pe}_f$, where, $\text{Pe}_f = U_x L / 2D_i^\beta$ is the flow Peclet number, the inter-dendritic seed spacing $L = 100$ is considered as the reference length and V_d^{avg} is the drift velocity averaged across the simulation time. For the present set of two-dimensional phase-field simulations, the inter-seed spacing is considered as the reference length, as it does not influence the results. As shown in Fig. 8.8, the average drift velocity of the UO1 primary arm increases linearly with an increase in the flow Peclet number. During a conventional overgrowth behavior, the FO1 overgrows at the grain boundary and the UO1 dendrite position significantly lags behind. Contrarily, a considerable increase in the average drift velocity with Pe_f indicates that the displacement of the unfavorably oriented primary arm towards the inflow direction is larger than its counterpart, which in turn translates to an unusual overgrowth event at the grain boundary. As solidification progresses along the y -direction, the UO1 dendrite lateral drift towards the regions of higher chemical potential gradients result in the systematic elimination of an individual FO dendrite at the grain boundary. This linear dependency of the drift velocity reaffirms that the advected solute near the solid-liquid interface has a significant role on the overgrowth behavior among converging dendrites.

8.4.2 Effect of misorientation angle of UO dendrites

It is important to note that the above set of two-dimensional simulations have been performed at a fixed misorientation angle $\theta_{UO} = 15^\circ$, and the critical velocity to predict the inter-dendritic overgrowth behavior depends on the inclination angle of the UO dendrites. In this regard, the effect of the misorientation angle of the unfavorably oriented dendrites is investigated in detail. In order to have a direct comparison, the total number of dendrites and the boundary conditions have been kept the same in the present section, and the misorientation angle of the unfavorably oriented dendrites is systematically modified.

A microstructural selection map is depicted in Fig. 8.9, wherein the inter-dendritic overgrowth behaviors are diversified over a wide spectrum of misorientation angle θ_{UO} and flow Peclet numbers Pe_f . As shown, the unusual overgrowth phenomenon is restricted to higher flow Peclet numbers and lower misorientation angles only. On the other hand, it is observed that the conventional overgrowth region increases with an increase in the inclina-

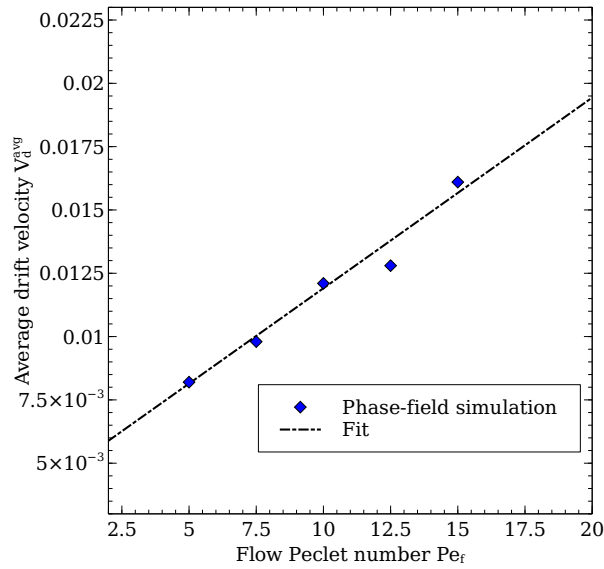


Figure 8.8: Calculated average drift velocity of UO dendrite arm as a function of flow Peclet number. As the flow Peclet number increases, a strong convective regime displaces the UO1 dendrite arm towards the solid-solid grain boundary. A linear fit follows the relation $V_d^{avg} = n_1 * Pe_f + n_2$, where n_1 and n_2 are proportionality constants.

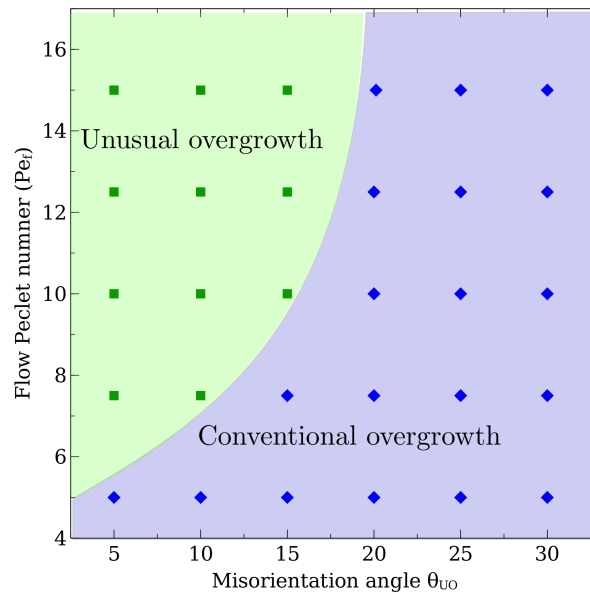


Figure 8.9: A microstructural selection map for various misorientation angles θ_{UO} and flow Peclet numbers Pe_f . The unusual overgrowth mechanism is limited within a narrow region only, and for $\theta_{UO} > 15^\circ$, the conventional overgrowth behavior dominates at the grain boundary. The transition between the two dendritic overgrowth mechanisms is sketched schematically, and does not represent a sharp division.

tion angle of the unfavorably oriented dendrites. As the imposed misorientation restricts the inclination of the UO1 dendritic tip towards the grain boundary, the inter-dendritic growth competition results in the elimination of an unfavorably oriented dendrite at the solid-solid grain boundary. Henceforth, the critical lateral melt velocity to predict the transition between the two dendritic overgrowth behaviors at the grain boundary increases with the increase in the misorientation angle θ_{UO} , and for $\theta_{UO} \geq 20^\circ$, the conventional overgrowth behavior is always observed at the solid-solid grain boundary.

8.5 Unusual overgrowth mechanism

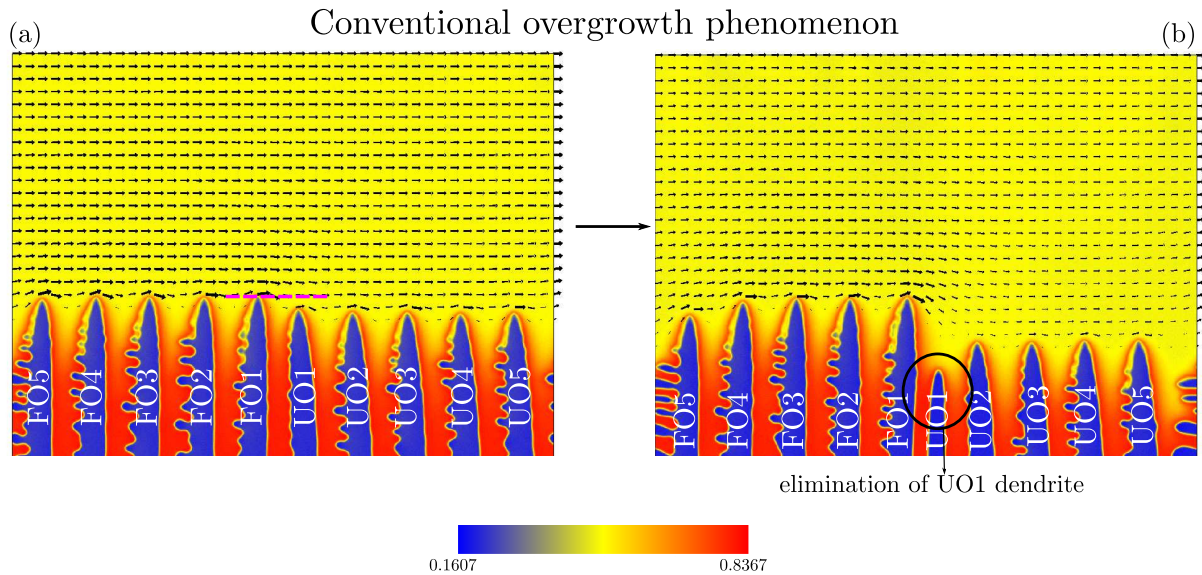


Figure 8.10: (a)-(b) For $U_x = 1.0 \times 10^{-1}$, the concentration and velocity fields during a conventional overgrowth event at the grain boundary. The FO1 dendrite impinges and eliminates the UO1 dendrite and undergoes the conventional overgrowth mechanism at the grain boundary. The size of the black arrows indicate the magnitude of the velocity fields. The dashed lines indicate the position at which the 1D concentration fields are extracted.

From the above two-dimensional phase-field simulations, it is evident that the liquid phase convection modifies the overgrowth mechanism at the solid-solid grain boundary. Therefore, in the present section, the unusual overgrowth phenomenon during the competitive growth of converging dendrites is analyzed in detail. Figs. 8.10 and 8.11 portrays the solutal and velocity fields of FO and UO dendrites at low and high convection velocities, respectively. Due to the presence of an additional convective mass transport in the bulk liquid phase, the amount of solute advected varies, and as illustrated at $t = 3000$, the solutal fields near the solidification front are different in Figs. 8.10(a) and Figs. 8.11(a). At $U_x = 1.0 \times 10^{-1}$, the FO1 dendrite is already ahead of the UO1 dendrite, and as the rate of evolution of the UO1 dendrite arm is much lower than the FO1 dendrite arm, the UO1 dendrite is subsequently blocked by the FO1 dendrite primary arm. In contrast,

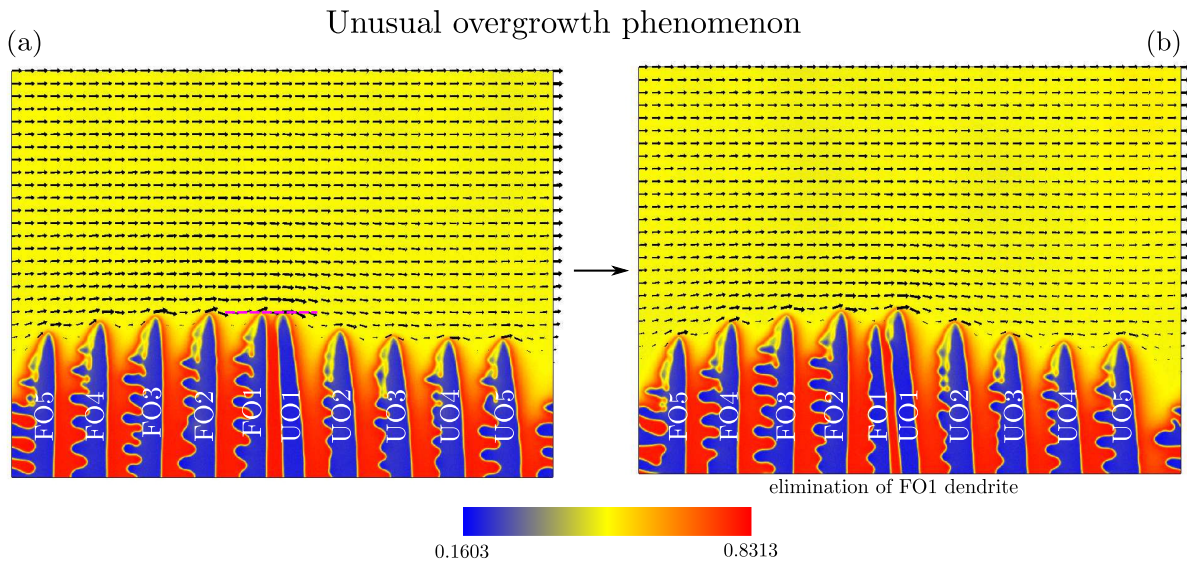


Figure 8.11: (a)-(b) Concentration and velocity fields during an unusual overgrowth event at $U_x = 2.5 \times 10^{-1}$. Here, the UO1 dendrite shifts towards the GB and subsequently eliminates the FO1 dendrite. Since the imposed melt velocity and the amount of advected solute near the tip is high, the UO1 dendrite outgrows its counterpart at the grain boundary. The size of the black arrows indicate the magnitude of the velocity fields. The dashed lines indicate the position at which the 1D concentration fields are extracted.

due to the imposed misorientation $\theta_{UO} = 15^\circ$, the misoriented UO1 dendrite initially falls behind the FO1 dendrite tip in Fig. 8.11. However, on account of the imposed convection velocity and the resultant solute, the relative driving force at the UO1 dendrite tip is high for $U_x = 2.5 \times 10^{-1}$. The enriched solute layer around the unfavorably oriented dendritic network becomes thinner on the upstream direction, which in turn assists the lateral movement of the UO1 dendrite. Hereafter, the UO1 dendrite retains its position and eventually outgrows the FO1 dendrite at $t = 4500$ in Fig. 8.11(b). For an unusual overgrowth behavior in Fig. 8.11, the dendrite UO1 migrates towards the upstream direction and reduces its inter-dendritic spacing with the FO1 dendrite rapidly. Additionally, the lag of a misaligned dendrite is not so large for $U_x = 2.5 \times 10^{-1}$ which compels the UO1 dendrite be also able to overgrow the FO1 dendrite. Therefore, when the GB dendrite cannot recover from the overgrowth of its FO neighbor, it shall always be blocked by the approaching UO dendrite. This behavior is elucidated via the one-dimensional solutal fields near the FO1 and UO1 dendrites in Fig. 8.12. The contrasting nature of the lateral profiles causes an asymmetric field at the grain boundary, which in turn enforces a restricted motion of the FO1 dendrite, resulting in an unusual overgrowth event at the GB. Besides, the absence of the UO1 concentration peak in Fig. 8.12 at $U_x = 1.0 \times 10^{-1}$ signifies the lag of the UO1 dendrite at the grain boundary.

For both dendritic overgrowth mechanisms, it is interesting to note that the solutal movement in-between the FO5-FO2 and UO2-UO5 dendrites promotes an asymmetric

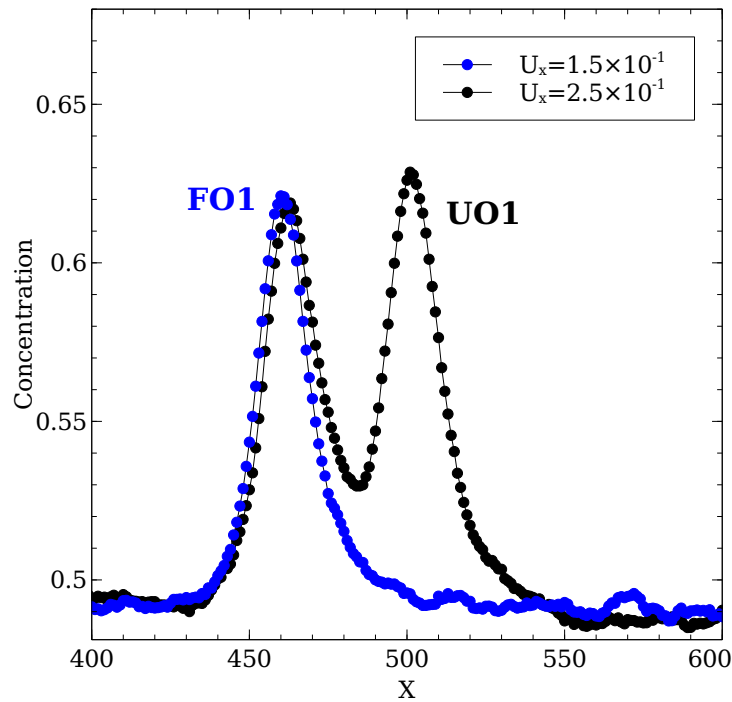


Figure 8.12: Lateral solutal profiles near the FO1 and UO1 dendrites at two different convection velocities. Contrasting nature of the solutal field modifies the overgrowth mechanism for converging dendrites at the grain boundary. The fluctuations indicate the imposed noise in the supersaturated melt.

formation of secondary dendrites. It is observed that the sidebranches are found to be largely favored on the upstream (left) direction of the primary arms and completely suppressed on the otherside. The presence of the left-to-right melt flow causes a cumulative solute enrichment at the downstream direction, which in-turn lowers the local undercooling and correspondingly hinders the growth of the secondary dendrites along the downstream (right) direction.

The unusual overgrowth mechanism in the present chapter agrees in spirits with the previous experimental investigations [66, 67, 69], where the overgrowth behavior of converging dendrites was studied for bicrystal samples. From the systematic in-situ experiments, it was concluded that the overgrowth of a well aligned columnar dendrite was hindered and the dendritic spacing with its immediate neighbour decreased at the grain boundary. Similarly, previous phase-field investigations [71, 76] have also reported the presence of an unusual overgrowth phenomenon for a binary alloy system. While the unidirectional solidification study of Li et al. [71] reported that the modification of diffusion length for GB dendrites at low pulling velocities was influential for the overgrowth of UO dendrites, Takaki et al. [76] analyzed the trajectories of the dendritic tips and reported that the presence of an asymmetric diffusion layer in front of the FO and UO dendrites was responsible for the unusual overgrowth phenomenon among columnar dendrites at the solid-solid grain boundary.

8.6 Effect of interfacial anisotropy

Over past many years, it is well known that the solid-liquid interfacial anisotropy is an important parameter to determine the shape of a dendrite [91]. In general, the strength of the imposed solid-liquid interfacial anisotropy dictates the morphology and in turn modifies the solutal fields near a dendritic tip. As the inter-dendritic growth competition deals with the overlap of the concentration fields at the solid-solid grain boundary, the role of the solid-liquid interfacial anisotropy on the grain selection mechanism is investigated in the present section.

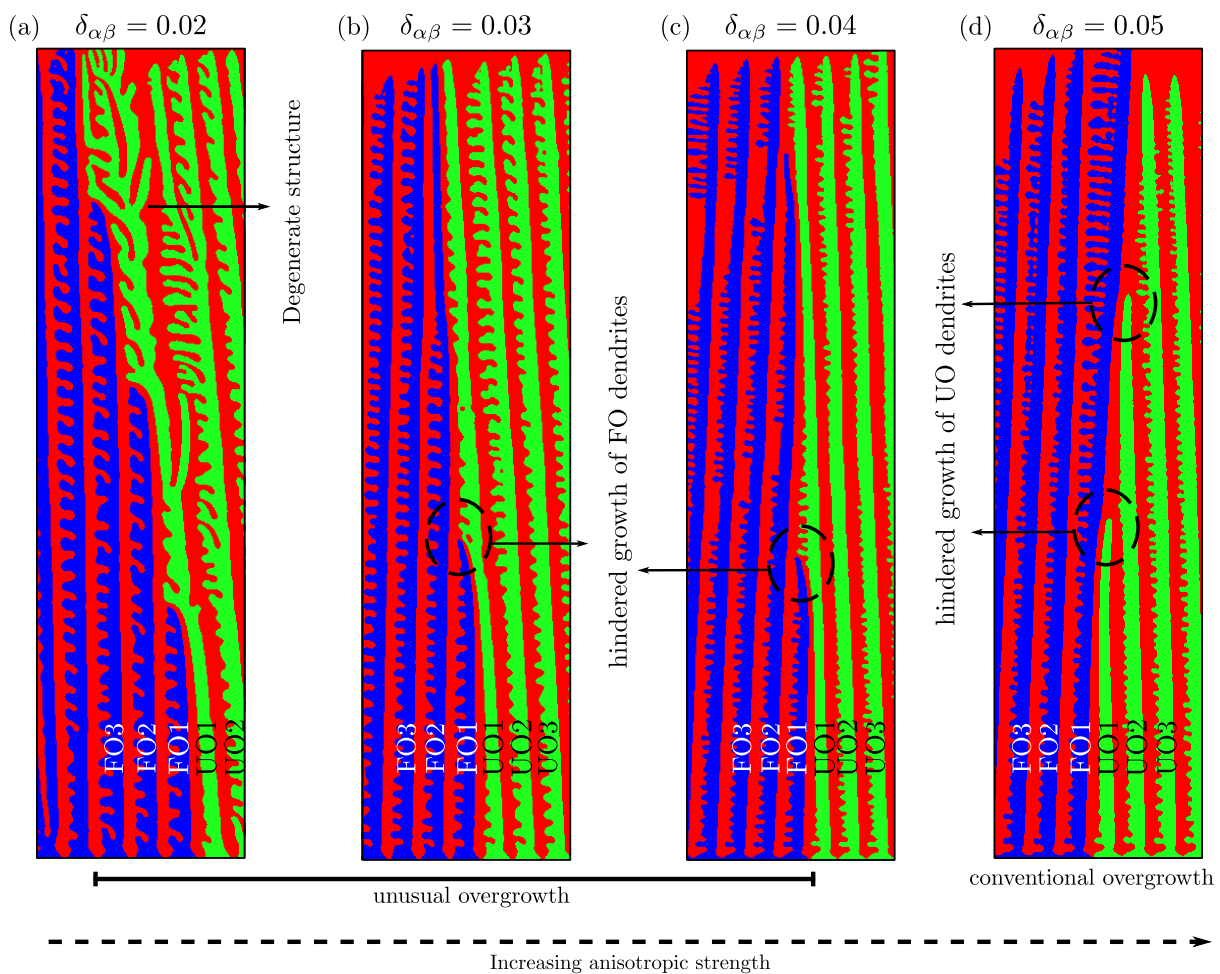


Figure 8.13: Inter-dendritic growth competition of columnar dendrites at various anisotropic strengths $\delta_{\alpha\beta}$. The unusual overgrowth phenomenon observed for $\delta_{\alpha\beta} \leq 0.04$ translates into a conventional overgrowth behavior at the grain boundary as the anisotropic strength gradually increases. A degenerate and a branched UO1 dendrite is generated for weaker anisotropic strengths.

At an imposed convection velocity $U_x = 2.5 \times 10^{-1}$, Fig. 8.13 depicts the simulation screenshots of the two-dimensional simulations of converging dendrites at different anisotropic strengths $\delta_{\alpha\beta}$. With an increase in the imposed anisotropic strength, the unusual overgrowth in Fig. 8.13 translates into a conventional overgrowth phenomenon at

the grain boundary. The growth competition shown in the previous section is recaptured for weaker strengths $\delta_{\alpha\beta} \leq 0.04$, wherein the UO1 dendrite protrudes and retards the primary arm of the FO1 dendrite. However, for $\delta_{\alpha\beta} = 0.05$, a strong crystalline anisotropy in the solid-liquid surface energy completely locks the preferred growth direction of the dendritic tips, and thus the inter-dendritic growth competition is in accordance with the conventional overgrowth model by Walton and Chalmers [229]. For a directionally solidified columnar dendrite, the advected solute near the solid-liquid interface and the tip shape oversees the behavior of columnar dendrites. At higher $\delta_{\alpha\beta}$, the contribution from the anisotropy in the surface energy dominates, and therefore the dendritic tip responds to the concentration field in order to change its growth direction towards the steepest chemical gradient in the alloy melt. Subsequently, the FO1 dendrite arm eliminates an unfavorably oriented dendrite at the grain boundary. The interfacial energy and advected solute in the liquid melt near the dendritic tip dynamically compete with each other to determine the overgrowth mechanism at the grain boundary. Besides, since the imposed crystalline anisotropy is weak for $\delta_{\alpha\beta} = 0.02$, the flow pattern near the solid-liquid interface induces oscillations to the UO1 dendrite tip and triggers tip splitting events. Thereafter, any further decrease in the solid-liquid interfacial anisotropic strength ($\delta_{\alpha\beta}$) results in the formation of strongly tilted seaweed microstructures as discussed in Chapter 6.

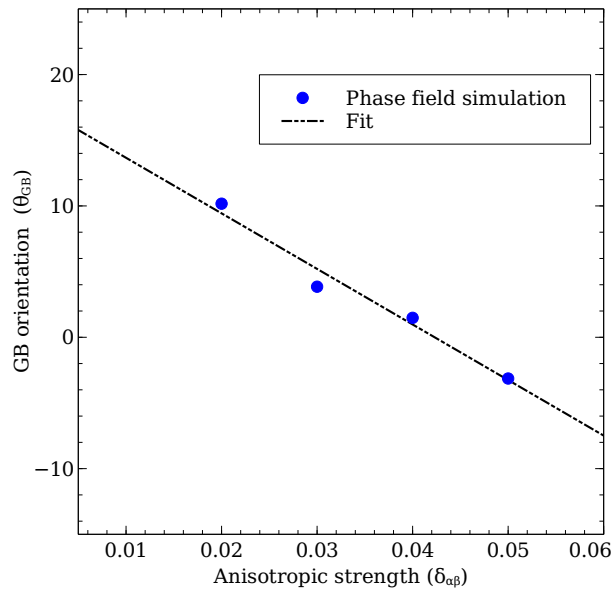


Figure 8.14: At an imposed convection velocity $U_x = 2.5 \times 10^{-1}$, the grain boundary orientation θ_{GB} at various anisotropic strengths. The by-product of a positive GB orientation is the elimination of a FO dendrite, whereas, a negative GB orientation indicates the overgrowth of FO dendrites. A linear fit provides us with a scaling law $\theta_{GB} \propto \delta_{\alpha\beta}$. The blue colored line indicates the transition region between the two overgrowth behaviors.

Next, the grain boundary orientation θ_{GB} as a function of anisotropic strength is determined in Fig. 8.14, where θ_{GB} is the inclination angle of the grain boundary with respect to the growth direction. A best linear analytical fit provides us with the scaling law

of the form $r_1 + r_2\delta_{\alpha\beta}$, where r_1 and r_2 are proportionality constants. Until $\delta_{\alpha\beta} \leq 0.04$, the grain boundary with an anti-clockwise orientation monotonously tilts towards the upstream direction, whereas, at $\delta_{\alpha\beta} = 0.05$, the GB is inclined along the downstream direction as a result of an unfavorably oriented dendrite elimination. In Fig. 8.13, although the lateral displacement of the GB is profound for weak $\delta_{\alpha\beta}$, a restricted lateral drift of GB dendrite is noticed for higher anisotropic strengths. Here, the GB orientation systematically goes negative (clockwise direction), which means that well-oriented dendrites shall never get eliminated by misoriented dendrites at the solid-solid grain boundary. It is also observed that the rate at which the UO1 dendrite impinges the favorably oriented dendrites decreases with an increase in the anisotropic strength.

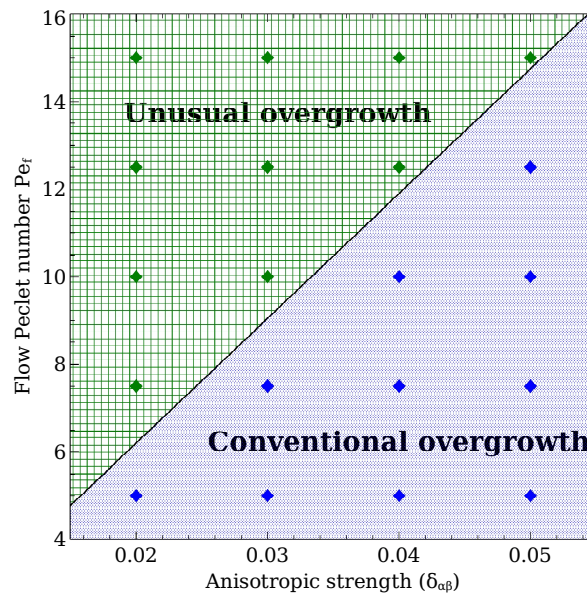


Figure 8.15: A microstructural selection map for inter-dendritic growth competition at various combinations of $(\delta_{\alpha\beta}, Pe_f)$. While the unusual overgrowth phenomenon dominates at higher melt velocities, an increase in the anisotropic strength produces the widely known conventional overgrowth behavior at the solid-solid grain boundary. The schematic transition zone is represented by the solid line.

Lastly, a novel microstructural selection map is depicted in Fig. 8.15, wherein the overgrowth behaviors are diversified over a wide range of anisotropic strength $\delta_{\alpha\beta}$ and flow Peclet numbers Pe_f . On one hand, it is observed that the unusual overgrowth phenomenon is restricted to higher Peclet numbers and lower anisotropic strengths only, while on the other hand, it is noticed that the conventional overgrowth region increases with an increase in the anisotropic strength. Since the imposed anisotropic strength restricts the movement of the UO1 dendritic tip towards the upstream direction, the inter-dendritic growth competition results in the elimination of an unfavorably oriented dendrite at the grain boundary. Furthermore, this tendency to restrict the displacement of the UO1 dendrite decreases with the decrease in the imposed anisotropic strength. It is noteworthy that the critical convection velocity to predict the transition between the

overgrowth behaviors increases with an increase in the anisotropic strength. From the microstructural selection map, it is also emphasized that the solid line in Fig. 8.15 is a schematic division of the two overgrowth mechanisms and not a strict transition zone. Nevertheless, based on the series of two-dimensional simulations, it is concluded that the strength of the solid-liquid interfacial anisotropy also plays a key role in determining the overgrowth mechanism among columnar dendrites at the grain boundary.

8.7 Summary

In this chapter, systematic two-dimensional phase-field simulations are performed to investigate the growth competition of columnar dendrites under the cooperative presence of diffusion and convection in the liquid phase. Illustrated in previous experimental studies, the overgrowth behaviors of columnar dendrites at the grain boundary is captured and analyzed. Under pure diffusive regime, it is shown that the growth competition in converging dendrites follows the classical grain selection mechanism of Walton and Chalmers, where a favorably oriented dendrite impinges and eliminates an unfavorably oriented dendrite at the grain boundary. However, after the introduction of melt convection, the overgrowth model translates into an anomalous overgrowth phenomenon. Distinguished as an unusual overgrowth behavior, it is concluded that the presence of an additional mass transport in the bulk liquid phase advects the solute near the FO and UO dendrite tips, which in turn modifies the overgrowth mechanism at the grain boundary. The findings in this chapter further broaden our understanding on the overgrowth mechanism under diffusive-convective conditions, which has been ignored in earlier phase-field studies.

The role of solid-liquid interfacial anisotropy on the prediction of inter-dendritic growth competition is also emphasized in the present chapter. For anisotropic strengths $\delta_{\alpha\beta} \leq 0.04$, the unusual overgrowth behavior is always observed for columnar dendrites at the grain boundary. A major conclusion from the present chapter is that a strong solid-liquid anisotropic strength $\delta_{\alpha\beta} > 0.04$ locks the direction of the dendritic tips resulting in a conventional overgrowth phenomenon, in accordance with the classical model of Walton and Chalmers. The numerical results also indicate that the critical melt velocity to predict the overgrowth mechanism increases with an increase in the anisotropic strength.

The results shown in the present chapter can be further extended to a polycrystalline dendritic network with several misoriented grains, where the role of combined presence of diverging and converging grains shall be investigated. Furthermore, although the present chapter provides realistic insights into the grain selection mechanism, in future, three-dimensional phase-field simulations are planned to study the growth competition among columnar dendrites for converging and diverging grains, and the role of solute interaction in the presence of melt flow.

Part IV
Conclusions and Outlook

Chapter 9

Conclusions and Outlook

9.1 Summary

Microstructures are strategic link for governing and processing materials behavior. In solidification processes, the convective transport near a solid-liquid interface is an integral part of microstructure formation. The cooperative effect of diffusive and convective fields can modify the morphology of a dendrite, induce the structural transition from equiaxed to a globular microstructure, or coarsen dendritic networks in cast products. Building upon previous experimental and theoretical studies under pure diffusive regime, in this dissertation, the behavior of unidirectionally solidified microstructures is predicted under diffusive-convective conditions. A graphical summary of the topics covered in this thesis is depicted in Fig. 9.1.

Following the motivation and outlook for the present study, Chapter 2 addresses the essential topics in directional solidification. Beginning with the development of morphological perturbations, the theory of constitutional supercooling along with the linear morphological instability for a planar interface is discussed. Afterwards, the formation of equiaxed and columnar dendrites under different growth conditions is reviewed. The fundamental aspects of the phase-field method is summarized in Chapter 3, where a thorough literature review highlighting the recent developments of the phase-field approach in dendritic solidification is presented. Moreover, the dynamics of conserved and non-conserved order parameter is interpreted through classical examples. In Chapter 4, the governing equations for phase, concentration and velocity fields to model unidirectionally solidified microstructures in the diffusive-convective regime are elucidated in detail.

The next part of the thesis pertains to results and discussion section, where the theory of liquid grooving at the grain boundaries is extensively studied in Chapter 5. At first, the present phase-field model is validated and benchmarked via comparing the groove kinetics as well as the groove geometries with the seminal theory of Mullins [6]. Next,

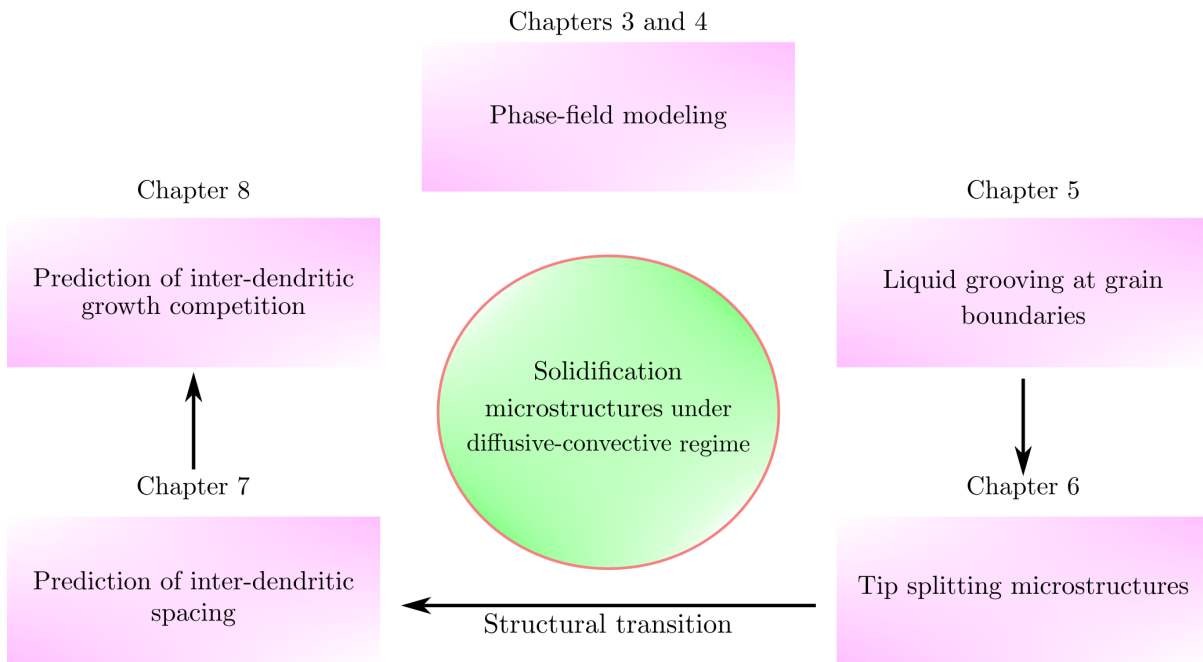


Figure 9.1: Graphical representation of the topics addressed in this dissertation.

for the first time through phase-field simulations, the theory of grain boundary grooving is reported in the diffusive-convective regime. It is observed that the groove kinetics under convective transport is completely modified when compared with the volume diffusion governed groove profiles. Besides, the simulated groove profiles depict an excellent agreement when compared dynamically with previous experimental and sharp interface theory. Consistent with experimental studies, it is shown that the interfacial instabilities are first observed at the grain boundary ridges. In unidirectional solidification, these perturbations develop into a complex network of tip splitting microstructures. Although these microstructures display a random morphology, the deterministic behavior of tip splitting structures is examined in Chapter 6. Having found a very good agreement with the sharp interface analytical criterion, it is revealed that the curvature driven fluxes stimulate the formation of rotation points at the solid-liquid interface, which in turn promote systematic tip splitting events in a complex microstructure. In addition, the structural transition of seaweed microstructures is shown in the presence of lateral flow. Herein, the degenerate seaweed structures transformed into strongly tilted structures as the convective forces dominated near the solidifying isotropic interface. Furthermore, a novel seaweed to columnar dendrite transition due to the dynamic competition between bulk and interfacial forces at the interface is showcased.

The variation of composition in-between the advancing primary dendrites and the surrounding interdendritic region gives rise to microsegregation within the solidified crystal. Normal to the growth direction, this segregation is characterized with a stable dendritic array. In the presence of lateral convective flow, it is shown that the selection mechanism as well as the primary dendrite morphology is modified in Chapter. 7. Interestingly, the

spacing selection after planar destabilization yielded reduced spacings with the introduction of convective transport in the inter-dendritic spaces. While the selection mechanism in diffusive conditions is driven by the overgrowth of neighbouring dendrites in the array stability limit, the generation as well as the amplification of the tertiary branches is the underlying principal during the cooperative effect of convection and diffusion in the liquid phase. Under realistic situations, the formation of axisymmetric dendrites is sensitive to growth conditions, and more often the growth of several misoriented dendrites is widely observed in castings. In Chapter 8, it is demonstrated that the converging dendrites at the grain boundary follow the widely accepted overgrowth theory of Chalmers and Walton [229], and the advection of solutal fields near the UO dendrites enhance the recently observed unusual overgrowth behaviour at the grain boundary. Lastly, through morphological maps, for the first time the effect of interfacial anisotropy is also investigated, where the strength of the imposed anisotropy transformed the overgrowth behavior among converging dendritic networks at the grain boundary.

9.2 Future directions

Although the present study comprehensively unravels the unidirectional solidification of microstructures in the diffusive-convective regime, the following open topics can be addressed in future.

Firstly, the network of solid-solid grain boundary represents a key microstructural element in nanocrystalline thin films. Accordingly, they determine the physical, mechanical and functional properties of diverse applications. While the common mode of failure in thin films has been studied extensively through the groove kinetics in Chapter 5, the morphological development as well as the growth kinetics of a three-dimensional polycrystalline thin film could be investigated in future. Widely observed in metallic and ceramic applications [147–150], a study on the preferential intergranular liquid penetration at the solid-solid grain boundary network shall furnish more quantitative information on thin film breakups. The role of grain size, temperature gradient, surface energies and other parameters could be investigated too. In order to provide realistic insights into thin film dynamics, the corrosive behavior of polycrystals via condensation and evaporation of vapour phases could also be incorporated in the model formulation. Furthermore, in this study, the diffusion of solutal species has been restricted to liquid phase only, thereafter, a phase-field study to address the role of an additional transport mechanism along the grain boundaries could be performed.

Secondly, from the preceding chapters, it has been shown that the phenomenon of microsegregation in binary alloys detrimentally modifies the solidification microstructures. In a three-dimensional dendritic network, since the melt flow is impeded by the primary arms, it is important to study the flow permeability in the mushy zones and obtain precise

microsegregation results in castings and ingots [234]. Therefore, predicting flow permeabilities via three-dimensional simulations shall be a promising topic to systematically evaluate various solidification conditions. Likewise, the phase-field model could be extended to include the role of natural convection driven by local density gradients in the alloy melt.

Thirdly, apart from dendritic microstructures, the equilibrium solidification of three phases trigger rod-like microstructures in binary eutectic and monotectic alloys [235]. In general, the monotectic alloys with a homogeneous liquid phase L_1 generates liquid phase L_2 droplets embedded in the solid matrix through the monotectic reaction at a constant monotectic temperature [235]. Systems such as Al-Bi, Fe-Sn, Al-In undergo liquid phase separation and offer interesting pathways for alloy development [236]. Due to the presence of thermocapillary forces near the liquid-liquid interfaces in monotectic alloys, the present work could be extended to investigate the behavior of polyphase microstructures in potential materials for automotive applications.

Part V
Appendices

Appendix A

Effect of numerical parameters on grain boundary grooving

A1 Effect of temporal and spatial discretization

In most alloy systems, the solid-liquid interfaces are roughly atomic scale, that is, the transition between the ordered solid and the disordered liquid takes place gradually over a distance of several atomic spacings. It is impractical and computationally challenging to perform phase field simulations in the realistic length scale, and the only viable path is to use models in which the *numerical* interface thickness is much larger than the thickness of the physical interface. Therefore, through the advantage of thin interface limit [5, 88, 110], the phase-field simulations are generally performed at micrometer length scale and thereafter replicate the atomistic scale interfacial features. To show that the results presented in this dissertation are not affected by the chosen numerical parameters, a systematic convergence study is performed to illustrate that the temporal and spatial discretizations do not effect the kinetics as well as the morphology of the grain boundary grooving phenomenon.

Firstly, the effect of temporal discretization Δt is shown in Fig. A1, where the grain boundary groove profiles for different Δt are simulated and compared. As depicted in Fig. A1, the groove profiles corresponding $\phi_\alpha = 0.5$ are extracted and compared. Here, the complete overlap of the groove profiles at various Δt confirm that the groove geometries are unaffected by the magnitude of the time step.

On the other hand, the effect of spatial discretization is studied, whereby the ratio $\frac{\Delta x}{\epsilon}$ is systematically decreased and then the steady state groove root position d_g^{ss} is evaluated for all the simulations with finite bicrystal grains. Here, Fig. A2 depicts the groove root position as a function of the ratio $\frac{\Delta x}{\epsilon}$, where it is observed that the chosen grid spacing has little influence on the growth rate, and primarily does not change its

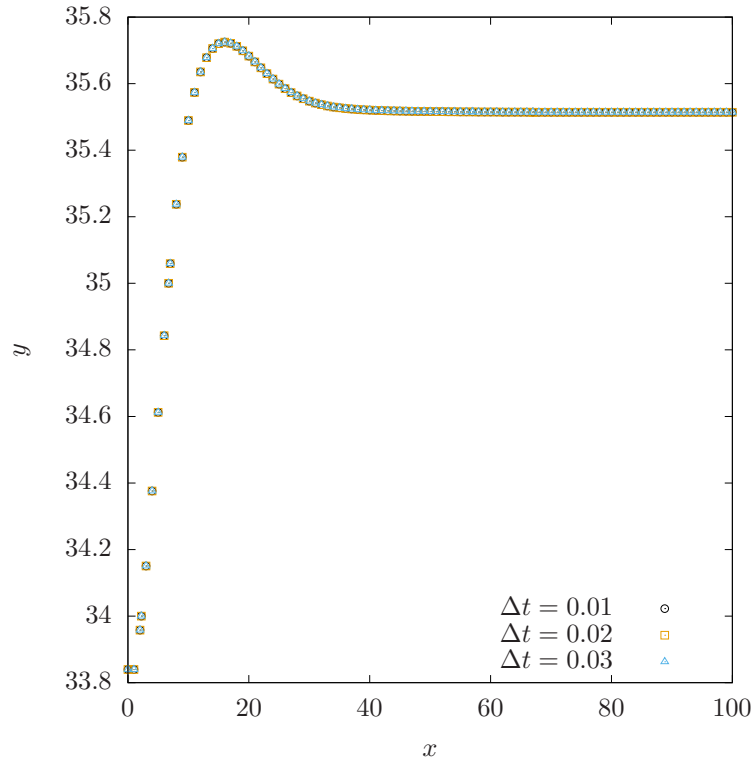


Figure A1: Effect of temporal discretization Δt on the grain boundary groove profile. The complete overlap of the isolines illustrate that the chosen numerical parameters have no influence on the groove geometry.

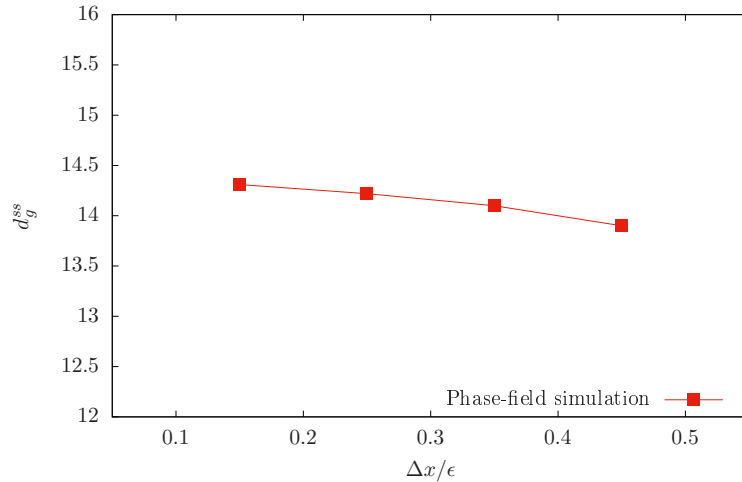


Figure A2: For finite bicrystal grain, steady state groove root position d_g^{ss} as a function of the ratio $\frac{\Delta x}{\epsilon}$. For all two-dimensional simulation in Chapter 6, $\frac{\Delta x}{\epsilon} = 0.25$ is chosen, and thereby the grid discretization has no influence on our numerical results.

value by more than 2%. For the present study grain boundary grooving, the chosen discretization spacing $\Delta x = 0.50$ and interface width $\epsilon = 2.0$, and therefore the ratio $\frac{\Delta x}{\epsilon} = 0.25$ accounts very well for all our two-dimensional phase-field simulations.

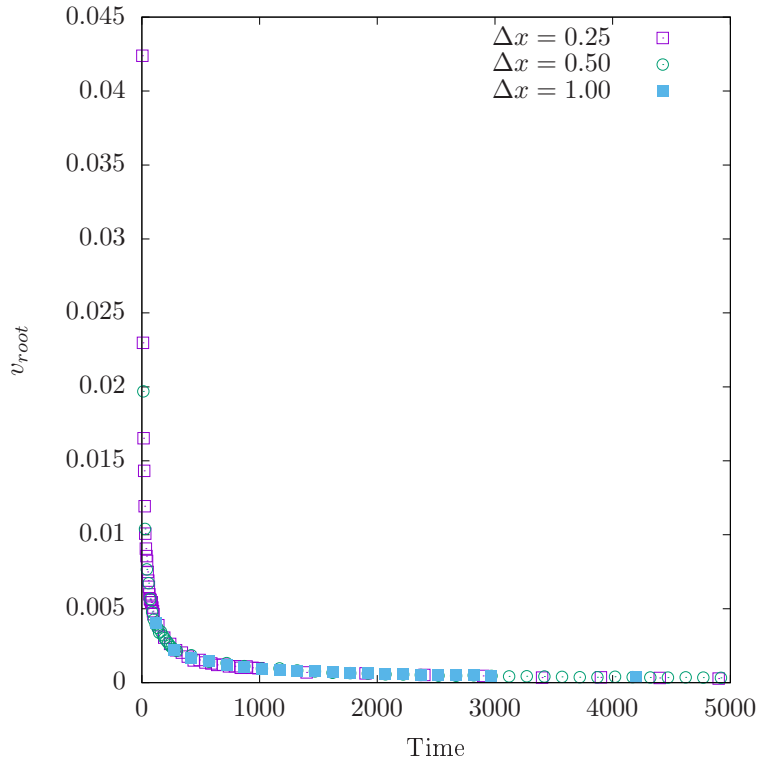


Figure A3: Effect of spatial discretization Δx on the grain boundary grooving. The convergence of groove root velocities indicate that the spatial discretizations does not play any role in the present work.

In addition, at different spatial resolutions, the steady state velocity is shown in Fig. A3 where the groove root velocity v_{root} is calculated numerically from the position of the groove root between the successive time for various mesh sizes. As shown in Fig. A3, it is observed that for different grid resolutions Δx the convergence in the root velocities is systematically achieved, thereby confirming that the groove kinetics are unaffected by the grid effects.

A2 Effect of third order parameter

By performing the simulations with different interface energy parameters, artificial third phases appear in the two-phase interfaces [125]. In the phase-field model, the appearance of artificial third phases at the trijunction is suppressed by the addition of a third order term in the obstacle potential. In addition, the magnitude of the artificial phase value does not only depend on the ratio of the interface energies, but also on the interface width. Henceforth, in the present section, the effect of the third order term on the groove profiles is illustrated in Figs. A4 and A5. As depicted in Fig. A4, the presence of an additional third order term modifies the groove profile in finite grains, especially for $\delta_{\alpha\beta\delta} = 10$. Furthermore, the groove depth is calculated for various $\delta_{\alpha\beta\gamma}$ in Fig. A5, where

an increase in the third order term seemingly modifies the temporal evolution of the groove root. A pinning effect is also observed at the root positions, wherein oscillations arise and relatively affect the dynamics at the root position.

In order to model liquid grooving at the grain boundaries, the magnitude of the third order parameter is chosen as $\delta_{\alpha\beta\gamma} = 2.0$, and thereby from the simulated profiles in this section, it is confirmed that the third order parameter has no influence on the numerical results in Chapter. 5.

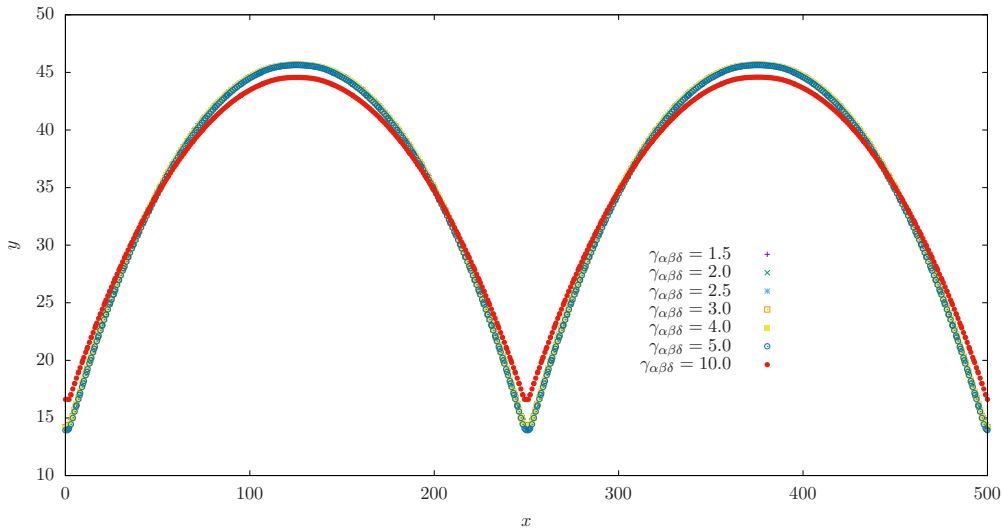


Figure A4: Effect of third-order term on the groove profiles. A pinning effect is observed for $\gamma_{\alpha\beta\delta} = 10.0$, where the grain boundary groove profile is significantly altered under steady state conditions.

A3 Determination of equilibrium angle

The equilibrium angle at the groove root derived from the phase-field simulations is verified in this section. Assuming that the phase boundaries are isotropic, the equilibrium angle Φ at the groove root with respect is given by $\Phi = 2 \cos^{-1} \left(\frac{\gamma_{gb}}{2\gamma_{sl}} \right)$. In Chapter 5, the ratio $\frac{\gamma_{gb}}{\gamma_{sl}} = 1.0$ is considered, and the equilibrium angle Φ at the groove root is calculated as 120° . Consequently, the angle at the groove root is derived from the simulated two-dimensional grain boundary profile. In order to calculate the equilibrium, the $\phi = 0.5$ isoline is fitted on the either side of the grain boundary with a fourth order polynomial, as shown in Fig. A6 with a solid black line, and the point of intersection between these two polynomials is first determined. Next, the equilibrium angle made by the tangent to the polynomial at this point of intersection is calculated analytically to be 120.8° . A direct comparison of the theoretically obtained equilibrium angle Φ , and the fourth order polynomial fit of the interface shapes shows an excellent agreement between the

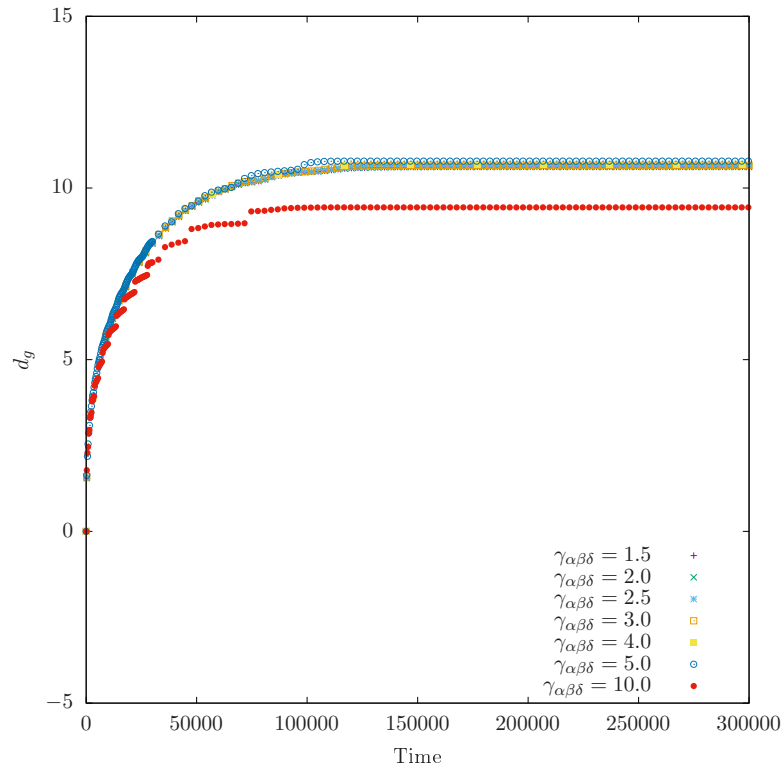


Figure A5: Effect of additional third-order term on the groove root position. For $\gamma_{\alpha\beta\delta} = 10.0$ the groove root position is affected under steady state conditions where a pinning effect at the trijunction is observed.

two methods. Henceforth, the present analysis also concludes that the chosen obstacle potential does not effect the equilibrium angle at the groove root.

A4 Parameters

Although the numerical and material parameters used in this study are dimensionless, for better understanding, the typical order of magnitudes are given below.

Table A.1: Typical order of magnitudes for key phase-field parameters.

Description	Parameter	Value
Discretized grid space	$\Delta x = \Delta y$	$1.0 \times 10^{-7} \text{m}$
Interface width	ϵ	$4.0 \times 10^{-7} \text{m}$
Diffusivity	D_i^β	$1.0 \times 10^{-9} \text{m}^2/\text{s}$
Kinematic viscosity	ν	$1.00 \times 10^{-6} \text{m}^2/\text{s}$
Fluid density	ρ	$1.00 \times 10^3 \text{Kg}/\text{m}^3$

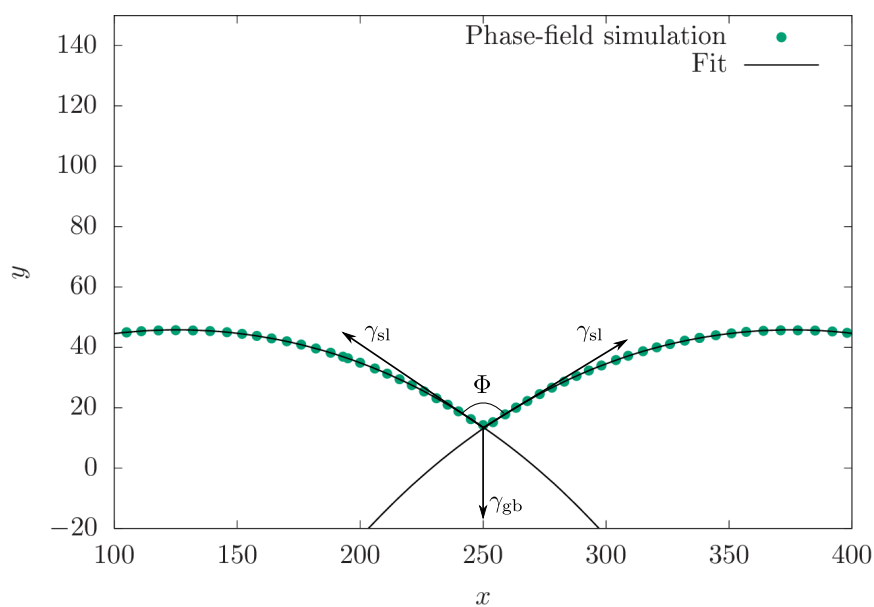


Figure A6: Determination of the equilibrium groove angle from the phase-field simulations. A fourth-order polynomial is fitted to the extracted $\phi = 0.5$ isolines. Subsequently, the equilibrium angle made by the tangent to the polynomial at the point of intersection is calculated. The equilibrium angle is schematically represented at the trijunction.

Appendix B

Effect of grid discretization and lattice anisotropy on tip splitting phenomenon

B1 Effect of interface width and spatial discretization

In order to show that the tip splitting phenomenon discussed in Chapter 6 is not an numerical artifact due to the chosen finite interface width thickness, the convergence of interface velocity is shown. Here, all other numerical parameters have been kept same and several two-dimensional simulations are performed at different interface thickness ϵ , through the advantage of thin interface limit. Moreover, all the simulations are run long enough to attain steady state velocities. In Fig. B1, it is systematically observed that with the decrease in ϵ the convergence in the interface velocities is completely achieved at $\Delta x = 1.0$ spatial discretization. Thereby, confirming that simulations with a large interface thickness do not influence our results.

Furthermore, the role of discretization spacing on our numerical simulations is also studied, where a four-fold anisotropic dendrite in an supersaturated melt of composition $\Delta = 0.5$ and with an anisotropic strength $\delta_{\alpha\beta} = 0.02$ is simulated. In order to investigate the effect of discretization spacing, the ratio $\frac{\Delta x}{\epsilon}$ is systematically decreased and then the steady state tip velocity V_{tip} is evaluated for all the simulations. Here, Fig. B2 depicts the tip velocity as a function of the ratio $\frac{\Delta x}{\epsilon}$, where it is observed that the chosen grid spacing has little influence on the growth rate and primarily does not change its value by more than 3%. For the present study, the chosen discretization spacing $\Delta x = 1.0$ and interface width $\epsilon = 4.0$, and therefore the ratio $\frac{\Delta x}{\epsilon} = 0.25$ accounts very well for all our two-dimensional phase-field simulations.

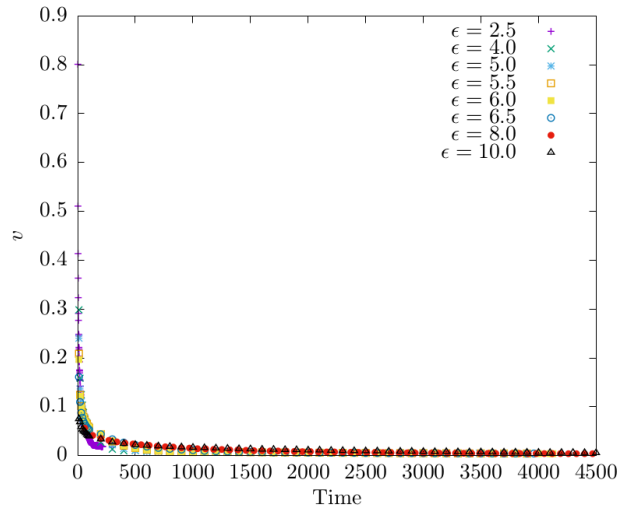


Figure B1: Convergence at various interface widths confirms that the numerical result is not influenced by the finite width of the diffuse interface.

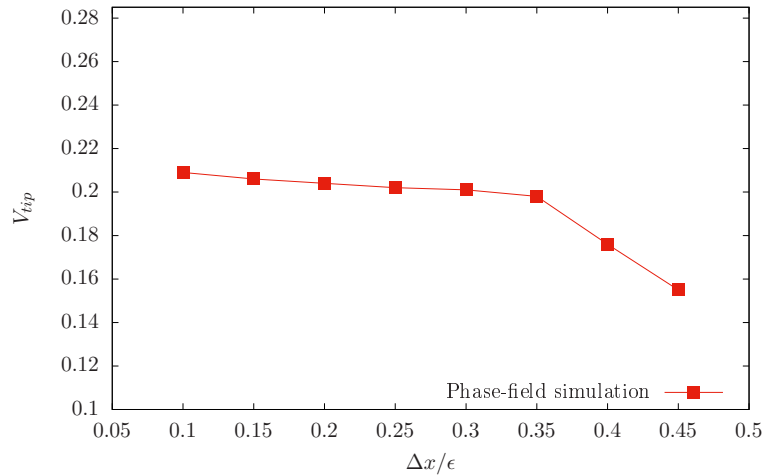


Figure B2: Tip velocity as a function of the ratio $\frac{\Delta x}{\epsilon}$. For all two-dimensional simulation in Chapter 6, $\frac{\Delta x}{\epsilon} = 0.25$ is chosen, and thereby the grid discretization has no influence on our numerical results.

B2 Effect of lattice anisotropy

In continuation with the study on lattice anisotropy in Chapter 6, the procedure is repeated for stronger anisotropic strengths $\delta_{\alpha\beta}$ and a direct comparison is shown in Fig. B3. For stronger $\delta_{\alpha\beta}$, an excellent agreement between the phase-field simulated equilibrium shape and the sharp-interface crystal shape is achieved.

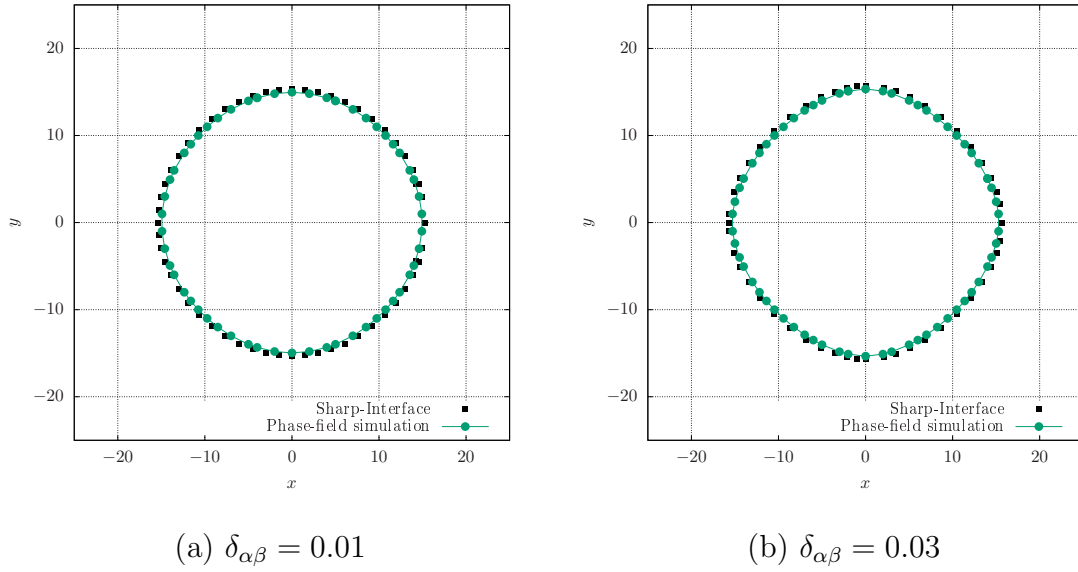


Figure B3: (a)-(b) For an equilibrium shape with radius $R_{00} = 15$, the effect of lattice anisotropy at two different anisotropic strengths. A direct comparison shows an excellent agreement with the sharp interface theory for both cases. Here, the obtained effective anisotropies are $\delta_{\alpha\beta}^e = 0.0096$ for $\delta_{\alpha\beta} = 0.01$, and , $\delta_{\alpha\beta}^e = 0.028$ for $\delta_{\alpha\beta} = 0.03$ respectively.

Furthermore, for various spherical crystal radii R_{00} , the role of lattice anisotropy is also investigated. For three different seed radius, it is noticed from Fig. B4, Fig. B5 and Fig. B6 that the effective anisotropy depends weakly on the selected R_{00} . Lastly, it is important to note and emphasize that for all cases, the effective anisotropy $\delta_{\alpha\beta}^e$ varies less than 5% of the imposed value, and in turn represents the accuracy in our phase-field results.

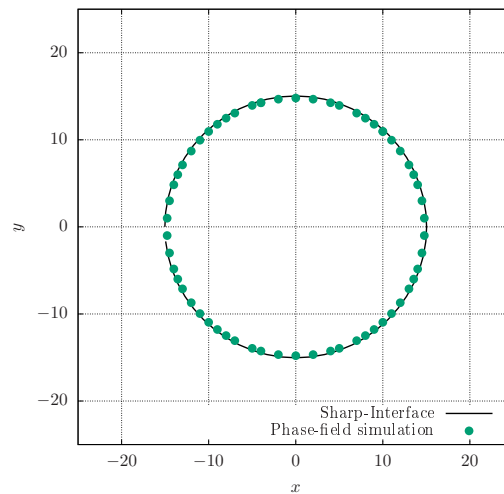


Figure B4: Effect of lattice anisotropy on an equilibrium crystal seed with radius $R_{00} = 15$, where an excellent agreement with the sharp interface theory is observed, and the obtained effective anisotropy $\delta_{\alpha\beta}^e = 0.0005$.

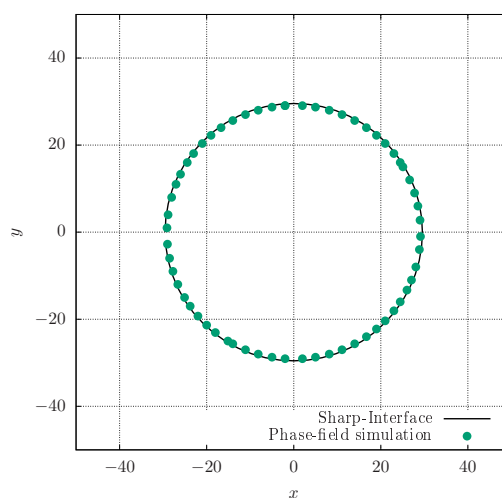


Figure B5: Effect of lattice anisotropy on an equilibrium crystal seed with radius $R_{00} = 30$, where an excellent agreement with the sharp interface theory is observed, and the obtained effective anisotropy $\delta_{\alpha\beta}^e = 0.0002$.

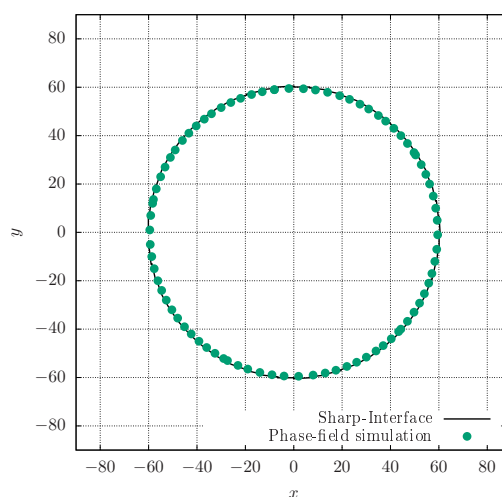


Figure B6: Effect of lattice anisotropy on an equilibrium crystal seed with radius $R_{00} = 60$, where an excellent agreement with the sharp interface theory is observed, and the obtained effective anisotropy $\delta_{\alpha\beta}^e = 0.00009$.

Appendix C

Influence of interfacial curvature on tip splitting phenomenon

In order to further testify, the tip splitting phenomenon is elucidated for various interfacial curvatures during initialization. While a crystal growth follows the typical Mullins-Sekerka theory [30], the formation and the position of the two symmetric tips are predicted by the sharp interface analytical criterion only. Based on the present theory, any shape with a non-uniform curvature that varies non-linearly with its arc length undergoes splitting. An example in Fig. C1 shows the influence of interfacial curvature on the tip splitting mechanism. Fig. C1(a)-(b) depicts that for any initial condition where $\nabla_s \kappa$ is large, the tip splitting is pronounced. The two tips symmetrically evolve on either side of the trough region. Now, from the crystal shapes with decreasing $\nabla_s \kappa$ in Fig. C1(c)-(d), it is discovered that the splitting process diminishes, and with $\nabla_s \kappa = 0$, it is finally observed that the time evolution of a planar interface has no branching or perturbances. This is in accordance with the sharp-interface theory, since $\nabla_s \kappa = 0$, the analytical criterion $\nabla_s^2 \kappa$ disappears and therefore in practice, the tip splitting is completely restricted. Now, if the aforementioned comparison is carried out for the interface profiles where $\nabla_s \kappa$ decreases, is also observed that the magnitudes of surface fluxes subsides. Therefore, the two tips in Fig. C1(c) shall never acquire the pronounced state as $\alpha_0 = 0.02$ or $\alpha_0 = 0.04$, as long as the simulation domain is exhausted. Surface fluxes at the tip are considered to be negligible for the cases where $\nabla_s \kappa$ is small, as the difference between the two magnitudes is relatively large. On the other hand, weak gradients throughout the profile do not generate any protuberances too. Lastly, through the present study, it is reaffirmed that the tip splitting mechanism is deterministic and initiated by the presence of the curvature driven fluxes.

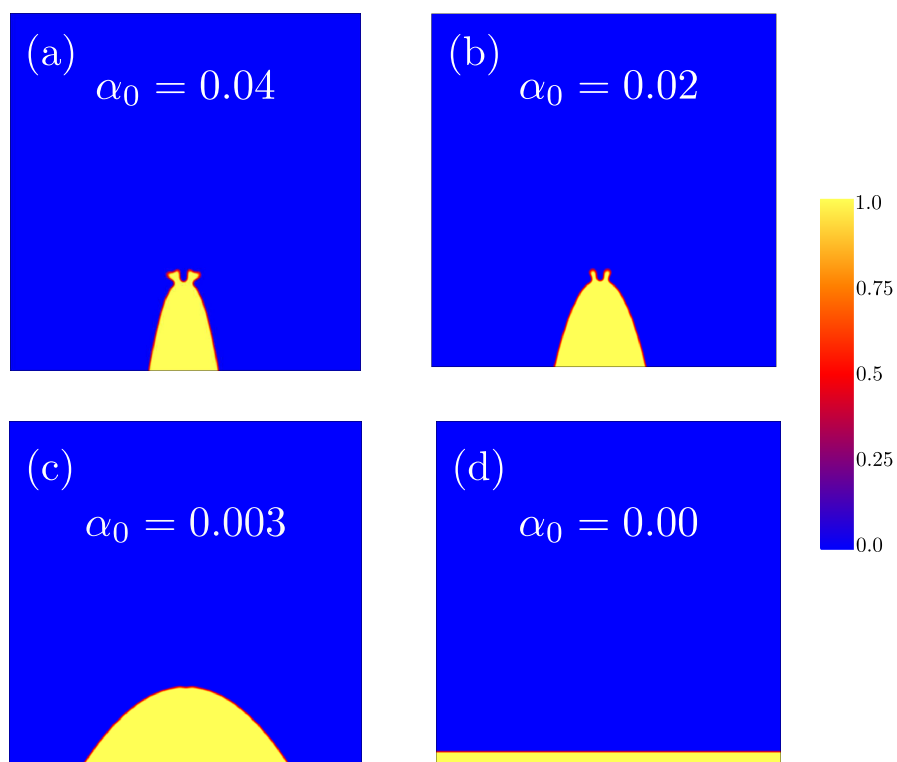


Figure C1: The influence of non-uniform curvature during the morphological evolution of tip splitting microstructure. Pronounced tips observed for large $\nabla_s \kappa$ diminish as $\nabla_s \kappa$ decreases. Finally, as predicted by the theory, the absence of splitting and perturbances for $\nabla_s \kappa = 0$ is observed. Here, α_0 is the dimensionless shape factor in $f(x) = -\alpha_0(x - h)^2 + p$.

Bibliography

- [1] Wilfried Kurz and David J Fisher. *Fundamentals of solidification*. Trans Tech Publications, Switzerland, 1989.
- [2] VE Fradkov. Rapid liquid metal corrosion along grain boundaries. *Scripta metallurgica et Materialia*, 30(12):1599–1603, 1994.
- [3] Kaveh Meshinchi Asl and Jian Luo. Impurity effects on the intergranular liquid bismuth penetration in polycrystalline nickel. *Acta Materialia*, 60(1):149–165, 2012.
- [4] SM Copley, Anthony F Giamei, SM Johnson, and MF Hornbecker. The origin of freckles in unidirectionally solidified castings. *Metallurgical Transactions*, 1(8):2193–2204, 1970.
- [5] Abhik Choudhury and Britta Nestler. Grand-potential formulation for multicomponent phase transformations combined with thin-interface asymptotics of the double-obstacle potential. *Physical Review E*, 85:021602, Feb 2012.
- [6] WW Mullins. Grain boundary grooving by volume diffusion. *Transactions of the American Institute of Mining and Metallurgical Engineers*, 218(2):354–361, 1960.
- [7] V Pavan Laxmipathy, Fei Wang, Michael Selzer, and Britta Nestler. Phase-field simulations of grain boundary grooving under diffusive-convective conditions. *Acta Materialia*, 204:116497, 2021.
- [8] Martin E Glicksman. Mechanism of dendritic branching. *Metallurgical and Materials Transactions A*, 43(2):391–404, 2012.
- [9] V Pavan Laxmipathy, Fei Wang, Michael Selzer, Britta Nestler, and Kumar Ankit. Influence of melt convection on the morphological evolution of seaweed structures: Insights from phase-field simulations. *Computational Materials Science*, 170:109196, 2019.
- [10] V Pavan Laxmipathy, Fei Wang, Michael Selzer, and Britta Nestler. A two-dimensional phase-field study on dendritic growth competition under convective conditions. *Computational Materials Science*, 186:109964.

-
- [11] M Asta, Christoph Beckermann, Alain Karma, Wilfried Kurz, R Napolitano, Mathis Plapp, G Purdy, Michel Rappaz, and Rohit Trivedi. Solidification microstructures and solid-state parallels: Recent developments, future directions. *Acta Materialia*, 57(4):941–971, 2009.
- [12] Wilfried Kurz, David J Fisher, and Rohit Trivedi. Progress in modelling solidification microstructures in metals and alloys: dendrites and cells from 1700 to 2000. *International Materials Reviews*, 64(6):311–354, 2019.
- [13] Lorne D Kenny and Martin Thomas. Process for shape casting of particle stabilized metal foam, January 25 1994. US Patent 5,281,251.
- [14] J. A. Spittle. Grain refinement in shape casting of aluminium alloys. *International Journal of Cast Metals Research*, 19(4):210–222, 2006.
- [15] AJ Elliott and TM Pollock. Thermal analysis of the bridgman and liquid-metal-cooled directional solidification investment casting processes. *Metallurgical and Materials Transactions A*, 38(4):871–882, 2007.
- [16] GP Syrcos. Die casting process optimization using taguchi methods. *Journal of Materials Processing technology*, 135(1):68–74, 2003.
- [17] Martin Eden Glicksman. *Principles of solidification: an introduction to modern casting and crystal growth concepts*. Springer Science & Business Media, New York, NY, 2010.
- [18] FC Frank. Snow crystals. *Contemporary Physics*, 23(1):3–22, 1982.
- [19] Ethan K Scott and Liqun Luo. How do dendrites take their shape? *Nature Neuroscience*, 4(4):359–365, 2001.
- [20] Morteza Amoozraei, Sebastian Gurevich, and Nikolas Provatas. Orientation selection in solidification patterning. *Acta Materialia*, 60(2):657–663, 2012.
- [21] WA Tiller, KA Jackson, JW Rutter, and B Chalmers. The redistribution of solute atoms during the solidification of metals. *Acta Metallurgica*, 1(4):428–437, 1953.
- [22] RJ Schaefer and ME Glicksman. Initiation of dendrites by crystal imperfections. *Metallurgical Transactions*, 1(7):1973–1978, 1970.
- [23] Hui Xing, CaiFang Wang, JianYuan Wang, and ChangLe Chen. Morphological evolution of the solid-liquid interface near grain boundaries during directional solidification. *Science China Physics, Mechanics and Astronomy*, 54(12):2174–2180, 2011.

- [24] N Noël, H Jamgotchian, and B Billia. In situ and real-time observation of the formation and dynamics of a cellular interface in a succinonitrile-0.5 wt% acetone alloy directionally solidified in a cylinder. *Journal of Crystal Growth*, 181(1-2):117–132, 1997.
- [25] N. Noël, H. Jamgotchian, and B. Billia. Influence of grain boundaries and natural convection on micro structure formation in cellular directional solidification of dilute succinonitrile alloys in a cylinder. *Journal of Crystal Growth*, 187(3-4):516–526, 1998.
- [26] D. Benielli, N. Bergeon, H. Jamgotchian, B. Billia, and Ph. Voge. Free growth and instability morphologies in directional melting of alloys. *Physical Review E*, 65:051604, May 2002.
- [27] K Murakami, H Aihara, and T Okamoto. Growth direction of columnar crystals solidified in flowing melt. *Acta Metallurgica*, 32(6):933–939, 1984.
- [28] LR Morris and WC Winegard. The development of cells during the solidification of a dilute Pb-Sb alloy. *Journal of Crystal Growth*, 5(5):361–375, 1969.
- [29] AG Borisov. Pattern formation during directional solidification of bicrystals. *Journal of Crystal Growth*, 156(3):296–302, 1995.
- [30] William W Mullins and RF Sekerka. Stability of a planar interface during solidification of a dilute binary alloy. *Journal of Applied Physics*, 35(2):444–451, 1964.
- [31] James S Langer. Instabilities and pattern formation in crystal growth. *Reviews of Modern Physics*, 52(1):1, 1980.
- [32] S De Cheveigne, C Guthmann, and M-M Lebrun. Nature of the transition of the solidification front of a binary mixture from a planar to a cellular morphology. *Journal of Crystal Growth*, 73(2):242–244, 1985.
- [33] W Losert, BQ Shi, and HZ Cummins. Evolution of dendritic patterns during alloy solidification: Onset of the initial instability. *Proceedings of the National Academy of Sciences*, 95(2):431–438, 1998.
- [34] James A Warren and JS Langer. Stability of dendritic arrays. *Physical Review A*, 42(6):3518, 1990.
- [35] James A Warren and JS Langer. Prediction of dendritic spacings in a directional-solidification experiment. *Physical Review E*, 47(4):2702, 1993.
- [36] T Ihle and H Müller-Krumbhaar. Fractal and compact growth morphologies in phase transitions with diffusion transport. *Physical Review E*, 49(4):2972, 1994.

- [37] Silvere Akamatsu, Gabriel Faivre, and Thomas Ihle. Symmetry-broken double fingers and seaweed patterns in thin-film directional solidification of a nonfaceted cubic crystal. *Physical Review E*, 51(5):4751, 1995.
- [38] GP Ivantsov. Temperature field around a spherical, cylindrical, and needle-shaped crystal, growing in a pre-cooled melt. *Temperature field around a spherical*, 58:567–569, 1985.
- [39] DE Temkin. Growth rate of the needle-crystal formed in a supercooled melt. *Soviet Physics Doklady*, 5:609, 1960.
- [40] GF Bolling and WA Tiller. Growth from the melt. III. dendritic growth. *Journal of Applied Physics*, 32(12):2587–2605, 1961.
- [41] GF Bolling and WA Tiller. Erratum: Growth from the melt. III. dendritic growth. *Journal of Applied Physics*, 33(7):2400–2400, 1962.
- [42] R Trivedi and WA Tiller. Interface morphology during crystallization I. single filament, unconstrained growth from a pure melt. *Acta Metallurgica*, 26(5):671–678, 1978.
- [43] JS Langer and H Müller-Krumbhaar. Theory of dendritic growth I. elements of a stability analysis. *Acta Metallurgica*, 26(11):1681–1687, 1978.
- [44] M Rappaz and Ph Thevoz. Solute diffusion model for equiaxed dendritic growth. *Acta Metallurgica*, 35(7):1487–1497, 1987.
- [45] M Rappaz and Ph Thévoz. Solute diffusion model for equiaxed dendritic growth: Analytical solution. *Acta Metallurgica*, 35(12):2929–2933, 1987.
- [46] JA Spittle and SGR Brown. Computer simulation of the effects of alloy variables on the grain structures of castings. *Acta Metallurgica*, 37(7):1803–1810, 1989.
- [47] R Trivedi and K Somboonsuk. Constrained dendritic growth and spacing. *Materials Science and Engineering*, 65(1):65–74, 1984.
- [48] JAE Bell and WC Winegard. Dendrite spacing in tin-lead alloys. Technical report, Toronto Univ. (Ontario), 1963.
- [49] K Somboonsuk and R Trivedi. Dynamical studies of dendritic growth. *Acta Metallurgica*, 33(6):1051–1060, 1985.
- [50] JD Hunt and Shu-Zu Lu. Numerical modeling of cellular-dendritic array growth: spacing and structure predictions. *Metallurgical and Materials Transactions A*, 27(3):611–623, 1996.

- [51] JD Hunt. Cellular and primary dendrite spacings. In *Solidification and Casting of Metals Proc. Conf. Sheffield, England, July 1977*, volume 1, pages 3–9, 1979.
- [52] Rohit Trivedi. Interdendritic spacing: Part II. a comparison of theory and experiment. *Metallurgical and Materials Transactions A*, 15(6):977–982, 1984.
- [53] Seung Hoon Han and Rohit Trivedi. Primary spacing selection in directionally solidified alloys. *Acta Metallurgica et Materialia*, 42(1):25–41, 1994.
- [54] K Somboonsuk, JT Mason, and R Trivedi. Interdendritic spacing: Part I. experimental studies. *Metallurgical and Materials Transactions A*, 15(6):967–975, 1984.
- [55] DJ Fisher and W Kurz. A theory of branching limited growth of irregular eutectics. *Acta Metallurgica*, 28(6):777–794, 1980.
- [56] W Losert, ON Mesquita, JMA Figueiredo, and HZ Cummins. Direct measurement of dendritic array stability. *Physical Review Letters*, 81(2):409, 1998.
- [57] JD Hunt. A numerical analysis of dendritic and cellular growth of a pure material investigating the transition from array to isolated growth. *Acta Metallurgica et Materialia*, 39(9):2117–2133, 1991.
- [58] Shu-Zu Lu and JD Hunt. A numerical analysis of dendritic and cellular array growth: the spacing adjustment mechanisms. *Journal of Crystal Growth*, 123(1-2):17–34, 1992.
- [59] Huang Weidong, Geng Xingguo, and Zhou Yaohe. Primary spacing selection of constrained dendritic growth. *Journal of Crystal Growth*, 134(1-2):105–115, 1993.
- [60] QY Pan, WD Huang, X Lin, and YH Zhou. Primary spacing selection of Cu-Mn alloy under laser rapid solidification condition. *Journal of Crystal Growth*, 181(1-2):109–116, 1997.
- [61] RN Grugel and Y Zhou. Primary dendrite spacing and the effect of off-axis heat flow. *Metallurgical Transactions A*, 20(5):969–973, 1989.
- [62] Silvere Akamatsu and Thomas Ihle. Similarity law for the tilt angle of dendrites in directional solidification of non-axially-oriented crystals. *Physical Review E*, 56(4):4479, 1997.
- [63] CH A Gandin, M Eshelman, and Rohit Trivedi. Orientation dependence of primary dendrite spacing. *Metallurgical and Materials Transactions A*, 27(9):2727–2739, 1996.
- [64] A Wagner, BA Shollock, and M McLean. Grain structure development in directional solidification of nickel-base superalloys. *Materials Science and Engineering: A*, 374(1-2):270–279, 2004.

- [65] Ch-A Gandin, J-L Desbiolles, Michel Rappaz, and Ph Thevoz. A three-dimensional cellular automation-finite element model for the prediction of solidification grain structures. *Metallurgical and Materials Transactions A*, 30(12):3153–3165, 1999.
- [66] YZ Zhou, A Volek, and NR Green. Mechanism of competitive grain growth in directional solidification of a nickel-base superalloy. *Acta Materialia*, 56(11):2631–2637, 2008.
- [67] Honglei Yu, Junjie Li, Xin Lin, Lilin Wang, and Weidong Huang. Anomalous overgrowth of converging dendrites during directional solidification. *Journal of Crystal Growth*, 402:210–214, 2014.
- [68] N D’souza, MG Ardakani, A Wagner, BA Shollock, and M McLean. Morphological aspects of competitive grain growth during directional solidification of a nickel-base superalloy, CMSX4. *Journal of Materials Science*, 37(3):481–487, 2002.
- [69] XB Meng, Q Lu, XL Zhang, JG Li, ZQ Chen, YH Wang, YZ Zhou, T Jin, XF Sun, and ZQ Hu. Mechanism of competitive growth during directional solidification of a nickel-base superalloy in a three-dimensional reference frame. *Acta Materialia*, 60(9):3965–3975, 2012.
- [70] Damien Tournet and Alain Karma. Growth competition of columnar dendritic grains: A phase-field study. *Acta Materialia*, 82:64–83, 2015.
- [71] Junjie Li, Zhijun Wang, Yaqin Wang, and Jincheng Wang. Phase-field study of competitive dendritic growth of converging grains during directional solidification. *Acta Materialia*, 60(4):1478–1493, 2012.
- [72] Tomohiro Takaki, Munekazu Ohno, Yasushi Shibuta, Shinji Sakane, Takashi Shimokawabe, and Takayuki Aoki. Two-dimensional phase-field study of competitive grain growth during directional solidification of polycrystalline binary alloy. *Journal of Crystal Growth*, 442:14–24, 2016.
- [73] Alexandre Viardin, Miha Založnik, Youssef Souhar, Markus Apel, and Hervé Combeau. Mesoscopic modeling of spacing and grain selection in columnar dendritic solidification: Envelope versus phase-field model. *Acta Materialia*, 122:386–399, 2017.
- [74] Damien Tournet, Younggil Song, Amy Jean Clarke, and Alain Karma. Grain growth competition during thin-sample directional solidification of dendritic microstructures: A phase-field study. *Acta Materialia*, 122:220–235, 2017.
- [75] Chunwen Guo, Junjie Li, Zhijun Wang, and Jincheng Wang. Non-uniplanar competitive growth of columnar dendritic grains during directional solidification in quasi-2D and 3D configurations. *Materials & Design*, 151:141–153, 2018.

- [76] Tomohiro Takaki, Takashi Shimokawabe, Munekazu Ohno, Akinori Yamanaka, and Takayuki Aoki. Unexpected selection of growing dendrites by very-large-scale phase-field simulation. *Journal of Crystal Growth*, 382:21–25, 2013.
- [77] Youn-Woo Lee, Richard N Smith, Martin E Glicksman, and Matthew B Koss. Effects of buoyancy on the growth of dendritic crystals. *Annual Review of Heat Transfer*, 7, 1996.
- [78] M Kind, WN Gill, and R Ananth. The growth of ice dendrites under mixed convection conditions. *Chemical engineering communications*, 55(1-6):295–312, 1987.
- [79] H. Jamgotchian, N. Bergeon, D. Benielli, Ph. Voge, B. Billia, and R. Guérin. Localized microstructures induced by fluid flow in directional solidification. *Physical Review Letters*, 87:166105, Oct 2001.
- [80] Y-J Chen and Stephen H Davis. Flow-induced patterns in directional solidification: localized morphologies in three-dimensional flows. *Journal of Fluid Mechanics*, 421:369–380, 2000.
- [81] Y. Lu, C. Beckermann, and J. C. Ramirez. Three-dimensional phase-field simulations of the effect of convection on free dendritic growth. *Journal of Crystal Growth*, 280(1-2):320–334, 2005.
- [82] Christoph Beckermann, H-J Diepers, Ingo Steinbach, Alain Karma, and Xinglin Tong. Modeling melt convection in phase-field simulations of solidification. *Journal of Computational Physics*, 154(2):468–496, 1999.
- [83] X Tong, Christophe Beckermann, Alain Karma, and Q Li. Phase-field simulations of dendritic crystal growth in a forced flow. *Physical Review E*, 63(6):061601, 2001.
- [84] CC Chen, YL Tsai, and CW Lan. Adaptive phase field simulation of dendritic crystal growth in a forced flow: 2D vs 3D morphologies. *International Journal of Heat and Mass Transfer*, 52(5-6):1158–1166, 2009.
- [85] N Shevchenko, O Roshchupkina, O Sokolova, and S Eckert. The effect of natural and forced melt convection on dendritic solidification in Ga–In alloys. *Journal of Crystal Growth*, 417:1–8, 2015.
- [86] William J Boettinger, James A Warren, Christoph Beckermann, and Alain Karma. Phase-field simulation of solidification. *Annual Review of Materials Research*, 32(1):163–194, 2002.
- [87] William J Boettinger and James A Warren. Simulation of the cell to plane front transition during directional solidification at high velocity. *Journal of Crystal Growth*, 200(3-4):583–591, 1999.

- [88] Alain Karma and Wouter-Jan Rappel. Quantitative phase-field modeling of dendritic growth in two and three dimensions. *Physical Review E*, 57(4):4323, 1998.
- [89] Alain Karma. Phase-field formulation for quantitative modeling of alloy solidification. *Physical Review Letters*, 87(11):115701, 2001.
- [90] William J Boettinger and James A Warren. The phase-field method: simulation of alloy dendritic solidification during recalescence. *Metallurgical and Materials Transactions A*, 27(3):657–669, 1996.
- [91] Ryo Kobayashi. Modeling and numerical simulations of dendritic crystal growth. *Physica D: Nonlinear Phenomena*, 63(3-4):410–423, 1993.
- [92] Nikolas Provatas and Ken Elder. *Phase-field methods in materials science and engineering*, volume 1. John Wiley & Sons, New York, 2011.
- [93] Alain Karma and Mathis Plapp. New insights into the morphological stability of eutectic and peritectic coupled growth. *The Journal of The Minerals, Metals & Materials Society*, 56(4):28–32, 2004.
- [94] Albert Schmid. A time dependent ginzburg-landau equation and its application to the problem of resistivity in the mixed state. *Physik der kondensierten Materie*, 5(4):302–317, 1966.
- [95] John W Cahn and John E Hilliard. Free energy of a nonuniform system. I. Interfacial free energy. *The Journal of Chemical Physics*, 28(2):258–267, 1958.
- [96] Pierre C Hohenberg and Bertrand I Halperin. Theory of dynamic critical phenomena. *Reviews of Modern Physics*, 49(3):435, 1977.
- [97] Ingo Steinbach, Franco Pezzolla, Britta Nestler, Markus Seeßelberg, Robert Prieler, Georg J Schmitz, and Joao LL Rezende. A phase field concept for multiphase systems. *Physica D: Nonlinear Phenomena*, 94(3):135–147, 1996.
- [98] B Nestler and AA Wheeler. A multi-phase-field model of eutectic and peritectic alloys: numerical simulation of growth structures. *Physica D: Nonlinear Phenomena*, 138(1-2):114–133, 2000.
- [99] Britta Nestler and Adam A Wheeler. Phase-field modeling of multi-phase solidification. *Computer Physics Communications*, 147(1-2):230–233, 2002.
- [100] JS Langer. Models of pattern formation in first-order phase transitions. In *Series on Directions in Condensed Matter Physics: Memorial Volume in Honor of Shang-Keng Ma*, volume 1, pages 165–186. World Scientific, Singapore, 1986.

- [101] Gunduz Caginalp and Paul Fife. Phase-field methods for interfacial boundaries. *Physical Review B*, 33(11):7792, 1986.
- [102] Gunduz Caginalp and Xinfu Chen. Phase field equations in the singular limit of sharp interface problems. In *On the Evolution of Phase Boundaries*, volume 43, pages 1–27. Springer, Switzerland, 1992.
- [103] Gunduz Caginalp. An analysis of a phase field model of a free boundary. *Archive for Rational Mechanics and Analysis*, 92(3):205–245, 1986.
- [104] Ryo Kobayashi. A numerical approach to three-dimensional dendritic solidification. *Experimental Mathematics*, 3(1):59–81, 1994.
- [105] GB McFadden, AA Wheeler, RJ Braun, SR Coriell, and RF Sekerka. Phase-field models for anisotropic interfaces. *Physical Review E*, 48(3):2016, 1993.
- [106] Bruno Grossmann, KR Elder, Martin Grant, and JM Kosterlitz. Directional solidification in two and three dimensions. *Physical Review Letters*, 71(20):3323, 1993.
- [107] Adam A Wheeler, William J Boettinger, and Geoffrey B McFadden. Phase-field model for isothermal phase transitions in binary alloys. *Physical Review A*, 45(10):7424, 1992.
- [108] Adam A Wheeler, William J Boettinger, and Geoffrey B McFadden. Phase-field model of solute trapping during solidification. *Physical Review E*, 47(3):1893, 1993.
- [109] Alain Karma and Wouter-Jan Rappel. Phase-field method for computationally efficient modeling of solidification with arbitrary interface kinetics. *Physical Review E*, 53(4):R3017, 1996.
- [110] Alain Karma. Phase-field formulation for quantitative modeling of alloy solidification. *Physical Review Letters*, 87:115701, Aug 2001.
- [111] BT Murray, AA Wheeler, and ME Glicksman. Simulations of experimentally observed dendritic growth behavior using a phase-field model. *Journal of Crystal Growth*, 154(3-4):386–400, 1995.
- [112] Nagendra Palle and Jonathan A Dantzig. An adaptive mesh refinement scheme for solidification problems. *Metallurgical and Materials Transactions A*, 27(3):707–717, 1996.
- [113] Nikolas Provatas, Nigel Goldenfeld, and Jonathan Dantzig. Efficient computation of dendritic microstructures using adaptive mesh refinement. *Physical Review Letters*, 80(15):3308, 1998.

- [114] Robert F Almgren. Second-order phase field asymptotics for unequal conductivities. *SIAM Journal on Applied Mathematics*, 59(6):2086–2107, 1999.
- [115] Blas Echebarria, Roger Folch, Alain Karma, and Mathis Plapp. Quantitative phase-field model of alloy solidification. *Physical Review E*, 70(6):061604, 2004.
- [116] Gunduz Caginalp and Weiqing Xie. Phase-field and sharp-interface alloy models. *Physical Review E*, 48(3):1897, 1993.
- [117] Seong Gyoon Kim, Won Tae Kim, and Toshio Suzuki. Phase-field model for binary alloys. *Physical Review E*, 60(6):7186, 1999.
- [118] Mathis Plapp. Unified derivation of phase-field models for alloy solidification from a grand-potential functional. *Physical Review E*, 84:031601, Sep 2011.
- [119] Britta Nestler, Harald Garcke, and Björn Stinner. Multicomponent alloy solidification: phase-field modeling and simulations. *Physical Review E*, 71(4):041609, 2005.
- [120] Johannes Hötzer, Philipp Steinmetz, Anne Dennstedt, Amber Genau, Michael Kellner, Irmak Sargin, and Britta Nestler. Influence of growth velocity variations on the pattern formation during the directional solidification of ternary eutectic Al-Ag-Cu. *Acta Materialia*, 136:335 – 346, 2017.
- [121] Johannes Hötzer, Marcus Jainta, Philipp Steinmetz, Britta Nestler, Anne Dennstedt, Amber Genau, Martin Bauer, Harald Kstler, and Ulrich Rde. Large scale phase-field simulations of directional ternary eutectic solidification. *Acta Materialia*, 93:194 – 204, 2015.
- [122] Philipp Steinmetz, Michael Kellner, Johannes Hötzer, Anne Dennstedt, and Britta Nestler. Phase-field study of the pattern formation in AlAgCu under the influence of the melt concentration. *Computational Materials Science*, 121:6 – 13, 2016.
- [123] Britta Nestler, Harald Garcke, and Björn Stinner. Multicomponent alloy solidification: Phase-field modeling and simulations. *Physical Review E*, 71:041609, Apr 2005.
- [124] Nele Moelans. A quantitative and thermodynamically consistent phase-field interpolation function for multi-phase systems. *Acta Materialia*, 59(3):1077–1086, 2011.
- [125] Johannes Hötzer, Oleg Tschukin, Marouen Ben Said, Marco Berghoff, Marcus Jainta, Georges Barthelemy, Nikolay Smorchkov, Daniel Schneider, Michael Selzer, and Britta Nestler. Calibration of a multi-phase field model with quantitative angle measurement. *Journal of Materials Science*, 51(4):1788–1797, 2016.

- [126] Johannes Hötzer, Andreas Reiter, Henrik Hierl, Philipp Steinmetz, Michael Selzer, and Britta Nestler. The parallel multi-physics phase-field framework pace3d. *Journal of Computational Science*, 26:1–12, 2018.
- [127] S-C Huang and ME Glicksman. Fundamentals of dendritic solidificationII development of sidebranch structure. In *Dynamics of Curved Fronts*, pages 263–280. Elsevier, 1988.
- [128] Roger Pieters and JS Langer. Noise-driven sidebranching in the boundary-layer model of dendritic solidification. *Physical Review Letters*, 56(18):1948, 1986.
- [129] Michael N Barber, Angelo Barbieri, and JS Langer. Dynamics of dendritic sidebranching in the two-dimensional symmetric model of solidification. *Physical Review A*, 36(7):3340, 1987.
- [130] DA Kessler and H Levine. Determining the wavelength of dendritic sidebranches. *EPL (Europhysics Letters)*, 4(2):215, 1987.
- [131] JS Langer. Dendritic sidebranching in the three-dimensional symmetric model in the presence of noise. *Physical Review A*, 36(7):3350, 1987.
- [132] Alain Karma. Fluctuations in solidification. *Physical Review E*, 48:3441–3458, Nov 1993.
- [133] Alain Karma and Wouter-Jan Rappel. Phase-field model of dendritic sidebranching with thermal noise. *Physical Review E*, 60:3614–3625, Oct 1999.
- [134] George Marsaglia and Thomas A Bray. A convenient method for generating normal variables. *SIAM review*, 6(3):260–264, 1964.
- [135] Michael Selzer. *Mechanische und Strömungsmechanische Topologieoptimierung mit der Phasefeldmethode*. Dissertation, KIT-Bibliothek, 2014.
- [136] Nigel Saunders and A Peter Miodownik. *CALPHAD (calculation of phase diagrams): A comprehensive guide*, volume 1. Pergamon Materials Series, Oxford, United Kingdom, 1998.
- [137] PJ Spencer. A brief history of calphad. *Calphad*, 32(1):1–8, 2008.
- [138] Tomonori Kitashima, Jincheng Wang, and Hiroshi Harada. Phase-field simulation with the CALPHAD method for the microstructure evolution of multi-component Ni-base superalloys. *Intermetallics*, 16(2):239–245, 2008.
- [139] J-L Fattebert, ME Wickett, and PEA Turchi. Phase-field modeling of coring during solidification of Au-Ni alloy using quaternions and CALPHAD input. *Acta Materialia*, 62:89–104, 2014.

- [140] Abhik Choudhury, Michael Kellner, and Britta Nestler. A method for coupling the phase-field model based on a grand-potential formalism to thermodynamic databases. *Current Opinion in Solid State and Materials Science*, 19(5):287–300, 2015.
- [141] R Rosenberg and M Ohring. Void formation and growth during electromigration in thin films. *Journal of Applied Physics*, 42(13):5671–5679, 1971.
- [142] HB Aaron and H I Aaronson. Growth of grain boundary precipitates in Al-4% Cu by interfacial diffusion. *Acta Metallurgica*, 16(6):789–798, 1968.
- [143] RL Eadie, GC Weatherly, and KT Aust. A study of sintering of spherical silver powder I. the intermediate stage. *Acta Metallurgica*, 26(5):759–767, 1978.
- [144] Robert L Coble. Effects of particle-size distribution in initial-stage sintering. *Journal of the American Ceramic Society*, 56(9):461–466, 1973.
- [145] RL Coble. A model for boundary diffusion controlled creep in polycrystalline materials. *Journal of Applied Physics*, 34(6):1679–1682, 1963.
- [146] Fuqian Yang and JCM Li. Impression creep of a thin film by vacancy diffusion. II. Cylindrical punch. *Journal of Applied Physics*, 74(7):4390–4397, 1993.
- [147] DJ Srolovitz and SA Safran. Capillary instabilities in thin films. I. energetics. *Journal of Applied Physics*, 60(1):247–254, 1986.
- [148] DJ Srolovitz and SA Safran. Capillary instabilities in thin films. II. kinetics. *Journal of Applied Physics*, 60(1):255–260, 1986.
- [149] Shihui Yu, Lingxia Li, Weifeng Zhang, Zheng Sun, and Helei Dong. Multilayer thin films with compositional PbZr 0.52 Ti 0.48 O 3/Bi 1.5 Zn 1.0 Nb 1.5 O 7 layers for tunable applications. *Scientific Reports*, 5:10173, 2015.
- [150] Junhua Xu, Koichiro Hattori, Yutaka Seino, and Isao Kojima. Microstructure and properties of CrN/Si₃N₄ nano-structured multilayer films. *Thin Solid Films*, 414(2):239–245, 2002.
- [151] SR Srinivasan and R Trivedi. Theory of grain boundary grooving under the combined action of the surface and volume diffusion mechanisms. *Acta Metallurgica*, 21(5):611–620, 1973.
- [152] William W Mullins. Theory of thermal grooving. *Journal of Applied Physics*, 28(3):333–339, 1957.
- [153] SC Hardy, GB McFadden, SR Coriell, Peter W Voorhees, and RF Sekerka. Measurement and analysis of grain boundary grooving by volume diffusion. *Journal of Crystal Growth*, 114(3):467–480, 1991.

- [154] Z Suo. Motions of microscopic surfaces. *Advances in applied mechanics*, 33:193–294, 1997.
- [155] WM Robertson. Grain boundary grooving and scratch decay on copper in liquid lead. *Transaction of the Metallurgical Society of AIME*, 233(7):1232–1236, 1965.
- [156] N Eustathopoulos. Energetics of solid/liquid interfaces of metals and alloys. *International Metals Reviews*, 28(1):189–210, 1983.
- [157] BS Bokstein, L Mt Klinger, and IV Apikhtina. Liquid grooving at grain boundaries. *Materials Science and Engineering: A*, 203(1-2):373–376, 1995.
- [158] Arnab Mukherjee, Kumar Ankit, Rajdip Mukherjee, and Britta Nestler. Phase-field modeling of grain-boundary grooving under electromigration. *Journal of Electronic Materials*, 45(12):6233–6246, 2016.
- [159] W Zhang and I Gladwell. Thermal grain boundary grooving with anisotropic surface free energy in three dimensions. *Journal of Crystal Growth*, 277(1-4):608–622, 2005.
- [160] Charles Archibald Steidel, Che-Yu Li, and CW Spencer. *Grain boundary grooving in the presence of a liquid*. PhD thesis, Cornell University, 1963.
- [161] KT Miller, FF Lange, and DB Marshall. The instability of polycrystalline thin films: Experiment and theory. *Journal of Materials Research*, 5(1):151–160, 1990.
- [162] DRH Jones and GA Chadwick. Experimental measurement of the solid-liquid interfacial energies of transparent materials. *Philosophical Magazine*, 22(176):291–300, 1970.
- [163] L Ratke and HJ Vogel. Theory of grain boundary grooving in the convective-diffusive regime. *Acta Metallurgica et Materialia*, 39(5):915–923, 1991.
- [164] TP Nolan, R Sinclair, and R Beyers. Modeling of agglomeration in polycrystalline thin films: Application to TiSi₂ on a silicon substrate. *Journal of Applied Physics*, 71(2):720–724, 1992.
- [165] S Pramanick, Yu N Erokhin, BK Patnaik, and GA Rozgonyi. Morphological instability and si diffusion in nanoscale cobalt silicide films formed on heavily phosphorus doped polycrystalline silicon. *Applied Physics Letters*, 63(14):1933–1935, 1993.
- [166] Spencer L Thomas, Kongtao Chen, Jian Han, Prashant K Purohit, and David J Srolovitz. Reconciling grain growth and shear-coupled grain boundary migration. *Nature Communications*, 8(1):1–12, 2017.
- [167] Huifang Zhang and Harris Wong. Coupled grooving and migration of inclined grain boundaries: Regime II. *Acta Materialia*, 50(8):1995–2012, 2002.

- [168] K Ikeuchi, Y Zhou, H Kokawa, and TH North. Liquid-solid interface migration at grain boundary regions during transient liquid phase brazing. *Metallurgical Transactions A*, 23(10):2905–2915, 1992.
- [169] Fuqian Yang. Effect of grain boundary migration on grain boundary grooving. *Computational Materials Science*, 7(3):279–284, 1997.
- [170] Seong Gyoon Kim and Yong Bum Park. Grain boundary segregation, solute drag and abnormal grain growth. *Acta Materialia*, 56(15):3739–3753, 2008.
- [171] Yuchuan Shao, Yanjun Fang, Tao Li, Qi Wang, Qingfeng Dong, Yehao Deng, Yongbo Yuan, Haotong Wei, Meiyu Wang, Alexei Gruverman, et al. Grain boundary dominated ion migration in polycrystalline organic–inorganic halide perovskite films. *Energy & Environmental Science*, 9(5):1752–1759, 2016.
- [172] A Seifert, A Vojta, JS Speck, and FF Lange. Microstructural instability in single-crystal thin films. *Journal of Materials Research*, 11(6):1470–1482, 1996.
- [173] K Ogrady, LE Fernandez-Outon, and G Vallejo-Fernandez. A new paradigm for exchange bias in polycrystalline thin films. *Journal of Magnetism and Magnetic Materials*, 322(8):883–899, 2010.
- [174] D Amram, L Klinger, N Gazit, H Gluska, and E Rabkin. Grain boundary grooving in thin films revisited: The role of interface diffusion. *Acta Materialia*, 69:386–396, 2014.
- [175] Hui Xing, Xianglei Dong, Hongjing Wu, Guanhua Hao, Jianyuan Wang, Changle Chen, and Kexin Jin. Degenerate seaweed to tilted dendrite transition and their growth dynamics in directional solidification of non-axially oriented crystals: a phase-field study. *Scientific Reports*, 6:26625, 2016.
- [176] N Noël, H Jamgotchian, and B Billia. Influence of grain boundaries and natural convection on microstructure formation in cellular directional solidification of dilute succinonitrile alloys in a cylinder. *Journal of Crystal Growth*, 187(3-4):516–526, 1998.
- [177] SY Yeh, CC Chen, and CW Lan. Phase field modeling of morphological instability near grain boundary during directional solidification of a binary alloy: The hump formation. *Journal of Crystal Growth*, 324(1):296–303, 2011.
- [178] W Miller, A Popescu, and G Cantù. Solidification of multicrystalline silicon simulation of micro-structures. *Journal of Crystal Growth*, 385:127–133, 2014.
- [179] E Brener, H Müller-Krumbhaar, and D Temkin. Kinetic phase diagram and scaling relations for stationary diffusional growth. *EPL (Europhysics Letters)*, 17(6):535, 1992.

- [180] Eshel Ben-Jacob, G Deutscher, Peter Garik, Nigel D Goldenfeld, and Y Lareah. Formation of a dense branching morphology in interfacial growth. *Physical Review Letters*, 57(15):1903, 1986.
- [181] B. Utter, R. Ragnarsson, and E. Bodenschatz. Alternating tip splitting in directional solidification. *Physical Review Letters*, 86(20):4604–4607, 2001.
- [182] Johann Nittmann and H Eugene Stanley. Tip splitting without interfacial tension and dendritic growth patterns. *Nonlinear Physics for Beginners: Fractals, Chaos, Solitons, Pattern Formation, Cellular Automata and Complex Systems*, 321:166, 1998.
- [183] Martin E Glicksman. Capillary-mediated interface perturbations: Deterministic pattern formation. *Journal of Crystal Growth*, 450:119–139, 2016.
- [184] JA Dantzig, Paolo Di Napoli, J Friedli, and M Rappaz. Dendritic growth morphologies in Al-Zn alloys part II: phase-field computations. *Metallurgical and Materials Transactions A*, 44(12):5532–5543, 2013.
- [185] David A Kessler, Joel Koplik, and Herbert Levine. Geometrical models of interface evolution. II. numerical simulation. *Physical Review A*, 30(6):3161, 1984.
- [186] Richard C. Brower, David A. Kessler, Joel Koplik, and Herbert Levine. Geometrical models of interface evolution. *Physical Review A*, 29:1335–1342, Mar 1984.
- [187] Olivier Martin and Nigel Goldenfeld. Origin of sidebranching in dendritic growth. *Physical Review A*, 35(3):1382, 1987.
- [188] Andrew M Mullis. Deterministic side-branching during thermal dendritic growth. *IOP Conference Series: Materials Science and Engineering*, 84(1):012071, 2015.
- [189] PW Voorhees, SR Coriell, GB McFadden, and RF Sekerka. The effect of anisotropic crystal-melt surface tension on grain boundary groove morphology. *Journal of Crystal Growth*, 67(3):425–440, 1984.
- [190] JI Cahn and DI Hoffman. A vector thermodynamics for anisotropic surfaces II. curved and faceted surfaces. *Acta Metallurgica*, 22(10):1205–1214, 1974.
- [191] Shan Shang, Zhipeng Guo, and Zhiqiang Han. On the kinetics of dendritic side-branching: A three dimensional phase field study. *Journal of Applied Physics*, 119(16):164305, 2016.
- [192] Alexander Vondrous, Michael Selzer, Johannes Hötzer, and Britta Nestler. Parallel computing for phase-field models. *The International Journal of High Performance Computing Applications*, 28(1):61–72, 2014.

- [193] B. Utter and E. Bodenschatz. Dynamics of low anisotropy morphologies in directional solidification. *Physical Review E - Statistical, Nonlinear, and Soft Matter Physics*, 66(5):1–11, 2002.
- [194] Kumar Ankit, Hui Xing, Michael Selzer, Britta Nestler, and Martin E Glicksman. Surface rippling during solidification of binary polycrystalline alloy: Insights from 3-d phase-field simulations. *Journal of Crystal Growth*, 457:52–59, 2017.
- [195] Nikolas Provatas, Quanyong Wang, Mikko Haataja, and Martin Grant. Seaweed to dendrite transition in directional solidification. *Physical Review Letters*, 91(15):155502, 2003.
- [196] R. Rezakhaniha, A. Agianniotis, J. T. C. Schrauwen, A. Griffa, D. Sage, C. V. C. Bouten, F. N. van de Vosse, M. Unser, and N. Stergiopoulos. Experimental investigation of collagen waviness and orientation in the arterial adventitia using confocal laser scanning microscopy. *Biomechanics and Modeling in Mechanobiology*, 11(3):461–473, Mar 2012.
- [197] F. Gesellchen, A. L. Bernassau, T. Djardin, D. R. S. Cumming, and M. O. Riehle. Cell patterning with a heptagon acoustic tweezer application in neurite guidance. *Lab Chip*, 14:2266–2275, 2014.
- [198] Timothy Fee, Crawford Downs, Alan Eberhardt, Yong Zhou, and Joel Berry. Image-based quantification of fiber alignment within electrospun tissue engineering scaffolds is related to mechanical anisotropy. *Journal of Biomedical Materials Research Part A*, 104(7):1680–1686.
- [199] W Kurz and DJ Fisher. Dendrite growth at the limit of stability: tip radius and spacing. *Acta Metallurgica*, 29(1):11–20, 1981.
- [200] I Steinbach. Pattern formation in constrained dendritic growth with solutal buoyancy. *Acta Materialia*, 57(9):2640–2645, 2009.
- [201] N DSouza, R Beanland, C Hayward, and HB Dong. Accuracy of composition measurement using X-ray spectroscopy in precipitate-strengthened alloys: Application to ni-base superalloys. *Acta Materialia*, 59(3):1003–1013, 2011.
- [202] N Dsouza and HB Dong. Solidification path in third-generation ni-based superalloys, with an emphasis on last stage solidification. *Scripta Materialia*, 56(1):41–44, 2007.
- [203] Hongbiao Dong, Wei Wang, and Peter D Lee. Simulation of the thermal history dependence of primary spacing during directional solidification. *Superalloys*, 2004:925–931, 2004.

- [204] D Welton, N DSouza, J Kelleher, S Gardner, ZH Dong, GD West, and Hongbiao Dong. Discontinuous precipitation in Ni-base superalloys during solution heat treatment. *Metallurgical and Materials Transactions A*, 46(9):4298–4315, 2015.
- [205] CL Brundidge, D Van Drasek, B Wang, and TM Pollock. Structure refinement by a liquid metal cooling solidification process for single-crystal nickel-base superalloys. *Metallurgical and Materials Transactions A*, 43(3):965–976, 2012.
- [206] R Trivedi and JT Mason. The effects of interface attachment kinetics on solidification interface morphologies. *Metallurgical Transactions A*, 22(1):235–249, 1991.
- [207] Jun Hui, R Tiwari, X Wu, Surendra N Tewari, and R Trivedi. Primary dendrite distribution and disorder during directional solidification of Pb-Sb alloys. *Metallurgical and Materials Transactions A*, 33(11):3499–3510, 2002.
- [208] HS Whitesell and RA Overfelt. Influence of solidification variables on the microstructure, macrosegregation, and porosity of directionally solidified Mar-M247. *Materials Science and Engineering: A*, 318(1-2):264–276, 2001.
- [209] Anthony F Giamei and BH Kear. On the nature of freckles in nickel base superalloys. *Metallurgical Transactions*, 1(8):2185–2192, 1970.
- [210] MLNM Melo, EMS Rizzo, and RG Santos. Predicting dendrite arm spacing and their effect on microporosity formation in directionally solidified Al-Cu alloy. *Journal of Materials Science*, 40(7):1599–1609, 2005.
- [211] JD Hunt. Pattern formation in solidification. *Science and Technology of Advanced Materials*, 2(1):147–155, 2001.
- [212] Hui Chen, Yu Shi Chen, X Wu, and SN Tewari. History dependence of primary dendrite spacing during directional solidification of binary metallic alloys and interdendritic convection. *Journal of Crystal Growth*, 253(1-4):413–423, 2003.
- [213] H-J Diepers, D Ma, and I Steinbach. History effects during the selection of primary dendrite spacing. comparison of phase-field simulations with experimental observations. *Journal of Crystal Growth*, 237:149–153, 2002.
- [214] Myung-Jin Suk, Young-Min Park, and Young-Do Kim. Dendrite spacing and microstructure evolution dependent on specimen history. *Scripta Materialia*, 57(11):985–987, 2007.
- [215] RM Sharp and A Hellawell. The microscopy and composition of quenched solid-liquid interfaces. *Journal of Crystal Growth*, 5(3):155–161, 1969.
- [216] N Tunca and RW Smith. Variation of dendrite arm spacing in Al-rich Zn-Al off-eutectic alloys. *Journal of Materials Science*, 23(1):111–120, 1988.

- [217] DH Kirkwood. A simple model for dendrite arm coarsening during solidification. *Materials Science and Engineering*, 73:L1–L4, 1985.
- [218] Eli Vandersluis and Comondore Ravindran. Comparison of measurement methods for secondary dendrite arm spacing. *Metallography, Microstructure, and Analysis*, 6(1):89–94, 2017.
- [219] Theo Z Kattamis. Influence of coarsening on dendrite arm spacing of aluminum-copper alloys. *Transaction of the Metallurgical Society of AIME*, 239:1504–1511, 1967.
- [220] DH Kirkwood. Microsegregation. *Materials Science and Engineering*, 65(1):101–109, 1984.
- [221] A Mortensen. On the rate of dendrite arm coarsening. *Metallurgical Transactions A*, 22(2):569–574, 1991.
- [222] Machiko Ode, Seong Gyoon Kim, Won Tae Kim, and Toshio Suzuki. Numerical prediction of the secondary dendrite arm spacing using a phase-field model. *Iron and Steel Institute of Japan International*, 41(4):345–349, 2001.
- [223] Ang Zhang, Shaoxing Meng, Zhipeng Guo, Jinglian Du, Qigui Wang, and Shoumei Xiong. Dendritic growth under natural and forced convection in Al-Cu alloys: From equiaxed to columnar dendrites and from 2D to 3D phase-field simulations. *Metallurgical and Materials Transactions B*, 50(3):1514–1526, 2019.
- [224] Sonja Steinbach and Lorenz Ratke. The influence of fluid flow on the microstructure of directionally solidified AlSi-base alloys. *Metallurgical and Materials Transactions A*, 38(7):1388–1394, 2007.
- [225] JA Spittle and DM Lloyd. *Solidification and Casting of Metals*, volume 192. Metals Society, 1979.
- [226] Dominique Bouchard and John S Kirkaldy. Prediction of dendrite arm spacings in unsteady-and steady-state heat flow of unidirectionally solidified binary alloys. *Metallurgical and Materials Transactions B*, 28(4):651–663, 1997.
- [227] Merton C Flemings. Solidification processing. *Metallurgical Transactions*, 5(10):2121–2134, 1974.
- [228] Tresa M Pollock and Sammy Tin. Nickel-based superalloys for advanced turbine engines: chemistry, microstructure and properties. *Journal of propulsion and power*, 22(2):361–374, 2006.

- [229] D Walton and B Chalmers. The origin of the preferred orientation in the columnar zone of ingots. *Transactions of the American Institute of Mining and Metallurgical Engineers*, 215(3):447–457, 1959.
- [230] Michel Rappaz and Ch-A Gandin. Probabilistic modelling of microstructure formation in solidification processes. *Acta Metallurgica et Materialia*, 41(2):345–360, 1993.
- [231] Michel Rappaz, Ch A Gandin, Jean-Luc Desbiolles, and Ph Thevoz. Prediction of grain structures in various solidification processes. *Metallurgical and Materials Transactions A*, 27(3):695–705, 1996.
- [232] R Trivedi, Yunzue Shen, and Shan Liu. Cellular-to-dendritic transition during the directional solidification of binary alloys. *Metallurgical and Materials Transactions A*, 34(2):395–401, 2003.
- [233] Ch-A Gandin and Michel Rappaz. A 3D cellular automaton algorithm for the prediction of dendritic grain growth. *Acta Materialia*, 45(5):2187–2195, 1997.
- [234] Tomohiro Takaki, Shinji Sakane, Munekazu Ohno, Yasushi Shibuta, and Takayuki Aoki. Permeability prediction for flow normal to columnar solidification structures by large-scale simulations of phase-field and lattice boltzmann methods. *Acta Materialia*, 164:237–249, 2019.
- [235] V Pavan Laxmipathy, Fei Wang, Michael Selzer, and Britta Nestler. Microstructural transition in monotectic alloys: A phase-field study. *International Journal of Heat and Mass Transfer*, 159:120096, 2020.
- [236] Akihiko Kamio, Shinji Kumai, and Hiroyasu Tezuka. Solidification structure of monotectic alloys. *Materials Science and Engineering: A*, 146(1-2):105–121, 1991.